NORTHWESTERN UNIVERSITY

Kinematics and Segregation in Granular Flows: Modeling Density
Difference, Shape Effects, and Unsteady Flow Fields

A DISSERTATION

SUBMITTED TO THE GRADUATE SCHOOL

IN PARTIAL FULFILLMENT OF THE REQUIREMENTS

for the degree

DOCTOR OF PHILOSOPHY

Field of Mechanical Engineering

By

Hongyi Xiao

EVANSTON, ILLINOIS

September 2018

ABSTRACT

Kinematics and Segregation in Granular Flows: Modeling Density Difference, Shape Effects, and Unsteady Flow Fields

Hongyi Xiao

Segregation of granular materials with different particle properties (e.g., size and density) is a ubiquitous phenomenon in nature and industry. In this thesis, different segregation mechanisms are studied in steady granular heap flows. Flow kinematics and segregation in transient granular flows are also explored.

First, this thesis studies segregation of flowing density bidisperse materials. The flow kinematics are extracted from Discrete Element Method (DEM) simulations, and a relation between the density segregation velocity and the particle density ratio, the local shear rate, and the local concentration is found. A continuum segregation model is adapted to include the density segregation velocity and the model is capable of quantitatively predicting density segregation in bounded heap flows. Segregation of rod-shaped particles with different lengths is also investigated. DEM simulations of cylindrical rod particles reveal a relation between the segregation velocity and the local shear rate, the local species concentration, and the rod length ratio, similar to the relation for spherical particles. This relation is again incorporated into the continuum segregation model which accurately predicts segregation of rod-shaped particles in bounded heap flows.

By modulating the feed rate in size bidisperse bounded heap flows, unsteady flows are generated leading to stratification of small and large particles, which is different from the streamwise segregation formed in steady flows. The stratification pattern formed in the modulated flow can be controlled by modulation parameters and demonstrates better mixing than the streamwise segregation. The stratification mechanism is related to non-uniform deposition during transient heap flows. When the feed rate suddenly changes, a growing (or vanishing) wedge of materials originates on the free surface near the feed zone and propagates downstream, indicating non-uniform deposition or erosion occurring during the transient process. The transient flux and surface height profile can be modeled by a local relationship between the local flux and the local slope angle in combination of a continuity equation. Modulating the feed rate is not the only method to generate unsteady heap flows. By increasing the water content in damp granular materials, a transition from steady to unsteady flow can occur. The unsteady flow is a time-periodic flow with each period consisting of a non-depositing downslope avalanche and an upslope propagating granular jump. The transition occurs when the surface angle of the heap is increased (as a result of increasing cohesion) beyond the neutral angle of deposition. The unsteady flow results in inhomogeneous packing density in the deposited heap. In addition, hopper discharge segregation is studied, which is a transient industrial process which occurs after heap formation (hopper filling). DEM simulations reveal that segregation mainly occurs in a surface layer where particles are transported from the sidewall to the hopper center. The continuum segregation model is applied to modeling the particle concentration distribution in the surface layer and the bulk region using velocity profiles developed based on a kinematic model and DEM observations.

Acknowledgements

I would like to thank my academic advisors, Rich Lueptow, Julio Ottino, and Paul Umbanhowar, for their support throughout my time at Northwestern. They have provided me an excellent platform to develop a good understanding of scientific research and to build relevant technical skills. I am grateful that they gave me enough freedom to explore and realize my own ideas, and that they kept me motivated and offered great guidance to make my work better. They have also demonstrated to me that being a top academic researcher is not just about performing advanced experiments and simulations, but is also about educating people, spreading ideas, making impact, and more importantly, enjoying all of these. I also thank my thesis committee members, Gregory Wagner and James Hambleton, for helpful feedback on my work.

I would like to thank the colleagues in my research group, Zafir Zaman, Austin Isner, Paul Park, Darius Wheeler, Alex Fry, Mengqi (Miki) Yu, Zhekai Deng, Ryan Jones, Adithya Shankar, Thomas Lynn, Lachlan Smith, Vidushi Dwivedi, and John Hruska. This is a truly interdisciplinary group of researchers. Discussions and collaborations with them have been inspiring and very helpful. The time we spent together on non-scientific activities is also good memory.

In addition, I would like to acknowledge collaborators out of my research group including Yongzhi Zhao from Zhejiang University, Yi Fan, Madhu Kodam, Karl Jacob, and Jim Koch from the Dow Chemical Company, and Jinhui Yan here at Northwestern. These

collaborations are valuable experiences that broadened my horizons. I also gratefully acknowledge the financial support from NSF Grant No. CBET-1511450.

Finally, I would like to thank my parents, friends, and my girlfriend, Maxin Chen. This journey would not have been possible without their support and encouragement.

Table of Contents

List of Tables

List of Figures

CHAPTER 1

Introduction

1.1. Granular flows

A granular material is a state of matter composed of individual solid particles [**1, 2**]. Granular materials are processed ubiquitously in industries such as chemical, pharmaceutical, agricultural, food, mining, building, and construction. They are the second most used form of matter behind water in industry, and processing granular materials consumes roughly 10% of all the energy produced on earth [**3**]. They also play important roles in some fast growing technologies such as additive manufacturing, where plastic and metal powders are frequently used, and advanced energy technologies, where they can appear in many forms such as biofuel feedstock and nuclear pebbles [**4**]. Granular materials also have important implications in nature such as debris flows [**5**] and pyroclastic flows [**6**], and in extraterrestrial exploration [**7, 8**].

Although granular materials are ubiquitous, a complete understanding of their physics and the technologies for effectively modeling and processing granular materials are still lacking. This is because granular materials are complicated as they are disordered and heterogeneous materials. They are often far from equilibrium and exhibit non-linear responses to external forces [**2, 9**]. Also, granular materials are dissipative due to the inelastic collisions and friction that occur between particles. The variety of particle shapes and inter-particle interactions such as electrostatic forces, liquid bridge forces, and adhesion forces can also complicate the behavior of the materials [**10, 11, 12, 13**]. In addition, the separation of length scales, which occurs in the study of fluid systems, is sometimes lacking in granular materials [**2, 14, 15**]. The particle scale often overlaps with the system scale, evident by force chains [**16**] and non-local behaviors of materials [**17, 18**]. As a result, granular materials can often display complicated behaviors [**2**]. They can behave
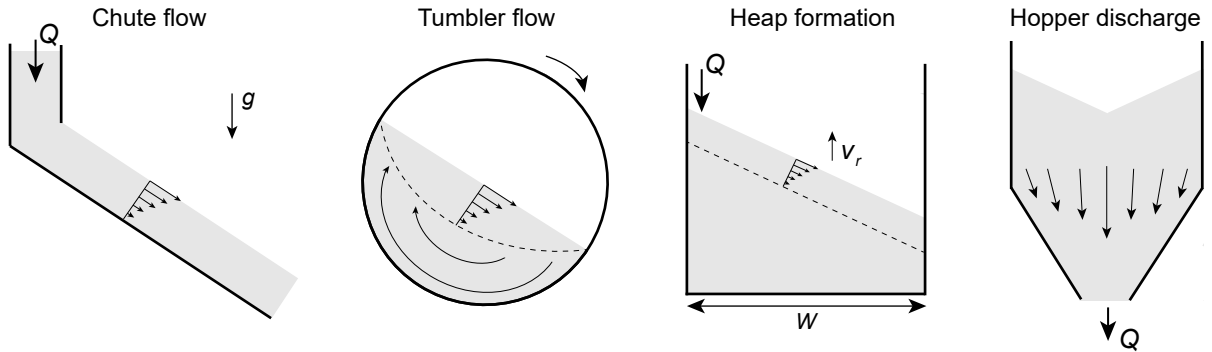
Figure 1.1. Canonical granular free surface flow geometries.

like solids by remaining static and are able to bear loads, like sand on a beach. They can also be liquid-like and flow when driven by external forces such as gravity. Under strong external excitation such as vibration or when they are entrained by air, they can behave like a gas where intermittent binary collisions dominate the contact between particles. Although this study focuses primarily on granular flows, it should be kept in mind that the other two phases often coexist with the flowing phase in the same system, evident in this study as a fixed bed of particles below a flowing layer or bouncing particles above the surface of a flowing layer.

Granular flow occurs when materials are being processed, transferred, and deposited. Figure 1.1 illustrates four canonical gravity-driven flow geometries that are extracted from nature and industrial applications: chute flow, tumbler flow, heap flow, and hopper discharge flow [19]. In the first three geometries, particles flow due to gravity and the motion is localized in a thin flowing layer near the free surface with the largest velocity occurs near the free surface. In chute flows (with sidewalls) or inclined plane flows (without sidewalls), particles flow down an inclined bottom surface and exit the chute. In rotating tumbler flows, particles flow down the angled surface of the partially-filled tumbler, deposit on the fixed bed below, and then circulate back to the flowing layer under solid body rotation. In heap flows, particles flow down the angled surface in a flowing layer over a static bed of particles. When a bounding wall is present at the downstream end, as shown in Fig. 1.1, the free surface rises as particles are deposited onto the heap, indicating

material exchange between the flowing layer and the static bed [**20, 21**]. As the velocity at the free surface is often larger than the velocity at the bottom of the flowing layer, shear often exists in the flowing layer as depicted in the velocity profiles in Fig. 1.1, inducing important phenomena such as segregation and diffusion [**22**]. Hopper discharge flow occurs as particles in the hopper flow toward the outlet. It is not a free surface flow, and the velocity field can become rather complicated within the hopper [**23**]. However, this is an important flow that occurs widely in industry. Granular flow can also occur under external shear, such as in annular shear cells [**24**] and split-bottom shear cells [**25, 26**], or driven by fluid flow such as sedimentary transport [**27**], which is not the focus of this work. This thesis mainly focuses on heap flows and hopper discharge flows. Note that these two flows can become a combined process in industry, as hopper filling is essentially heap formation.

Since granular flow has important implications in industrial and geophysical processes, characterizing and modeling granular flow is of great importance. However, this is challenging because granular flow exhibits many differences from the flow of conventional Newtonian fluids [**19, 14, 15**]. The first noticeable difference is that a bed of particles can remain static while its free surface is inclined, as evident by sand piles and heaps of coal and agricultural products. Flow only occurs when the surface of the heap exceeds an angle called the static angle of repose [**28**]. The interface between static materials and flowing materials can be complicated due to erosion and deposition but is also important for granular flows. Examples include modeling deposition in heap formation (Fig. 1.1) and predicting natural hazards in geophysical situations such as landslides and debris flows [**29, 30, 31, 32, 33**].

Modeling the kinematics in the flowing layer is also challenging, as the shear stress is nonlinearly dependent on the shear rate and the pressure [**19, 14**]. Phenomenological constitutive theories have been proposed to model granular flows with the most well-accepted approach being the $\mu(I)$ rheology [**19, 34, 35, 36**], which posits that the shear stress τ is related to the normal stress P as $\tau = \mu(I)P$. In this relation, the friction coefficient μ depends on the inertial number $I = \dot{\gamma}d/(P/\rho)^{0.5}$, where $\dot{\gamma}$ is the shear rate and

ρ is the particle density. This rheology is capable of predicting the velocity field in rapid shallow flows such as chute flows, and it can capture unsteady flows [37, 38]. However, this type of rheology is not suitable for capturing the quasi-static region in depositing flows, as shear independent non-local phenomena often exist [17], which are just starting to be resolved by non-local rheology models developed in the last few years [17, 18, 39]. Therefore, for canonical systems such as the ones shown in Fig. 1.1, it is possible to develop kinematic descriptions based on measurements from experiments and computational simulations [21, 40], which will be discussed later.

While steady flows are already challenging to understand and model, unsteady granular flows exhibits more complicated behaviors. A handful of studies on unsteady granular flows have revealed complicated kinematics during transient processes. For example, in rotating tumblers under a periodic forcing protocol [41, 42], phase lags between the external forcing and the response of granular flow occur, indicating a delayed response of the granular system to external excitation. In heap flows, instantaneous velocity profiles measured during intermittent avalanches show that the acceleration and deceleration of the flow during each avalanche is significantly different [43]. In addition, unsteady free surface flows are often accompanied by a variety of traveling waves [44, 31, 29, 45, 46, 47, 48], which also requires further understanding. It is important to understand unsteady granular flows, as most industrial and geophysical processes involve unsteady flow, and unsteady flow can have significant influence on granular segregation. Hence, the focus of this research is on such unsteady granular flows.

1.2. Segregation in granular flows

Due to the polydispersity of most granular materials, segregation of particles with different properties often occurs [49, 22]. For example, in geophysical situations such as landslides and debris flows, segregation can alter the local flow properties, which can trigger levee formation and extend the run-out distance [50, 51]. In industry, segregation in bulk solids handling processes such as transport and storage often results in poor product quality, which can cause significant economic loss [52, 53]. Thus, predicting and controlling segregation is important. Yet the understanding of the underlying physics

Size segregation   Density segregation
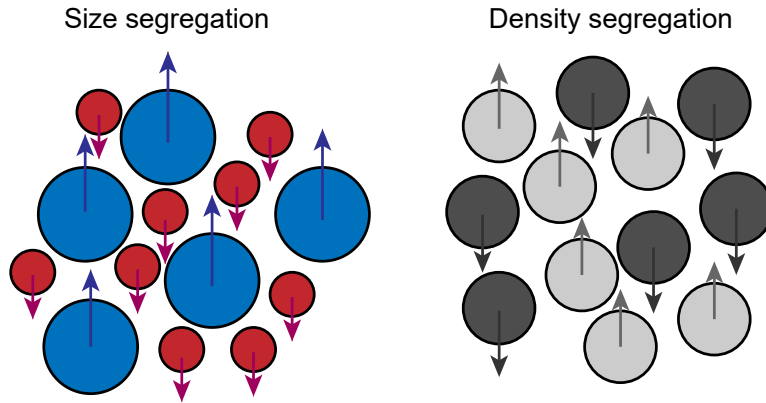
Figure 1.2.   Size segregation and density segregation (dark for heavy particles and light gray for light particles).

is still incomplete in terms of segregation mechanisms as well as segregation in complicated situations such as unsteady flows. Moreover, advanced technologies for minimizing segregation in industrial situations are needed.

Segregation of granular materials can be caused by the difference in various material properties such as size [**54, 55**], density [**56, 57**], surface roughness [**44, 58**], and particle elasticity [**59**]. Among these properties, size and density segregation are the most prominent mechanisms, as depicted in Fig. 1.2. For size segregation in dense, sheared granular flows, a widely accepted percolation-based mechanism posits that voids between particles are generated because of shear and smaller particles are more likely to fall into the voids under gravity [**55**]. Consequently, large particles are pushed upward to the free surface. In granular flows, this mechanism often leads to the formation of segregation patterns, such as particle segregation in chute flows [**60**], see Fig. 1.3a, where small particles are located near the chute surface and large particles are located near the free surface.

Density segregation is driven by a similar mechanism to size segregation, where heavy particles tend to sink toward the bottom of the flow, while light particles tend to rise toward the free surface [**61, 57, 56**]. This mechanism often results in patterns similar to size segregation, see Fig. 1.3b, where, in a tumbler, heavy particles accumulate near the tumbler core and light particles accumulate at the tumbler periphery. Note that
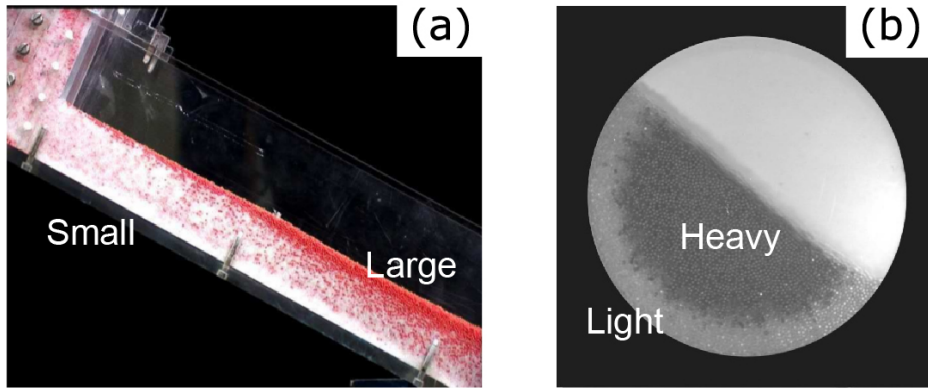
Figure 1.3. Segregation in granular flows. (a) Size segregation of small (white) and large (red) particles in an inclined chute flow, from Thornton et al. [60], ©2012 World Scientific. (b) Density segregation in a circular tumbler, from Jain et al. [61], ©2005 American Physical Society.

most previous studies have focused on segregation of spheres; segregation of non-spherical particles has been significantly less explored.

In recent decades, experimental, computational, and theoretical studies have been carried out to study segregation in granular flows [49, 22]. Experiments have long been used for understanding granular flow and segregation. These experiments are performed in relatively simple geometries characteristic of industrial settings and geophysical situations such as inclined chute flows, rotating tumblers, heap formation, and hopper discharge (e.g., [62, 63, 20, 64]), as shown in Fig. 1.1. For quasi-2D bounded heaps flows, mixtures of particles are added into the system at the left end at a volumetric feed rate Q. The flow is confined within a narrow silo with thickness T and width W made by vertical sidewalls and bounding walls [20]. The free surface of the heap is inclined due to the inter-particle friction and the wall friction [28, 34]. This flow configuration is important to understand as it can be viewed as a simplified version of the 3D conical heap, variations of which occur widely in nature and in industrial processes such as hopper filling. Under steady feed rates, binary mixtures of particles will enter the system in a well mixed state and then segregate as they flow downstream. Small particles segregate out of the flowing layer
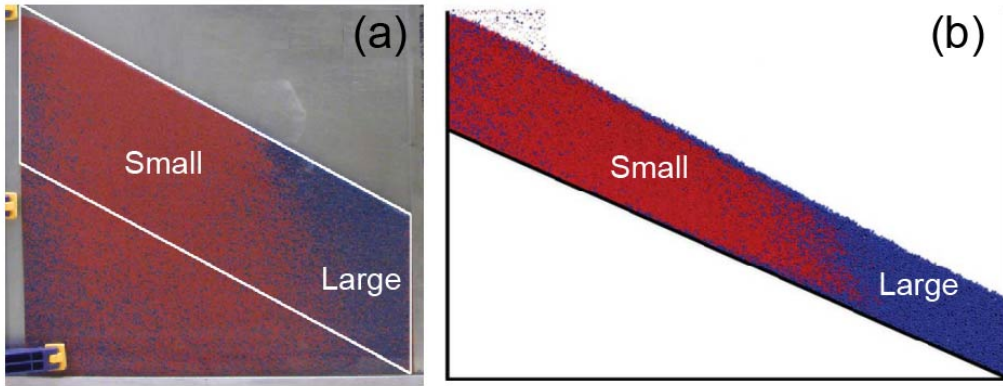
Figure 1.4. Segregation of a size bidisperse mixture ($2\,\text{mm}$ and $1\,\text{mm}$) of (a) experiments and (b) simulations in a quasi-2D bounded heap with width $W = 0.44\,\text{m}$ and gap thickness $T = 0.09\,\text{m}$, from Schlick et al. [65], ©2015 John Wiley & Sons.

first and deposit in the upstream portion of the heap, while large particles rise to the free surface and flow further to be deposited downstream, see Fig. 1.4a.

While experiments are suitable for observing phenomenological features, measuring detailed kinematics at the particle scale is challenging and often requires sophisticated measurement techniques [66, 67, 68, 69]. Alternatively, kinematic information can be extracted from experimentally validated computer simulations at lower cost. With the advance of computational techniques, various types of discrete particle simulations that compute particle trajectories and interactions between particles have been developed [70, 71]. For dense granular flows, Discrete Element Method (DEM) simulation is often applied [71]. In DEM simulations, inter-particle interaction forces are calculated and the translational and rotational momenta of the particles are determined. By integrating Newton's Second Law, the acceleration, velocity, and displacement of every particle in the simulation can be determined at each time step [72]. An example of DEM simulation results [65] for segregation in a quasi-2D bounded heap is shown in Fig. 1.4b, which demonstrates that the DEM simulation can reproduce the experimental segregation patterns. In DEM simulations, because the position, velocity, and acceleration of each individual particle can be calculated, the properties at the continuum level can also be extracted, such as the velocity field, packing density, concentration distribution, and

stress distribution, providing more details than is possible with experiments. However, although DEM simulations can be highly parallelized to be able to simulate lab-scale granular flows efficiently [**65**], it is currently too expensive to model large-scale systems in real applications as these system usually contain extremely large quantities of particles. For example, a box of volume $1\,\text{m}^3$ can hold approximately 10^{12} particles with $0.1\,\text{mm}$ diameter, which is several order of magnitude larger than what DEM simulations can handle (millions of particles). Thus, modeling segregation using continuum models that can be applied to industrial systems is important.

Various types of continuum models have been proposed for characterizing and modeling segregating granular flows. To model segregation, a modified transport equation with the inclusion of a segregation term is often adopted (e.g., [**73, 74, 75, 76, 77, 78, 40**]) and can be applied to the flowing layer. A general form can be written as

$$(1.1) \qquad \frac{\partial c_i}{\partial t} + \nabla \cdot (\boldsymbol{u} c_i) + \frac{\partial}{\partial z}(w_{s,i} c_i) - \nabla \cdot (D \nabla c_i) = 0,$$

where c_i is the concentration of species i, $\boldsymbol{u}$ is the mean velocity field, $w_{s,i}$ is the segregation velocity for species i, and D is the diffusion coefficient. The streamwise direction is x and the direction normal to the flow is z, which is the direction in which segregation occurs.

To close the model, kinematics quantities including $\boldsymbol{u}$, $w_{s,i}$, and D need to be provided. For the advection field, two approaches are typically applied. The first approach is to couple Eq. 1.1 with constitutive theories [**56, 77, 46**]. As discussed earlier, constitutive theories [**19, 34, 35, 36, 17, 18**] have only been tested in relatively simple geometries such as steady chute flow, which is essentially one dimensional. For more complicated geometries such as tumbler flows and heap flows, the streamwise gradient needs to be considered and special treatments are needed to account for deposition and erosion between the flowing layer and the static bed [**79, 80, 30, 32, 30, 29, 81**]. Moreover, most constitutive theories have been developed under the assumption that the particles are monodisperse, thus coupling with the segregation model requires non-trivial modifications to these constitutive theories [**50, 51, 82**]. Alternatively, for particle flow systems commonly encountered in nature and industry, such as chute, tumbler, and heap flows, it
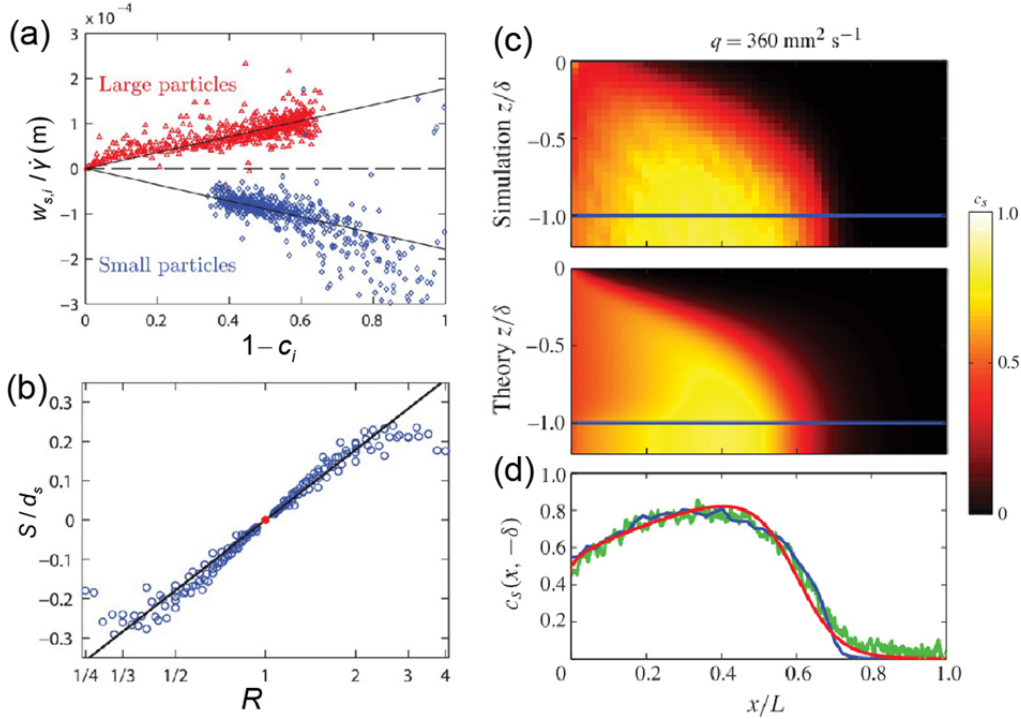
Figure 1.5. (a) The relation of segregation velocity to the shear rate and concentration of small particles, c_s, from Schlick et al. [65], ©2015 John Wiley & Sons. (b) The relation of the segregation length scale to the particle size ratio, R, and the small particle diameter, from Schlick et al. [65], ©2015 John Wiley & Sons. (c) Comparison of c_s from the DEM simulation with the theoretical prediction from the continuum model, from Fan et al. [40], ©2014 Cambridge University Press. (b) Comparison of the concentration profile in the deposited bed from theory (red), experiment (green), and simulation (blue), from Fan et al. [40], ©2014 Cambridge University Press.

is possible to measure the kinematics directly from experiments and simulations to develop universal scaling laws that can be applied to systems of various sizes [21, 83, 65, 60]. This approach is capable of providing accurate velocity fields to the continuum segregation model, which in turn yields accurate predictions of the concentration fields [40, 83]. Furthermore, simulations can provide other parameters such as the diffusion coefficient, D [56, 40]. However, for the quasi-2D bounded heap, only the kinematics for steady flows have been measured, and the unsteady kinematics remain unexplored.

The segregation velocity, $w_{s,i}$, is essential to the continuum model, Eq. 1.1. Savage & Lun proposed a model for percolation based on statistical arguments and derived a size segregation velocity which is related to particle properties, the local concentration, and the local shear rate [55]. Since that work was published, in 1988, various forms of $w_{s,i}$ have been proposed. Some forms derived from mixture theories indicate that the segregation is due to the unequal partition of the stresses between large and small particles [84, 76, 77, 85]. In a recent work [40], a simple but accurate form for the segregation velocity was proposed as

$$(1.2) \qquad\qquad w_{s,i} = S\dot{\gamma}(1 - c_i),$$

where S is a segregation length scale that depends on the particle size ratio R and particle size [65]. This relation has been validated using DEM simulations of bidisperse flow in heaps as shown in Fig. 1.5a. Here, the quantity $w_{s,i}/\dot{\gamma}$ is plotted as a function of $1 - c_i$ for many locations in a bounded heap flow. By Eq. 1.2, the slope of the line through the data is S. Note that for the large particles, $w_{s,l} > 0$, while for small particles, $w_{s,s} < 0$. Fig. 1.5b shows the dependence of S on the particle size ratio R. By substituting Eq. 1.2 into Eq. 1.1, along with other kinematics information measured in DEM simulations, the continuum model can accurately predict the concentration field in various steady flows [40, 83, 86, 57, 87]. The continuum model can be solved numerically, and an example [40] of its prediction is shown in Fig. 1.5c, where the concentration fields of small particles in the flowing layer (of depth δ and length L) from the theoretical predictions and DEM simulation are shown. Near the feed zone on the left, the small particle concentration is close to 0.5 indicating a mixed inlet. At the upstream region, segregation can be observed with c_s larger at the bottom than near the free surface. At the downstream region, c_s is zero indicating that this region is completely occupied by large particles due to segregation, similar to Fig. 1.4. Further validation is shown in Fig. 1.5d, where the concentration profiles of the small particles deposited on the bed are shown. In both Fig. 1.5c and 1.5d, the transport model predictions agree quantitatively with experimental and simulation results, showing that the continuum model is able to capture size segregation accurately. While this approach was developed for size segregation of spherical particles, it is useful to
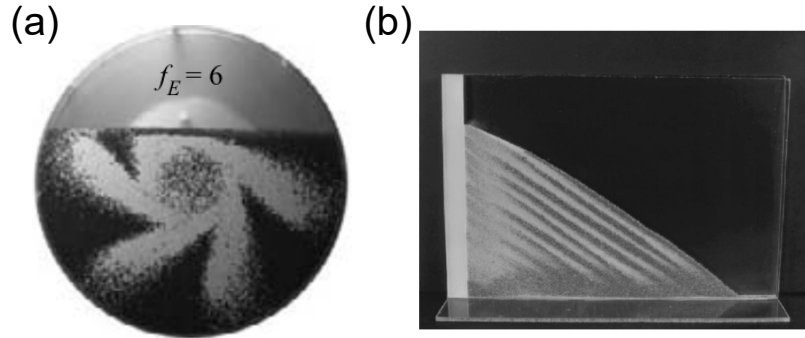
Figure 1.6. Size segregation in unsteady granular flows. (a) Streak formation in a circular tumbler with large (dark) and small (light gray) particles under modulated rotation rate, from Fiedor & Ottino [**62**], ©2005 Cambridge University Press. (b) Stratification of small rounded particles (light gray) and large irregular-shaped particles (dark gray) in a quasi-2D heap, from Makse et al. [**88**], ©1998 American Physical Society.

extend the model to capture size segregation of non-spherical particles as well as density segregation, which will be discussed in detail in Chapters 2 and 3.

Understanding and modeling segregation in unsteady granular flows is also challenging, as both the kinematics and the flowing domain change along with the concentration field for small and large particles. As segregation strongly depends on details of the flow kinematics, segregation in unsteady flows is likely to differ significantly from segregation in steady flows [**46, 89, 83, 90**]. The more complicated kinematics in unsteady flows suggest increased challenges in understanding and predicting segregation of granular materials, but also a richer range of possibilities for mixing or segregation-induced pattern formation [**91, 62, 92, 93, 94, 63, 45, 88, 95**]. An example, shown in Fig. 1.6a, is the dynamics of segregation pattern formation in time-periodic tumbler flows where the tumbler rotation rate is modulated [**62, 92**]: discrete streaks of small particles form instead of the typical semicircular segregated core of small particles that occurs for steady flow, and the properties of the streaks depend on the modulation scheme. Another example, shown in Fig. 1.6b, is the spontaneous stratification of particles differing in both shape and size in a quasi-2D heap [**44, 88**]. The difference in particle shape triggers a periodic unsteady

flow which (in combination with segregation) results in layering of small round particles and large irregular-shaped particles [**88**]. These segregation patterns in unsteady flows are more complicated than the patterns formed in steady flows (Figs. 1.3 and 1.4). Better understanding of transient kinematics and unsteady segregation should offer insights for predicting and controlling segregation in granular systems.

1.3. Organization of the dissertation

In this dissertation, experiments, computational simulations, and theoretical modeling are utilized to understand two important aspects of granular flow and segregation.

The first part of the dissertation, Chapters 2 and 3, focuses on generalizing the continuum model (Eq. 1.1) to include more segregation mechanisms. Chapter 2 extends the continuum model to capture segregation of density bidisperse materials in granular heap flows, and Chapter 3 further considers the segregation of non-spherical rod-like particles with different lengths but equal diameters. In both studies, DEM simulations are used to obtain the kinematics of the flow and the corresponding segregation mechanisms, and the continuum model is adapted to predict concentration distributions that quantitatively agree with experiments and DEM simulations.

The second part of the dissertation, Chapters 4-7 focuses on understanding and modeling kinematics and segregation in transient granular flows, and generating unsteady flows to minimize segregation.

Chapter 4 explores the pattern formation of size bidisperse materials under unsteady heap flows triggered by modulating the feed rate. Controlled stratification of large and small particles that result from the modulated flow can enhance the overall mixing.

Chapter 5 further studies the underlying transient flow in a bounded heap during a sudden change in the feed rate which reveals how the stratification described in Chapter 4 forms.

Chapter 6 explores a different approach of generating unsteady granular flows by mixing a small amount of water with granular materials. A transition from steady to unsteady flow occurs during heap formation when the granular materials become more

damp, which opens up another possibility for generating unsteady flow to minimize overall segregation.

Chapter 7 presents the results of applying the continuum model to predict size segregation in hopper discharge flows, which is a subsequent process to hopper filling where segregation during heap formation occurs. This is a transient process with important applications in industry.

Chapter 8 summarizes the main results of the dissertation and outlines possible future directions for study.

CHAPTER 2

Modeling density segregation in flowing bidisperse granular materials

SUMMARY

Understanding and modeling segregation of granular materials due to density difference is important for preventing segregation in industrial processes that involve the handling of bulk solids. In this chapter, the continuum segregation model (Eq. 1.1) is extended to include density-driven segregation, thereby validating the approach for two important cases of practical interest (size and density). DEM simulations of density bidisperse flows of mono-sized particles in a quasi-two-dimensional-bounded heap were performed to determine the dependence of the density-driven segregation velocity on local shear rate and particle concentration. The model yields theoretical predictions of segregation patterns that quantitatively match the DEM simulations over a range of density ratios and flow rates. Matching experiments reproduce the segregation patterns and quantitative segregation profiles obtained in both the simulations and the model, thereby demonstrating that the modelling approach captures the essential physics of density-driven segregation in granular heap flow.

2.1. Introduction

Granular materials with different particle properties tend to segregate spontaneously when they are flowing [**96, 69, 49, 97**] or vibrating [**98, 99, 100**]. Such segregation is frequently encountered in industrial processes that involve handling bulk solids [**52, 101**]

as well as in geophysical transport such as debris flows [5], pyroclastic flows [6], and mineral transport [102]. Thus, modeling and predicting segregation is important, yet accurate models that can be broadly applied are only just now being developed.

Among different particle properties that can drive segregation, particle size [55] and density [103] are critical factors. The focus of this work is the segregation due to differences in particle density, which can occur in vibrated granular mixtures [104, 105, 106, 107, 108], free surface flows [56, 61, 109, 110, 76], and vertical chute flows [111]. In gravity-driven free surface flows, particles with lower density are more likely to rise to the free surface while particles with higher density are more likely to segregate to the bottom of the flowing layer, resulting in segregation patterns such as a segregated core or streaks of heavier particles in rotating tumblers [103, 61, 109, 110]. While particle based simulation methods can reproduce density driven segregation phenomena on a small scale, an accurate continuum-based model would be of clear practical and theoretical value.

Various continuum models have been proposed for predicting segregation in granular flows. Bridgwater [73] developed a continuum-based model that uses a segregation velocity based on percolation due to particle size differences. Savage & Lun [55] applied a statistical mechanics approach based on kinetic sieving and squeeze expulsion mechanisms and derived a size segregation velocity related to the particle properties, the local concentration, and the shear rate, which was assumed constant. Variations of these continuum models have been applied to other geometries such as chute [84, 75, 46, 76, 74, 68, 112, 60, 113, 77, 114] and annular shear [24] flows, and some have achieved qualitative agreement with simulations and experiments. The continuum models are also evolving with more details being considered. Gray & Chugunov [75] successfully included the effect of diffusion into the continuum modeling framework. Marks *et al.* [77] included the effect of local shear rate on the segregation flux and achieved qualitative agreement with simulations. Recently, Tripathi & Khakhar [56], Tunuguntla *et al.* [76], and Gray & Ancey [114] incorporated bidisperse density segregation into the continuum model. These studies applied segregation velocities proportional to the normalized density difference and other parameters. Though the models showed a degree of agreement with simulations,

validation of the segregation velocity or segregation patterns was not considered in detail. Here, we propose a continuum model for density bidisperse segregation with a different approach to defining the segregation velocity, and we validate it by comparing predictions of this approach to both discrete element method (DEM) simulations and experiments.

In our recent work, we developed a continuum based approach for predicting segregation of granular materials that achieves quantitative agreement with simulations and experiments of size bidisperse, multidisperse, and polydisperse granular materials in different geometries [**40, 83, 65, 86**]. Similar to the previous models discussed above, this model is also based on the transport equation

$$(2.1) \qquad \frac{\partial c_i}{\partial t} + \nabla \cdot (\boldsymbol{u} c_i) + \frac{\partial}{\partial z}(w_{s,i} c_i) - \nabla \cdot (D \nabla c_i) = 0,$$

which includes the affects of advection, segregation, and diffusion. Eq. 2.1 is applied to the thin flowing layer (having length L and depth δ), where segregation occurs in most gravity driven flows. We define x as the streamwise direction ($0 < x < L$) and z as the normal direction ($-\delta < z < 0$), with $z = 0$ at the surface of the flowing layer. Terms with subscripts i represent the properties for species i in a bidispere mixture (h for heavy and l for light in the case of density segregation), while terms without subscripts represent the average flow properties of both species. The concentration of species i is defined as $c_i = f_i/f$, where f_i is the volume fraction for species i, and f is the total volume fraction of both species. The mean 2D velocity field is $\boldsymbol{u} = u\hat{\boldsymbol{x}} + w\hat{\boldsymbol{z}}$, and D is the diffusion coefficient. The segregation velocity, $w_{s,i}$, is defined as the relative normal velocity component of species i with respect to the total normal velocity component of both species: $w_{s,i} = w_i - w$. In the segregation term $\frac{\partial}{\partial z}(w_{s,i} c_i)$, only flows normal to the free surface are considered, since segregation occurs primarily in this direction, and the gradient of concentration in the streamwise direction is small. Unlike previous approaches where unknown free constants are retained in the models [**84, 75**], or closure relations are proposed by coupling the transport equation with constitutive theories [**77, 56**], we inform our model with physical control parameters and kinematic parameters acquired from DEM simulations [**65**] or experiments in a similar way as explored in Thornton *et*

al. [**60**] for segregation in a chute flow. Thus, no fitting parameters are needed. While we consider the quasi-2D case here, the model can be extended to fully three-dimensional systems.

In this research, this continuum model is used to predict the segregation of density bidisperse granular materials in a quasi-2D bounded heap, which typically exhibits complicated kinematics [**30, 115, 81, 21**] with different segregation patterns including stratified layers of the two types of particles [**116**], fully segregated particles [**117, 118**], and mixed particles with no segregation [**20**]. Here we study the continuous flow regime for which stratification does not occur [**20**]. DEM simulations are performed to determine the kinematics of density bidisperse flows, and experiments are performed to verify the results of simulations and theoretical predictions. Sec. 2.2 describes the quasi-2D bounded heap geometry, the DEM simulation methods, and the experiments. In Sec. 2.3, we show that the simulations quantitatively reproduce the experimental results and discuss the flow kinematics. In Sec. 2.4, the continuum model (Eq. 2.1) is non-dimensionalized and solved numerically. The results are compared with simulation and experimental results for different cases, and the influence of physical control parameters on segregation is discussed. Sec. 2.5 presents the conclusions.

2.2. Simulation and experimental methods

2.2.1. DEM simulations

In DEM simulations, the translational and rotational momenta of each particle are tracked using integration of Newton's Second Law. As in previous work [**40, 83, 65, 21**], the normal force model used here is the linear-spring dashpot model [**72, 119, 120**], in which the normal contact force between two particles is $\boldsymbol{F}_{ij}^n = [k_n\epsilon - 2\gamma_n m_{eff}(\boldsymbol{V}_{ij} \cdot \hat{\boldsymbol{r}}_{ij})]\,\hat{\boldsymbol{r}}_{/ij}$. In this relation, ϵ and $\boldsymbol{V}_{ij}$ represent the overlap and relative velocity between two contacting particles i and j, respectively. The unit normal vector between two particles is $\hat{\boldsymbol{r}}_{ij}$, and $m_{eff} = m_i m_j/(m_i + m_j)$ denotes the effective mass. The normal stiffness k_n and damping γ_n are determined from the restitution coefficient e and binary collision time t_c: $k_n = [(\pi/t_c)^2 + \gamma_n^2]m_{eff}$ and $\gamma_n = -\ln(e)/t_c$, where ln is the natural logarithm. The
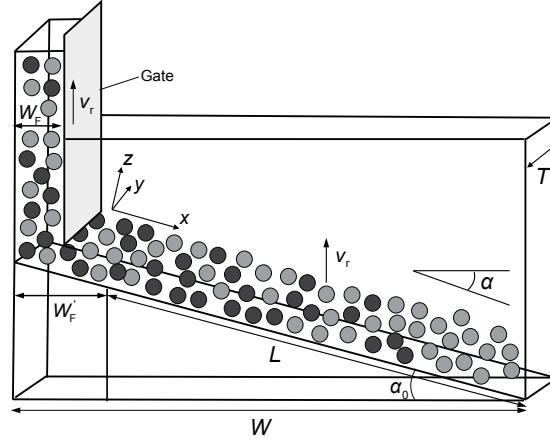
Figure 2.1. Schematic (not to scale) of a quasi-2D bounded heap for DEM simulations and experiments (with flowing layer length L and gap thickness T). In simulations, the bottom wall is inclined at an angle $\alpha_0 = 16°$ to reduce the number of particles and thus the simulation time. The surface rise velocity, v_r, depends on the flow rate which is controlled by the vertical rise velocity of the gate located a distance W_F from the upstream wall.

tangential force model is the linear spring model with Coulomb friction [119], which can be expressed as $\boldsymbol{F}_{ij}^t = -\min(|k_s\beta|, |\mu\boldsymbol{F}_{ij}^n|)\mathrm{sgn}(\beta)\hat{\boldsymbol{s}}$. Here, the tangential stiffness $k_s = \frac{2}{7}k_n$, and the tangential displacement is $\beta(t) = \int_{t_s}^t \boldsymbol{V}_{ij}^s dt$ [121], where t_s is the initial contact time and $\boldsymbol{V}_{ij}^s$ is the relative tangential velocity. The friction coefficient is μ, and the unit vector in the tangential direction is $\hat{\boldsymbol{s}}$. In real granular systems, materials with different densities ρ often have different surface and elastic properties. Here, to ensure that density is the only driving mechanism for segregation in simulations, identical material properties are applied except for the density. The binary collision time is $t_c = 10^{-3}\,\mathrm{s}$, which is small enough to accurately describe the flow of hard spheres [21]. The restitution coefficient is $e = 0.9$ and the friction coefficient is $\mu = 0.2$. These values are selected so that the dynamic repose angle α in simulations matches the dynamic repose angle in experiments. Negligible differences in segregation occur over a range of values for t_c, e, and μ, indicating that the simulations are relatively insensitive to the specific values used within the range of feed rates and density ratios tested in this specific geometry. For particle-wall contact, the same forces models and material properties are used with the walls, which have infinite

mass and radius. The time step for the simulations is set to $t_c/40 = 2.5 \times 10^{-5}$ s, which ensures numerical stability [65].

A schematic of the simulation geometry is shown in Fig. 2.1. The quasi-2D bounded heap consists of two parallel plates with two bounding endwalls. The width between the bounding endwalls is $W = 0.5$ m and gap thickness between the parallel plates is $T = 0.016$ m. To save computation time, the bottom wall is inclined at an angle $\alpha_0 = 16°$, which is smaller than the dynamic repose angle α (which ranges from $18°$ to $21°$ in different cases). Initially the bottom wall is covered with a layer of immobilized particles. After the particles flowing into the system form a 10-15 particle diameters thick layer, the velocity profiles and concentration profiles in the flowing layer become steady, indicating that the effect of the bottom wall can be neglected. In simulations, density bidisperse particles enter the system at a volume feed rate of Q and volume ratio of 1:1. The particle diameter d is uniformly distributed with a variance of $\pm 0.1d$ to reduce crystallization. Particles of 2, 3, and 4 mm diameters are simulated. The flow of mixed particles onto the heap is controlled by a rising gate. The rising gate eliminates bouncing particles caused by free fall of the particles [20], which can influence density segregation dramatically in small systems like this one. The gate, located at $W_F = 0.06$ m, controls the vertical rise velocity $v_r = Q/WT$ of the heap surface. For data analysis, we neglect flow in the feed zone and the area affected by the feed zone which extends to $W_F' \approx 0.15$ m (with small adjustments in different cases), resulting in an effective flowing layer length $L = (W - W_F')/\cos\alpha$. An effective 2D feed rate can be defined as $q = v_r' L = v_r L \cos\alpha$, where $v_r' = v_r \cos\alpha$ is the rise velocity normal to the free surface. In the moving reference frame of the rising flowing layer, the origin is located on the free surface at W_F'. It is oriented such that x is in the streamwise direction, y is in the thickness direction, and z is normal to the surface of the flowing layer. u, v, and w are the velocities in the x, y, and z directions, respectively.

As in our recent work[65], simulations were performed on an Nvidia GTX 780 graphics card (Graphics Processing Unit) with a parallelized DEM algorithm. Simulations with different feed rates, density ratios, and particle sizes were performed. Details of the kinematics are discussed in Sec. 2.3.
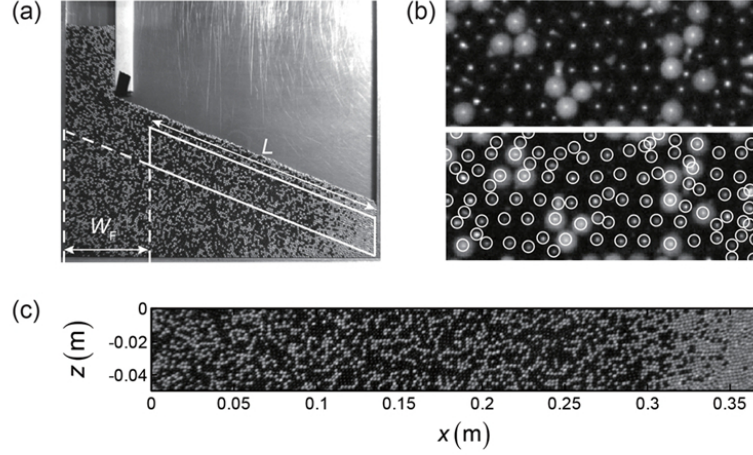
Figure 2.2. Image processing of frames captured by a high speed camera using steel (dark) and ceramic particles (white). (a) A portion (solid white box) of the original image is extracted that captures the final segregation pattern of particles deposited on the heap. (b) Particles are identified for the PTV algorithm in a close-up of the image. (c) Boxed region in (a) after rotating and shearing.

2.2.2. Experiments

To validate the DEM simulations and theoretical predictions, experiments were performed with equal diameter particles with different densities, as indicated in table 2.1. For each particle type, 100 sample particles were randomly selected and the diameter and the total weight of each was measured. Table 2.1 lists the average and standard deviation of the diameter and the density calculated by dividing the sum of the volume of each individual particle by the total weight measured for each particle type.

Table 2.1. Particle properties in experiments.

Material	Color	Diameter (mm)	Density (g/cm^3)
Steel	Dark	2.98 ± 0.04	7.84
Glass	Clear	3.00 ± 0.03	2.58
Ceramic (Zirconium silicate)	White	3.05 ± 0.09	4.17
High density ceramic (Zirconium oxide)	White	3.12 ± 0.10	6.32

The geometry of the experimental system is the same as the simulation geometry ($W = 0.5\,\mathrm{m}$ and $T = 0.016\,\mathrm{m}$). Particle mixtures were held in a hopper and fed into the system by an auger feeder (Acrison, Inc., NJ, USA) at the desired volume feed rate. The rising gate was implemented as a vertical metal bar lifted by a linear actuator (Firgelli Automations Inc., WA, USA) with a control board (Firgelli Technologies Inc, Canada). The experiments were recorded using a high speed camera (Point Grey Research Inc., Canada) with frame rates up to 400 frames/s. Video images were obtained during steady filling of the heap at the downstream end of the flowing layer in contact with the vertical bounding wall and were analyzed to provide concentration profiles of the segregation pattern in the fixed bed and velocity profiles in the flowing layer.

The average image intensity was used to calculate the concentration profile in the streamwise direction for particles in the fixed bed below the flowing layer. The region in Fig. 2.2a outlined by the white box was analyzed to characterize the final segregation pattern achieved during steady filling. The boxed image was rotated by the repose angle and sheared into a rectangular domain so that each column of the image has the same streamwise coordinate [20], as shown in Fig. 2.2c. The average image intensity at each streamwise location was calculated from the image. Reference image intensities of pure heavy particles and pure light particles were used to calibrate the grey scale.

Particle tracking velocimetry (PTV) was used to determine the velocity profiles in the flowing layer. In this case, the portion of the system to be analyzed extended to the surface of the flow (shifting the box in Fig. 2.2a upward so its top edge coincided with the surface of the flowing layer). In close-up images of steady heap flow and with proper lighting conditions, the steel particles can be identified as dark regions with small specular highlights (bright spots) on them, and the ceramic particles can be identified as white or gray spheres. This allows us to apply a MATLAB based PTV code [67] to filter noise and identify the center positions of all the particles (Fig. 2.2b). Using a series of images, we computed the velocity of every particle and obtained the streamwise and normal velocity profiles at various locations along the length of the flowing layer for steady filling of a steel and ceramic particle mixture. The resulting velocity field was used to validate the

simulation results. Small errors could potentially result from particles that are not at the wall but visible in gaps between particles at the wall and are therefore not well lighted, as shown in Fig. 2.2b. However, the misidentified particles are fewer than 5% of the total particles identified, and this error is minimized by spatial and temporal averaging, so it only causes slight fluctuation in the resulting velocity field, but not any systematic error. Thus, any possible error does not influence the comparison with DEM simulation results.

2.2.3. Validation of the simulations

Results from a typical DEM simulation and experiment with 3 mm steel and ceramic particles are compared in Fig. 2.3. In both cases, the particles are mixed in the inlet region on the left and become more segregated downstream. More ceramic particles flow to the end of the heap forming a region with high ceramic particle concentration. The angle of repose for the simulation (21.4°) is also similar to that for the experiment (22.1°). A quantitative comparison of light particle concentration (c_l) profiles at the bottom of the flowing layer (deposited on the heap) vs. position (Fig. 2.3c) shows good agreement between simulation and experiment, demonstrating that the DEM simulation is able to capture the physics of bidisperse density segregation. Validation of the kinematics of the flow in DEM is described in the next section.

2.3. Kinematics of density bidisperse flow

2.3.1. Streamwise velocity

The streamwise velocity for the steel and ceramic particle example described in Sec. 2.2 in both simulations and experiments calculated using the volume average binning method [21] is shown in Fig. 2.4. For the binning, we use equal and non-overlapping bins of $\Delta x \times \Delta y \times \Delta z$. In simulations, we use $\Delta x = 0.01$ m, $\Delta y = 0.016$ m, and $\Delta z = 0.001$ m. In experiments, we use $\Delta x = 0.02$ m and $\Delta z = 0.004$ m (only particles adjacent to the wall can be observed). In the binning process, we bin the particles based on their partial volumes inside each bin in the z direction, similar to the method used by Freireich, *et al.* [122]. By doing this, along with time averaging over about 5 s, we are able to use small
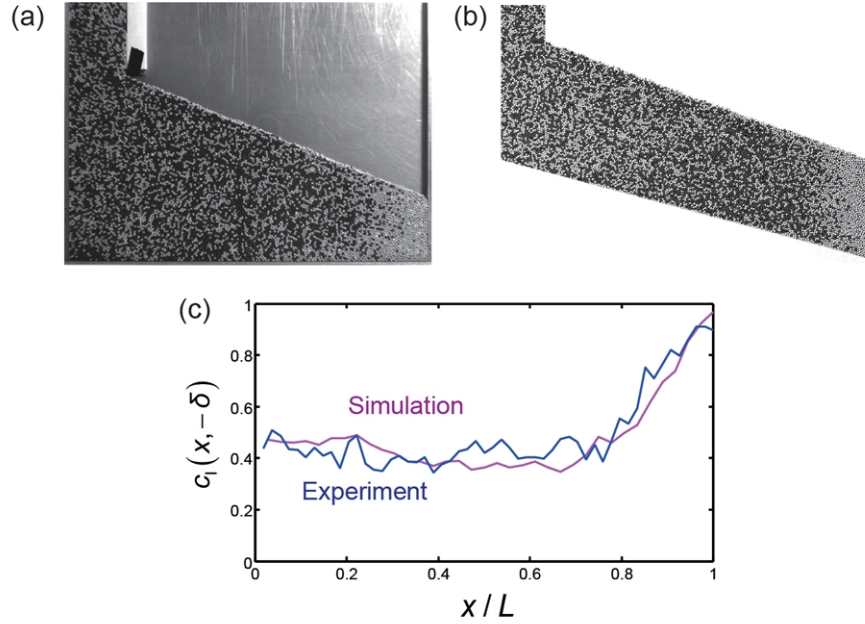
Figure 2.3. Images comparing segregation in (a) experiment and (b) simulation of lighter ceramic (white) and heavier steel (dark) particles with $q = 0.0032\,\mathrm{m^2/s}$. (c) Ceramic particle concentration in the fixed bed beneath the flowing layer.

Table 2.2. Nine simulations with different density ratios, feed rates, and particle diameters.

Symbol	R_D	$q\ (\mathrm{m^2/s})$	$d\ (\mathrm{mm})$
□	1.88	0.0022	3
∗	1.88	0.0041	3
▽	1.88	0.0061	3
×	1.43	0.0022	2
○	1.88	0.0022	2
▷	2.00	0.0022	2
△	1.43	0.0022	4
◇	1.88	0.0022	4
◁	2.00	0.0022	4
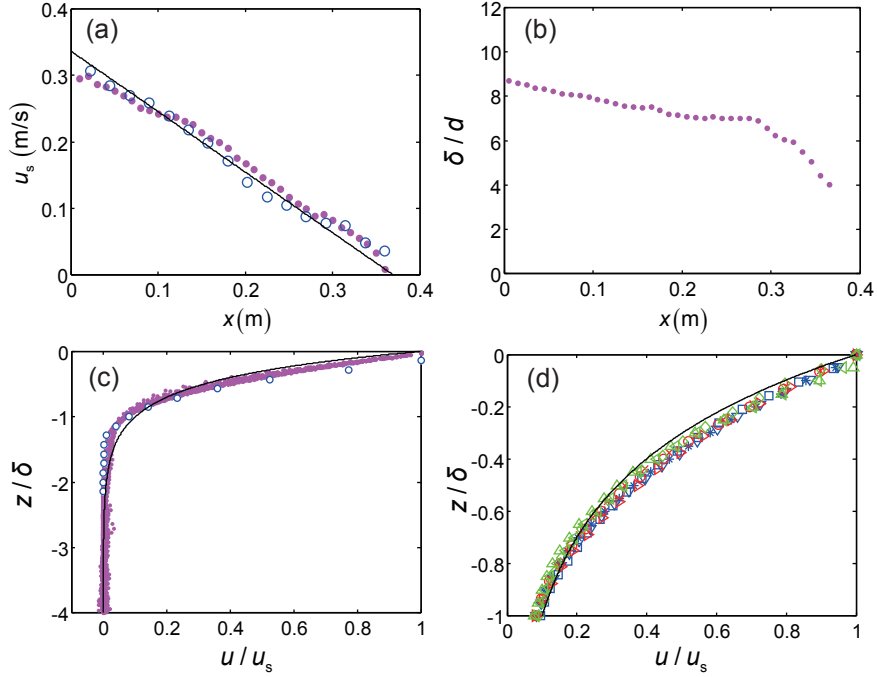
Figure 2.4. Streamwise velocity profiles in simulation (dots, purple or light gray) and experiment (circles, blue or dark gray), using ceramic and steel particles at feed rate $q = 0.0032\,\mathrm{m^2/s}$. (a) Surface streamwise velocity along streamwise direction. The solid line is $u(x,0) = \frac{kq}{\delta(1-e^{-k})}\left(1 - \frac{x}{L}\right)$. (b) Normalized flowing layer thickness along streamwise direction. (c) Normalized streamwise profile at various positions along the length of the flowing layer. The solid curve is $u/u_s = e^{kz/\delta}$. (d) Streamwise velocity profiles at $x/L = 0.5$ for 9 different simulation cases in table 2.2 collapse on to the solid curve $u/u_s = e^{kz/\delta}$.

bin sizes in the z direction to capture more details while still maintaining accuracy [21]. Figure 2.4a shows the free surface streamwise velocity, u_s, along the length of the flowing layer. Results from the experiment and the simulation agree well, exhibiting a nearly linear decrease along the streamwise direction, which is again consistent with a uniform deposition of particles on the heap with an approximately constant flowing layer thickness [21]. Figure 2.4b shows the flowing layer thickness $\delta(x)$ along the streamwise direction based on the streamwise velocity profile, calculated using the criteria $u(x, -\delta) = 0.1u(x, 0)$ [21].

The flowing layer thickness remains almost constant at 7-8.5 particle diameters for most of the length of the flowing layer, except near the downstream end, again consistent with previous results [21]. For simplicity in the theoretical model, a constant flowing layer depth $\delta = \bar{\delta}$ is assumed, where $\bar{\delta}$ is the average of the flowing layer depth along the entire length of the flowing layer. Based on the local surface velocity and flowing layer depth, the normalized streamwise velocity profiles in the normal direction are plotted in Fig. 2.4c for various positions along the length of the flowing layer. The velocity profiles at different streamwise positions in the simulation agree with PTV results and collapse to a single curve, indicating a self-similar exponential velocity profile. The streamwise velocity profiles measured here are consistent with previous results for monodisperse and size bidisperse experiments and simulations [21], so the same exponential expression for the streamwise velocity is used here:

$$(2.2) \qquad u(x, z) = \frac{kq}{\delta(1 - e^{-k})} \left(1 - \frac{x}{L}\right) e^{kz/\delta}.$$

Equation 2.2 includes a linear decrease in the velocity in the streamwise direction, corresponding to the surface velocity in Fig. 2.4a, and an exponential dependence on the normal direction, consistent with the self-similar velocity profiles in Fig. 2.4c. Here, k is a scaling constant set to $\ln(10) \approx 2.3$, which ensures $u(x, -\delta) = 0.1u(x, 0)$ [40, 21]. To verify the general applicability of Eq. 2.2, the velocity profiles at $x/L = 0.5$ are plotted in Fig. 2.4d for nine simulation cases with different feed rates, density ratios $R_D = \rho_h/\rho_l$, and particle diameters (table 2.2), along with the exponential fit $u/u_s = e^{kz/\delta}$. The collapse of the data to the exponential fit demonstrates that Eq. 2.2 describes the self-similar streamwise velocity profiles in the density bidisperse quasi-2D bounded heap flows studied here.

2.3.2. Normal velocity

Using the same method, normal velocity profiles were extracted from the simulations and the experiment. Figure 2.5a shows a comparison of normal velocities between simulation
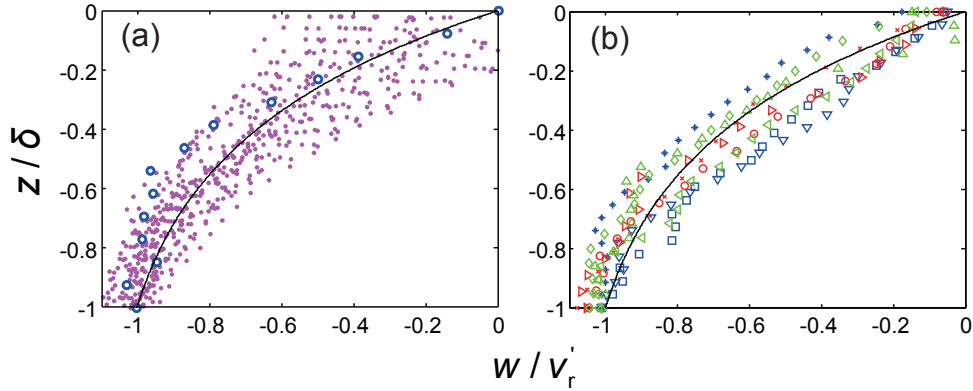
Figure 2.5. Normal velocity profiles. (a) Normalized normal velocity profiles at various positions along the length of the flowing layer in simulation (dots, purple or light gray), experiment (circles, blue or dark gray), and the predicted normal velocity profile (solid curve) based on the assumption of incompressibility, using ceramic and steel particles at $q = 0.0032\,\mathrm{m^2/s}$. (b) Normalized streamwise velocity profiles for the nine cases in table 2.2 at $x/L = 0.5$ collapse onto the predicted velocity profile (solid curve).

and experiment for the same case shown in Fig. 2.4c. Because normal velocity is typically an order of magnitude smaller than streamwise velocity, the data are more scattered. Yet there is reasonable agreement between the simulation and the experiment. In the coordinate system moving upward with the rise velocity v_r', the normal velocity is zero on the free surface ($z/\delta = 0$) and decreases to $-v_r'$ at the bottom of the flowing layer ($z/\delta = -1$). Based on Eq. 2.2 and the continuity equation, the normal velocity is [21]:

$$(2.3) \qquad w(z) = \frac{q}{L(1 - e^{-k})}(e^{kz/\delta} - 1).$$

This equation automatically satisfies the bottom boundary condition $w(-\delta) = -q/L = -v_r \cos\alpha$. To verify this expression, normalized normal velocity profiles at $x/L = 0.5$ for the nine different simulation cases in table 2.2 are plotted along with $w/v_r' = (e^{kz/\delta} - 1)/(1 - e^{-k})$ in Fig. 2.5b. The results from the simulations collapse and are quite similar to the theoretical profile, confirming that Eq. 2.3 is a reasonable approximation of the normal velocity profiles of density bidisperse flows in quasi-2D bounded heaps.
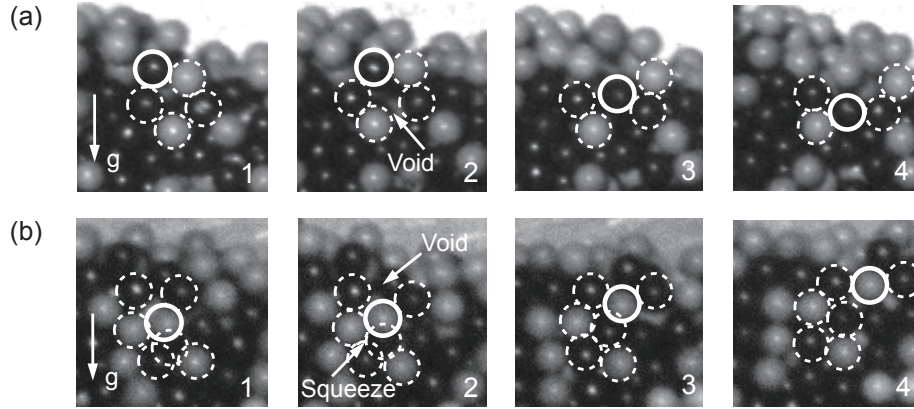
Figure 2.6. Experimental observation of density segregation of 3 mm particles. (a) A series of images showing a steel particle (solid circle) falling into a void generated by surrounding particles (dashed circles). The time between each image is about 0.015 s. (b) A ceramic particle (solid circle) is squeezed up into a void in the surrounding particles (dashed circles).

2.3.3. Segregation velocity

Previous studies of size segregation indicate that kinetic sieving and squeeze expulsion are the dominant segregation mechanisms in gravity driven free surface flows [**55, 112, 60**]. Here, analogous phenomena are observed in density bidisperse flows. When voids are generated due to shear, particles with higher density are more likely to fall into voids below them, while particles with lower density are more likely to be squeezed up to voids above them. Two typical examples of these processes from experiment are shown in Fig. 2.6. Figure 2.6a shows a sequence of images in which a steel particle falls into a void generated below it. Figure 2.6b shows a sequence of images in which a ceramic particle is pushed into a void above it while its original place is taken by a steel particle. An explanation of these phenomena invokes a force imbalance between the gravitational force and contact forces from neighbouring particles, such that a heavier particle on average experiences a net force in the gravitational direction and a lighter particle a net force in the direction opposite gravity. This has been referred to as "buoyancy" in previous studies [**56, 123**].
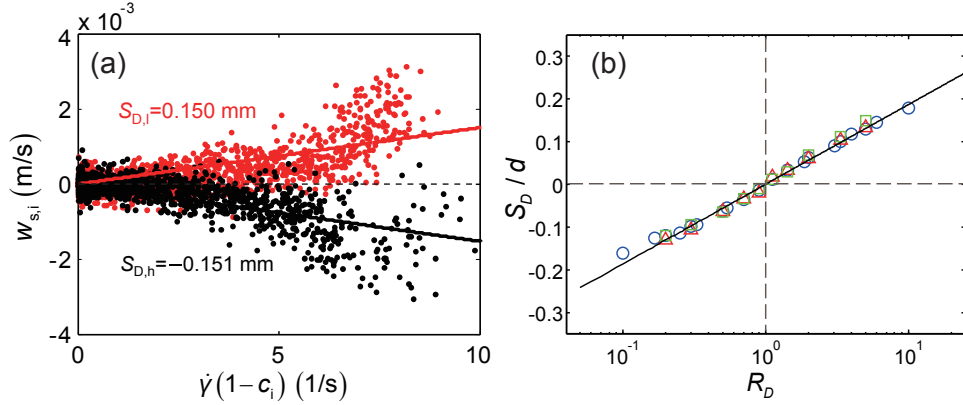
Figure 2.7. Simulation data for the segregation velocity. (a) Dependence of the segregation velocity on the local shear rate and the local concentration for $R_D = 1.88$, $d = 3\,\mathrm{mm}$ and $q = 0.0032\,\mathrm{m^2/s}$. Data points and the fitted lines are for light particles (red or light gray) and heavy particles (black). (b) Scaling of density segregation length scale vs. R_D on a semi-log plot for 20 cases of 50:50 mixtures with density ratio R_D ranging from 0.1 to 10, particle diameters of $2\,\mathrm{mm}$ (triangles), $3\,\mathrm{mm}$ (circles), and $4\,\mathrm{mm}$ (squares), and $q = 0.0022\,\mathrm{m^2/s}$.

Though the segregation mechanism at work here results from density differences instead of size differences, the essence of kinetic sieving and squeeze expulsion appears to be similar, and the resulting segregation patterns for density segregation are similar to those for size segregation in quasi-2D bounded heaps [**40, 65, 21, 20**]. This suggests that the factors that drive density segregation are the same as for size segregation. These factors include the local shear rate, $\dot{\gamma} = \partial u/\partial z$, which determines how frequently voids are generated, and the local concentration of the other species, $1 - c_i$, which determines the nature of the contact forces a particle might encounter. To examine the relation between segregation velocity and these factors, the segregation velocity $w_{s,i}$ is plotted as a function of $\dot{\gamma}(1 - c_i)$ for heavy and light particles for an example case in Fig. 2.7a. For both light particles and heavy particles, the data suggests an approximately linear relation between $w_{s,i}$ and $\dot{\gamma}(1 - c_i)$, just as for size segregation [**40, 65, 83**]. Consequently, the density segregation velocity can be expressed as:

$$(2.4) \qquad w_{s,i} = S_D \dot{\gamma}(1 - c_i),$$

where S_D, defined as the segregation length scale, is the slope of the fitted line for the dependence of $w_{s,i}$ on $\dot{\gamma}(1 - c_i)$, as shown for the example in Fig. 2.7a. Analogous to the segregation length scale in size bidisperse systems [40], S_D is positive for light particles and negative for heavy particles. For the data in Fig. 2.7a, the characteristic segregation length scales for light ($S_{D,l} = 0.150\,\text{mm}$) and heavy ($S_{D,h} = -0.151\,\text{mm}$) particles are nearly identical in magnitude but have opposite signs due to mass conservation [40]. Although Eq. 2.4 has the same functional form as in size segregation [40, 65, 83], it represents the segregation velocity resulting from differences in particle densities instead of particle sizes. Thus the segregation length scale, S_D, should vary with density related properties. Values for S_D were found for 20 simulation cases using 50:50 mixtures with density ratio R_D ranging from 0.1 to 10 and particle diameters of 2, 3, and 4 mm at $q = 0.0022\,\text{m}^2/\text{s}$. Simulations with different feed rates were also performed, but no significant difference in S_D was found, as expected. As shown in Fig. 2.7b, S_D varies with the density ratio R_D and the particle diameter d. The relation between S_D and R_D can be approximated by

$$(2.5) \qquad \frac{S_D}{d} = C_D \ln R_D,$$

where C_D is a constant with the value 0.081. 40 data points are shown in Fig. 2.7b, since each simulation produces two data points: one for $S_{D,h}$ (corresponding to $R_D > 1$) and one corresponding to $S_{D,l}$ (corresponding to $R_D < 1$). This functional relation differs from the assumed linear dependence of the segregation flux on the density difference $\rho_h - \rho_l$ used in previous studies [56, 76]. Equation 2.5 expresses the relation of S_D to particle differences in a manner analogous to size segregation [65], but the constant C_D is roughly three times smaller than the corresponding constant, $C_S = 0.26$, measured in size segregation [65], which, in Eq. 2.5, indicates that the density ratio needs to be raised to approximately the power of three to produce equivalent segregation velocity for the same size ratio. This agrees well with the model by Tunuguntla $et\ al.$ [76] where the segregation
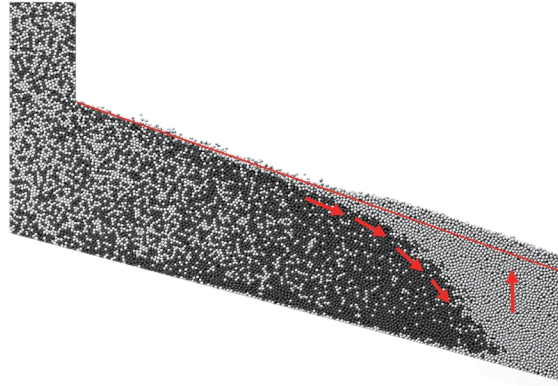
Figure 2.8. Density segregation at $R_D = 10$, $d = 3\,\text{mm}$, and $q = 0.0040\,\text{m}^2/\text{s}$. Heavy particles undercut the light particles toward the end of the heap, pushing light particles upward. The free surface is no longer flat in this case.

velocity scales as the third power of the size ratio and the first power of the density ratio, though it is inconsistent with the model by Marks *et al.* [77] where the size ratio and the density ratio are interchangeable. In an experimental study of combined size and density segregation [124], size segregation dominates density segregation unless the size ratio is much smaller than the density ratio, confirming the difference in the contribution to the segregation velocity of the size and the density differences.

For DEM simulations with a density ratio $R_D \geq 5$, there is a gradual change in the overall kinematics of the flow in the downstream portion of the heap as R_D increases. At $R_D = 10$ (Fig. 2.8), the segregation in the upstream portion of the flow still results from local buoyancy, generating a segregation pattern with strongly segregated regions of light and heavy particles having a clear interface in between. However, in the downstream portion a global flow occurs. The resistance of the light particles to the motion of the heavy particles is not significant at this high density ratio, so the heavy particles undercut the light particles toward the end of the heap, pushing the bulk of light particles upward, such that the free surface is no longer flat. Such penetration is analogous to group intruder penetration [125], where the depth of penetration is related to the intruder's speed and density. Since density ratios this large are uncommon in industrial granular flows, and
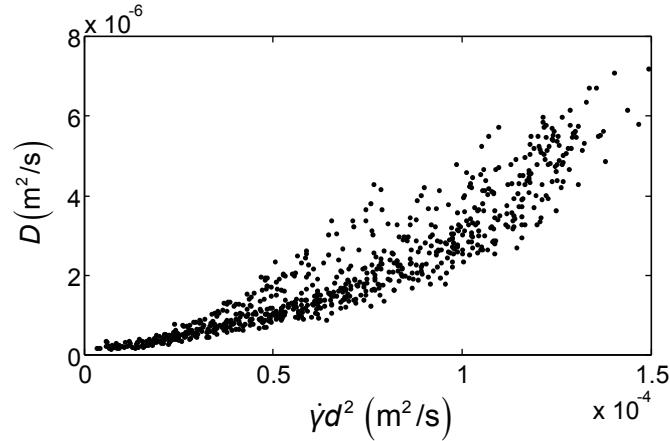
Figure 2.9. Simulation results for the diffusion coefficient vs. $\dot{\gamma}d^2$ for $R_D = 1.88$, $d = 3\,\text{mm}$, and $q = 0.0032\,\text{m}^2/\text{s}$.

this phenomenon introduces more complexity into the kinematics of the flow, we focus on cases with density ratio $R_D \leq 5$ in this study. Note, however, that we are still able to extract local data for density segregation in the flow for $R_D > 5$, thus accounting for these data points in Fig. 2.7b.

2.3.4. Diffusion

The diffusion coefficient of the mixture, D, was determined in the normal direction by tracking the non-affine portion of particle trajectories using the mean square displacement as a function of time, $\langle \Delta Z(\Delta t)^2 \rangle$ [40]. The diffusion coefficient was then calculated based on $\langle \Delta Z(\Delta t)^2 \rangle = 2D\Delta t$ [40, 126]. An example simulation result, shown in Fig. 2.9, demonstrates that in density bidisperse flows, the diffusion coefficient is shear rate-dependent, which is consistent with previous studies in dense granular flows [56, 126]. In this study, we use the spatial average of the diffusion coefficient over the entire flowing layer domain for the continuum model. We previously showed that for size-disperse granular materials, using the average value of D provides sufficient accuracy to successfully apply the theory, though it is possible to use a locally varying value for D in the theory [40].

2.4. Predictions of the theoretical model

2.4.1. Nondimensionalization and boundary conditions

When applying the transport equation 2.1 to modeling density bidisperse segregation in a quasi-2D bounded heap, it is convenient to nondimensionalize the equation using the nondimensionalized parameters [**40, 65**]

$$(2.6) \qquad \tilde{x} = \frac{x}{L}, \quad \tilde{z} = \frac{z}{\delta}, \quad \tilde{t} = \frac{t}{\delta L/2q}, \quad \tilde{u} = \frac{u}{2q/\delta}, \quad \text{and} \quad \tilde{w} = \frac{w}{2q/L}.$$

Substituting the nondimensionalized parameters into Eq. 2.1 gives the nondimensional transport equation for species i:

$$(2.7) \qquad \frac{\partial c_i}{\partial \tilde{t}} + \tilde{u}\frac{\partial c_i}{\partial \tilde{x}} + \tilde{w}\frac{\partial c_i}{\partial \tilde{z}} \pm \Lambda \frac{\partial}{\partial \tilde{z}}\left[h(\tilde{x}, \tilde{z})c_i(1 - c_i)\right] = \frac{1}{Pe}\frac{\partial^2 c_i}{\partial \tilde{z}^2}.$$

In Eq. 2.7, segregation and diffusion in the streamwise direction x are neglected as assumed previously [**56, 76, 40, 83**], since these terms are small in comparison with other terms in the equation so long as $\delta/L \ll 1$. The sign of the segregation term is positive for light particles and negative for heavy particles. The nondimensional shear rate is $h(\tilde{x}, \tilde{z}) = \dot{\gamma}\delta^2/2q$. The Péclet number is $Pe = 2q\delta/DL$, which represents the ratio of a diffusion time scale ($t_d = \delta^2/D$) to an advection time scale ($t_a = L\delta/2q$). The other nondimensional parameter $\Lambda = S_D L/\delta^2$, where $S_D = |S_{D,l}|/2 + |S_{D,h}|/2$, represents the ratio of the advection time scale (t_a) to a segregation time scale ($t_s = \delta^3/2qS_D$). These two nondimensional parameters depend on control parameters (feed rate q and flowing layer length L) and kinematic parameters (flowing layer thickness δ, diffusion coefficient D, and segregation length scale S_D), and they represent the interplay of advection, diffusion, and segregation.

Boundary conditions are also identical to previous studies for size bidisperse flow [**40, 65**]. At the inlet, the particles are well mixed, so $c_l(0, \tilde{z}) = c_h(0, \tilde{z}) = 0.5$. At the top and bottom boundaries of the flowing layer, the segregation flux and diffusion flux are set

equal according to the no flux boundary condition suggested by Gray and Chugunov[**75**], which allows Eq. 2.7 to be written as

$$(2.8) \qquad \Lambda h(\tilde{x}, \tilde{z}) c_i (1 - c_i) = \frac{1}{Pe} \frac{\partial c_i}{\partial \tilde{z}}, \ \tilde{z} = 0, -1.$$

The bottom boundary condition ensures that particles leave the flowing layer only due to advection at velocity $w = -v_r \cos\alpha$, and no particles leave the flowing layer at the top surface. At the downstream boundary, advection, diffusion, and segregation included in Eq. 2.7 are in the normal direction. Thus, no boundary condition is needed. Here, we note that with our method of informing the model with kinematics measured from simulations, the model itself does not include the feedback between velocity field and segregation as was considered by Marks, *et al.* [**77**]. However, we are solving for steady state solutions where the kinematics do not change, and the kinematics are measured directly from the steady state bidisperse flow simulations. As a result, the kinematics included in our model represent the final result of the interaction between segregation and kinematics. With the velocity profiles (Eqs. 2.2, 2.3), Eq. 2.7 can be solved numerically for steady-state flow using an operator splitting method with a mapping method for the advection step and the implicit Crank-Nicolson method for the diffusion and segregation step [**40, 127, 128**].

2.4.2. Validation of the theoretical model

To demonstrate that the theoretical model quantitatively predicts bidisperse density segregation in the quasi-2D bounded heap, theoretical, experimental, and simulation results for three example cases with different particle density ratios R_D are shown in Fig. 2.10. Each contour subplot (left and center columns) represents the concentration of light particles c_l in the flowing layer extending horizontally from W_F' at $\tilde{x} = 0$ to the end of the flowing layer at $\tilde{x} = 1$ and vertically from the top of the flowing layer at $\tilde{z} = 0$ to the bottom at $\tilde{z} = -1$. Comparing the concentration contours for theory and DEM simulations, it is clear that the theoretical model reproduces the segregation patterns in simulations with good accuracy. In all cases, the particles are well mixed at $\tilde{x} = 0$ and then begin
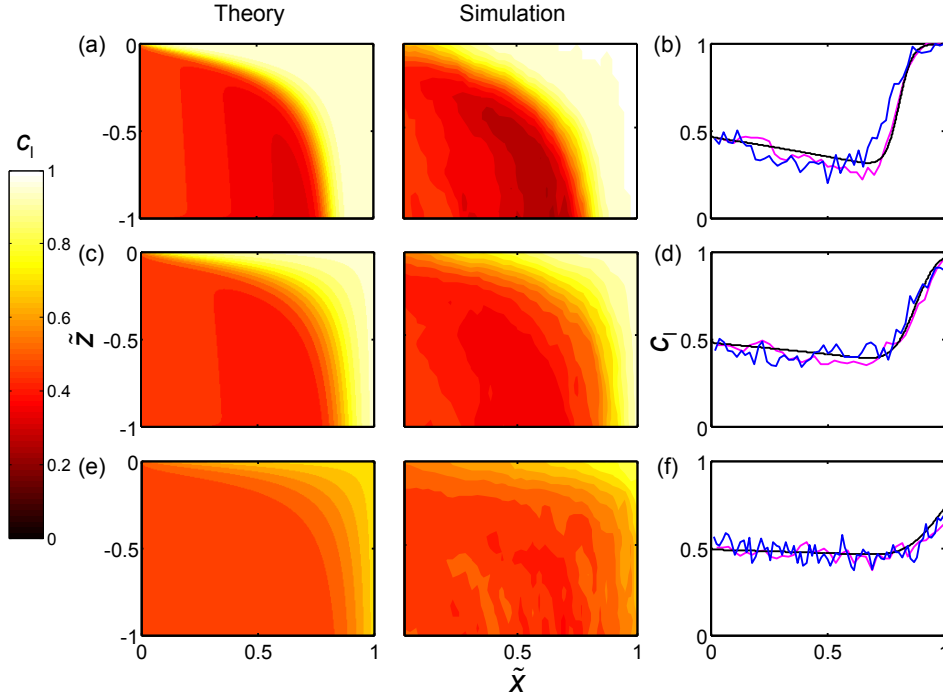
Figure 2.10. Comparison of theory, simulation, and experiment for density bidisperse segregation with different density ratios. Left and middle columns show concentration contours of light particles in the flowing layer from theory and simulation, respectively. The right column compares theoretical predictions (black), experimental results (blue or dark gray), and simulation results (purple or light gray) at steady state for the concentration profile at the bottom of the flowing layer, which reflects the concentration of the particles deposited on the heap. Top row: glass and steel particles with $R_D = 3.04$, $q = 0.0035\,\mathrm{m^2/s}$, $S_D = 0.29\,\mathrm{mm}$, $D = 2.24\,\mathrm{mm^2s^{-1}}$, $L = 0.40\,\mathrm{m}$, $\delta = 0.024\,\mathrm{m}$, $Pe = 189$, and $\Lambda = 0.21$. $RMSD_{t,e} = 0.082$ and $RMSD_{t,s} = 0.039$. Middle row: ceramic and steel particles with $R_D = 1.88$, $q = 0.0036\,\mathrm{m^2/s}$, $S_D = 0.15\,\mathrm{mm}$, $D = 2.17\,\mathrm{mm^2s^{-1}}$, $L = 0.40\,\mathrm{m}$, $\delta = 0.023\,\mathrm{m}$, $Pe = 189$, and $\Lambda = 0.12$. $RMSD_{t,e} = 0.049$ and $RMSD_{t,s} = 0.072$. Bottom row: high density ceramic and steel particles, with $R_D = 1.24$ and $q = 0.0035\,\mathrm{m^s/s}$, $S_D = 0.05\,\mathrm{mm}$, $D = 2.27\,\mathrm{mm^2s^{-1}}$, $L = 0.39\,\mathrm{m}$, $\delta = 0.024\,\mathrm{m}$, $Pe = 192$, and $\Lambda = 0.04$. $RMSD_{t,e} = 0.039$ and $RMSD_{t,s} = 0.033$.

to segregate: as they flow downstream, heavy particles move toward the bottom of the flowing layer to settle out further upstream (smaller $\tilde{x}$), while light particles rise toward the top of the flowing layer and flow further down the heap (larger $\tilde{x}$). The position and shape of the interface between segregated heavy and light particles for the theoretical results agree well with simulation results, indicating that the theoretical model captures the essential physics of density bidisperse segregation. It is also possible to compare the theory and simulation directly with experimental results using the concentration of light particles, c_l, deposited onto the heap at the bottom of the flowing layer [40], see right column in Fig. 2.10. The root-mean-square deviation (RMSD) is applied to quantify the quality of the theoretical predictions, and is calculated as $RMSD_{t,i} = \sqrt{\sum_{j=1}^{n}(c_{j,t} - c_{j,i})^2 / n}$, where $c_{j,t}$ denotes the data points from the theoretical predictions and $c_{j,i}$ denotes corresponding data points from the reference ($i = e$ for experiments and $i = s$ for simulations), and n is the total number of data points in each case. In all three cases, the $RMSD_{t,e}$ and $RMSD_{t,s}$ are small, indicating that the theoretical predictions match the experimental and simulation results.

The theoretical predictions are determined completely by the two dimensionless parameters Pe and Λ, in the same manner as in previous work [75, 60]. Pe describes the interplay between advection and diffusion: as Pe becomes larger, advection dominates diffusion, causing the interface between segregated heavy and light particles to become sharper and more easily distinguishable. We note that the Pe we use here is different from the Péclet number defined in Thornton $et\ al.$ [60] for chute flows, where it represents the interplay between segregation and diffusion. Λ describes the interplay between segregation and advection. For larger Λ, segregation is stronger so particles tend to segregate before they flow very far down the heap. The influence of these two parameters on segregation has been investigated in detail in the context of size bidisperse systems [40]. Since the form of the theoretical model here is identical to that in previous work for size segregation [40, 65] (except that the percolation length scale S is replaced by the density segregation length scale S_D), the discussion is not repeated here.
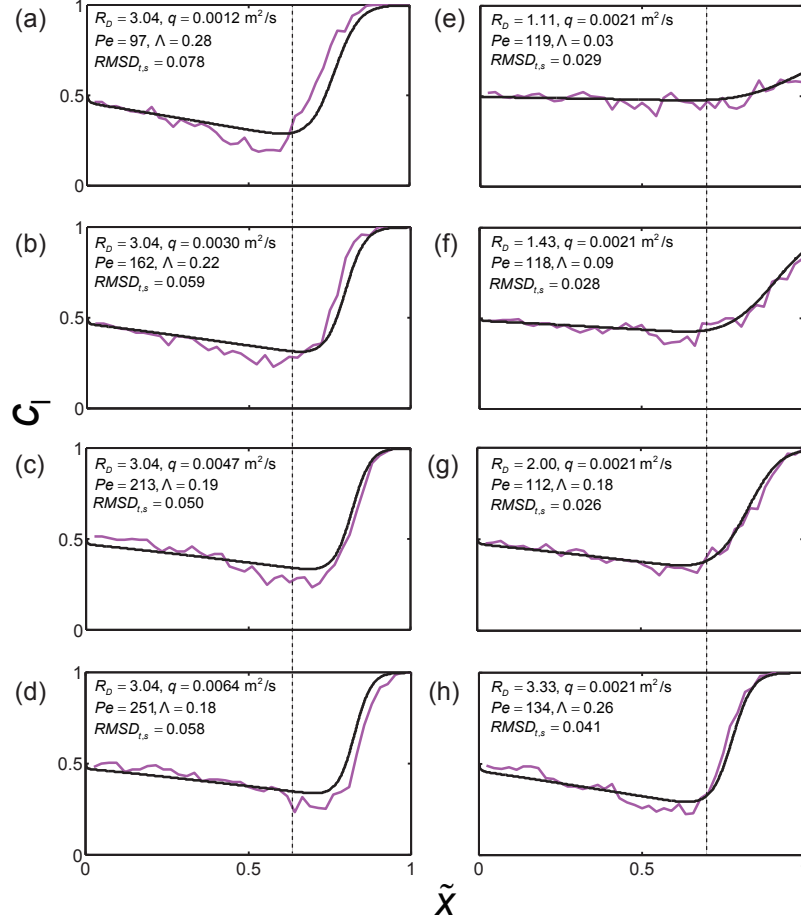
Figure 2.11. Theoretical predictions (black curves) and simulation results (purple or light gray curves) for the light particle concentration profile at the bottom of the flowing layer, which represent material deposited on the heap. Vertical dashed lines mark the streamwise locations where lowest theoretical concentrations occur in (a) and (e). (a)-(d) Density ratio $R_D = 3.04$ and different feed rates q (labeled on each plot). (e)-(h) $q = 0.0022\,\mathrm{m^2/s}$ and different density ratios R_D (labeled on each plot).

2.4.3. Predictions of segregation under different physical control parameters

Since Pe and Λ depend on physical control parameters, it is interesting to explore how theoretical predictions of segregation change when the physical control parameters are

varied. Among the parameters, density ratio R_D and feed rate q have the greatest influence on the segregation [**65**]. Figure 2.11 shows a series of theoretical predictions and simulation results for the concentration of the light particles at the bottom of the flowing layer (which are deposited on the heap) for different R_D and q. In all cases, the diffusion coefficient, D, is the average diffusion coefficient based on the simulation for each set of conditions and S_D is from the relation shown in Fig. 2.7b. In Figs. 2.11a-d, it is clear that increasing q, which results in Pe increasing and Λ decreasing, results in less segregation (the transition from mixed particles to pure light particles occurs further downstream), and a sharper transition between segregated heavy and light particles, which is made more readily apparent in the figures with the aid of a vertical dashed benchmark line. In Figs. 2.11e-h, increasing R_D, which results in Λ increasing while Pe varies only a small amount, leads to an obvious increase in segregation, with almost no segregation at $R_D = 1.11$ and strong segregation with $R_D = 3.33$. In all cases, $RMSD_{t,s}$ is small, indicating that the theoretical predictions match the simulation results well, again demonstrating that the theory is capable of accurately predicting segregation when the physical control parameters are varied.

To further demonstrate the generality of the theory and the form of the segregation velocity, cases with different inlet particle concentrations were simulated and predicted using the theory, as shown in Fig. 2.12. In both cases, D is from simulations with $c_l(0, \tilde{z}) = c_h(0, \tilde{z}) = 0.5$ at the same flow rate and the value for S_D is from Fig. 2.7b, rather than using these values from the simulations for the $c_l(0, \tilde{z}) = 0.2$ or $c_l(0, \tilde{z}) = 0.8$ cases. The left column shows the case with inlet light particle concentration $c_l(0, \tilde{z}) = 0.2$ and the right column shows the case with $c_l(0, \tilde{z}) = 0.8$. In Fig. 2.12, row 1 shows the general segregation patterns in both cases from the DEM simulations. The segregation patterns are consistent with the patterns for 50:50 mixtures shown in Figs. 2.3 and 2.9, in which the heavy particles settle out of the flowing layer in the upstream portion of the heap while the light particles flow further toward the downstream end of the heap. Using the segregation length scale predicted by Eq. 2.5 ($S_D = 0.27\,\mathrm{mm}$), the theoretical predictions of the concentration distribution of the light particles in the flowing layer (row 2 in Fig. 2.12)
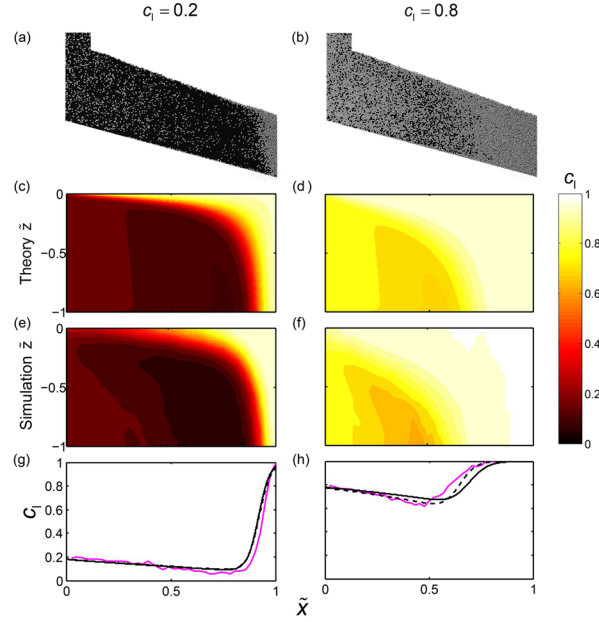
Figure 2.12. Segregation with different inlet particle concentrations. Left column: inlet light particle concentration $c_l(0, \tilde{z}) = 0.2$, $R_D = 3.04$, $q = 0.0027\,\mathrm{m^2/s}$, $d = 3\,\mathrm{mm}$, $S_D = 0.27\,\mathrm{mm}$, $D = 1.96\,\mathrm{mm^2 s^{-1}}$. $Pe = 146$ and $\Lambda = 0.23$. Right column: inlet light particle concentration $c_l(0, \tilde{z}) = 0.8$, $R_D = 3.04$, $q = 0.0027\,\mathrm{m^2/s}$, $d = 3\,\mathrm{mm}$, $S_D = 0.27\,\mathrm{mm}$, $D = 1.96\,\mathrm{mm^2 s^{-1}}$. $Pe = 143$ and $\Lambda = 0.23$. Row 1: segregation patterns from simulations. Row 2: contours of c_l in the flowing layer from theory. Row 3: contours of c_l in the flowing layer from simulations. Row 4: concentration profiles of light particles at the bottom of the flowing layer from theory (black curves) and simulations (pink or light gray solid curves). The black solid curves for predictions using S_D from equation 2.5 result in $RMSD_{t,s}$=0.056 for $c_l(0, \tilde{z}) = 0.2$ and $RMSD_{t,s}$=0.054 for $c_l(0, \tilde{z}) = 0.8$. The black dashed curves for predictions using S_D measured in each specific simulations result in $RMSD_{t,s}$=0.052 for $c_l(0, \tilde{z}) = 0.2$ and $RMSD_{t,s}$=0.034 for $c_l(0, \tilde{z}) = 0.8$.

agree reasonably well with the simulation results (row 3). The comparison of the light particle concentration profiles at the bottom of the flowing layer from simulations and theory (row 4) demonstrates that the theory is also accurate for particle mixtures with different volume ratios, even when using parameters obtained from a 50:50 mixture.

While examining the effect of different volume ratios on the segregation, we found a difference in the segregation length scale S_D calculated in the simulations with $c_l(0, \tilde{z}) = 0.2$ and $c_l(0, \tilde{z}) = 0.8$ (instead of using Eq. 2.5). Based on S_D calculated in each simulation, we recalculated Λ (Pe is independent of S_D): $S_D = 0.34 \, \text{mm}$, $\Lambda = 0.28$ for $c_l(0, \tilde{z}) = 0.8$ and $S_D = 0.25 \, \text{mm}$, $\Lambda = 0.21$ for $c_l(0, \tilde{z}) = 0.2$, compared to $S_D = 0.27 \, \text{mm}$, $\Lambda = 0.23$ for $c_l(0, \tilde{z}) = 0.5$. The theoretical predictions using Pe and Λ recalculated in the two cases are also shown in Figs. 2.12g, h as dashed curves. For $c_l(0, \tilde{z}) = 0.2$, the new prediction is almost identical to the prediction using S_D from Eq. 2.5. For $c_l(0, \tilde{z}) = 0.8$, the new prediction shows only a slightly better match to the simulation result. These results indicate that it is reasonable to use Eq. 2.5 for S_D determined for $c_l(0, \tilde{z}) = 0.5$ even for cases with different inlet concentrations.

The difference in S_D for different inlet concentrations is intriguing, because it indicates that the segregation for a few heavy particles in many light particles is stronger than the segregation for a few light particles in many heavy particles. This is analogous to recent work which shows that small particles segregate faster when surrounded by large particles than vice versa [129, 130]. This asymmetry can possibly be explained in terms of the way that a heavy (or small) particle is able to continually push its way downward in the gravitational direction while waiting for a void below it to open when it is surrounded by light (or large) particles. In contrast, a light (or large) particle can only wait for the combination of a void opening above it at the same time as surrounding particles are pushing it upward against gravity when it is surrounded by heavy (or small) particles.

This asymmetry suggests that S_D depends on local particle concentrations. To further explore this, nine simulations with $R_D = 3.04$, and $q = 0.0027 \, \text{m}^2/\text{s}$, and $d = 2 \, \text{mm}$ were performed with the inlet light particle concentration varying from 0.1 to 0.9. The segregation velocity shown in Fig. 2.13 includes data from all nine simulations. To reduce the noise, we average the data into 100 equal-sized bins along the horizontal axis, and the averaged results are also shown in Fig. 2.13 as two yellow curves. The data for different inlet light particle concentrations are consistent with each other, forming two continuous curves (one for light particles and one for heavy particles). Upon closer examination, the
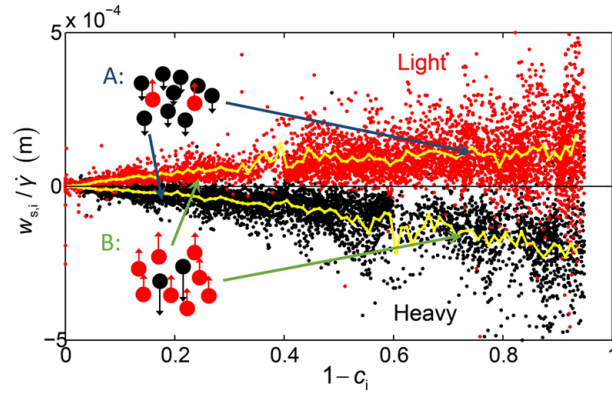
Figure 2.13. Averaged dependence of segregation velocity on the local shear rate and the local concentration from nine simulations with inlet light particle concentrations ranging from 0.1 to 0.9. In all the cases, $R_D = 3.04$, and $q = 0.0027 \, \mathrm{m^2/s}$, and $d = 2 \, \mathrm{mm}$. The data was initially extracted as in Fig. 2.7, and then averaged in 100 equal-sized bins along the horizontal axis. The original data extracted from the nine simulation cases (red dots for light and black dots for heavy) and the bin-averaged values for both species (yellow lines) are shown. Data for $c_i \leqslant 0.05$ are neglected because there are too few particles (species i) to get well-averaged data. Case A refers to large $1 - c_i$ in the light particle curve and small $1 - c_i$ in the heavy particle curve. Case B refers to small $1 - c_i$ in the light particle curve and large $1 - c_i$ in the heavy particle curve.

curve for heavy particles, when compared to the curve for light particles, has a slightly smaller slope when $1 - c_i$ is small, corresponding to a high local concentration of heavy particles (case A in the figure), and a slightly larger slope when $1 - c_i$ is large, corresponding to a lower local concentration of heavy particles (case B in the figure). This asymmetry in density segregation reveals the reason for the difference in S_D measured in cases with different inlet light particle concentrations: S_D for $c_l(0, \tilde{z}) = 0.2$ was measured mainly using data from case A, and thus it is smaller than S_D measured for $c_l(0, \tilde{z}) = 0.8$, which mainly used data from case B. Although this asymmetry suggests a slightly non-linear relation between the segregation velocity and the concentration, the theoretical predictions using the linear approximation still show quantitative agreement with simulation results, as Fig. 2.12 demonstrates. However, in situations where the concentration of one species is significantly higher than that of the other, incorporating the nonlinear segregation

velocity might be necessary. The segregation velocity derived from statistical mechanics by Savage & Lun [55] as well as the models by Marks *et al.* [77] and Tunuguntla *et al.* [76] should automatically include this nonlinearity, but its effect was not discussed in detail. Recent studies on asymmetry in size segregation used a cubic function to represent the asymmetric flux [78, 129] resulting in better agreement with experiments [129]. For density segregation, this asymmetry could also be taken into account in the theory by using an S_D that is a function of c_i, which we are currently investigating.

2.5. Conclusions

In this study we have demonstrated that our recently developed continuum model for size bidisperse systems [40, 83, 65] accurately predicts granular segregation for density bidisperse systems, specifically for bounded heap flow, though it is likely applicable to other flow geometries and multi- or polydisperse particle distributions, as we have already shown for size segregation [83]. Using experimental techniques and DEM simulations to investigate the kinematics, we developed an approximation for the segregation velocity that depends on local shear rate $\dot{\gamma}$, local concentration of the other species $1 - c_i$, and a dimensional parameter defined as the density segregation length S_D, which depends primarily on the density ratio R_D and, to a lesser extent, on the local particle concentration. The model is based on the transport equation and includes the interplay of advection, diffusion, and segregation. In the model, no arbitrary fitting parameters are needed as the system configurations are determined by two dimensionless parameters $Pe = 2q\delta/DL$ and $\Lambda = S_D L/\delta^2$, which depend only on physical control parameters and kinematic parameters measured from simulations (or experiments, if available). The theoretical predictions quantitatively agree with results from both simulations and experiments under different physical control parameters.

Compared to our model for size segregation [40, 65], the primary difference in this study is the segregation length scale in the equation for the segregation velocity, which is related to the density ratio here, as opposed to the size ratio for size segregation. However, apart from this constant, the two models are identical and the resulting segregation patterns for size and density segregation are very similar. This suggests that although

the driving force for granular segregation is different in the two cases, the shear-generated segregation mechanism for gravity driven free surface flows is similar. This also suggests that the model has potential to predict combined size and density segregation [**76, 114**]. The asymmetry observed in density segregation for different inlet concentrations indicates that more accurate predictions will require that variations of S_D with concentration be included in the theoretical model. Moreover, the model is not limited to quasi-2D bounded heaps. For other typical geometries with gravity driven free surface flows, the continuum model combined with the segregation velocity defined in Eq. 2.3 should also be applicable. To adapt the continuum model to segregation in other geometries, similar to studies of segregation in rotating tumblers[**103, 131**], the corresponding boundary conditions need to be included and kinematic information for the specific geometry needs be used. This is not difficult and can be accomplished using constitutive theories[**77, 56**] or direct measurements from simulations or experiments[**40, 83**]. This approach has already been used to successfully model size segregation in circular tumblers[**83**] and chutes[**86**]. Given the similarities between size and density segregation, it is quite likely that the model will accurately predict density segregation in tumblers, chutes, unbounded heaps, and even 3D geometries.

CHAPTER 3

Simulation and Modeling of Segregating Rods in Quasi-2D Bounded Heap Flow

SUMMARY

Many products in the chemical and agricultural industries are pelletized in the form of rod-like particles that often have different aspect ratios. However, the flow, mixing, and segregation of non-spherical particles such as rod-like particles are poorly understood. In this chapter, we use the discrete element method (DEM) utilizing super-ellipsoid particles to simulate the flow and segregation of rod-like particles differing in length but with the same diameter in a quasi-2D one-sided bounded heap. The DEM simulations accurately reproduce the segregation of size bidisperse rod-like particles in a bounded heap based on comparison with experiments. Rod-like particles orient themselves along the direction of flow, although bounding walls influence the orientation of the smaller aspect ratio particles. The flow kinematics and segregation of bidisperse rods having identical diameters but different lengths are similar to spherical particles. The segregation velocity of one rod species relative to the mean velocity depends linearly on the concentration of the other species, the shear rate, and a parameter based on the relative lengths of the rods. A continuum model developed for spherical particles that includes advection, diffusion, and segregation effects accurately predicts the segregation of rods in the flowing layer for a range of physical control parameters and particle species concentrations.

analyzing DEM simulation results, performing continuum model calculation and writing and editing the sections in the manuscript corresponding to Sections 3.1 and 3.4.

3.1. Introduction

Segregation of flowing granular material due to differences in particle size is commonly encountered in industrial systems that handle bulk solids [**96, 133, 52**]. This phenomenon has been studied extensively, both experimentally and computationally, in various geometries including chutes, tumblers, and heaps [**20, 21, 124, 116, 44, 46, 68, 55**]. In dense granular flows, size segregation results from a percolation-based mechanism called kinetic sieving in which small particles tend to fall into shear-generated voids while large particles are forced upward to balance the volume flux [**96, 55, 49**]. Most granular segregation studies have focused on idealized spherical particles or coarse particles that are generally spherical in shape and that can be simulated or modeled relatively easily without concern for the influence of particle shape on the flow kinematics and segregation. However, in many practical industrial situations the particles are non-spherical. Thus, understanding the flow kinematics and modeling the segregation of non-spherical particles is important for predicting and preventing segregation due to varying particle size or shape in real systems. In this study, we take an initial step in this direction by modeling size segregation of cylindrical rods differing in length, which are common in the chemical and agricultural industries for materials pelletized in the form of rods or cylinders including polymers, herbicides, pesticides, fertilizer, wood, and animal feed.

Currently, the understanding of the flow of non-spherical particles, particularly rod-like particles, is limited due to the challenges in studying these particles. Studies based on experiments [**134**] and DEM simulations [**135, 136, 137**] have shown that rods tend to align with the flow. DEM simulation has proven to be a particularly useful tool for studying rod-like particles because it provides information about the behavior at both the particle scale and the laboratory scale. The particle models used in previous DEM simulations of rod-like particles include the glued sphere model and the real shape model. However, due to the low accuracy of the glued sphere model [**136, 138**] and the high

computational cost of real shape models [**139, 140, 141**], these approaches are not suitable for simulating granular flows that contain millions of rod-like particles or more. On the other hand, super-ellipsoids have been demonstrated to efficiently simulate the flow of rod-like particles [**142, 143**]. The method can be applied to the segregation of rods with different aspect ratios and is suitable for large scale simulations that contain millions of particles [**142, 144**].

In this chapter, we use super-ellipsoid particle-based DEM simulations to study the segregation of length bidisperse rods in a quasi-2D one-sided bounded heap, which is a canonical geometry for studying segregating granular systems [**20, 21, 44, 30, 81, 144, 145, 146**]. The quasi-2D bounded heap geometry consists of two parallel plates with a narrow gap between them and two vertical walls at each end, shown schematically in Fig.3.1. Particles are fed onto the heap at one end and flow down the slope in a thin flowing layer [**21, 81**]. Particles that fall out of the bottom of the flowing layer are deposited on the heap. Bounded heap flow differs substantially from chute flow in that the particles are deposited on the sloped surface of the heap rather than simply flowing down the surface of a chute. (Note that a sloped surface may be used in simulations or experiments to replace the static particles at the bottom of the heap bed. When such a sloped surface is used, only the layer of particles flowing down and depositing on top of the bed of particles previously deposited on the heap is considered.) As a result of the downstream end wall in bounded heap flow, the free surface rises uniformly for a sufficiently high feed rate [**21, 30, 81**]. For bidisperse mixtures of spherical particles, the particles segregate as they flow downstream4 forming different segregation patterns of the particles deposited on the heap including streamwise segregated particles (small particles are deposited in the upstream portion of the heap and large particles in the downstream portion) [**20, 118**], stratified layers of particles when the flow is intermittent [**20, 116, 44, 147**], or relatively mixed particles depending on the particle size ratio, feed rate, and heap size. In this study, we focus on a continuously flowing surface layer (as opposed to periodic or intermittent avalanches), which results in streamwise segregation or mixed particles, depending on the particle properties and the flow conditions [**20**].

While experiments and DEM simulations are useful for understanding the kinematics of flowing rods, a scalable and accurate continuum-based model would be helpful for predicting mixing in granular flows. To this end, Bridgwater et al. [73] proposed the first continuum model that includes segregation as a percolation flux term in a transport equation, and Savage and Lun [55] derived a model for the percolation velocity for spherical particles using a statistical mechanics approach. Over the years, continuum models based on these pioneering studies have evolved as more details such as collisional diffusion [75] and the influence of the local shear rate have been considered [77]. Continuum models of this type have been applied to various geometries [46, 68, 75, 77, 84, 78, 60, 74, 24] and both size and density segregation [76, 56, 114, 112] mechanisms with some of the models obtaining qualitative or quantitative agreement with simulations and experiments. Comprehensive reviews and comparison of the continuum models are provided by Tunuguntla et al. [85] and Gray [22]. However, these segregation models were derived for spherical particles. It is our goal here to determine whether and how such continuum approaches can be applied to predicting the segregation of flowing bidisperse rod-like particles.

To do so, we apply a form of a continuum model that has been successfully applied to quantitatively predict bidisperse size segregation of spherical particles in different geometries [65, 83, 148, 40] as well as bidisperse density segregation [57] and multi- and polydisperse size segregation [86]. This continuum segregation model has the general form

$$(3.1) \qquad \frac{\partial c_i}{\partial t} + \nabla \cdot (\boldsymbol{u} c_i) + \frac{\partial}{\partial z}(w_{s,i} c_i) - \nabla \cdot (D \nabla c_i) = 0,$$

where c_i is the concentration of species i (l for long and s for short) such that $c_i = f_i/f$, where f_i is the local volume fraction of species i, and f is the total volume fraction for all species. Equation 3.1, which includes the interplay of advection, segregation, and diffusion, is applied to the thin flowing layer (with length L and depth δ) at the surface where segregation occurs in heap flow. In the flowing layer, x denotes the streamwise direction ($0 < x < L$), and z denotes the depthwise direction ($-\delta < z < 0$), with $z = 0$ at the flowing layer surface and $z = -\delta$ at the bottom of the flowing layer. The mean

2D velocity field is $\boldsymbol{u} = u\hat{x} + w\hat{z}$ and D denotes the coefficient characterizing collisional diffusion. (Variables without subscripts represent the average flow properties of both particle species together.) A crucial aspect of this model is the segregation velocity, $w_{s,i}$, which is the relative normal velocity of species i with respect to the normal velocity of both species: $w_{s,i} = w_i - w$. Only segregation in the normal direction is considered because the streamwise direction is dominated by advection [65, 83, 40]. We consider bidisperse mixtures of rods for which the diameter d of the two species of rods is the same and their length l are varied.

To solve this model, kinematic information including the 2D mean velocity field, the segregation velocities, and the diffusion coefficient are required. Unlike previous approaches where scaling constants are retained in the model [75, 84] or constitutive models are coupled with the transport equation [77, 56], we use DEM simulations to directly inform the continuum model, similar to the approach of Thornton et al. [60]. In this way, there are no arbitrarily fitted parameters.

In the following sections, the DEM simulation model and setup are described first. The results of the DEM simulations are then presented, and the kinematics are discussed. Then, the non-dimensional form of the transport equation is derived and used to generate predictions under different physical control parameters, which are validated by simulation. The last section presents the conclusions.

3.2. DEM simulations

The shape of the rods is described mathematically as a super-ellipsoid [149] using the function:

$$(3.2) \qquad f(x, y, z) = \left(\left| \frac{x}{a} \right|^{s_2} + \left| \frac{y}{b} \right|^{s_2} \right)^{\frac{s_1}{s_2}} + \left| \frac{z}{c} \right|^{s_1} - 1 = 0,$$

where a, b, and c are the half-dimensions of the particles principle axes, and shape indices s_1 and s_2 control the curvature of the particle edges. For the rod-like particles, $s_2 = 2$ and $a = b$. The edge of the end of a particle becomes sharper as s_1 is increased beyond 2. In this study, we use $s_1 = 8$, which has been shown to be accurate for simulating

rod-like particles [**142**]. By changing a, b, and c, cylinders with different aspect ratios can be modeled. When c is larger than a and b, the cylinder is rod-like. Thus, a variety of cylindrical particle shapes can be specified using the super-ellipsoid formulation. The equations of motion for rod-like particles are the same as those for spherical particles. The translational and rotational motion of a rod-like particle can be calculated from Newtons second law. The major difference between spherical and rod-like particles is the rotational motion. For spherical particles, particle orientation is inconsequential, but for rod-like particles, orientation affects the rotational motion and contact detection. Details of modeling non-spherical particles using DEM are described in recent review [**150**]. Once particle contacts are determined, the standard linear spring-dashpot model [**72**] based on the soft particle assumption is used to calculate the contact forces between particles, and the contact torques are obtained using these contact forces and the contact positions. To determine the overlap and the contact point between rod-like particles, a deepest point method [**150**] is employed, as described elsewhere [**142**]. Once the overlap and the contact point are determined, the contact force and torque along with the subsequent motion of each particle are calculated as in traditional DEM for spherical particles. For two contacting particles i and j, the normal contact force is $\boldsymbol{F}_{n,ij} = -k_n \boldsymbol{\delta}_{n,ij} - \eta_{n,ij} \boldsymbol{v}_{n,ij}$, and the tangential contact force is $\boldsymbol{F}_{t,ij} = -k_t \boldsymbol{\delta}_{t,ij} - \eta_{t,ij} \boldsymbol{v}_{t,ij}$. The torque resulting from the contact force and sliding friction are included in the current model, similar to traditional DEM simulations for spherical particles in our previous papers [**21, 151, 152, 153, 154**]. Here, k_n and k_t are the normal and tangential spring stiffness, respectively; $\eta_{n,ij}$ and $\eta_{t,ij}$ are the normal and tangential damping, respectively, which can be calculated using the effective mass of two contacting particles (or a particle contacting a wall) and the coefficient of restitution; $\boldsymbol{\delta}_{n,ij}$ and $\boldsymbol{\delta}_{t,ij}$ are the displacements between the particles in the normal and tangential direction respectively; $\boldsymbol{v}_{n,ij}$ and $\boldsymbol{v}_{t,ij}$ are the relative velocities of particles in the normal and tangential direction respectively. When the relation $|\boldsymbol{F}_{t,ij}| > \mu |\boldsymbol{F}_{n,ij}|$ is satisfied, the Coulomb friction model for sliding is adopted to calculate the tangential contact force as $|\boldsymbol{F}_{t,ij}| = -\mu |\boldsymbol{F}_{n,ij}| \boldsymbol{\delta}_{t,ij} / |\boldsymbol{\delta}_{t,ij}|$, where μ is the coefficient of friction. The simulation method has been validated by comparison with a variety of
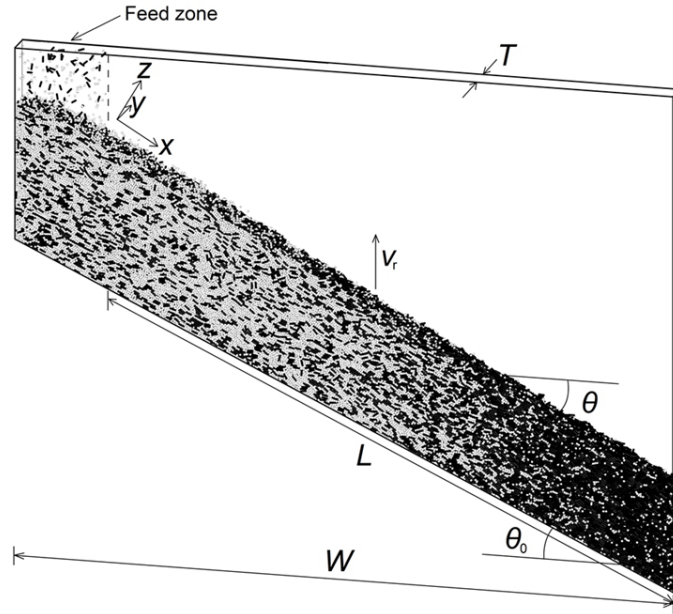
Figure 3.1. Quasi-2D bounded heap DEM simulations (with flowing layer length L and gap thickness T). The bottom wall is inclined at an angle $\theta_0 = 25°$ to reduce the simulation time. The surface rise velocity, v_r, depends on the feed rate.

analytical solutions and experiments [132] for the segregation of a 50:50 mixture of ~ 2 mm diameter cylindrical particles with lengths of about 2 mm and 6.7 mm.

Here we perform similar simulations for a range of different particle length ratios to investigate the nature of the segregation of rod-like particles. We further consider the orientation of the rods to better understand the flow and segregation of rod-like particles. Similar to previous work for bidisperse spherical particles [21], a 50:50 mixture of rod-like particles is fed into one side of a quasi-2D rectangular box formed by two parallel rectangular plates ($W = 0.69$ m wide by 0.91 m high) and separated by a narrow gap (T=32 mm), which is four times the length of the longest rods (see Fig. 3.1). We simulate 2 mm diameter rod-like particles with length-to-diameter aspect ratios of 1, 2, 3, and 4. Thus, the rods have $a = b = 1$ mm (2 mm diameter) and $c =$1, 2, 3, and 4 mm (2, 4, 6 and 8 mm length). To reduce particle ordering, the diameter and length of each species of rods are distributed uniformly over a range of 0.2 mm around the average diameter and length. Otherwise the rods have the same physical properties (friction coefficient

$\mu =0.3$, restitution coefficient $e=0.9$, which are reasonable to mimic the physical properties of glass beads), shape indices ($s_1 = 8$, $s_2 = 2$), and material density of $2500\,\mathrm{kg/m^3}$. Detailed simulation parameters for this research are provided in Table 3.1. The physical properties of particles such as the friction coefficient and restitution coefficient can affect segregation [155], but the effect is minimal over the range of parameter values used here. To reduce the number of particles in the simulations, the bottom wall of the silo (box) is sloped at 25°. Particles contacting the bottom wall are immobilized to mimic particles already forming the heap. The size bidisperse rod mixtures are fed from $0.2\,\mathrm{m}$ above the leftmost point of the bottom sloped wall with volumetric feed rate Q of particles only (excluding space between the particles). The simulation time step is $3{\times}10^{-5}\,\mathrm{s}$, which is smaller than the critical time step [156]. For the simulations described here (Table 3.2), up to 300,000 rod-like particles are simulated. The flow of rod-like particles with an aspect ratio less than 4 is continuous and steady with a relatively flat free surface. In contrast, particles with aspect ratios greater than 4 often display unsteady flow or periodic avalanches, so aspect ratios greater than 4 are not considered further.

Table 3.1. Parameter values used in the simulations. Note that the contact parameters between particles and between a particle and a wall are identical.

Parameters	Value
Density(kg/m^3)	2500
Normal spring stiffness (N/m)	1400
Tangential spring stiffness (N/m)	400
Coefficient of restitution	0.9
Coefficient of friction	0.3
Time step (s)	$3{\times}10^{-5}$
Number of particles	Up to 300000

Figure 3.2 shows snapshots of how the size bidisperse mixtures of rod-like particles orient themselves as they flow down the surface of the bounded heap. The upper blue line represents the dynamic repose angle of the flow and the lower red line marks the approximate bottom of the flowing layer. From this figure, particles appear to be oriented such that their major axes tend to align with the flow direction, especially for rods with

Table 3.2. Segregation and diffusion results for various simulation conditions. (Note that $R_L = L_l/L_s$ is specified as a ratio of the particle lengths to provide additional information.)

R_L	$d\,(\mathrm{mm})$	$L_s\,(\mathrm{mm})$	$L_l\,(\mathrm{mm})$	$Q\,(\mathrm{cm^3/s})$	$S_l\,(\mathrm{mm})$	$S_s\,(\mathrm{mm})$	k_D
4/2	2	2	4	22.5	0.093	-0.094	0.070
4/2	2	2	4	45	0.092	-0.095	0.083
4/2	2	2	4	90	0.085	-0.089	0.092
4/2	2	2	4	180	0.073	-0.076	0.096
6/2	2	2	6	22.5	0.149	-0.154	0.076
6/2	2	2	6	45	0.147	-0.143	0.090
6/2	2	2	6	90	0.135	-0.149	0.102
6/2	2	2	6	180	0.114	-0.128	0.117
8/2	2	2	8	45	0.175	-0.198	0.098
8/2	2	2	8	90	0.179	-0.197	0.115
6/4	2	4	6	22.5	0.054	-0.064	0.072
6/4	2	4	6	45	0.058	-0.057	0.082
6/4	2	4	6	90	0.060	-0.061	0.102
6/4	2	4	6	180	0.051	-0.057	0.123
8/4	2	4	8	22.5	0.089	-0.083	0.071
8/4	2	4	8	45	0.101	-0.094	0.092
8/4	2	4	8	90	0.088	-0.092	0.122
8/4	2	4	8	180	0.083	-0.092	0.135
8/6	2	6	8	45	0.036	-0.038	0.103
8/6	2	6	8	90	0.039	-0.038	0.128
4/1.33	1.33	1.33	4	90	0.083	-0.094	0.103
8/2.67	2.67	2.67	8	90	0.195	-0.206	0.096

an aspect ratio greater than 1. Similar behavior was reported in previous studies of rod-like particles in dense shear flow [**134, 157, 136**]. It is also evident that longer rods are more aligned with the flow direction than shorter rods, regardless of whether they are mixed with short rods (Figs. 3.2a-c) or longer rods (Figs. 3.2d-f). This alignment alters the interaction between the flowing particles, since the longer particles tend to slide over each other along their length, thereby reducing fluctuations normal to the flow direction, as will be discussed in a later section in the context of diffusion perpendicular to the flow direction.

To describe the particle orientation quantitatively, two angles are used to define the angle of the major axis of the particle: α is the angle between the horizontal plane and
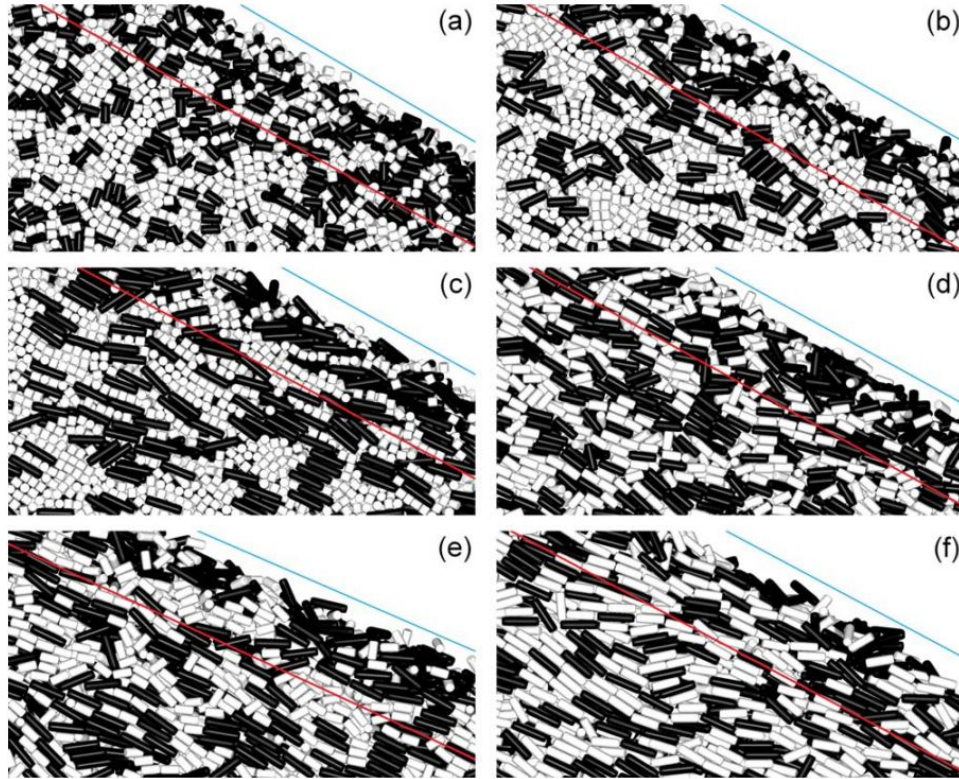
Figure 3.2. Snapshots of the behavior of a bidisperse mixture of rod-like particles with the same diameter of 2 mm at the horizontal middle position of the bounded heap (front view): (a) 2 mm and 4 mm rods, (b) 2 mm and 6 mm rods, (c) 2 mm and 8 mm rods, (d) 4 mm and 6 mm rods, (e) 4 mm and 8 mm rods, and (f) 6 mm and 8 mm rods.

the major axis of the particle; β is the angle between the plane parallel to the vertical (front and back) bounding walls and the major axis of the particle. Due to the geometric symmetry of a rod-like particle, α and β are limited to the range $\pi/2$ to $\pi/2$ and are calculated from the Euler angles of all particles in the final heap when the simulation is finished.

Fig. 3.3 shows the probability distributions of rod orientations in the heap for two bidisperse mixtures having size ratios of 4 (8 mm and 2 mm rods) and 2 (8 mm and 4 mm rods). The feed zone (extending 0.08 m from the left wall) is excluded in this analysis because of the strong vertical motion of particles as they impact the heap. Particle orientation in other mixtures considered in this study is similar to that for the two mixtures
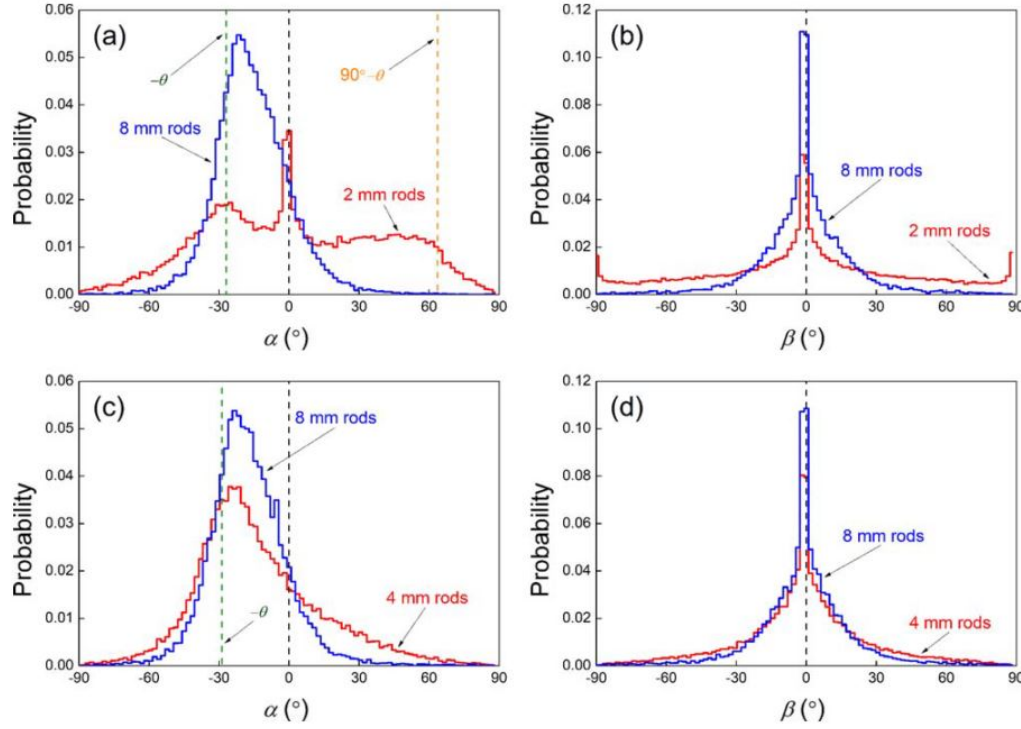
Figure 3.3. Probability distributions of rod orientation vs. α and β for a bidisperse mixture of $d = 2\,\text{mm}$ rods measured over the entire bounded heap excluding the feed zone: (a) distribution of α in a mixture of $2\,\text{mm}$ and $8\,\text{mm}$ rods, (b) distribution of β in a mixture of $2\,\text{mm}$ and $8\,\text{mm}$, (c) distribution of α in a mixture of $4\,\text{mm}$ and $8\,\text{mm}$ rods, and (d) distribution of β in a mixture of $4\,\text{mm}$ and $8\,\text{mm}$ rods. Orientation probability data resolution is $1.8°$.

shown in Fig. 3.3, so the results are not included here. Figs. 3.3a and 3.3c show that most of the $8\,\text{mm}$ and $4\,\text{mm}$ particles have an orientation between horizontal ($\alpha = 0°$) and the dynamic repose angle ($\alpha = -\theta$). Even though most $8\,\text{mm}$ particles fall in the range between the angle of repose and horizontal, a significant number of particles are up to $30°$ to either side of this range, consistent with previous results for pure shear flows [134, 135, 136]. Note further that the orientation of the $8\,\text{mm}$ particles changes little with the mixture size ratio. It is also evident that the most likely values of α occur at angles slightly smaller than the repose angle value θ. This phenomenon was previously observed in shear flows of ellipsoidal particles and rod-like particles [158],

with the speculation that the preferred orientation may minimize end-over-end rotation of particles under shear [158]. The angle β with respect to the boundary planes is near zero for both 4 and 8 mm particles, as shown in Figs. 3.3b and 3.3d. Furthermore, the distribution is very narrow, indicating that most particles are oriented nearly parallel to the front and back walls of the bounded heap, which is not surprising given that longer rods near the wall tend to slide along the wall as they flow, as shown in Fig. 3.2.

The orientation distribution of the short 2 mm rods (aspect ratio 1) differs from that of the long rods for both α and β. Short rods have a very broad distribution of angles with respect to horizontal, as shown in Fig. 3.3a, and the distribution has two distinct maxima, at zero and at the repose angle $-\theta$, as well as a broad distribution. The reason for the difference between short rod and long rod distributions lies in the alignment of short rods with respect to the boundary walls. As is evident in Figs. 3.2a-c, the major axis of the short rods can align with the flow direction, similar to the long rods, resulting in a broad maximum at the angle of repose $-\theta$ in Fig. 3.3a. However, due to the boundary wall, some short rods end up with their flat end against the wall so their major axis is parallel to the horizontal plane, resulting in a narrow peak at $0°$. Otherwise, a broad range of orientations can occur from when the axis of a short rod is similar to that of the long rods (corresponding to $-\theta$) to when the short rod is approximately perpendicular to the axis of the long rods, often with the flat end of a short rod in contact with the curved side of a long rod that has aligned with the flow (corresponding to $90° - \theta$). For the short rods, the probability distribution of β has a large peak near 0 and a small one near $90°$ (or -$90°$), as shown in Fig. 3.3b. Like the long rods, the peak near $0°$ for short rods indicates that the rod axis aligns with the flow. The peak close to $90°$ (or -$90°$) results from short rods aligning their flat surface against the side wall. Note also that due to their small aspect ratio, many more short rods than longer rods do not align with the flow, accounting for the non-zero probably across the entire range of β. The orientation distribution plays a role in the kinematics of the flow as discussed shortly.

3.3. Kinematics of bidisperse rods flow

To apply the continuum model for segregation (Eq. 3.1) to segregating bidisperse mixtures of rods, it is necessary determine kinematic information related to the flow, including the 2D mean velocity field and the flowing layer thickness as well as the segregation velocity, which characterizes the segregation of the particle species, and the diffusion coefficient, which characterizes the collisional remixing of the flowing particles. We use DEM simulations to obtain these properties for bidisperse rods in quasi-2D bounded heap flow.

3.3.1. Streamwise velocity and normal velocity

The streamwise velocity and normal velocity of the rod-like particles in the simulations are calculated using the volume average binning method [21]. To accomplish this with rods that can span more than a single bin, we consider an equivalent line of spheres, each with an effective diameter such that their total volume is the same as the rod. For example, a 2 mm diameter by 8 mm long rod is assumed to be made up of a line of four ∼2.29 mm diameter spheres that are touching. A portion of a rod is within a bin if the center of one of its equivalent spheres lies in the bin. In this way, a single long rod may be included simultaneously in several bins.

The free surface streamwise velocity, u_s, along the length of the flowing layer is shown in Fig. 3.4a. The surface velocity decreases linearly along the length of the flowing layer surface, as is the case for spherical particles in bounded heap flow, and consistent with the uniform deposition of particles on the heap assuming an approximately constant flowing layer thickness [21, 65]. The surface velocity decreases to zero at the downstream end of the flowing layer (i.e., the end wall) at $x = L$ (the precise value for L depends on the angle of repose of the heap). The flowing layer thickness δ is defined as the depth where the streamwise velocity is one-tenth the surface velocity, that is $u(x, -\delta) = 0.1u(x, 0)$, consistent with the approach used by Fan et al. [21]. for spherical particles in bounded heap flow. As shown in Fig. 3.4b, the flowing layer thickness is approximately 5-8 rod diameters along most of the length of the flowing layer. Near the feed zone the flowing
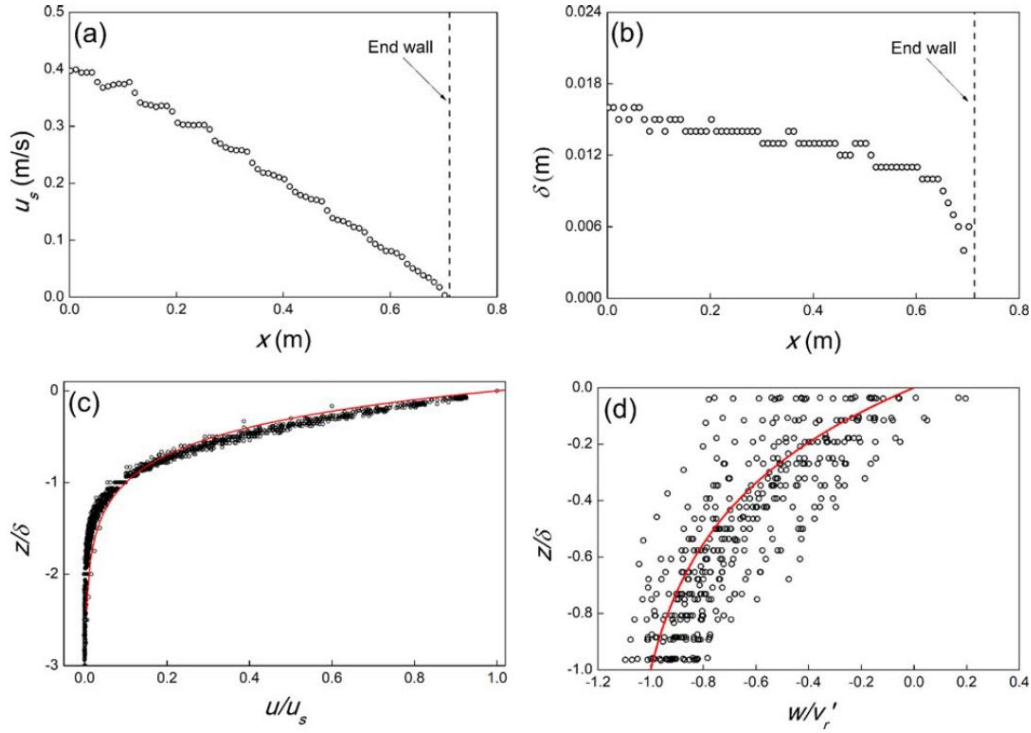
Figure 3.4. Streamwise and normal velocity profiles in simulation using a mixture of $2\,\mathrm{mm}$ rods and $4\,\mathrm{mm}$ rods with $d = 2\,\mathrm{mm}$ at feed rate $Q = 90\,\mathrm{cm}^3/\mathrm{s}$: (a) surface streamwise velocity along the streamwise direction; (b) flowing layer thickness along the streamwise direction; (c) normalized streamwise profile at various positions along the length of the flowing layer (the solid curve is $u/u_s = e^{kz/\delta}$); and (d) normalized normal velocity profile at various positions along the length of the flowing layer (the solid curve is $w/v_r' = (e^{kz/} - 1)/(1 - e^{-k})$).

layer is slightly thicker, and at the downstream end of the heap, the flowing layer thickness decreases, similar to previous results for spherical particles [21].

Based on the local surface velocity and the flowing layer depth, the normalized streamwise velocity profiles in the normal direction are plotted in Fig. 3.4c for several locations along the length of the flowing layer. The simulation results collapse onto a single curve, consistent with self-similar velocity profiles for spherical particles [21, 57], so the same exponential expression for the streamwise velocity is used:

$$(3.3) \qquad u(x, z) = \frac{kq}{\delta(1 - e^{-k})} \left(1 - \frac{x}{L}\right) e^{kz/\delta}.$$

Here k is a scaling constant set to 2.3 according Fan et al. [40], so that the streamwise velocity at $z = -\delta$ is $0.1u(x, 0)$, consistent with the definition of the flowing layer thickness. The constant k and the definition of the flowing layer thickness are the same as those for spherical particles, since spheres and rods have nearly identical self-similar streamwise velocity profiles in the flowing layer. For quasi-two-dimensional heap flow, the two-dimensional bulk feed rate $q = Q_{feed}/(Tf_v)$ of particles entering the flowing layer is used to characterize the feed rate. Here, Q_{feed} is the volumetric flow rate of particles only (not including space between particles) entering the flowing layer just downstream of the feed zone, T is the gap thickness between the two sidewalls, and f_v is the approximate volume fraction of the particles in the flowing layer, which was measured to be $f_v = 0.61$ for all particle combinations considered here. Since particles are deposited uniformly on the heap and noting that the width of the heap is $W = 0.69\,\text{m}$ including the $0.08\,\text{m}$ wide feed zone at the top of the heap, the volume flow rate of particles entering the flowing layer is $Q_{feed} = Q(0.69 - 0.08)/0.69$. In some cases, it was necessary to include only a $0.04\,\text{m}$ portion of the feed zone in the flowing layer due to fast segregation of particles even in the feed zone in which case the volume flow rate of particles entering the flowing layer is $Q_{feed} = Q(0.69 - 0.04)/0.69$.

The normalized normal velocity profile is shown in Fig. 3.4d for various locations along the length of the flowing layer. The data has wide scatter for two reasons. First, the normal velocity is typically an order of magnitude smaller than streamwise velocity and normalized by a much smaller velocity, the rise velocity v_r of the heap. As is the case for spherical particles, this results in more scatter. Second, the flow of rod-like particles is more random and disordered than that of spherical particles for several reasons. First, rod-like particles are imperfectly aligned with the flow with each particle having a slightly different orientation, see Fig. 3.2. Second, unlike spherical particles that easily roll down the slope, rods typically slide over one another instead of rolling.

Finally, spherical particles have simple particle contacts, whereas rod-like particles have more complicated contact modes (end-to-end, end-to-side, and side-to-side). All of these effects likely contribute to local fluctuations in the velocity profile. Of course, averaging over longer simulations or for larger systems may reduce the scatter, but are much more computationally-intensive for rods compared than for spherical particles. In the coordinate system moving upward with the rise velocity $v_r' = v_r \cos\theta$, the normal velocity is zero on the free surface ($z/\delta = 0$) and decreases to $-v_r'$ at the bottom of the flowing layer ($z/\delta = -1$), where particles are deposited on the heap bed. Based on Eq. 3.3 and the continuity equation, the predicted normal velocity is [**21**]:

$$(3.4) \qquad\qquad w(z) = \frac{q}{L(1 - e^{-k})} \left(e^{kz/\delta} - 1 \right).$$

This equation automatically satisfies the bottom boundary condition $w(-\delta) = -q/L = -v_r \cos(\theta)$. Note that the scatter of data in Fig. 3.4d is distributed around the curve determined by Eq. 3.4.

3.3.2. Segregation velocity and diffusion

Previous research on size segregation of spherical particles indicates that kinetic sieving and squeeze expulsion are the dominant segregation mechanisms in gravity driven free surface flows [**55, 60, 112**]. Similar mechanisms appear to drive segregation in flows of size bidisperse rod-like particles. Essentially, short rods preferentially fall into small voids below them, filling the lower portion of the flowing layer and subsequently squeezing the long rods upward into voids above them.

Given that the segregation mechanism for rod-like particles appears similar to that for spherical particles, and that the segregation results are similar to those for spherical particles in quasi-2D bounded heaps in that short rods are deposited on the upstream portion of the bed and long particles are deposited downstream [**21, 65, 40**] (Fig. 4.1), the factors that drive rod segregation are likely similar to those that drive the segregation of spherical particles. These factors include the local shear rate, , which is related to the

frequency of void generation, and the local concentration of the other species, $1 - c_i$, which is related to the propensity for segregation (particles will only segregate when surrounded by particles of the other species). As with the segregation of size or density bidisperse spherical particles [65, 40, 57], we assume the segregation velocity $w_{p,i}$ for rods of species i can be expressed as

$$(3.5) \qquad\qquad\qquad w_{p,i} = S\gamma(1 - c_i),$$

where S is a parameter dependent on the two types of rods making up the bidisperse mixture. An example of the dependence of $w_{p,i}/\dot{\gamma}$ on $1 - c_i$ for $2\,\text{mm}$ diameters rods is shown in Fig. 3.5a for a 50:50 mixture by volume of $2\,\text{mm}$ short rods and $6\,\text{mm}$ long rods. The parameter S, which is the slope of the linear relation, represents a segregation length scale [65]. It is positive (upward) for long rods and negative (downward) for short rods. For the simulation data shown in Fig. 3.5a, the characteristic length scales for long rods (S_l=0.135 mm) and short rods (S_s=-0.149 mm) are similar in magnitude, as is the case for spherical particles of different sizes [65]. Although the relation between $w_{s,i}$, and $(1 - c_i)$ appears to be linear for a 50:50 mixture by volume, recent studies of the segregation of spheres [78, 129] have shown that the segregation flux is larger for concentrations of small particles less than 50%. In other words, small particles surrounded by mostly large particles segregate more quickly than large particles surrounded by mostly small particles. This asymmetric behavior is reflected as a slightly nonlinear relation between the segregation velocity ($w_{s,i}$) and the local concentration of the other species ($1 - c_i$) for particles segregating by density [57].

To confirm that the linear relation in Eq. 3.5 applies to rod-like particles, we consider nine simulation cases with feed mixtures ranging from 10% to 90% short particles. In this way, the entire range of values for $1 - c_i$ on the horizontal axis is covered, as shown in Fig. 3.5b. As evident from the plot, the data from the nine simulation cases are consistent with each other and form two straight lines. This indicates that for size bidisperse rods with equal diameters, the relation between $w_{s,i}/\dot{\gamma}$ and $1 - c_i$ is indeed linear as indicated in Eq. 3.5. This result is intriguing because the cylindrical shape of the rods must play
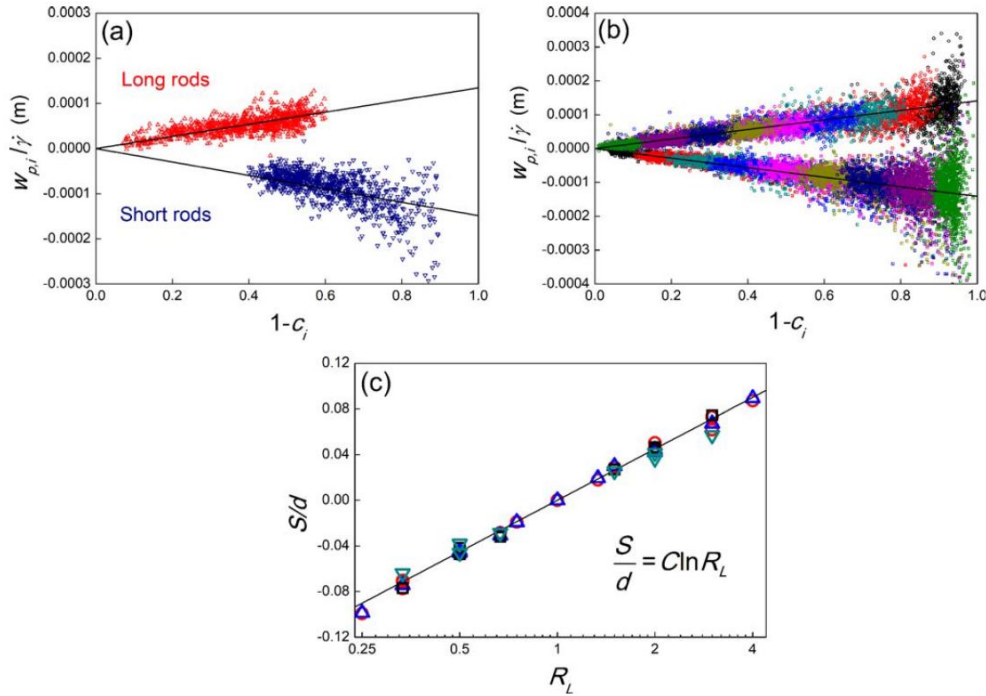
Figure 3.5. Segregation data from the DEM simulations. (a) Dependence of percolation velocity on particle concentration for 2 mm and 6 mm rods with d=2 mm and $Q = 90\,\mathrm{cm}^3/\mathrm{s}$. Symbols are for long rods (red or gray) and short rods (blue or black). Solid lines are linear fits to the data, yielding $S_s = -0.149\,\mathrm{mm}$ and $S_l = 0.135\,\mathrm{mm}$. (b) Dependence of segregation velocity on the local shear rate and the local concentration from nine simulations (different colors) with inlet short rod concentrations ranging from 0.1 to 0.9 in mixtures of 2 mm and 6 mm rods with $Q = 90\,\mathrm{cm}^3/\mathrm{s}$ and d=2 mm. (c) Scaling of S vs. R_L from 22 cases of 50:50 mixtures with length ratio from 0.25 to 4 and rod diameters of 1.33, 2, and 2.67 mm at $Q = 22.5\,\mathrm{cm}^3/\mathrm{s}$, $45\,\mathrm{cm}^3/\mathrm{s}$, $90\,\mathrm{cm}^3/\mathrm{s}$, and $180\,\mathrm{cm}^3/\mathrm{s}$. Different shapes and colors represent different flow rates.

a role in this difference from spherical particles. One possible reason for this is that for spherical particle, size differs in three dimensions, whereas for rods with equal diameters, the size differs in only one dimension, which happens to be the rod length that is nearly always oriented in the flow direction. As a result, in flows with spherical particles, a small segregating sphere needs a void that is larger than its own size in both the flow direction and the transverse direction (gap direction). In flows with rod-like particles, a short rod

needs a void that is larger only in the flow direction. However, this mechanism is purely speculative, since the detailed physics behind the relation between $w_{s,i}/\dot{\gamma}$ and $1 - c_i$ given in Eq. 3.5 is not clear.

Values of S are obtained from 22 simulations using 50:50 mixtures with length ratio RL ranging from 0.25 to 4 and common rod diameters of 1.33, 2, and 2.67 mm at $Q = 22.5\,\mathrm{cm^3/s}$, $45\,\mathrm{cm^3/s}$, $90\,\mathrm{cm^3/s}$, and $180\,\mathrm{cm^3/s}$, see Table 3.2. Figure 3.5c includes 44 data points, since each simulation produces two data points: one for S_l (for long rods) and one corresponding to S_s (for short rods). In addition, points for monodisperse rods at $R_L = 1$ (corresponding to no segregation: $S/d = 0$) are included. As shown in Fig. 3.5c, different feed rates have no significant effect on S, as expected for a local model (Eq. 3.5). Furthermore, S normalized by rod diameter d varies with the logarithm of length ratio R_L, which is analogous to the dependence of S normalized by the small particle diameter on the logarithm of the size ratio for spherical particles [65, 57]. An empirical scaling relation for S is:

$$(3.6) \qquad \frac{S}{d} = C \ln R_L,$$

where C is a constant with the value 0.065. This relationship is limited to rods with equal diameter and different lengths with aspect ratios no more than 4. DEM simulations of rods with aspect ratios greater than 4 were also performed but are not included because it is difficult to obtain a smoothly flowing surface layer due to the easy jamming of long rod-like particles. Nevertheless, the result that segregating bidisperse rods follow the same general relations for the percolation velocity (Eq. 3.5) and for the dependence of the segregation length scale S on particle size ratio (Eq. 3.6) that is successful for size and density segregation for spherical particles [65, 83, 40, 57, 86] suggests that the approach embodied in Eqs. 3.5 and 3.6 is robust over widely differing types of particle mixtures. The value of C for rod-like particles is different than that for spherical particles [65], as would be expected since the parameter is based on a different ratio in each case (diameter ratio for spherical particles and length ratio for rod-like particles).
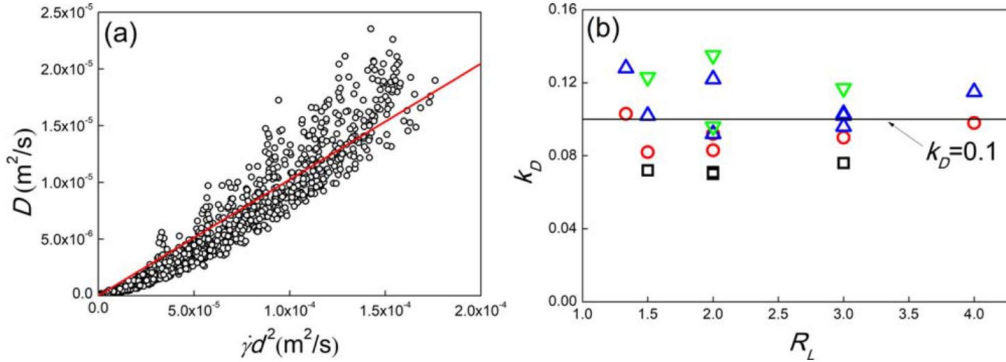
Figure 3.6. Diffusion coefficient measurements. (a) D vs. $\dot{\gamma}d^2$ for $2\,\text{mm}$ and $6\,\text{mm}$ rods with $d = 2\,\text{mm}$ and $Q = 90\,\text{cm}^3/\text{s}$. Solid line is a linear fit of the data, yielding $k_D = 0.102$. (b) D vs. R_L for 22 simulations of 50:50 mixtures with length ratios from 0.25 to 4 and rod diameters of 1.33, 2, and $2.67\,\text{mm}$ at $Q = 22.5\,\text{cm}^3/\text{s}$ (black square), $45\,\text{cm}^3/\text{s}$ (red circle), $90\,\text{cm}^3/\text{s}$ (blue upward triangle), and $180\,\text{cm}^3/\text{s}$ (green downward triangle).

The collisional diffusion coefficient of the mixture, D, was obtained in the direction normal to the surface (because segregation is in this direction) by tracking the particle trajectories using the mean squared displacement as a function of time, $\langle \Delta z(\Delta t)^2 \rangle$ [40]. The diffusion coefficient is calculated using $\langle \Delta z(\Delta t)^2 \rangle = 2D\Delta t$ [40, 126]. Figure 3.6a shows an example simulation result for the diffusion coefficient of bidisperse rods indicating that the diffusion coefficient is approximately linearly dependent on the shear rate, consistent with previous studies of dense granular flows for spherical particles [56, 40, 126, 159, 160, 161]. As such, D can be modeled as

$$(3.7) \qquad\qquad D = k_D \dot{\gamma} d^2.$$

The values of k_D for 22 simulations using 50:50 mixtures with length ratio R_L ranging from 0.25 to 4 and rod diameters of 1.33, 2, and $2.67\,\text{mm}$ at $Q = 22.5\,\text{cm}^3/\text{s}$, $45\,\text{cm}^3/\text{s}$, $90\,\text{cm}^3/\text{s}$, and $180\,\text{cm}^3/\text{s}$ are shown in Table 3.2. The values of k_D plotted in Fig. 3.6b are in the range $0.07 < k_D < 0.13$. We have also conducted additional simulations of dense shear flow (volume fraction> 0.4) for monodisperse rod-like particles in a shear cell with Lees-Edwards boundary conditions [162] that yield similar results such that $k_D \approx 0.1$. In

subsequent model results presented here, we use the locally varying value for D (Eq. 3.7) with $k_D = 0.1$ for all cases, noting that this nominal value for k_D is appropriate only for bidisperse mixtures of rods with the same diameter and individual rods having aspect ratios no greater than 4.

3.4. Predictions of the model

3.4.1. Transport model

Now that the kinematic and segregation parameters for rod-shaped particles have been obtained, we apply the transport model (Eq. 3.1) to demonstrate how it can be used to model segregation for a variety of physical control parameters. Using the nondimensional variables [65, 40, 57]

$$(3.8) \qquad \tilde{x} = \frac{x}{L}, \quad \tilde{z} = \frac{z}{\delta}, \quad \tilde{t} = \frac{t}{\delta L/2q}, \quad \tilde{u} = \frac{u}{2q/\delta}, \quad \text{and} \quad \tilde{w} = \frac{w}{2q/L}.$$

the transport model (Eq. 3.1) for the concentration of species i becomes [40]:

$$(3.9) \qquad \frac{\partial c_i}{\partial \tilde{t}} + \tilde{u}\frac{\partial c_i}{\partial \tilde{x}} + \tilde{w}\frac{\partial c_i}{\partial \tilde{z}} \pm \Lambda\frac{\partial}{\partial \tilde{z}}\left[h(\tilde{x}, \tilde{z})c_i(1 - c_i)\right] = \frac{1}{Pe}\left(\frac{1}{Pe}\frac{\partial c_i}{\partial \tilde{z}}\right).$$

The last term on the left-hand side of Eq. 3.9 is derived from Eq. 3.5 for the segregation velocity (positive for large particles and negative for small particles), which includes the concentration of the other species $1 - c_i$ and the nondimensional shear rate, $h(\tilde{x}, \tilde{z}) = \dot{\gamma}\delta^2/2q$. The Péclet number, $Pe = 2q\delta/DL$, is the ratio of a diffusion time scale ($t_d = \delta^2/D$) to an advection time scale ($t_a = L\delta/2q$). The diffusion coefficient, D, varies spatially as specified by Eq. 3.7, which results in a spatially varying value for Pe. This provides a better representation of the collisional diffusion in the flowing layer than a constant value for Pe based on a spatially averaged diffusion coefficient as done previously for spherical particles [40]. The nondimensional parameter, $\Lambda = SL/\delta^2$, represents the ratio of an advection time scale ($L\delta/2q$) to a segregation time scale ($\delta^3/2qS$) [40].

Segregation and diffusion in the streamwise direction can be neglected because they are negligible compared to advection in this direction since $\delta/L \ll 1$ [65, 40].

The boundary conditions are defined in a similar way to previous models for spherical particles [40]. For the inlet (left) boundary, where the two species enter the system in a well-mixed condition, the concentrations are $c_s(0, \tilde{z}) = c_0$ or $c_i = 1 - c_0$, where c_0 is the concentration of short particles in the mixture ($c_0 = 0.5$ unless specified otherwise). At the downstream boundary (right end), the advection, diffusion, and segregation fluxes are all in the normal direction, so no boundary condition needs to be specified. For the top and bottom boundaries, the diffusion flux and the segregation flux are set equal to one another corresponding to the no flux boundary condition proposed by Gray and Chugunov [75]:

$$(3.10) \qquad \Lambda h(\tilde{x}, \tilde{z}) c_i (1 - c_i) = \frac{1}{Pe} \frac{\partial c_i}{\partial \tilde{z}}.$$

According to the boundary condition specified by Eq. 3.10, particles exit the bottom of the flowing layer to deposit on the heap due to advection alone, and no particles leave the flowing layer through the top boundary because there is no advective flux in the normal direction at the top boundary. Similar to previous work [75, 60], Eqs. 3.9 and 3.10 demonstrate that the model depends only on the two nondimensional parameters, Pe and , which have clear physical interpretations. Since the two nondimensional parameters in this model are calculated based on the physical control parameters and kinematic information that can be generalized from simulations, no arbitrarily fitting parameters are used in the model.

3.4.2. Prediction of segregation under different physical control parameters

To validate the model predictions for the segregation of size bidisperse rods, we compare the concentration profile in the flowing layer from the model to the results from DEM simulations as shown in Fig. 3.7 for the same rod length ratio and different feed rates. Figures 3.7a and 3.7c show the concentration of short rods in the flowing layer. For all
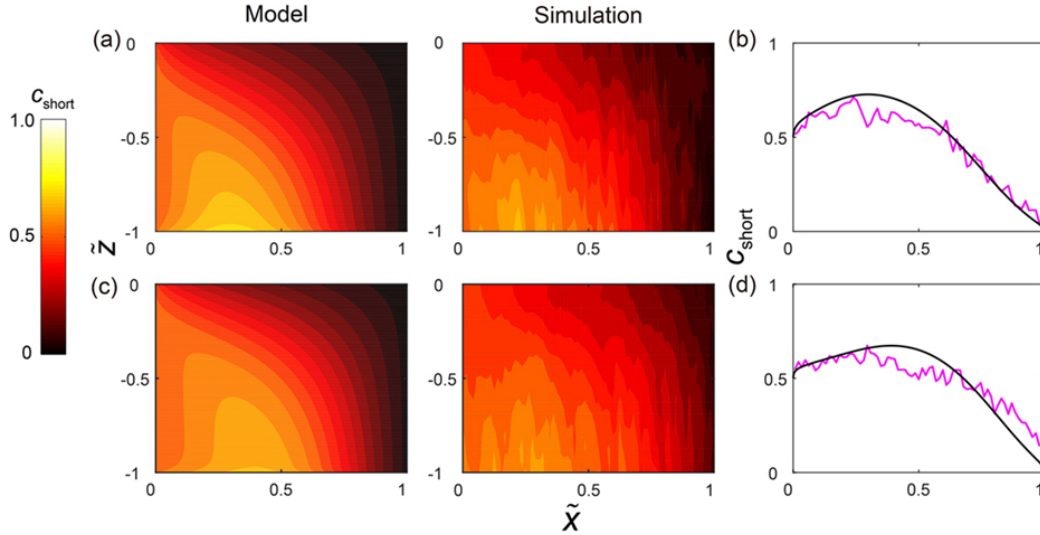
Figure 3.7. Comparison of model and simulation predictions of short particle concentration, c_s, for size bidisperse segregation of $2\,\text{mm}$ and $6\,\text{mm}$ length rods ($R_L = 3$) with the same diameter ($d = 2\,mm$) and $c_0 = 0.5$. Left and middle columns show concentration contours of short rods in the flowing layer from model and simulation, respectively. The right column compares model predictions (black) and simulation results (magenta or gray) at steady state for the concentration profile at the bottom of the flowing layer, which reflects the concentration of the particles deposited on the heap. Top row: $Q = 45\,\text{cm}^3/\text{s}$, $k_D = 0.1$, $L = 0.737\,\text{m}$, $\delta = 0.016\,\text{m}$. Bottom row: $Q = 90\,\text{cm}^3/\text{s}$, $k_D = 0.1$, $L = 0.74\,\text{m}$, $\delta = 0.013\,\text{m}$.

cases, the concentrations near the inlet ($\tilde{x} = 0$) are close to 0.5, corresponding to the mixed particle concentration for the left inlet boundary condition. Outside the feed zone, short rods are concentrated in the upstream region, particularly in the lower part of the flowing layer as a result of downward segregation, while long rods are concentrated in the upper part of the flowing layer due to upward segregation and in the downstream region, similar to the segregation of small and large spherical particles in quasi-2D bounded heaps [40]. The areas having high concentrations of short and long particles in the model predictions and simulations agree well, although the simulation results are not as smooth as the model results due to stochastic variations in the flow. To validate the model quantitatively, we plot the concentration profiles of the short particles at the bottom of the flowing layer, which represents the concentration of the particles deposited on the

heap. Figures 3.7b and 3.7d demonstrate that the concentration profiles from the model match the simulation results reasonably well, indicating that the model captures the essential physics of rod segregation. Moreover, the slightly higher degree of segregation observed at a low feed rate (Fig. 3.7b) than at a high feed rate (Fig. 3.7d) indicates that the influence of physical control parameters on the segregation is captured by the model, as is the case for spherical particles [**65, 40, 57**].

To further investigate the influence of the physical control parameters on the segregation results and to test the accuracy of the model predictions under a range of parameters, we compare model predictions for twelve cases having different length ratios and feed rates with the corresponding DEM simulations. The short particle concentration profiles for the particles deposited on the heap (similar to Figs. 3.7b and 3.7d) are shown in Fig. 3.8. Each row corresponds to two cases with the same particle length ratio but different feed rates. In both model predictions and simulations, for small length ratios R_L, the deposited particles remain relatively well mixed ($c_s \approx 0.5$) with only a small amount of segregation, particularly noticeable at large $\tilde{x}$ where c_s is only slightly smaller than 0.5. As R_L increases, the segregation of the deposited particles becomes more significant. Comparing the concentration profiles at low and the high feed rates, it is evident that the segregation is slightly stronger for low feed rates, as would be expected when advection decreases compared to segregation [**40**].

It is also clear in Fig. 3.8 that the model predictions generally match the simulation results, especially when R_L is small. Comparing similar length ratios, the model predictions deviate from simulations results a bit more for $R_L = 4/2$ ($d = 2\,\mathrm{mm}$, $l_l = 4\,\mathrm{mm}$, and $l_s = 2\,\mathrm{mm}$) than for $R_L = 8/4$ ($d = 2\,\mathrm{mm}$, $l_l = 8\,\mathrm{mm}$, and $l_s = 4\,\mathrm{mm}$). A possible reason for the difference is that the shortest rods ($d = 2\,\mathrm{mm}$ and $l_s = 2\,\mathrm{mm}$) do not have a highly uniform orientation as discussed earlier (Figs. 3.2 and 3.3), thereby influencing the segregation.

To further demonstrate the capability of the model, we also change the inlet concentration conditions to $c_0 = 0.2$ and $c_0 = 0.8$. Figs. 3.9a and 3.9b show snapshots from the two simulations, where the differences in the segregation due to the overall
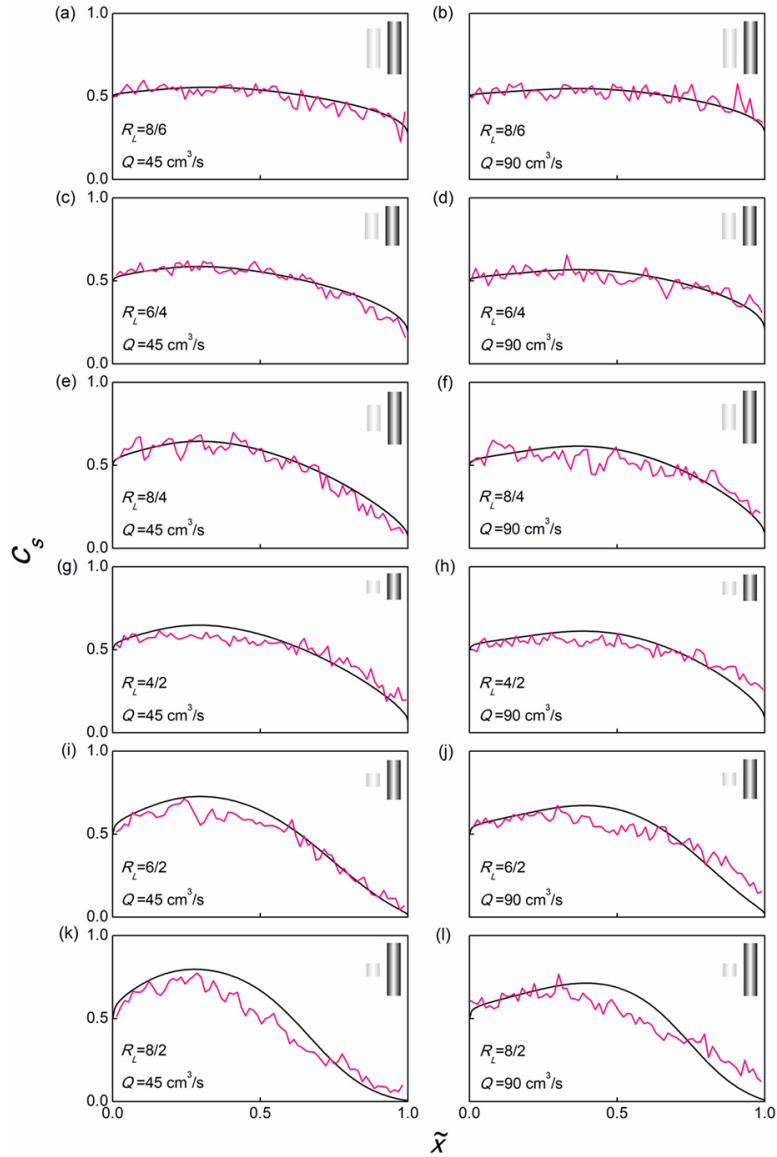
Figure 3.8. Model prediction (black curves) and simulation results (magenta or gray) for the short rod concentration profile at the bottom of the flowing layer, which represent material deposited on the heap. In all cases, the diameter of the rods is $d = 2\,\text{mm}$. The relative size of the particles is shown in the upper right of each subfigure. For cases where the short particle is $2\,\text{mm}$ long and the case where $R_L = 6/4$ and $Q = 45\,\text{cm}^3/\text{s}$, the feed zone is assumed to be $0.04\,\text{cm}$ wide; otherwise the feed zone is assumed to be $0.08\,\text{cm}$ wide.
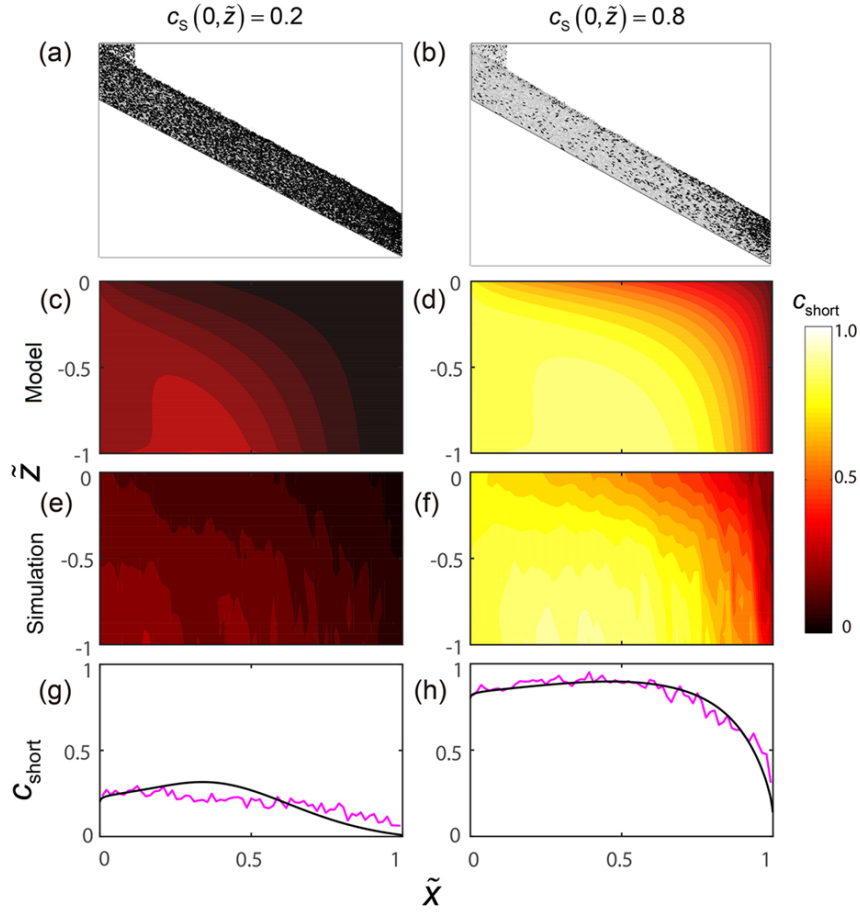
Figure 3.9. Segregation with different inlet particle concentrations of $2\,\mathrm{mm}$ and $6\,\mathrm{mm}$ rods ($R_L = 3$) with $d = 2\,\mathrm{mm}$. Left column: inlet short rod concentration $c_s(0, \tilde{z}) = 0.2$, $Q = 90\,\mathrm{cm}^3/\mathrm{s}$, $k_D = 0.1$, $L = 0.742\,\mathrm{m}$, $\delta = 0.017\,\mathrm{m}$. Right column: inlet short rod concentration $c_s(0, \tilde{z}) = 0.8$, $Q = 90\,\mathrm{cm}^3/\mathrm{s}$, $k_D = 0.1$, $L = 0.745\,\mathrm{m}$, $\delta = 0.017\,\mathrm{m}$. Row 1: segregation pattern from simulations. Row 2: contours of c_s in the flowing layer from model. Row 3: contours of c_s in the flowing layer from simulations. Row 4: concentration profiles of short particles at the bottom of the flowing layer from the continuum model using S from Eq. 3.6 (black curve) and simulation (magenta or gray curves).

species concentrations are evident. Figs. 3.9c-f demonstrate how the model predictions for the concentration of the short rods match the simulation results. Likewise, the concentration profile for short particles from the model at the bottom of the flowing layer,

corresponding to the short particles deposited on the heap, matches the simulation results (Figs 3.9g and 3.9h). Thus, the model provides accurate predictions of the segregation regardless of species concentration, again demonstrating that the model captures the essential physics of the segregation of rods with different lengths.

3.5. Conclusions

The segregation of rod-like particles in a bounded heap was simulated using super-ellipsoid particles. The flow of rod-like particles with aspect ratios less than 4 is smooth, and a steady flowing layer can be obtained. The rod-like particles tend to align with the flow direction, especially for rods with aspect ratio larger than 1, though the walls also influence the orientation of rod-like particles. For the short rods with aspect ratio close to 1, the rods orient with their flat end aligned with the wall or with their axes roughly parallel or perpendicular to the flow direction. The kinematics of bidisperse rods flow resemble those of spherical particle flow, including the streamwise velocity, the normal velocity, the segregation velocity, and the diffusion. The segregation mechanism of rod-like particles is also similar to spherical particlesthe factors that drive rod segregation appear to be kinetic sieving and squeeze expulsion.

Also similar to spherical particle segregation, the segregation velocity $w_{s,i}$ for rods depends on local shear rate $\dot{\gamma}$, the local concentration of the other species $1 - c_i$, and a dimensional parameter, the segregation length S, which depends primarily on the length ratio R_L and rod diameter. However, unlike spherical particles, for size bidisperse rods with equal diameters, the relation between $w_{s,i}/\dot{\gamma}$ and $1 - c_i$ is linear. This difference between rod-like particles and spherical particles may be related to the alignment of rod-like particles, but deserves further investigation.

The flow kinematics, segregation velocity, and diffusion coefficient obtained from DEM simulations were applied in a modified advection diffusion equation that has been previously used to model segregating spherical particles. The model predictions for rod-like particles having the same diameter but different lengths quantitatively agree with the simulation results under different flow rates, particle length ratios, and relative particle concentrations. It is important to note that even though the model predictions match

the DEM simulation results, the model results are only based indirectly on the DEM simulations. It would be easy to match the model results to the simulation results by directly using the velocity profiles and values for S and D from a particular simulation in the model to match those for the simulations. However, that is not what we did here. Instead, we found general expressions for the self-similar velocity profile and for the dependence of S on the length ratio and D on the shear rate. Then we used these same general expressions in the model to compare to individual DEM simulations. As a result, the results are general to the flow of bidisperse rod-like particles, rather than specific to any particular flow rate or rod length ratio. Thus, we can model the segregation for any given volume feed rate Q and particle length ratio R_L within the range of parameters for which we have done DEM simulations.

Although we have successfully modeled the segregation of rods with the same diameter and different lengths, the situation is more complicated for rods differing in both length and diameter. While it is likely that a value for the segregation parameter S could be found for any particular pair of particles regardless of their diameters and lengths, a simple relation between S and both the length and diameter ratio like that found here for rods having the same diameter is unlikely. Furthermore, the segregation of spherical and rod-like particles could be explored to assess the impact of particle shape on segregation characteristics. At a more fundamental level, the impact of particle-scale interactions between rods of different diameters and lengths or between rods and spherical particles that drives the segregation needs further investigation.

CHAPTER 4

Controlling granular segregation using modulated flow

SUMMARY

Unsteady flows of granular media are ubiquitous yet remain largely unexplored. In this chapter, unsteady flows are applied to strongly segregating granular materials to control the segregation pattern and enhance overall mixing. Size-bidisperse granular mixtures with large size ratios flowing onto a quasi-2D bounded heap form stratified layers of large and small particles when the flow rate is modulated. These layers exhibit better average mixing than the segregated patterns generated by steady feed rates. The mechanisms of layer formation under modulated flow differ from those for spontaneous stratification and are related to changes in the composition of the flowing layer at different stages in each feed cycle. The thickness and length of the stratified layers can be controlled by changing the feed rates and feed cycle durations, which is potentially useful for reducing segregation in industrial processes.

4.1. Introduction

Segregation and mixing of disperse granular materials (differing in size, density, etc.) have important implications in situations ranging from material handling in industry to

natural phenomena [**53, 49**]. For example, in industry, segregation is frequently encountered in processes involving handling bulk solids such as ores, polymers, food, and pharmaceutical materials [**52, 69**]. In most cases, segregation of an initially well-mixed granular mixture is undesirable, because it impacts the efficacy of later processes or the quality of final products. Therefore, understanding the mechanisms of granular segregation and developing efficient mixing technologies are of great importance in many industrial applications.

During the past several decades, the understanding of segregation in flowing granular materials has been advanced by extensive experimental, computational, and theoretical studies, examples include [**96, 124, 163, 121, 56, 55, 84, 40, 164**]. For size segregation in dense, sheared granular flows, a widely accepted percolation-based mechanism (sometimes called kinetic sieving [**55**]) posits that voids between particles are generated by shear and smaller particles are more likely than larger particles to fall into the voids under gravity. Consequently, large particles are pushed upward to the free surface, resulting in segregation in various flow geometries such as bounded heaps [**20, 21, 165**], rotating tumblers [**61, 91**], and chutes [**68, 60**]. Most of these studies have focused on segregation in steady granular flows with relatively simple kinematics and time invariant pattern formation. For example, for continuous quasi-2D bounded heap flow, when depositing size bidisperse mixtures onto the heap at a constant feed rate, smaller particles are deposited on the upstream portion of the heap, while larger particles flow to the downstream region of the heap, resulting in a segregated pattern in the streamwise direction [**20, 21**]. As the particle size ratio increases, segregation becomes stronger, with a clear interface between the small and large particle enriched regions, which can cause inhomogeneity in subsequent processes such as hopper discharge or chute transfer. It is possible to minimize segregation by introducing counter-balancing mechanisms which include altering particle characteristics such as density [**124, 163, 164, 76, 114**] and inelasticity [**59**], adding a small amount of liquid to dry particle mixtures making them more cohesive [**166, 167, 168, 169, 170**] or completely submerging the particles [**170, 171, 172**]. However, these methods are not

always feasible in industrial applications, and in this work we focus on size segregation of dry spherical particles only.

Recent experimental [**68**] and theoretical [**40**] studies have shown that segregation strongly depends on details of the flow kinematics. As a result, segregation is likely to differ significantly between unsteady flows and steady flows. A handful of studies on unsteady monodisperse granular flows have revealed complicated kinematics during transient processes [**173, 37, 42, 43, 41, 38**]. For example, instantaneous velocity profiles measured during intermittent avalanches [**43**] exhibit a sharp increase and then a gradual decrease of the streamwise velocity during each avalanche. In rotating tumblers under a periodic forcing protocol [**41**], phase lags between the external forcing and the response of granular flow occur, indicating a delayed response of the granular system to external excitation. The more complicated kinematics in unsteady flows of monodisperse particles suggest increased challenges in understanding and predicting segregation in unsteady bidisperse flows, but also a richer range of possibilities for mixing or segregation-induced pattern formation [**91, 62, 92, 93, 94, 63, 85, 45**]. An example is the dynamics of segregation pattern formation in time-periodic tumbler flow [**62, 92**]: discrete streaks of small particles form instead of the typical semicircular segregated core of small particles that occurs for steady flow, and the properties of the streaks depend on the modulation scheme. Recent theoretical models have successfully captured the general structure of the patterns [**83**].

In this study, we explore the application of flow modulation to produce stratified layers in strongly segregating bidisperse mixtures with large size ratios by intentionally generating unsteady flows in a quasi-2D bounded heap. In bounded heap flows with constant feed rates, a stratified pattern of irregular, alternating layers can form spontaneously at low surface rise velocities due to intermittent avalanching [**20, 44, 116**]. At moderate surface rise velocities, the flow on the heap is steady and the stratified pattern transitions to the streamwise segregated pattern mentioned earlier. As the surface rise velocity is further increased, advection becomes the dominant transport mechanism and segregation is reduced [**20, 40**]. However, a very high rise velocity is required to eliminate segregation

of strongly segregating mixtures and is often hard to realize in practice since the rise velocity is inversely proportional to the cross-sectional area of the hopper [20]. In typical industrial settings, the rise velocity of bulk materials in a hopper often falls into the range where the streamwise segregated pattern occurs [20, 174, 175]. Although neither stratified nor streamwise segregated patterns are homogeneous, we will demonstrate that the stratified pattern represents the overall mixture when considered over the scale of several stratified layers. In addition, we show that, in comparison to the streamwise segregated pattern, the stratified pattern produced by feed flow modulation dramatically decreases the amount of segregation in hopper discharge flow due to layer remixing upon discharge. Therefore, using flow modulation to intentionally produce a stratified pattern when filling a hopper at industrially relevant operating conditions (e.g, at a feed rate where a streamwise segregated state otherwise occurs) could be valuable in many situations.

The remainder of the chapter is organized as follows: section 4.2 describes the experimental setup; section 4.3 examines the flow-modulation-induced stratified patterns, proposes a mechanism for the flow-modulation-induced stratification, and explores the relation between the stratification properties and the modulation parameters; and section 4.4 presents the conclusions.

4.2. Experimental methods

The experimental apparatus (Fig. 4.1) for the quasi-2D bounded heap flow consisted of a pair of parallel vertical rectangular plates – an aluminum back wall and a glass front wall for visualization. The vertical end walls and the base were aluminum. The width of the container was $W = 0.69$ m, comparable to the flowing layer length in small industrial-scale silos. The gap between the front and back walls was $T = 1.27$ cm. Further details regarding the experimental setup are described in Fan, *et al.* [20]. In this study, granular mixtures were dropped vertically into the gap between the front and back walls near the left bounding wall. Three mixtures of equal volumes of different-sized spherical glass particles were used: 0.50±0.04 mm and 1.69±0.05 mm (bidisperse); 0.50±0.04 mm and 2.00±0.07 mm (bidisperse); 1.00±0.05 mm, 2.00±0.07 mm, and 2.98±0.06 mm (tridisperse). The material density of all particles was 2.59 g/cm^3.
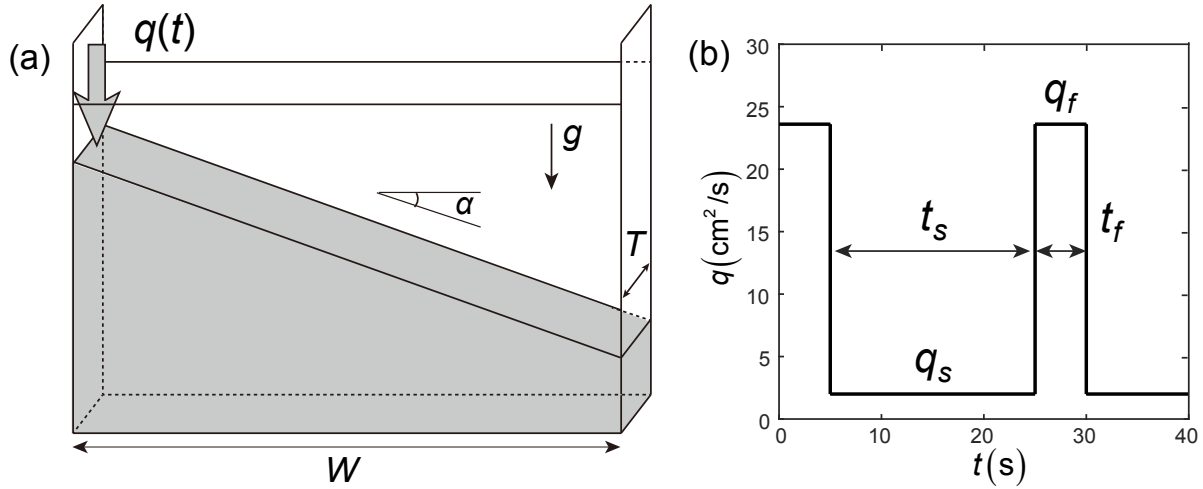
Figure 4.1. (a) Sketch of a quasi-2D bounded heap (not to scale) with width W and thickness T. Size bidisperse mixtures are fed onto the heap near the left end at modulated feed rate $q(t)$. (b) Feed rate modulation scheme for $q_f = 23.6\,\mathrm{cm}^2/\mathrm{s}$, $t_f = 5\,\mathrm{s}$, $q_s = 2.0\,\mathrm{cm}^2/\mathrm{s}$, and $t_s = 20\,\mathrm{s}$.

An auger feeder (101-1-DD/2, Acrison, Inc., NJ, USA) controlled by an adjustable frequency AC drive (Powerflex 40, Rockwell Automation, Inc., IL, USA) fed particles from a height 0.65 m above the base onto the left end of the heap. Flow modulation was achieved by feeding the particles at two different 2D feed rates, $q = Q/T$, where Q is the volumetric feed rate, see Fig. 4.1b. The flow was modulated between a fast phase at a higher feed rate q_f for duration t_f and a slow phase at a lower feed rate q_s for duration t_s. The time for steady feed to be established was short (within $0.2\,\mathrm{s}$) compared to the duration of each phase (several seconds or more), suggesting its influence on the observed results was negligible.

To quantify stratification induced by flow modulation, videos were recorded during each experiment using a digital camera (D5300, Nikon Corporation, Tokyo, Japan). Figure 4.2a shows an image from an experiment demonstrating a stratified pattern achieved by flow modulation. In this study, we only examine stratification that occurs after the downstream end of the heap reaches the bounding wall (white box in Fig. 4.2a) [20]. To characterize the degree of stratification, the image of the boxed area was rotated by the angle of repose α and then sheared into a rectangular area with width L corresponding

to the length of the flowing layer (Fig. 4.2b). The uppermost layer of particles was not included in the analysis because it is influenced by the transient when the feed is stopped. Within this domain, we define a coordinate system where x is the streamwise direction, z is the depthwise direction, and the origin is at the lower left corner. Note that this domain includes the feed zone, which is typically $0.1L$ wide in the cases tested. For each stratum (composed of a layer of large particles and a layer of small particles), x_L denotes the leftmost extent of the large particle layer, x_R denotes the rightmost extent of the small particle layer, and $\Delta x = x_R - x_L$ characterizes the interpenetration length, which quantifies the streamwise extent of stratification in the x-direction (Fig. 4.2b). Note that x_L and x_R were estimated visually for the set of strata in the image, which may introduce an error of as much as $\pm 1\,$cm. These parameters are non-dimensionalized by L: $X_L = x_L/L$, $X_R = x_R/L$, and $\Delta X = \Delta x/L$. In addition, the pixel intensity of each image was averaged in the x-direction to produce an intensity profile in the z-direction (Fig. 4.2c). The wavelength of the intensity fluctuation, ΔH, quantifies the thickness of pairs of strata in the z-direction [20, 176].

Particle Tracking Velocimetry (PTV) was used to determine the instantaneous velocity profiles near the transparent bounding sidewall of the apparatus. A high speed camera (FL3-U3-13Y3M-C, Point Grey Research Inc., Canada) recorded a series of images of the flowing layer at 400 frame/s. An example of a close up image of the particles is shown in Fig. 4.2d. With proper lighting, the positions of the small and large particles were identified in each frame using a standard PTV code [67], and the instantaneous velocities of the particles were then calculated using particle positions from two consecutive frames. The streamwise velocity profiles in the z-direction at various locations along the flowing layer were then obtained using a spatial binning average [57]. The particles were grouped into 2 mm bins according to their depth in the z direction, and an average of all particle velocities in each bin was calculated to obtain the velocity profiles. Combined with videos from the digital camera, PTV data was used to examine the mechanisms of stratification during modulated flow.
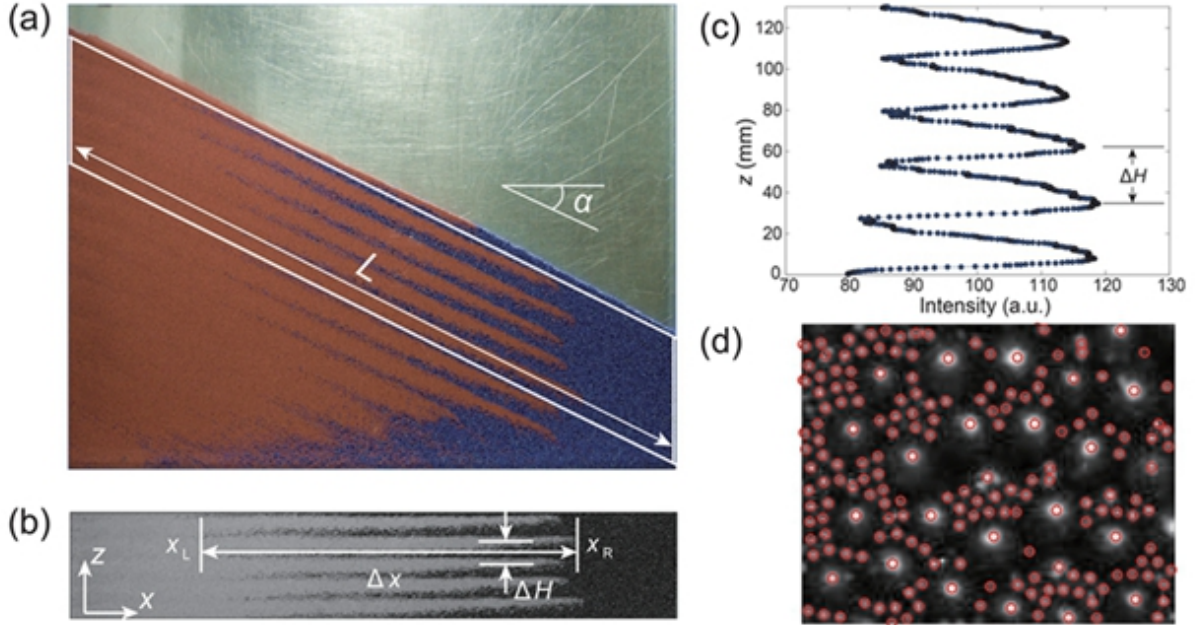
Figure 4.2. Analysis methods for experimental results. (a) An example of the final image in an experiment with 2 mm (blue) and 0.5 mm (red) glass spherical particles. The boxed area represents the pattern formed after the heap has reached its full horizontal extent. (b) Shearing the boxed area into a rectangular domain. (c) Streamwise-averaged image intensity vs. depth. (d) An example of particle identification in particle tracking velocimetry (identified particles are marked with a red circle).

4.3. Results and discussion

4.3.1. Comparing segregation with steady and modulated feed rates

Fig. 4.3 compares the final segregation patterns for constant and modulated feed rates for two cases using 2 mm and 0.5 mm particles. The average feed rate for modulated flow, $\bar{q} = (q_f t_f + q_s t_s)/(t_f + t_s)$, is the same as the constant feed rate for each case. Two different average feed rates were investigated: a high feed rate, $\bar{q} = 6.3$ cm^2/s, corresponding to continuous flow for steady filling (Fig. 4.3a and b) and a low feed rate, $\bar{q} = 1.5$ cm^2/s, corresponding to discrete avalanching flow for steady filling (Fig. 4.3c and 3d) [21], noting
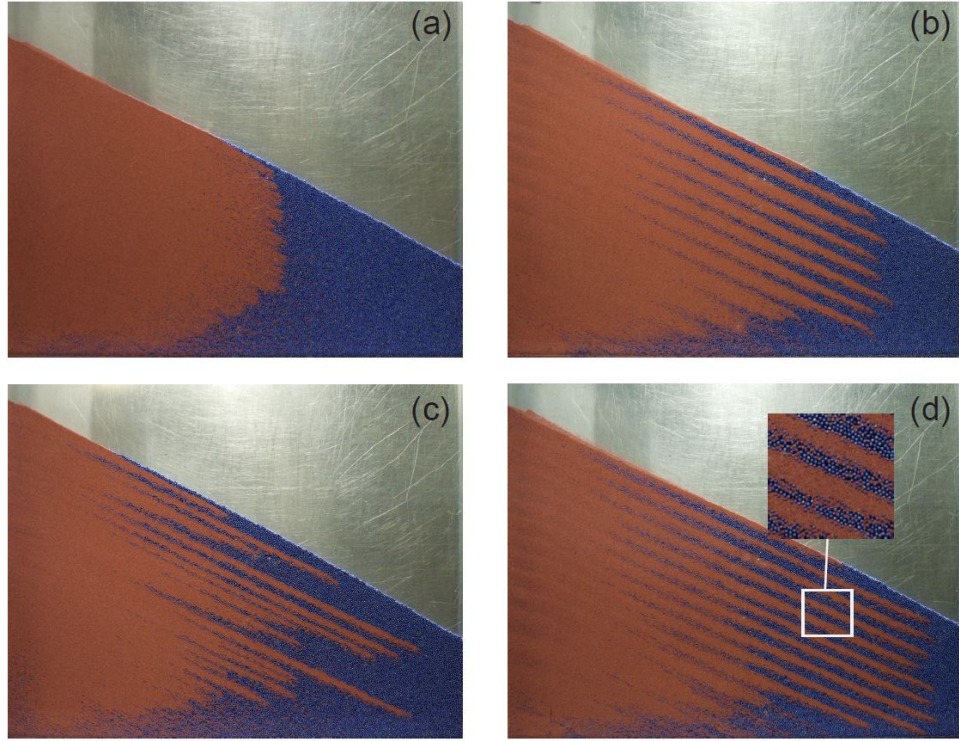
Figure 4.3. Patterns generated from steady (left column) and modulated (right column) filling using $2\,\mathrm{mm}$ (blue) and $0.5\,\mathrm{mm}$ (red) particles. (a) Uniform streamwise segregation with constant feed rate $q = 6.3\,\mathrm{cm}^2/\mathrm{s}$. (b) Uniform stratification with modulated flow at the same average flow rate as in (a), using $q_f = 23.6\,\mathrm{cm}^2/\mathrm{s}$, $t_f = 5\,\mathrm{s}$, $q_s = 2.0\,\mathrm{cm}^2/\mathrm{s}$, and $t_s = 20\,\mathrm{s}$. (c) Heterogeneous stratification in avalanching regime with constant $q = 1.5\,\mathrm{cm}^2/\mathrm{s}$. (d) Uniform stratification with modulated flow at same average flow rate as in (c), using $q_f = 31.0\,\mathrm{cm}^2/\mathrm{s}$, $t_f = 3\,\mathrm{s}$, $q_s = 0.3\,\mathrm{cm}^2/\mathrm{s}$, and $t_s = 77\,\mathrm{s}$.

that the transition feed rate from discrete avalanching flow to continuous flow occurs at about $q = 4\ \mathrm{cm}^2/\mathrm{s}$. For continuous flow (cases with the higher $\bar{q}$), the constant feed rate produces a strong, streamwise-segregated pattern, in which small particles are concentrated in the upstream region and large particles are concentrated in the downstream region of the heap with a clear interface between them (Fig. 4.3a). As discussed in previous studies [20, 65], this segregated pattern occurs in continuous heap flow at moderate feed rates. In contrast, Fig. 4.3b shows that a stratified pattern can be generated by using flow modulation at the same average feed rate as the constant feed rate used in

Fig. 4.3a. In this case, the streamwise segregation still occurs with more small particles concentrated in the far upstream region and more large particles concentrated in the far downstream region. However, between these two regions, small and large particles form alternating layers parallel to the free surface. This pattern results in better overall, or effective, mixing normal to the heap surface than the fully streamwise-segregated pattern (Fig. 4.3a), as discussed earlier.

At the lower $\bar{q}$, stratified patterns occur with both constant and modulated feed rates but with different characteristics. For constant feed rate, spontaneous stratification occurs due to the interplay between particle segregation and intermittent avalanches [20] (Fig. 4.3c). Due to the random nature of the discrete avalanche flow, the stratified pattern formed at constant feed rate is nonuniform, evidenced by different interpenetration lengths and thicknesses of the strata. However, by adding a short period of a fast feed rate, a more uniform stratified pattern occurs at the same $\bar{q}$, as shown in Fig. 4.3d, where the interpenetration length and thickness of each stratum are nearly identical.

4.3.2. Mechanisms for modulated-flow-induced stratification

To demonstrate the mechanisms of modulated-flow-induced stratification, we focus on the formation of a single stratum in a modulated-flow experiment ($q_f = 23.6 \, \text{cm}^2/\text{s}$, $t_f = 5 \, \text{s}$, $q_s = 2.0 \, \text{cm}^2/\text{s}$, and $t_s = 20 \, \text{s}$), shown in Fig. 4.4. A single cycle of flow modulation (a fast phase and a slow phase) results in a single stratum. We track the stratum formation from the beginning of the fast phase, setting the elapsed time, t, to zero at this point, as shown in Fig. 4.1b. When the fast phase starts, a large volume of mixed particles falls onto the upstream end of the heap and flows downstream. As the materials flow downstream, particles segregate resulting in an excess of large particles at a "front", where they form a thick region, as shown in the white box in Fig. 4.4a. These large particles are followed upstream by the small particles in the rest of the flowing layer. This happens because in percolation-driven segregation, large particles rise to the free surface and small particles settle to the bottom of the flowing layer. The large particles near the surface move downstream faster than the small particles lower in the flowing
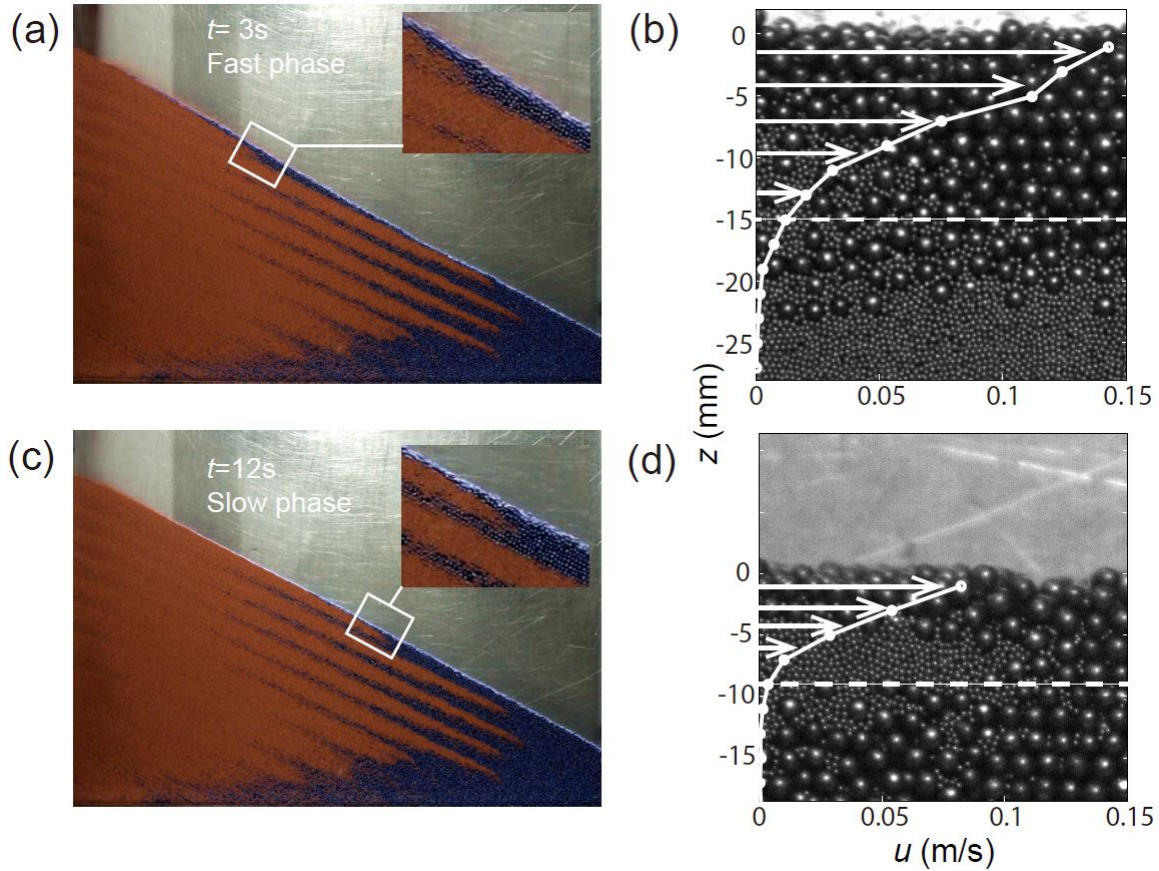
Figure 4.4. Dynamical process driving the formation of a single stratum for modulated feed rate with $q_f = 23.6\,\mathrm{cm^2/s}$, $t_f = 5\,\mathrm{s}$, $q_s = 2.0\,\mathrm{cm^2/s}$, and $t_s = 20\,\mathrm{s}$ using $2\,\mathrm{mm}$ (blue) and $0.5\,\mathrm{mm}$ (red) particles. The elapsed time is set to $t{=}0$ when the fast phase begins, and the origin of the z coordinate is aligned with the free surface. (left column) Images of the entire heap with insets showing the region where the velocity profile is measured. (right column) Images from the high speed camera with an overlay of the instantaneous streamwise velocity profile along the depth coordinate calculated by PTV and averaged over $0.05\,\mathrm{s}$ and across the width of the image. Dashed lines mark the bottom of the flowing layer below which the streamwise velocity is less than 10% of the surface streamwise velocity. (a) and (b) $t \approx 3\,\mathrm{s}$ and $x/L{=}0.34$ when the small and large particle layers are about to separate showing the large particle front. (c) and (d) $t \approx 12\,\mathrm{s}$ and $x/L{=}0.55$ when the small particle layer is traveling downstream showing the leading edge of the small particle layer.

layer [**21, 43, 41**], as shown in the streamwise velocity profile at the approximate location of the front (Fig. 4.4b). This difference in streamwise velocity allows the large particles to flow further downstream relative to the small particles, thus forming the front. This observation is analogous to the experimental and theoretical results of Gray & Kokelaar [**89**] and Gray & Ancey [**46**] for discrete avalanches, where large particles are preferentially transported toward the front of a discrete avalanche. As the fast phase continues, the large particle enriched front thickens as more large particles from upstream flow to the front. This results in deposition of some large particles onto the heap as they flow down the heap. The small particles behind the large particle front flow over the deposited large particles, leaving a band of large particles beneath them (Fig. 4.4b). The location where large particles deposition begins is the left bound, X_L, of the stratum.

The small particle layer continues to flow downstream in the flowing layer after the feed rate switches to the slow phase. Fig. 4.4c shows the leading edge of the small particle layer flowing downstream during the slow feed rate phase at $x/L = 0.55$ and $t = 12\,\mathrm{s}$. This small particle enriched layer flows over the deposited large particle layer while simultaneously being covered by the large particles flowing down from upstream, similar to the 'small particle sandwich' described by Gray & Kokelaar [**89**] and Gray & Ancey [**46**]. As shown in Fig. 4.4d, some of the small particles penetrate into the voids between previously deposited or slowly flowing large particles at the bottom of the flowing layer, resulting in small scale remixing at the interface between the small particle layer and the deposited large particle layer. This phenomenon, referred to as spontaneous percolation, occurs in large size ratio mixtures [**55, 60**], but it does not adversely affect the stratification in the experiments conducted. Note that the thickness of the flowing layer is only about 8 mm in Fig. 4.4d, so the large particles remain deposited beneath the flowing layer and are not carried further downstream by the flow. The flowing small particles are eventually buried by the flowing large particles above them, resulting in the small particles being deposited below the flowing layer. The position where the leading edge of the layer of small particles stops is X_R. For a slow phase with lower q_s, the leading edge of the small particle layer travels to a position further downstream because it remains in the flowing layer for a

longer time, resulting in larger X_R. For a higher q_s, the leading edge of the small particle layer stops further upstream due to its shorter residence time in the flowing layer, leading to a smaller X_R. Note that the slow feed rate in the modulated cases sometimes falls into the range where intermittent flow occurs for a steady feed rate [20, 177]. However, this does not seem to influence the uniformity of the stratified layers, because the flow in the transition from fast to slow feed rate is continuous.

In general, the fast phase results in a quick segregation of the particles in the upstream portion of the heap, where the large particles in a large particle enriched front are deposited as the front travels downstream, and small particles flow over these deposited large particles, initiating new layers of small and large particles along the streamwise direction. The slow phase allows the small particle layer to extend further downstream. The mechanism for the formation of the stratified layers in modulated flow is different from the mechanism for stratification of mixtures of different size and shape particles with a constant feed rate [44, 178, 88]. In the latter case, a difference in particle surface roughness or shape is necessary, and the stratification depends on the formation of kinks traveling upstream from the end wall [88]. The mechanism described here is more similar to that for the spontaneous stratification of different sized spherical particles with a similar repose angles (Fig. 4.3c) [20]. Under low steady feed rates, the flow is intermittent as the flowing layer "freezes" from time to time [20, 177]. And after the free surface ceases to flow, the new particles fed onto the heap accumulate near the feed zone, and soon starts to flow downstream again, possibly because the local maximum static angle [28] is reached due to the accumulation. This process plays a similar role as the fast phase does with modulated flow in terms of accumulating newly deposited particles far upstream. As these particles flow downstream, segregation occurs resulting in a large particle front where some of the large particles are deposited and then covered by a small particle layer that travels downstream, similar to the slow phase in the modulated cases, until the flowing layer freezes again and the formation of next layer starts. However, in spontaneous stratification, the formation of the stratified layers is less uniform due to the randomness in the "freezing" of the flowing layer [177], while the controlled modulation of the feed
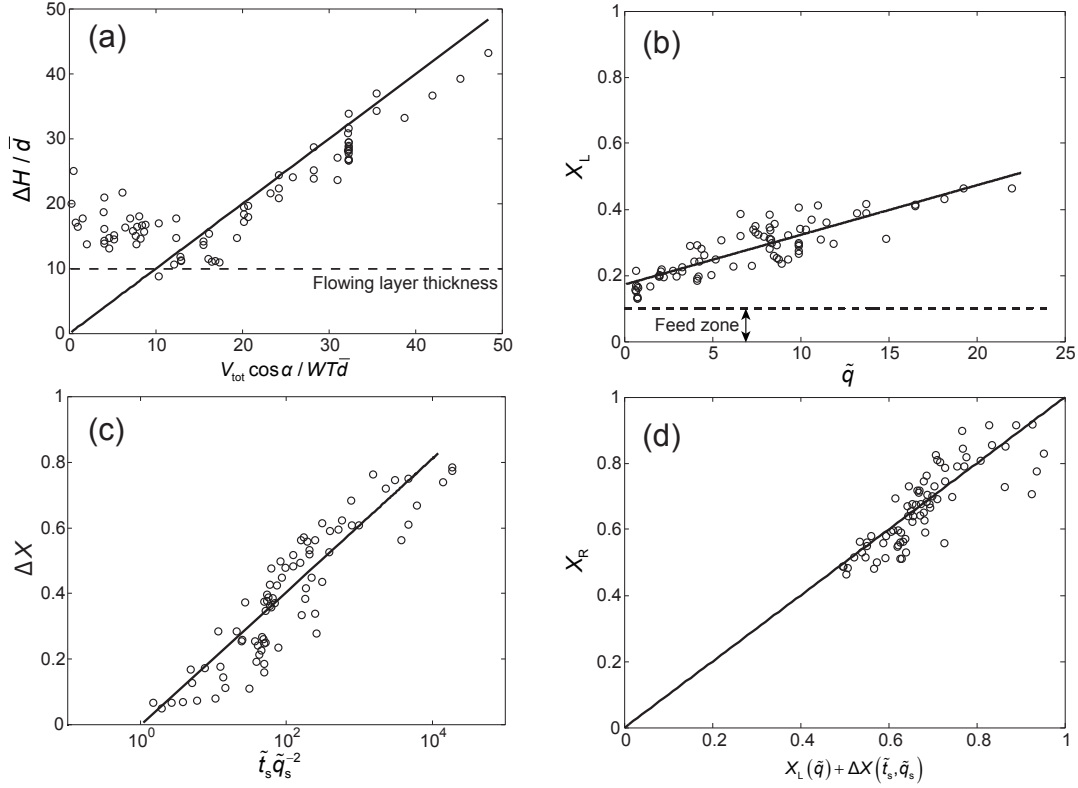
Figure 4.5. Dependence of stratification on feed rate modulation parameters. (a) Strata thickness ΔH vs. the predicted volume per feed cycle V_{tot}. The prediction of Eq. (4.1) is plotted as a line. (b) Left bound of strata X_L vs. the non-dimensional average feed rate $\tilde{q}$. The line is a linear fit to the data, $X_L = 0.015\tilde{q} + 0.172$. (c) Interpenetration length ΔX vs. a non-dimensional parameter related to the slow phase time and feed rate, $\tilde{t}_s\tilde{q}_s^{-2}$. The line is a fit to the data, $\Delta X = 0.088\ln\left(\tilde{t}_s\tilde{q}_s^{-2}\right)$. (d) Right bound of strata X_R vs. the predicted right bound (solid line) using relations for X_L in (b) and ΔX in (c), $X_R = X_L(\tilde{q}) + \Delta X(\tilde{t}_s, \tilde{q}_s)$.

rate results in stratified layers that are more uniform. More importantly from a practical standpoint, the modulated-flow-induced stratification can occur at higher average feed rates.

4.3.3. A parametric study

To study how the feed modulation parameters control stratification, we conducted 79 experiments using an equal volume mixture of 1.7 mm and 0.5 mm particles, and measured ΔH, X_L, ΔX, and X_R for each experiment to quantify stratification under various flow conditions. The 2D feed rate ranged from 0.6 cm^2/s to 33.9 cm^2/s and the phase durations varied from 2 s to 60 s. In each case, the stratification parameters (ΔH, X_L, ΔX, and X_R) were calculated by averaging over all strata that formed after the heap reached the downstream end of the apparatus (the white box in Fig. 4.2a and 4.2b).

The thickness of each stratum ΔH can be predicted from the total volume of particles in each feed cycle, $V_{tot} = (q_f t_f + q_s t_s)T$, assuming that each feed cycle results in a single layer of each particle size. The relation between ΔH and V_{tot} is

$$\Delta H = \frac{V_{tot} \cos \alpha}{WT},$$

(4.1)

where α is the dynamic repose angle of the mixture, which in the cases tested here ranged from approximately 27° to 33° depending on the feed rate and consistent with previous results [20]. Here, for simplicity, we use an average value of $\alpha = 30°$ for all feed rates. To confirm the relation in Eq. (4.1), experimental values of ΔH normalized by the nominal mean particle diameter $\bar{d} = (d_l + d_s)/2 = 1.1$ mm are plotted as function of the right hand side of Eq. (4.1), also normalized by $\bar{d}$. The experimental data match Eq. (4.1) for $V_{tot} \cos \alpha/WT\bar{d}$ above a critical value around 10 (equivalent to $V_{tot} = 110$ cm^3), corresponding to a minimum stratum thickness of approximately $10\bar{d}$, which is approximately the flowing layer thickness shown in Fig. 4.4. A stratum thinner than the flowing layer thickness, which is typically $5\bar{d}$ to $10\bar{d}$, is unlikely to form since the stratum will be entrained into the flowing layer in the subsequent feed cycle and combine with the new stratum. Therefore, for low V_{tot}, particles from more than one feed cycle end up merging into a single stratum, similar to the merging of streaks in modulated circular tumbler flow [92]. As a result, ΔH is greater than the value predicted by Eq. (4.1) for small V_{tot}.

As discussed in section 4.3.2, the left bound of the strata, X_L, indicates where small particles flow over previously deposited large particles. These large particles are from

either the previous slow phase or the large particle front during the fast phase. In both situations, a lower feed rate can deposit large particles closer to the feed zone (smaller X_L), because the streamwise segregation is generally stronger at a lower feed rate [20]. This suggests that the average feed rate $\bar{q}$ is the dominant factor determining X_L. Figure 4.5b confirms this conjecture within the ranges of parameters tested by showing a linear relation between X_L and the nondimensional feed rate $\tilde{q} = \bar{q}/\sqrt{g\bar{d}^3}$, where $g = 9.81\,\mathrm{m/s^2}$ is the gravitational acceleration. The nondimensionalization by $\sqrt{g\bar{d}^3}$ reflects a flux scale which is the product of a length scale $\bar{d}$ and a commonly used velocity scale $\sqrt{g\bar{d}}$, similar to scalings used previously [21, 37, 65]. X_L cannot be smaller than the width of the feed zone, which is about $0.1L$ in this study, as indicated by the dashed line in Fig. 4.5b.

The interpenetration depth ΔX, depends on the maximum distance that the small particle layer travels in the streamwise direction, which is determined by both the time small particles remain in the flowing layer and the speed at which small particles travel down the heap before being deposited. Since most of the small particle layer motion occurs during the slow phase, the slow phase time duration, t_s, and feed rate, q_s, are likely the dominant factors determining ΔX. Longer t_s allows more time for the small particle layer to grow, while larger q_s results in a faster rise velocity of the heap surface during the slow phase ($v_r = q_s/W$), which causes small particles to be buried faster by large particles as they travel down the heap. Fig. 4.5c shows a correlation between the non-dimensional interpenetration depth and a non-dimensional parameter that includes both modulation parameters, $\tilde{t}_s\tilde{q}_s^{-2}$, where $\tilde{t}_s = t_s/\sqrt{d/g}$ and $\tilde{q}_s = q_s/\sqrt{g\bar{d}^3}$, where $\sqrt{g\bar{d}}$ is the timescale for a particle to fall a particle diameter [37]. The data clearly show that when t_s increases or q_s decreases, ΔX can increase up to 0.8, which means strata span nearly the entire length of the slope. Note that the physics underlying the logarithmic relation between ΔX and $\tilde{t}_s\tilde{q}_s^{-2}$ in Fig. 4.5c is unclear and needs further investigation. In addition, there are several secondary effects that can influence ΔX including the fast phase flow parameters, the difference in the repose angle of the two phases, and the curved free surface that occurs at high feed rates [145], perhaps accounting for the data scatter
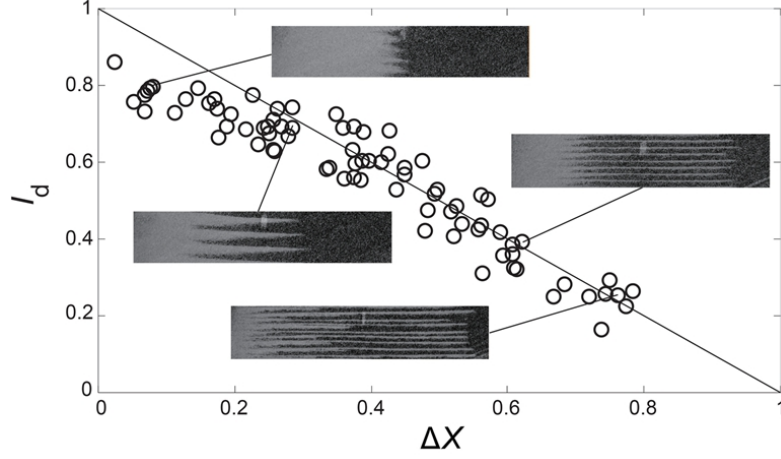
Figure 4.6. Correlation between the segregation index I_d and the inter-penetration length ΔX for the 79 cases in the parametric study compared to $I_d=1-\Delta X$ (line). Examples of stratified patterns are shown, where large (small) particles are dark (light) gray (enhanced contrast).

in Fig. 4.5c. Based on the correlations from Fig. 4.5b and 4.5c, the right bound of the strata, $X_R = X_L + \Delta X$, can be relatively accurately predicted, as shown in Fig. 4.5d.

To this point, we have demonstrated that it is possible to generate a wide range of stratified patterns with modulation of the heap feed rate. We now quantify the degree of inhomogeneity in the streamwise direction for these patterns using the Danckwerts intensity of segregation [179]:

$$I_d(c) = \frac{1}{\bar{c}(1-\bar{c})} \int_0^L [c(x) - \bar{c}]^2 dx,$$
(4.2)

where, $\bar{c} = (1/L) \int_0^L c(x)dx$ is the overall spatially averaged concentration for each species, and $c(x)$ is the local species concentration. The intensity of segregation is a measure of the deviation of local concentration from the overall average, and it ranges from $I_d = 0$, which indicates perfect mixing and corresponds to the strata extending the full length of the flowing layer, to $I_d = 1$, which indicates complete segregation corresponding to no strata at all, but instead a region of pure small particles in the upstream portion of the heap and pure large particles in the downstream portion. The concentration, c, is

measured using the pixel intensity of processed images (Fig. 4.2) by assuming a linear relation between the intensity and particle concentration at the wall [20]. The heap is divided into 20 equal-sized non-overlapping bins (each bin is $4\,\text{cm}$ wide) in the streamwise direction x, and the local concentration is averaged over the entire depth (z-direction). Figure 4.6 demonstrates how the intensity of segregation decreases as the interpenetration depth ΔX increases, indicating that ΔX is a reasonable proxy for the degree of mixing in the streamwise direction. For ΔX less than 0.2, I_d reaches its maximum value of about 0.8, which is equivalent to I_d for a completely streamwise segregated pattern at a constant feed rate around $q = 25\,\text{cm}^2/\text{s}$. When ΔX is larger than 0.2, I_d decreases linearly towards 0. In the cases tested, I_d never reaches 0 and ΔX never reaches 1, because mixed material is always present in the feed zone and a small region of large particles persists at the downstream end of the flowing layer.

The measured degree of mixing in the z-direction depends on the averaging length scale. If the bin size is smaller than ΔH in the z direction, the degree of mixing will be small. Thus, the metric for mixing in the z-direction will depend on the specific application. For example, as shown in the next section, the small scale inhomogeneity in the z-direction is immaterial during hopper discharge, because the discharge flow effectively remixes the particle layers as they exit the hopper.

4.3.4. Potential application in hopper discharge

In this section , we demonstrate the potential application of modulated-flow-induced stratification to improve mixture homogeneity during hopper discharge. To do so, the apparatus was slightly modified into a quasi-2D one-sided funnel flow hopper by inclining the bottom base and opening an outlet at the left end, see Fig. 4.7. Three different initial states were created by filling a size bidisperse mixture (0.5 mm and 2.0 mm particles) at the left end while the outlet was closed; a streamwise segregated pattern was obtained by filling the hopper at a constant feed rate, $q = 6.0\ \text{cm}^2/\text{s}$ and letting particles naturally segregate [20]; a stratified initial condition was obtained by filling the hopper using a modulated feed rate with $q_f = 40.0\,\text{cm}^2/\text{s}$, $t_f = 2.5\,\text{s}$, $q_s = 2.0\,\text{cm}^2/\text{s}$, and $t_s = 23\,\text{s}$; and
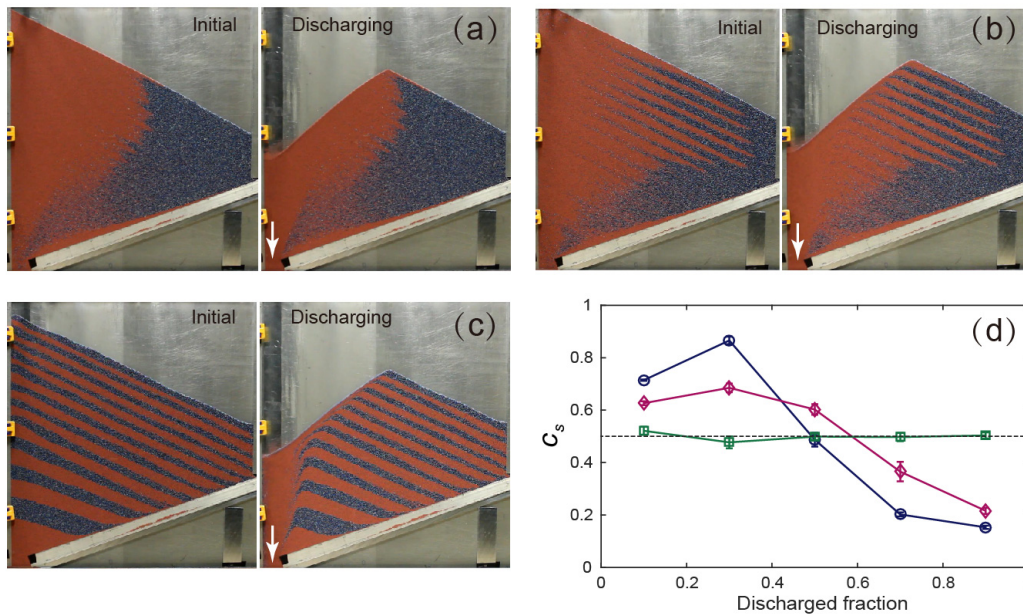
Figure 4.7. Influence of initial segregation pattern (left images, (a-c)) on discharge (right images, (a-c)) uniformity from a quasi-2D hopper (50 cm wide, 1.0 cm thick, bottom inclined at 19° and with a 3.5 cm wide exit on the bottom left). Discharge of (a) initially streamwise segregated pattern generated by filling the hopper with a uniform mixture (0.5 mm red and 2 mm diameter blue particles) at a constant feed rate, $q = 6.0$ cm^2/s; (b) initially stratified pattern generated by filling the hopper using a modulated feed rate with $q_f = 40.0$ cm^2/s, $t_f = 2.5$ s, $q_s = 2.0$ cm^2/s, and $t_s = 23$ s; and (c) initially completely stratified pattern generated by feeding large and small particles alternately. (d) Concentration of small particles, c_s, in the discharge collected for the three cases: streamwise segregated (blue circles), modulated-flow-induced stratified (purple diamonds), and completely stratified (green squares). Error bars indicating the standard deviation are shown (typically smaller than the data symbols). The dashed line indicates $c_s = 0.5$.

a completely stratified pattern was artificially generated by manually filling alternately with large and small particles.

To characterize the degree of mixing in the discharge, the outflow from the hopper was divided into 5 equal-volume samples sequentially, and the small particle concentration, c_s, in each sample was measured. An average of three identical experiments were

used for each initial condition, and the results are shown in Fig. 4.7d. In all cases, the particles on the left side of the hopper are the first to discharge. For the discharge of the initially streamwise segregated pattern (Fig. 4.7a right), the small particles concentrated in the left (upstream) region are discharged first followed by the large particles in the right (downstream) region, resulting in a significant decrease in the small particle concentration as hopper discharge progresses. For the discharge of the initially stratified pattern induced by modulated-flow (Fig. 4.7b right), both the small and large particle layers contribute to the outflow simultaneously, resulting in remixing. This leads to an increase of homogeneity in the discharge compared to the streamwise segregated pattern, although segregation still exists because the stratified layers do not extend the entire width of the hopper. When discharging materials from the initially completely stratified pattern (Fig. 4.7c right), which can be considered as an optimized version of the modulated-flow-induced stratified layers in Fig. 4.7b, all the stratified layers contribute to the outflow simultaneously during the entire discharge process, leading to almost perfect mixing in the outflow (Fig. 4.7d). Moreover, this homogeneity created by the stratified layers is independent of the sample size because the small and large particles contribute equally to the outflow at any instant. These results demonstrate the potential of applying flow modulation to increase mixture homogeneity during hopper discharge. Of course, more work is needed to optimize modulated-flow-induced stratification.

4.3.5. Tridisperse mixtures

Up to this point, we have shown the potential of flow-modulation-induced stratification for size bidisperse mixtures. The underlying mechanism does not limit the application to bidisperse mixtures. Fig. 4.8 shows a comparison between steady and modulated bounded heap flow at comparable average feed rates for a tridisperese granular mixture of equal volumes of 1 mm, 2 mm, and 3 mm glass particles. For the steady feed rate (Fig. 4.8a), the three species generally segregate in the streamwise direction, with small particles depositing upstream, large particles depositing downstream, and medium-sized particles depositing in the middle of the heap, consistent with previous results [86], though there is
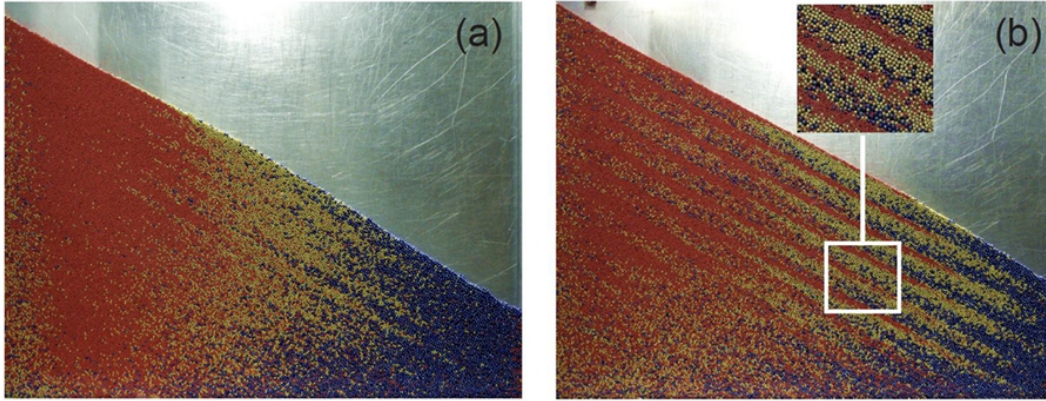
Figure 4.8. Tridisperese segregation patterns with $1\,\mathrm{mm}$ (red), $2\,\mathrm{mm}$ (gold), and $3\,\mathrm{mm}$ (blue) particles. (a) Steady flow at $q = 3.2\,\mathrm{cm}^2/\mathrm{s}$. (b) Modulated flow at $\bar{q} = 3.2\,\mathrm{cm}^2/\mathrm{s}$ for $q_f = 37.2\,\mathrm{cm}^2/\mathrm{s}$, $t_f = 4\mathrm{s}$, $q_s = 1.0\,\mathrm{cm}^2/\mathrm{s}$, and $t_s = 61\mathrm{s}$.

some minor stratification due to the low feed rate. For a modulated feed rate, stratification occurs in the same fashion as for bidisperse mixtures, forming distinct alternating layers, as shown in Fig. 4.8b. In the close-up image of the stratified region, ordered layers of small, medium, and large particles are clearly visible, and each species is in contact with the other two species. Although the global mixing is imperfect, the modulated stratified pattern has better mixing than the steady flow pattern, especially for small and large particles. In the steady flow pattern, large and small particles are completely separated by the medium-sized particle region, while in the modulated flow pattern they are interspersed with each other at the layer interfaces. Moreover, the medium-sized particles are more dispersed along the streamwise direction in the modulated flow pattern.

4.4. Conclusions

In this chapter, we have shown that flow modulation realized by alternating between high and low feed rates can generate stratified patterns of size disperse granular mixtures in a quasi-2D bounded heap. During the fast phase, large particles are deposited in the upstream portion of the heap behind the large particle front and then covered by the small particles flowing from upstream to initiate the stratified layers, while during the slow

phase, the small particle layer travels downstream until it is covered by large particles. We have quantified the relationships between the stratification patterns and the modulation parameters based on this mechanism. These relations indicate how to achieve stratified patterns rather than streamwise segregated patterns at the same average feed rate in heap flow by properly selecting the modulation parameters. Based on the Danckwerts intensity of segregation and a preliminary hopper discharge study, we demonstrated that the flow-modulated stratified pattern can reduce the overall inhomogeneity in a heap leading to better mixing during hopper discharge, which has great potential to limit particle segregation in many industrial processes.

Stratification via flow modulation occurs in tridisperse size mixtures and should also occur for mixtures of particles differing in material density, because density segregation in bounded heaps shares many similarities with size segregation [57] and layering of density bidisperse materials has been observed in rotating tumbler flow [110]. Further work is necessary to better explore these topics. Meanwhile, a continuum-based theoretical framework capable of predicting segregation at constant feed rates [40, 83, 65] can potentially be adapted to predict flow-modulated stratification and further optimize this approach. This work is currently underway.

CHAPTER 5

Transient response in granular quasi-2D bounded heap flow

SUMMARY

The formation of stratification (Chapter 4) is closely related to the underlying transient flows generated by modulating feed rates. This chapter further studies the transition between steady flows of noncohesive granular materials in quasi-two-dimensional bounded heaps by suddenly changing the feed rate. In both experiments and simulations, the primary feature of the transition is a wedge of flowing particles that propagates downstream over the rising free surface with a wedge front velocity inversely proportional to the square root of time. An additional longer duration transient process continues after the wedge front reaches the downstream wall. The entire transition is well modeled as a moving boundary problem with a diffusionlike equation derived from local mass balance and a local relation between the flux and the surface slope.

The material in this chapter was published in slightly different form as "Transient response in granular quasi-2D bounded heap flow" by H. Xiao, J. M. Ottino, R. M. Lueptow, and P. B. Umbanhowar, *Physical Review E* **96** (4), 040902 (2017) [**180**] ©American Physical Society.

Heaps of granular materials form in both geophysical and industrial systems, and exhibit kinematics that vary in both the streamwise and depthwise directions [**81, 21**]. While most previous studies of quasi-2D bounded heap formation have considered steady feed rates exclusively, e.g. [**181, 81, 20, 21, 161, 57, 145**], recent work with size bidisperse mixtures of spherical granular particles fed onto a quasi-2D bounded heap under alternating feed rates shows dramatic changes to the segregation pattern, indicating the

existence of complex transient flows [146]. This work raises the question of how granular flows relax to steady-state following a change to a control parameter such as the feed rate.

In bounded heap flows, particles travel down the surface in a thin flowing layer over a static bed with a rising free surface inclined at an angle determined by particle properties (e.g., shape and friction), the sidewall gap, and the feed rate [34, 20]. The evolution of the heap is determined by the surface rise velocity and particle exchange between the flowing layer and the underlying static bed [29, 30, 81, 31]. For steady feed rates, the entire free surface rises at a constant velocity $v_r = q/W$, where q is the volumetric feed rate divided by the gap thickness and W is the heap width [21, 30, 81]. However, it is unclear how material deposition varies in unsteady processes.

In this study, we experimentally and computationally study the transient processes in a quasi-2D bounded heap during single transitions between steady states at different feed rates using monodisperse spherical particles. During transition we observe a developing wedge on the rising surface with a downstream propagating front. The wedge front arises from the change in the feed rate and differs from an avalanche front triggered by a sudden release of material that propagates with a constant velocity [182, 157, 47, 183], and from transient phenomena in tumbler flows [43, 41] or streamwise invariant flows [37, 38, 79, 184]. Instead, our experiments and Discrete Element Method (DEM) simulations show that the wedge front velocity is proportional to $t^{-1/2}$, and that the surface undergoes a slow relaxation that continues long after the wedge front reaches the downstream bounding wall. We show that these transient processes originate in the relation between the local surface slope and the local flow rate in depositing flows, which leads to a model with the same form as the diffusion equation that accurately predicts the observed dynamics.

The experimental setup (Fig. 5.1) consists of two parallel vertical rectangular plates - an aluminum back wall and a glass front wall for visualization. The gap between the front and the back plates T and the width of the apparatus W are set by vertical spacers placed between the plates, as described previously [20]. Monodisperse non-cohesive glass spheres of diameter $d = 1.18 \pm 0.07$ mm and material density $\rho = 2440$ kg/m^3 are fed into the rectangular container near the left side from a height at 0.6 m above the bottom
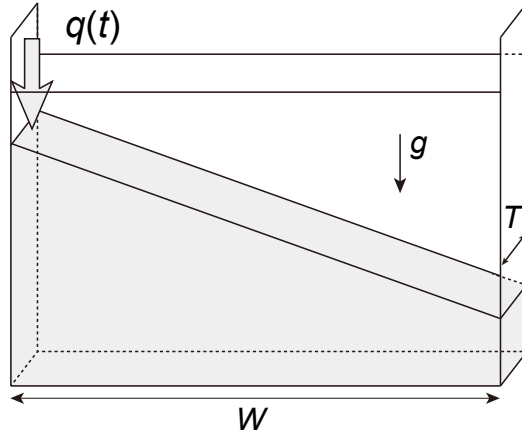
Figure 5.1.   Experimental setup (not to scale) of the quasi-2D bounded heap.

wall by an auger feeder to form a quasi-2D one sided heap. In each experiment, the feed rate $q(t)$ is first set to q_1 until the heap extends the entire width of the apparatus and the flow is fully developed [**20, 21**]. Then, the feed rate is changed to a different value q_2 in approximately 0.2 s, a negligible duration compared to the transient process duration (several seconds). Neither static electricity nor humidity appear to significantly influence the experimental results. To capture the heap evolution, videos of the entire heap are recorded at 60 frames/s with a spatial resolution of 0.7 mm. The free surface of the entire heap h is identified by the sharp transition in the image intensity between the background and particles. The location of the surface is averaged over 5 mm wide horizontal bins for 0.1 s (6 frames), and over five identical experiments to reduce uncertainty.

An example of a slow-to-fast feed rate transition ($q_2 > q_1$) starting at $t = 0$ is shown in Fig. 5.2. The coordinate system's origin is at the bottom left corner of the heap with x in the horizontal direction and z in the vertical direction. To demonstrate how the transient surface height trajectory $h(x, t)$ deviates from the q_1 steady state trajectory, where the entire surface rises with velocity $v_{r1} = q_1/W$, we plot the surface deviation, $\tilde{h}(x, t) = h(x, t) - h(x, 0) - v_{r1}t$, at different times (Fig. 5.2(a)). After the feed rate is increased to q_2, the surface near the feed zone rises faster than the downstream portion of the surface forming a wedge of material with an average surface angle $\bar{\alpha}_w$ steeper than the steady state average surface angle $\bar{\alpha}_1$ under q_1, while the rest of the surface continues
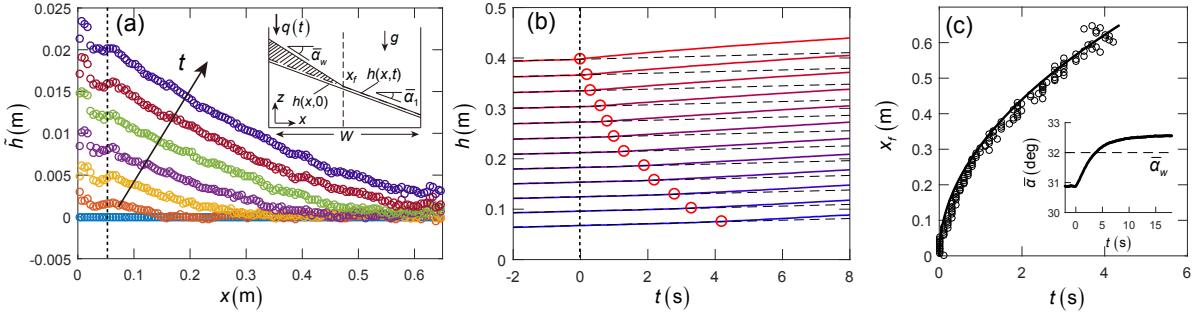
Figure 5.2. Wedge propagation in experiment after transition from $q_1 = 11\,\text{cm}^2/\text{s}$ to $q_2 = 26\,\text{cm}^2/\text{s}$ ($W = 0.65\,\text{m}$, $T = 1.2\,\text{cm}$). (a) Surface deviation profile at different times (t=0, 0.2 s, 0.75 s, 1.5 s, 2.5 s, 3.5 s, and 4.6 s from bottom to top) after change in q. The feed zone extends from x=0 to the dashed line. Inset: apparatus geometry and wedge propagation mechanism (see text). (b) Temporal evolution of surface height from upstream (largest h) to downstream (smallest h). Circles indicate the wedge front. (c) Front position vs. time from experiments (circles) and wedge-model prediction (solid curve). Inset: average surface slope $\bar{\alpha}$ vs. t with slope $\bar{\alpha}_1 = 30.8°$ at q_1, wedge angle $\bar{\alpha}_w = 32.0°$, and final slope $\bar{\alpha}_2 = 32.4°$ at q_2.

to rise at v_{r1}, indicated by $\tilde{h} = 0$. As time advances, the wedge grows until its front edge reaches the downstream wall. The propagation of the wedge front is clearer in Fig. 5.2(b), which shows the surface height evolution at equally spaced streamwise locations: the top (bottom) curve corresponds to the furthest upstream (downstream) location. The slope of these curves is the local surface rise velocity, which would be constant if the feed rate were unchanged. However, after the feed rate increases at t=0, the surface portion furthest upstream (top curve) responds almost instantaneously and starts to rise faster, resulting in its height deviating from $\tilde{h} = 0$ (dashed line), while the downstream portion (lower curves) remains in the state associated with $q = q_1$. The location of the wedge front, defined as the location where $\tilde{h}$ becomes larger than $d/2$, is indicated by circles in Fig. 5.2(b).

The transient process described above differs from those in tumblers [41, 43] and streamwise invariant flows [37, 38, 184, 79] where the entire flowing layer responds to the external change (e.g., in different rotation speed or tilt) instantaneously. Here, the transient process originates from the feed zone, and its influence propagates gradually

downstream in the form of a wedge front. The front slows as it travels downstream, see Fig. 5.2(b), which distinguishes it from avalanche fronts with constant propagation velocities observed [**31, 88, 157, 47, 183**] or assumed [**89, 30**] in previous studies. This slowing indicates a different driving mechanism. To model the evolution of free surface granular flows, depth integrated continuity and momentum equations have been applied using various constitutive laws [**31, 157, 47, 183**]. However, for bounded heap flows, special treatment of the erosion and deposition between the flowing layer and the static bed is necessary [**31, 79, 32**], and both the time development and the streamwise gradient have to be resolved, which substantially complicates the problem. Alternatively, a simple but effective approach based on geometric arguments describes the wedge development. By integrating $\tilde{h}$ in the x direction, an overall mass conservation equation is obtained:

$$(5.1) \qquad \int_0^W \tilde{h}\,dx = \int_0^W [h(x,t) - h(x,0)]\,dx - \int_0^W v_{r1}t\,dx.$$

The l.h.s. of Eq. (5.1) is the area of the growing wedge shown in the inset of Fig. 5.2(a), which can be approximated by the area of a triangle, $\frac{1}{2}x_f^2(\tan\bar{\alpha}_w - \tan\bar{\alpha}_1)$, where x_f is the instantaneous front position. The wedge angle $\bar{\alpha}_w$, which only varies slightly as the wedge front propagates, is measured as the mean heap surface angle $\bar{\alpha}$ at the point when the wedge reaches the endwall. The first term on the r.h.s. is the increase of the heap area, q_2t, while the second term is the increase in heap area had the feed rate been maintained at q_1, namely q_1t. Substituting these expressions into Eq. (5.1) gives an approximation for the instantaneous front position,

$$(5.2) \qquad x_f = \sqrt{Ct},$$

where $C = \frac{2(q_2-q_1)}{\tan\bar{\alpha}_w - \tan\bar{\alpha}_1}$ is a propagation constant dependent only on parameters of the problem. Eq. 5.2 agrees well with the experimentally measured front position (Fig. 5.2(c)), which implies that this transient process can be viewed as filling an additional wedge on
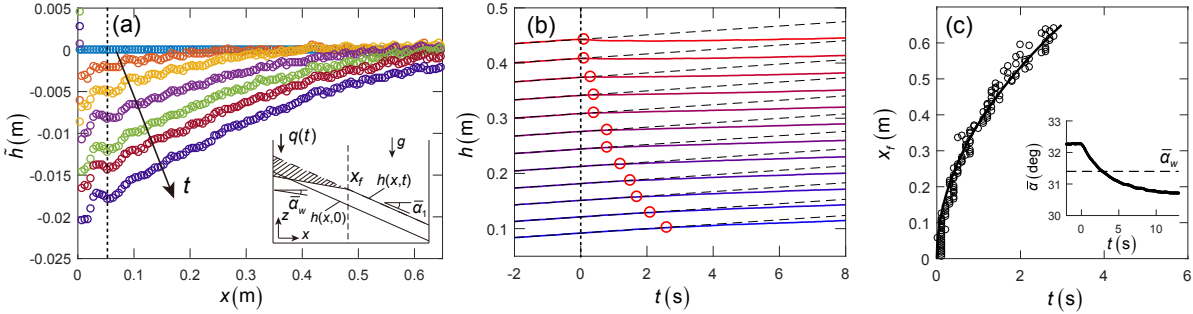
Figure 5.3. Wedge propagation details in experiment after transition from $q_1 = 26\,\mathrm{cm^2/s}$ to $q_2 = 11\,\mathrm{cm^2/s}$ ($W = 0.65\,\mathrm{m}$, $T = 1.2\,\mathrm{cm}$). (a) Surface deviation profile at different times (t=0, 0.3 s, 0.75 s, 1.5 s, 2.3 s, 3.0 s, and 4.0 s from bottom to top) after change in q. The feed zone extends from x=0 to the dashed line. Inset: wedge propagation mechanism (see text). (b) Temporal evolution of surface height from upstream (largest h) to downstream (smallest h). Circles indicate the wedge front. (c) Front position vs. time from experiment (circles) and model prediction (solid curve). Inset: average surface slope $\bar{\alpha}$ vs. t with slope $\bar{\alpha}_1 = 32.3°$ at q_1, wedge angle $\bar{\alpha}_w = 31.4°$, and final slope $\bar{\alpha}_2 = 30.8°$ at q_2.

top of a rising heap surface with the front propagation velocity decreasing as $1/\sqrt{t}$ as the wedge grows.

For the fast-to-slow feed rate transition ($q_2 < q_1$), the physics is similar. After q is reduced to q_2, the rise velocity of the surface near the feed zone decreases, resulting in $\tilde{h} < 0$ in the upstream portion of the flow, and a "negative" wedge propagating downstream (Fig. 5.3(a)) until it reaches the endwall. Figure. 5.3(b) shows the gradual deviation of the surface from the previous state (dashed line) from upstream to downstream, and a slowing front, similar to the slow-to-fast transition. Due to this similarity [1], Eq. (5.2) can be directly applied to this type of front propagation, but with negative $q_2 - q_1$ and $\tan\bar{\alpha}_w - \tan\bar{\alpha}_1$, and it again accurately predicts the observed $\sqrt{t}$ advance of the wedge front, see Fig. 5.3(c).

Although the wedge approximation is suitable for predicting front propagation for both increasing and decreasing feed rate, it is clear that the $\bar{h}$ profile in the upstream

---

[1]The 0.1° difference between $\bar{\alpha}$ at the high feed rate noted in the captions of Figs. 5.2 and 5.3 occurs because of different distances ($\approx$5 cm) between the feeder and the heap surface [**181**] when $\bar{\alpha}$ was measured in the two cases.

region of the front is slightly curved (Figs. 5.2(a) and 5.3(a)). Moreover, since the final slope $\bar{\alpha}_2 \neq \bar{\alpha}_w$ (inset of Figs.5.2(c) and 5.3(c)), an additional transient process exists after the wedge reaches the endwall, indicating that additional physics is needed to more accurately describe the transient response.

To explore the underlying physics, additional kinematic details are extracted from DEM simulations of single transitions using an in-house code that was previously applied and validated in heaps [21, 57, 161]. Particle interactions are modeled with a linear spring-dashpot normal force and a combination of linear spring and Coulomb friction tangential force [21]. To reduce computation cost, we simulate the system using slightly larger $d = 2 \pm 0.2$ mm particles with restitution coefficient $e =$0.8, particle-particle and particle-wall friction $\mu =$0.4, and a binary collision time of $t_c =$1×10^{-4} s [21]. The feed position is kept at a constant height ($\approx$20 cm) above the left end of heap surface to eliminate the influence of changing drop height [181]. The integration time step is $t_c/40$ for numerical stability [21]. Instantaneous horizontal flux profiles $q(x,t)$ and local surface slope $\partial h(x,t)/\partial x$ are calculated from the simulation results. To determine $q(x,t)$, the horizontal velocity $u(x,z)$ is computed using a volumetric binning method with bin size 10 mm×2 mm [21]. To further reduce uncertainty, data are averaged over 0.05 s and over 5 repeated simulations. The instantaneous horizontal flux profiles are calculated as $q(x) = \frac{1}{\phi} \int_0^h u\phi dz$, where ϕ is the local packing fraction and $\bar{\phi} = 0.58$ is the packing fraction averaged over the entire heap. The instantaneous local slopes are calculated by fitting a line to h over a 5 cm interval at each horizontal location corresponding to a bin center. Three feed rates are considered (11 cm^2/s, 35 cm^2/s, and 69 cm^2/s), and the single transitions between these feed rates as well as steady flows are simulated.

To better model the transient surface dynamics, we first quantify the relationship between the local slope, $\partial h/\partial x$ and the local flow rate $q(x)$. The inset in Fig. 7.3 shows local instantaneous measurements of $\partial h/\partial x$ vs. q for both steady flows and single transitions ($\approx$85000 data points). Note that $\partial h/\partial x = -\tan\alpha$, where α is the local surface angle. The data for both steady and transient flows collapse indicating that within the range of flow rates simulated, the relation between the local slope and the local flow

rate is universal, and unsteadiness (i.e. $\partial q/\partial t \neq 0$) plays only a minor role as evidenced by the scatter due to a small hysteresis between increasing and decreasing q. This relation can be approximated as $q = -A\partial h/\partial x + B$, where A and B are constants, and B/A gives the slope as q approaches zero. Similar to $\tilde{h}$, we introduce the flux deviation, $\tilde{q}(x,t) = q(x,t) - q_1(1 - x/W)$, as the deviation of the instantaneous local flux from the steady state value noting that the flow rate under q_1 decreases linearly with horizontal position [21]. Substituting $\tilde{q}$ and $\tilde{h}$ into the relation between q and $\partial h/\partial x$ gives,

$$(5.3) \qquad \tilde{q} = -A\frac{\partial \tilde{h}}{\partial x}.$$

Similarly, using expressions for $\tilde{q}$ and $\tilde{h}$, it can be shown that the continuity equation [31], $\partial h/\partial t + \partial q/\partial x = 0$, can be expressed as

$$(5.4) \qquad \frac{\partial \tilde{h}}{\partial t} + \frac{\partial \tilde{q}}{\partial x} = 0.$$

Note that Eq. 5.3 takes the form of Fick's law with $\tilde{h}$ in place of concentration, $\tilde{q}$ in place of the diffusion flux, and A in place of the diffusion coefficient. Eq. 5.3 can be used to express Eq. 5.4 in terms of $\tilde{h}$, i.e., $\partial \tilde{h}/\partial t = A\partial^2\tilde{h}/\partial x^2$, which results in an equation having the same form as the diffusion equation. Equivalently, differentiating Eq. 5.3 with respect to t and Eq. 5.4 with respect to x and then combining, gives

$$(5.5) \qquad \frac{\partial \tilde{q}}{\partial t} = A\frac{\partial^2 \tilde{q}}{\partial x^2}.$$

In the bounded heap, the upstream boundary condition is $\tilde{q}(0,t) = \tilde{q}_2$, where $\tilde{q}_2 = q_2 - q_1$. Before the wedge reaches the endwall, Eq. 5.5 applies only in the wedge which defines a downstream moving boundary condition of $\tilde{q}(x_f,t) = 0$, where x_f is given by Eq. 5.2. Since x_f increases as $\sqrt{t}$, a similarity solution can be obtained [185] by choosing a similarity variable $\xi = x/\sqrt{t}$:
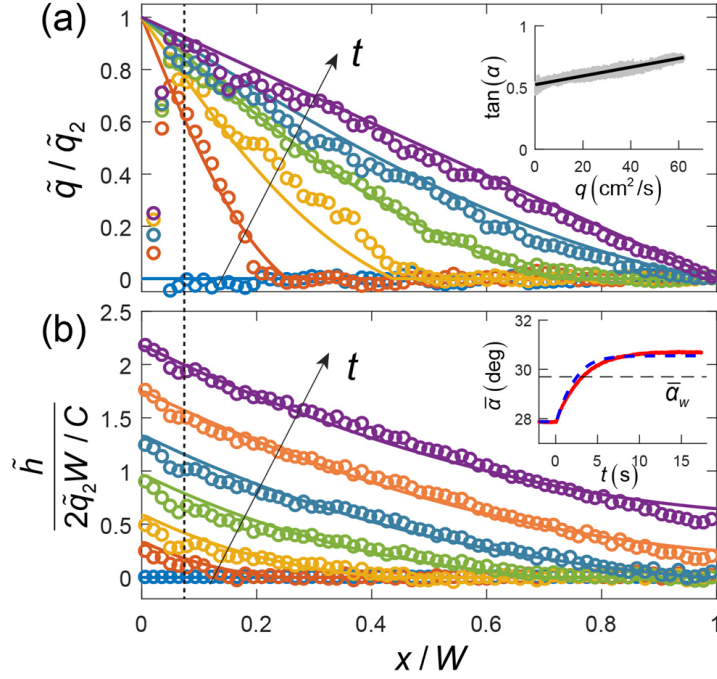
Figure 5.4.   DEM simulation results (circles) and model results (solid curves) for a single transition from $q_1 = 11\,\mathrm{cm^2/s}$ to $q_2 = 35\,\mathrm{cm^2/s}$ in a system with $W{=}0.69\,\mathrm{m}$ and $T{=}12\,\mathrm{cm}$. $\bar{\alpha}_1 = 27.9°$ and $\bar{\alpha}_w = 29.7°$. The feed zone extends from $x = 0$ to the dashed line. (a) $\tilde{q}(x,t)$ profiles at $t{=}0$, $0.25\,\mathrm{s}$, $0.75\,\mathrm{s}$, $2.0\,\mathrm{s}$, $3.8\,\mathrm{s}$, and $9.8\,\mathrm{s}$ from bottom to top. Inset: $\tan\alpha$ vs. q from steady flow and single transition measurements (gray dots) with solid line $q = -A\partial h/\partial x + B$, where $A{=}0.028\,\mathrm{m^2/s}$ and $B = -0.015\,\mathrm{m^2/s}$. (b) $\tilde{h}(x,t)$ profiles at $t{=}0$, $0.25\,\mathrm{s}$, $0.75\,\mathrm{s}$, $2.0\,\mathrm{s}$, $3.8\,\mathrm{s}$, $6.5\,\mathrm{s}$, and $9.8\,\mathrm{s}$ from bottom to top. Inset: $\bar{\alpha}$ vs. t from simulation (red curve) and our model (blue dashed curve).

$$\tag{5.6} \tilde{q}(x,t) = \tilde{q}_2 \left[1 - \frac{\mathrm{erf}\left(\frac{x}{\sqrt{4tA}}\right)}{\mathrm{erf}\left(\frac{x_f}{\sqrt{4tA}}\right)} \right].$$

For the region ahead of the front $(x_f < x \le W)$, $\tilde{q}(x,t) = 0$. After the wedge reaches the endwall, the right boundary condition becomes $\tilde{q}(W,t) = 0$, and transient solutions are

obtained numerically by a standard implicit finite difference method. $\tilde{h}(x,t)$ is determined numerically by integrating Eq. 5.4.

Examples of $\tilde{q}$ profiles (normalized by $\tilde{q}_2$) and $\tilde{h}$ profiles (normalized by $2\tilde{q}_2 W/C = W(\tan \bar{\alpha}_w - \tan \bar{\alpha}_1)$) using the above formalism in a slow-to-fast transition are shown in Fig. 5.4. The analytic approach agrees well with the corresponding DEM simulation. Near the beginning of the transition (t=0.25 s), $\tilde{q}$ increases sharply near the feed zone (Fig. 5.4(a)) and the strong gradient results in increased local deposition of particles on the heap leading to the formation of the wedge (Fig. 5.4(b)). As the change in $\tilde{q}$ further propagates downstream (t=0.75 s and 2.0 s), the transition at the front becomes smoother, and both the $\tilde{q}$ and $\tilde{h}$ profiles for $x \leq x_f$ become slightly curved because of Eq. 5.5. Here, a smaller A results in larger profile curvature, much like diffusion with a smaller diffusivity.

After the front reaches the endwall (t=3.8 s), the curved $\tilde{q}$ profile continues to evolve towards the new linear steady state (t=9.8 s). This slow evolution after the front reaches the endwall corresponds to the additional change in $\bar{\alpha}$ shown in the insets of Fig. 5.2(c) and 5.3(c), and is well captured by the model (Fig. 5.4(b) inset). Again, smaller A results in a longer transition duration, much like a substance with smaller diffusivity. Since the propagation constant C depends on average surface slope and feed rate, a relation between C and A likely exist, similar to that in other moving boundary problems [**185, 186, 187**]. Moreover, as A, B, and C are dimensional constants, scalings likely exist between these constants and physical parameters such as the particle diameter and the flowing layer depth. The small differences between the model and simulation results are likely due to approximating the relation between α and q as linear and neglecting $\partial q/\partial t$ and higher order spatial derivatives in Eq. 5.3. We have obtained similar quantitative agreement between the model and DEM simulation results for all combinations of the three feed rates including both fast-to-slow and slow-to-fast transitions.

The model developed here for transient granular flow in a bounded heap under a step change in the feed rate captures the heap transition dynamics observed in experiments and simulations, and can potentially be applied to other depositing flows such as open heap flows and tumbler flows. Note, however, that Eq. 5.5 depends on a linear relationship

between the local slope and flux, a relationship that is apparently due to the frictional interaction of the flowing grains with the sidewalls in a narrow gap geometry [**34, 188, 19**]. For transient heap flows with wider gaps where sidewall friction has a smaller influence or 3D conical heap flows, this relation may be non-linear [**34**], resulting in a different form for Eq. 5.5, which may produce different transients.

CHAPTER 6

Unsteady flows and inhomogeneous packing in damp granular heap flows

SUMMARY

Modulating the feed rate is not the only approach to generate unsteady flow. In this chapter, we explore unsteady heap flows that are generated by adding a small amount of liquid. We experimentally study the transition from steady flow to unsteady flow in a quasi-2D granular heap when small amounts of water are added to monodisperse glass spheres. Particles flow uniformly down both sides of the heap for low water content, but unsteady flow occurs as the water content increases. The unsteady flow mode consists of a non-depositing downslope avalanche and an upslope propagating granular jump. The transition from steady to unsteady flow occurs when the slope exceeds a critical angle as a result of water-induced cohesion. Under unsteady flow conditions, the deposited heap consists of loosely packed and densely packed layers, the formation of which is closely related to the unsteady flow dynamics.

This chapter is based on the manuscript "Unsteady flows and inhomogeneous packing in damp granular heap flows" by H. Xiao, J. Hruska, J. M. Ottino, R. M. Lueptow, and P. B. Umbanhowar that is in review with *Physical Review E* (American Physical Society) [**189**]. In this work, John Hruska, who is an undergraduate student I am advising, did preliminary experiments of unsteady damp flows, and I further designed and conducted experiments, analyzed the data, and wrote the manuscript.

6.1. Introduction

Flows of wet granular materials are common in nature and industry. By increasing the liquid content, the behavior of granular materials can change dramatically from cohesionless dry particles all the way to slurries and suspensions [**190, 191, 192, 193**]. In this

study, we focus on the first step of this transition where the particles are damp (slightly wet) and gravity-driven flow occurs. Many industrial and geophysical scenarios fall into this regime, for example, when granular materials exposed to environmental humidity become damp. Previous studies have shown that high relative humidity can significantly influence the flowability and slope stability of the materials [**194, 195, 196, 197**]. Also, a small amount of liquid can be mixed with particles intentionally to reduce segregation [**167, 166, 169, 168**] or suppress airborne dust [**198**]. However, the flow behaviors of damp granular materials differ from that of dry materials. Thus, it is important to understand the influence of small quantities of added liquid on the flow.

Gravity-driven free surface flows of wet granular materials exhibit unique behaviors that are relatively unexplored compared to those that occur in dry and cohesionless materials [**192**]. The most significant difference between wet and dry granular materials is the angle of repose. An inclined bed remains static below a critical angle, θ_s, defined as the maximum angle of repose [**28**]. Previous studies have shown that for wet granular materials, θ_s depends on the liquid content, W_c, defined here as the volume fraction of the added liquid in the total packed volume of the particles [**199, 200, 201, 202, 167, 170**]. At extremely low W_c, liquid is trapped in valleys between the asperities of particle surfaces [**203, 204, 205, 206**], and tiny liquid bridges may form between the asperities of two contacting particles, which introduces weak cohesion [**206, 205**]. Under damp (or slightly wet) conditions, where W_c is typically on the order of 10^{-4} to 10^{-3}, liquid bridges can form between contacting particles due to capillary forces, which introduces cohesion [**207, 12**]. The number of liquid bridges per particle, N, increases with increasing W_c until it reaches a maximum value of approximately six bridges per particle for mono-sized spheres [**12**]. As a result of increasing N, stronger cohesion between particles causes θ_s to rise significantly [**199, 200, 201, 202, 167, 170**]. Mechanical properties of the damp material, such as yield stress and tensile strength, also increase as N increases [**12, 204**]. In addition, increasing W_c can cause the free surface of the flowing material to become rough, and flow instabilities may occur [**167, 200, 208**], as discussed later. Further increasing W_c beyond where $N = 6$ leads to another regime where liquid

bridges merge and form more complex structures [**12**], so that the angle of repose and other mechanical properties become insensitive to W_c [**204**], which is not the focus of this study.

In this thesis, we study slightly wet granular flows during heap formation, which occurs widely in both geophysical and industrial systems [**81, 20, 21, 57, 146, 180, 167, 170**]. For quasi-two-dimensional (quasi-2D) bounded heap flow of dry spheres [**81, 20, 21, 57, 181**], particles are fed onto the heap and flow downslope in a relatively thin flowing layer along the surface of the previously deposited particles, which form a static bed. The free surface of the flowing layer is inclined at an angle, θ, which is usually slightly larger than θ_s for dry flows. For a sufficiently large and steady feed rate, the free surface rises uniformly, and particles are uniformly deposited from the flowing layer to the static bed [**21, 20, 81**]. When the particles are size bidisperse, with the smaller species being smooth and spherical and the larger species being rough and non-spherical, a second flow mode occurs and stratification of the two species can be observed [**44, 88, 209, 176, 91, 46**]. This flow mode is periodic with each period containing a downslope avalanche followed by a granular traveling jump that propagates upslope [**88**]. (The jump is also referred to as a kink, a granular bore, or a shock [**45, 210, 211, 212, 213**].) This flow mode is triggered by the interplay of particle size segregation [**49**] and the difference in the angle of repose between the two species [**209, 176**], which is also referred as the "segregation mobility feedback" [**46**]. Note that stratification due to size segregation can also occur for smooth spherical particles, but the underlying layer formation mechanism is different [**20, 146**].

In three-dimensional (3D) heap formation, the flow is often not axisymmetric and unsteady flow can occur. For example, pouring certain types of sand onto a 3D heap can result in unsteady flow that revolves around the feed zone [**214, 215**]. The unsteady flow may be related to the segregation mobility feedback [**215**], even after the particles were sifted to a relatively narrow size distribution [**214**]. However, since some of these experiments were conducted at relative humidities between 60% and 90% [**214**], there is a possibility that water condensed on the small diameter (0.1 mm) particles used in the study contributed to the unsteady flow [**197**]. For example, in experiments using damp

mono-sized spheres with $W_c = 4 \times 10^{-4}$ in rotating circular tumblers, unsteady flow occurs which consists of a downslope front followed by a second front traveling upslope [**200, 208**], similar to that due to particle size and shape differences. This suggests that using particles differing in size and shape may not be the only way to trigger unsteady flow, and it is possible that unsteady flows can also occur for slightly wet particles in heap flows.

In this study, we experimentally investigate the transition from steady to unsteady heap flow of damp (slightly wetted) mono-sized spheres in a quasi-2D center-filled bounded heap geometry. Section 6.2 describes the experimental methods. Section 6.3 presents the results showing the transition from steady flow with uniform deposition to unsteady and asymmetric flow. Section 6.4 discusses the formation of the inhomogeneous packing for particles deposited on the heap. Section 6.5 presents the conclusions.

6.2. Experimental methods

The apparatus (Fig. 6.1) for the quasi-2D bounded heap experiments consist of a glass front plate and an aluminum back plate, separated by acrylic bars which form the bounding walls and the bottom. The width of the heap, W, is 38 cm and the gap thickness, T, is 1.27 cm. A metal funnel placed above the center of the silo feeds the particles. The outlet cross section of the funnel is shaped into a $1.1 \times 1.02 \, \text{cm}^2$ rectangle to fit the quasi-2D silo. Four sizes of glass spheres with density $\rho = 2.62 \, \text{g/cm}^3$ (Ceroglass Technologies Inc., TN, USA) are used with diameters d of 0.63±0.07 mm, 0.53±0.04 mm, 0.35±0.05 mm, and 0.20±0.03 mm. The interstitial liquid is distilled water, with nominal density $\rho_w =$ 1 g/cm^3 and surface tension $\gamma = 74$ dynes/cm.

For each experiment, particles are first dried in an oven at 90 °C for at least half an hour and then cooled in air to room temperature (21 °C). A volume of water, V_w, is mixed into an as-poured bulk volume of particles, V_p, ($V_p = 1$ L) in a clean glass beaker to obtain wet granular material with water content $W_c = V_w/V_p$. Experiments begin by pouring the mixture into the funnel within one minute after the mixtures are prepared to minimize evaporation. Water lost to the beaker and funnel surfaces can be neglected, as their surface areas are over 100 times smaller than the total surface area of all the particles for the largest diameter particles used here. Furthermore, water does not drain from the
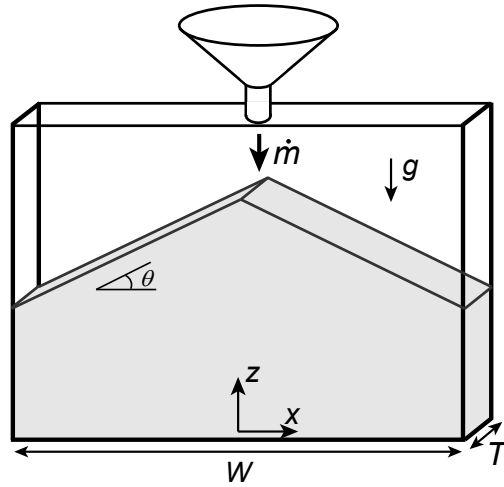
Figure 6.1. Schematic of the experimental quasi-2D bounded heap (not to scale).

particles due to gravity, as the particle diameters are much smaller than the capillary length of water, $l_c = \sqrt{\gamma/\rho_w g} \approx 2.7\,\text{mm}$, where g is the acceleration due to gravity.

We perform experiments varying W_c systematically from 0 to 1×10^{-3} for all particle sizes. The mass feed rate from the funnel $\dot{m}$ remains constant as the funnel empties, but decreases with increasing W_c, from $\dot{m} = 64\,\text{g/s}$ at $W_c = 0$ to approximately $\dot{m} = 30\,\text{g/s}$ at $W_c = 1 \times 10^{-3}$ for the particle sizes examined. Results from additional experiments studying the influence of the feed rate are reported later in the paper.

A digital camera (EOS Rebel T6, Canon Inc., Japan) records videos of the experiments at $30\,\text{frames/s}$ with a spatial resolution of about $0.4\,\text{mm}$, which is comparable to one particle diameter. The videos allow us to measure the instantaneous surface height profile $h(x,t)$ by examining the change of image intensity in each column of the image [180], where x is the coordinate in the horizontal direction, and z is the vertical direction with the origin at the center of the heap base, see Fig. 6.1. In addition, a high speed camera (Flea3, Point Grey Research Inc., Canada) records videos for specific smaller regions of the flow at 200 frames/s with a spatial resolution of $0.1\,\text{mm}$.
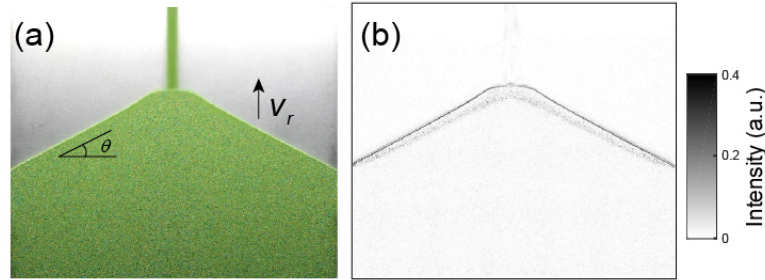
Figure 6.2. (a) Image of rising heap with uniform deposition, and (b) image differencing result with 0.2 s delay of steady heap flow. $d = 0.63$ mm, $W_c = 0$, and $\dot{m} = 64$ g/s.

6.3. Transition to unsteady flows

We first characterize the two flow modes observed at different W_c. With zero or small W_c, steady heap flow occurs with uniform deposition on both sides of the heap, as described in previous studies of dry bounded granular heap flows [81, 20, 21]. An example with $d = 0.63$ mm and $W_c = 0$ is shown in Fig. 6.2(a), where the free surface is symmetric about the center and inclined at $\theta = 27.7°$ during the flow. As more material is fed into the system, the free surface rises uniformly at a constant rise velocity, $v_r = \dot{m}/(\phi \rho W T)$, where $\phi = 0.60$ is the packing density of the heap for the dry particles used here. To visualize the flowing layer, we measure the image intensity difference between two frames with a time increment of 0.2 s. In this way, flowing regions have a large image difference (dark) while non-flowing regions have a negligible image difference (light). The result [e.g., Fig. 6.2(b)] shows that flow occurs in a thin layer corresponding to the gray region near the free surface. The thin dark layer on the free surface results from the surface rising uniformly.

At larger W_c, the flow is unsteady and asymmetric about the center of the heap. A time series of images for the flow with $d = 0.63$ mm and $W_c = 0.8 \times 10^{-3}$ is shown in Fig. 6.3. At $t = 0$, flow occurs only on the right side of the heap in the form of an avalanche propagating downstream. After the avalanche front reaches the bounding wall, an upstream traveling jump [213, 210, 211] forms ($t = 1.3$ s). After the jump reaches the feed zone near the center, it directs the feed stream toward the left side of the heap, which
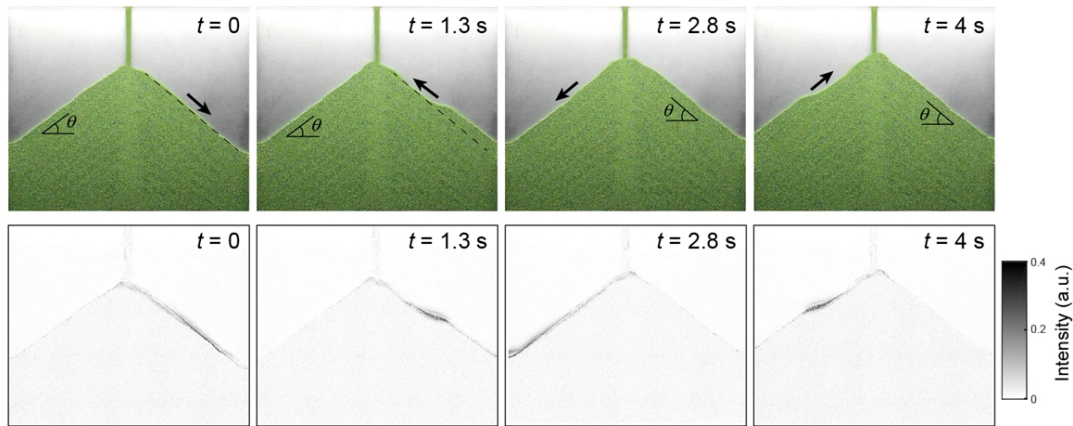
Figure 6.3. Images (top row) and image differencing results with $0.2\,\mathrm{s}$ delay (bottom row) of unsteady heap flow at different times with $d = 0.63\,\mathrm{mm}$, $W_c = 0.8 \times 10^{-3}$, and $\dot{m} = 35\,\mathrm{g/s}$ showing an oscillatory heap instability (alternating flow). The dashed reference lines are at the same location in the $t = 0$ and $t = 1.3\,\mathrm{s}$ images.

triggers a downslope avalanche on the left side ($t = 2.8\,\mathrm{s}$). In the meantime, the right side becomes static, as the image difference shows. When the front of the downslope avalanche reaches the left bounding wall, an upstream traveling jump forms at that bounding wall ($t = 4\,\mathrm{s}$). In this way, the flow is periodic and continues to alternate between the two sides of the heap.

The downslope avalanche and upslope traveling jump are similar to the unsteady and periodic flows observed in studies of spontaneous stratification due to "segregation mobility feedback" [44, 88, 209, 176, 91, 46]. However, since monodisperse spheres do not segregate, a different mechanism must govern the transition. In addition to the unsteady flow mode for $W_c = 0.8 \times 10^{-3}$, the surface incline of $\theta = 33.4°$ is steeper than that with no water ($\theta = 27.7°$). For unsteady alternating flow, the angle θ is measured as the angle of the free surface on the static side. This is the angle formed by the upslope traveling jump in the previous period, and is also the angle of the slope on which the next downslope avalanche will propagate. Another significant difference with the dry flow case is that slightly darker and lighter layers are evident in the deposited heap (observable in Fig. 6.3). The lighter layers are densely packed, and the darker layers are loosely

packed. The loosely packed layers have more voids which make them look darker when the apparatus is lit from above. The formation of these layers is discussed in detail in Section 6.4.

To quantify the transition from steady to unsteady flow, we first define an unsteadiness index, Φ:

$$(6.1) \qquad \Phi = \left\langle \left[\frac{1}{W} \int_{-W/2}^{W/2} \frac{(v_r(x,t) - v_{r0})^2}{v_{r0}^2} dx \right]^{1/2} \right\rangle.$$

In this relation, $v_r(x,t) = dh(x,t)/dt$ is the instantaneous local surface rise velocity, $v_{r0} = \dot{m}/\phi \rho W T$ is the average rise velocity, and $\langle\ \rangle$ denotes a temporal average measured from when the heap base first spans the entire width of the apparatus to when the feed is stopped. Thus, Φ is essentially a spatial and temporal average of the local deviation from steady flow. We exclude from the average the 5 cm wide feed zone in the center and the 2.5 cm wide regions adjacent to each downslope bounding wall to reduce the influence of bouncing particles on Φ. For steady flows (Fig. 6.2), $v_r(x,t) \approx v_{r0}$ (with small fluctuations), so that Φ is close to zero. For unsteady flows, static regions with $v_r(x,t) = 0$ yield a local deviation of 1, while $v_r(x,t)$ for the traveling fronts of the downslope avalanche and the upslope traveling jump are much greater than v_{r0}, and result in local fluctuations greater than 1. Thus, on average, the unsteadiness index Φ is typically greater than 0.5 for unsteady flows, and we define a transition water content, W_c^*, which corresponds to the water content when $\Phi = 0.5$ for a particular particle size.

Figure 6.4(a) shows how Φ varies with liquid content for the four particle sizes considered. For each particle size, Φ is close to zero at $W_c = 0$ and remains near zero at small W_c, indicating that the flow is steady. As W_c is further increased, Φ starts to increase, indicating unsteady flow. When W_c is only slightly larger than the transition water content, W_c^*, the propagating fronts are less distinct than those shown in Fig. 6.3 and sometimes do not propagate the entire length of the slope. Thus, the deviation of $v_r(x,t)$ from v_{r0} is relatively small resulting in Φ slightly above 1. When W_c is further increased, the propagating fronts are sharper which results in larger Φ. Near $W_c = 1 \times 10^{-3}$, the free surface
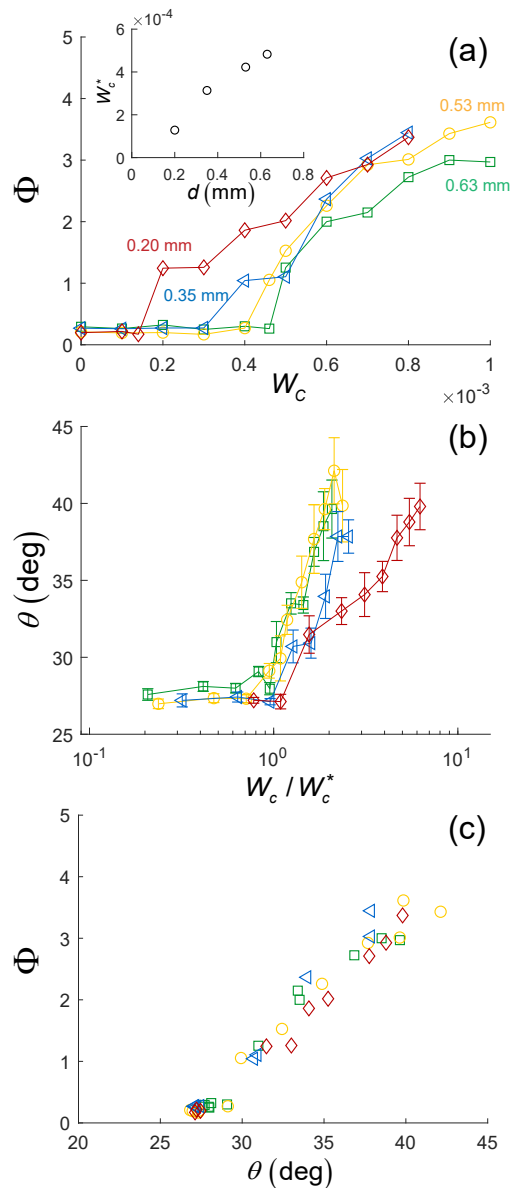
Figure 6.4. Results of the parametric study varying W_c and d. (a) Change of the flow unsteadiness index Φ with W_c. Inset: W_c^* vs. d. (b) Surface angle θ vs. W_c/W_c^*. (c) Change of Φ with θ. Particle sizes: $0.20\,\mathrm{mm}$ (red diamonds), $0.35\,\mathrm{mm}$ (blue triangles), $0.53\,\mathrm{mm}$ (yellow circles), and $0.63\,\mathrm{mm}$ (green squares).

becomes rough such that more localized flows (i.e., not spanning the entire slope) and avalanches occur [200, 208, 167], which results in a plateau in Φ for the larger particles

($d = 0.53\,\mathrm{mm}$ and $d = 0.63\,\mathrm{mm}$). Note that data for $W_c > 0.8 \times 10^{-3}$ for the smaller particles are not available because the feed funnel jams at and above this water content. Figure 6.4(a) also indicates that the transition to unsteady flow occurs at smaller water contents for smaller particles. To further demonstrate this trend, the transition water content W_c^* is plotted versus particle diameter d in the inset of Fig. 6.4(a), which shows that W_c^* increases with d. Note that a linear interpolation is applied to calculate W_c^* at $\Phi = 0.5$ using two neighboring data points.

The transition from steady to unsteady flow is likely related to the ratio between water-induced cohesion and particle weight. Steady flow occurs at zero or small cohesion, while unsteady flow occurs when cohesion is significant compared to the particle weight. The liquid bridge force between two particles can often be approximated as $\pi\gamma d$ [**191, 207, 193**], while the particle weight is $\frac{\pi}{6}\rho g d^3$. Thus, a Bond number that characterizes the ratio between liquid bridge force and particle weight can be defined as, $Bo = 6\gamma/\rho g d^2$ [**207, 216, 217**]. The Bond number scales with d^{-2}, indicating that liquid bridge force can dominate for smaller particles. However, the Bond number alone is not adequate to explain the increase of ϕ with W_c in Fig. 6.4(a) since Bo is independent of W_c. This is because that the liquid bridge force is relatively insensitive to the bridge volume [**207, 191, 193**].

To explain the dependence of Φ on W_c, two possible scenarios can be considered. The first one is related to particle roughness and predicts that the transition from steady to unsteady flow is determined by the initial formation of liquid bridges, which occurs when the valleys between surface asperities are filled with liquid [**203, 206, 205**]. This occurs at $W_{c,as} = 6\alpha\phi\delta/d$ [**203**], where α is the ratio of the area of valleys between asperities to the total surface area of a particle, and δ is the characteristic height of the asperities. Assuming that surface roughness does not vary with particle size, the asperity filling mechanism predicts that W_c^* should decrease with increasing d, which is opposite to the observations shown in Fig. 6.4(a). In the second scenario, the transition occurs at $W_c^* > W_{c,as}$, and the controlling parameter becomes the number of liquid bridges per particle, N, which increases with W_c from 1 to a saturating value of 6 [**203, 12, 204**]. In this regime, the overall force ratio for a particle is NBo, which increases with W_c, and

this causes the material properties such as tensile strength and yield stress to increase with W_c [204]. Similarly, the increase of NBo can also drive the increase of Φ with W_c in Fig. 6.4(a). In addition, the fact that lower water content is required to trigger the flow transition for smaller particles [Fig. 6.4(a) inset] can be explained: to reach the same overall force ratio required for the flow transition, fewer liquid bridges (N) are needed for smaller particles, which in turn lowers W_c^*. Note that the exact functional form for the relation between W_c^* and d is difficult to specify, as many complications likely come into play, such as the possible dependence of N on d [203].

Having identified the water content as a critical factor for the flow transition, we further discuss the mechanism for the transition and focus on another important property that is significantly influenced by W_c: the surface angle θ. Figure 6.4(b) shows that for the particle sizes examined, θ is approximately $27°$ for W_c approaching zero. It increases abruptly for $W_c/W_c^* > 1$ to approximately $40°$ for the maximum water content $W_c \approx 1 \times 10^{-3}$, which agrees qualitatively with previous studies [199, 200, 201, 202, 167, 170]. Again, this increase is most likely related to the increase of NBo: stronger cohesion requires steeper angle for gravity-driven flow to occur. Note that for $W_c/W_c^* < 1$, the increase in θ is small compared to the increase for $W_c/W_c* > 1$, as shown in Fig. 6.4(b). This is not unexpected because the surface slope in steady and unsteady flows develops under different flow dynamics and cohesion can play different roles in the formation of the slope in the two flow modes.

Figure 6.4(c) shows the relation between Φ and θ, which indicates a flow transition at $\theta \approx 30°$ for all particles sizes. For $\theta < 30°$, the flow is steady (Φ close to zero) and the surface rises uniformly (Fig. 6.2), indicating uniform particle deposition on the entire heap. For $\theta > 30°$, the flow becomes unsteady ($\Phi > 1$), as shown in Fig. 6.3, and no deposition occurs during the downslope avalanche ($t = 0$ and $t = 2.8\,\mathrm{s}$ in Fig. 6.3). This is evident by comparing the material above the dashed reference lines in Fig. 6.3 at $t = 0$ and $t = 1.3\,\mathrm{s}$, where the surface upslope from the traveling jump does not rise (i.e., there is no deposition in this region). Thus, the downstream flow experiences a transition from

steady deposition to unsteady deposition (only during the upslope traveling jump on one side of the heap) as θ increases beyond $30°$ due to the water-induced cohesion.

This transition is reminiscent of the concept of a "neutral angle," θ_n, that has been discussed in a number of studies focusing on material exchange between the flowing layer and the underlying static bed [**29, 30, 33**]. These studies propose that deposition of particles on the static bed during the downstream flow is only possible when $\theta < \theta_n$, where $\theta_n = 30°$ in this study. For the unsteady flows with $\theta > 30°$, deposition is only possible via the upslope traveling jump, where particles flow along the slope to the traveling jump and are deposited on the face of the jump. Previous studies of dry granular flows in a chute indicate that a minimum base incline angle and a downstream obstacle are required for the formation of the jump [**213, 210, 211**], as mentioned previously. Here, increased θ due to cohesion and the presence of the downstream bounding walls satisfy these two conditions, respectively. Note that no upslope propagating jumps were found in experiments where the bounding walls (the obstacles) are removed. In addition, the unsteady flow mode observed here resembles the unsteady flow mode formed due to the segregation of particles with size and shape differences [**44, 88, 209, 176, 91, 46**]. In that case, large and rough particles segregate to the free surface, which sets a higher surface angle (possibly higher than θ_n for the small spherical particles that segregate to the interface between the flowing layer and the static bed) to induce the downslope avalanche and the upslope traveling jump [**88**]. Thus, it appears that particle roughness in size-and-shape stratification flow and water-induced cohesion in slightly wet flow play similar roles in increasing θ beyond θ_n, resulting in a similar traveling jump flow mode.

Lastly, we consider the influence of the feed rate $\dot{m}$ on heap flow. As mentioned in Sec. 6.2, the feed rate from the funnel decreases as W_c increases. However, $\dot{m}$ plays a lesser role in the transition to unsteady flow than does W_c. Figure 6.5 shows three cases with the same particle diameter and water content but with different funnel sizes that produce different feed rates: $\dot{m} = 21\,\mathrm{g/s}$ (small funnel), $\dot{m} = 30\,\mathrm{g/s}$ (medium funnel which corresponds to the data in Fig. 6.4), and $\dot{m} = 75\,\mathrm{g/s}$ (large funnel), which is higher than the dry feed rate of the medium funnel ($64\,\mathrm{g/s}$). At all three feed rates, unsteady flow
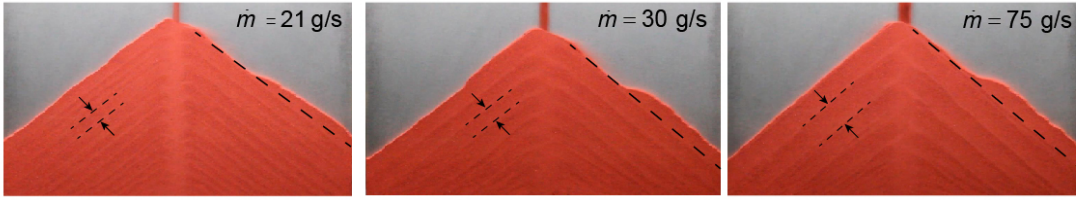
Figure 6.5.   Images of heap flow with $d = 0.20\,\text{mm}$ and $W_c = 0.7 \times 10^{-3}$ at different feed rates showing strong dependence of the jump height slope on the feed rate but weak dependence of the heap surface angle on the feed rate. Surface angle $\theta = 37.5°$ for $\dot{m} = 21\,\text{g/s}$, $\theta = 38.2°$ for $\dot{m} = 30\,\text{g/s}$, and $\theta = 38.8°$ for $\dot{m} = 75\,\text{g/s}$. Deposited layer thickness is indicated by the arrows.

occurs but the increase of θ due to $\dot{m}$ is only about $1°$, which is less significant than the increase of θ due to W_c (more than $10°$), indicating that the flow mode is less sensitive to $\dot{m}$ than to W_c. The shape and the height of granular jumps in the related problem of dry granular chute flows are mainly determined by the flow rate and the incline angle of the chute [210, 211]. Here, the height of the jump in slightly wet flows also increases with $\dot{m}$ as shown in Fig. 6.5. A consequence of varying $\dot{m}$ is that the thickness of the alternating layers deposited on the heap also varies, which will be discussed later. Quantifying the scaling and other details related to the influence of $\dot{m}$, W_c, and d on the shape and height of the traveling jump are topics for future work.

6.4. Inhomogeneous packing

The faint alternating lighter and darker layers evident in Figs. 6.3 and 6.5 are a consequence of heterogeneous packing in the deposited heap. Previous studies have shown that the poured packing density can be less dense for granular materials with cohesive forces due to adhesion (van der Waals forces) [218, 13, 219] or liquid addition [220, 221, 222]. Here, we also observe that the overall packing density in the deposited heap formed by slightly wet flows is less than that for dry flows. Figure 6.6(a) compares heaps of $d = 0.20\,\text{mm}$ particles for $W_c = 0$ and $W_c = 0.7 \times 10^{-3}$. Although the dry weight of the two heaps is equal, the volume for $W_c = 0.7 \times 10^{-3}$ is clearly larger than the volume for $W_c = 0$. In addition, it is also clear that the surface incline (the dynamic angle of
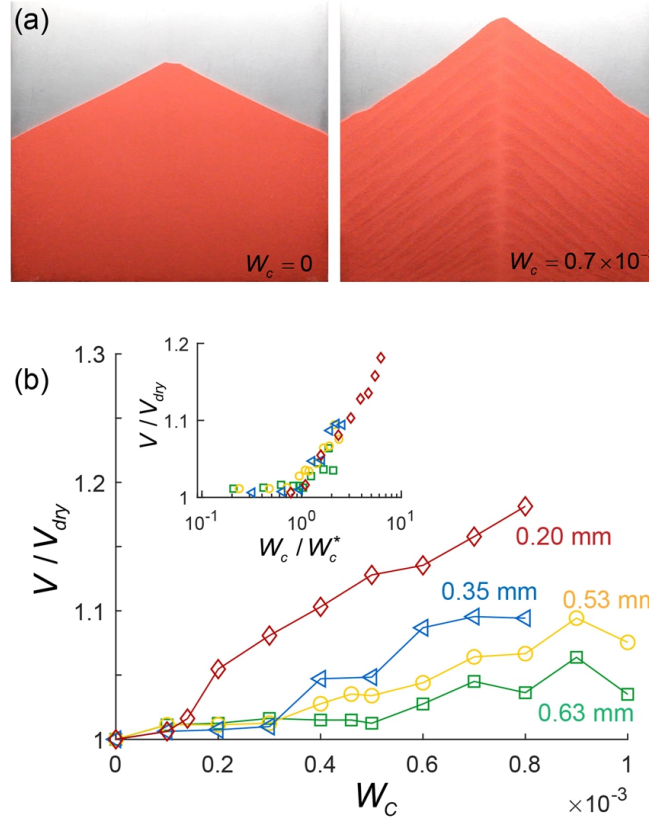
Figure 6.6. Increase in volume of the deposited heap in slightly wet granular flows. (a) Images of the final heap for different water contents with $d = 0.20\,\mathrm{mm}$ particles. (b) Volume ratio V/V_{dry} vs. W_c for the four particle sizes. Inset shows V/V_{dry} vs. W_c/W_c^*.

repose) is steeper for $W_c = 0.7 \times 10^{-3}$ and the layering in the deposited heap only occurs with the damp unsteady flow.

To quantify the change in the overall packing density, we plot the volume ratio V/V_{dry} versus W_c in Fig. 6.6(b), where the total volume $V = T \int_{-W/2}^{W/2} h(x)dx$ of the deposited heap for wet flows is larger than the volume for dry flows, V_{dry}. For all particle sizes, V/V_{dry} first increases slightly with W_c indicating that the packing is marginally less dense for steady heap flow. As W_c is further increased and the flow becomes unsteady, the increase in V/V_{dry} with W_c is much steeper. At W_c near 1×10^{-3}, V/V_{dry} plateaus except for the case of $d = 0.20\,\mathrm{mm}$ particles where data for $W_c > 0.8 \times 10^{-3}$ are not available

due to funnel jamming. In addition, for the same W_c, the increase in the heap volume V/V_{dry} is more significant for smaller particles. This is likely a result of the difference in the force ratio between water induced cohesion and particle weight for different sized particles, as discussed in Sec. 6.3. Thus, we apply the same scaling by plotting V/V_{dry} versus W_c/W_c^* in the inset of Fig. 6.6(b), resulting in the collapse of the data except for the few cases near $W_c = 1 \times 10^{-3}$ ($W_c/W_c^* \approx 2$ for the largest particles) where V/V_{dry} plateaus. This result is similar to the results in a previous computational study where the packing density decreases when the ratio between cohesion and gravity is increased [219], but that study reports no layers of differing packing densities. In addition, the inset of Fig. 6.6(b) also shows that the increase of V/V_{dry} with W_c/W_c^* transitions at $W_c/W_c^* \approx 1$, which corresponds to the transition from steady to unsteady flow, indicating that the transition to unsteady flow influences the packing structure of the deposited heap.

As mentioned earlier, slightly lighter and darker layers occur in the deposited heap for unsteady flow, as shown in Figs. 6.3, 6.5, and 6.6(a). Particles in the lighter layers are densely packed while particles in the darker layers are loosely packed with more voids evident, at least near the clear front wall. This inhomogeneous distribution of the packing density has not been reported in previous studies on packing of cohesive granular materials [13, 220, 221, 218, 219, 222]. Since it is known that wet particles pack loosely and dry particles pack densely, one may wonder if the particles in the densely packed layers are dryer and *vice versa*. This can be determined using fluorescent imaging. A green fluorescent dye (Model 295-17, Cole-Parmer Instrument Co., IL, USA) is added to distilled water at a concentration of $2.3\,\text{mg/ml}$, and experiments are conducted using the same protocol as with undyed water. An Ultraviolet (UV) light with wavelength $365\,\text{nm}$ (Model XX-15N, Spectronics Inc., NY, USA) illuminates the deposited heap, and a digital camera acquires images. A longpass filter (GG495, Thorlabs, Inc., NJ, USA) placed in front of the camera filters out visible light below a wavelength of $495\,\text{nm}$, and a UV filter (Model 54-058, Edmund Scientific Inc., NJ, USA) in front of the longpass filter blocks the UV light from reaching the longpass filter and the camera. No significant influence on the flow from the fluorescent dye is evident.
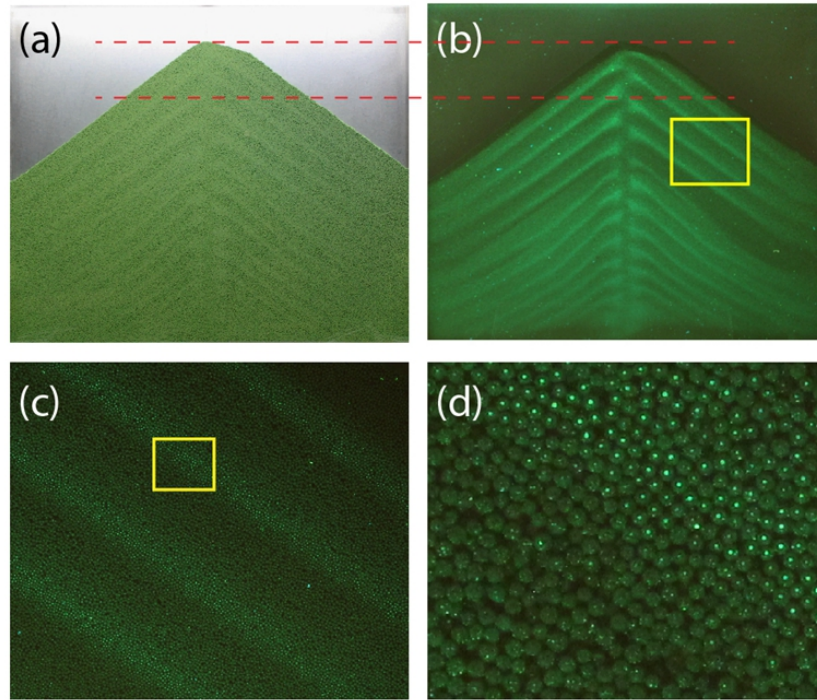
Figure 6.7. Fluorescent light images of a heap with $W_c = 0.8 \times 10^{-3}$, $d = 0.63\,\mathrm{mm}$, and $\dot{m} = 33\,\mathrm{g/s}$. (a) Image of the deposited heap under visible light. (b) Image of the deposited heap under UV light, and magnified images of (c) yellow box in (b), and (d) yellow box in (c). Horizontal lines in (a,b) show correspondence between features in (a) visible and (b) fluorescent images.

Figure 6.7 shows an example of the fluorescent imaging results with $d = 0.63\,\mathrm{mm}$ and $W_c = 0.8 \times 10^{-3}$. Figure 6.7(a) shows the deposited heap under visible light, where the lighter and darker layers are visible. The corresponding image under the UV light is shown in Fig. 6.7(b). Note that the top layer of the free surface is dark, probably due to evaporation immediately after the heap was deposited. More importantly, there are lighter and darker layers in the fluorescent image of the heap. Examination of Figs. 6.7(a) and (b) indicates that the lighter and densely packed layers in Fig. 6.7(a) are also the lighter layers in Fig. 6.7(b), demonstrating that the particles within these layers are not dry. To better understand this, Fig. 6.7(c) shows an enlarged image of the layers under UV light, and Fig. 6.7(d) shows an even further magnified image of two layers. Here,

in the densely packed layer [upper-right region in Fig. 6.7(d)], a lighter spot appears on each particle. These spots are liquid bridges formed between particles and the front glass wall. For the loosely packed layer [lower-left region in Fig. 6.7(d)], few liquid bridges between particles and the front glass wall are evident because the loosely packed particles make fewer contacts with the front wall. Thus, the loosely packed layers appear darker in Figs. 6.7(b) and (c), although particles from both the densely packed and loosely packed layers are wetted. Also, from Fig. 6.7(b), which shows the layering more clearly, it is evident that the layers on the left and right sides of the heap are asymmetric about the center of the heap, corresponding to the alternating unsteady flow and indicating a strong connection between the dynamics of the flow and the formation of the layers.

To demonstrate how the layers form during the unsteady flow, Fig. 6.8 shows a time series of images acquired by focusing on a small region of the heap using the high speed camera. The image in each panel is an average of frames recorded over a $0.05\,\mathrm{s}$ period: regions with moving particles are blurred and regions with no motion remain sharp. Figure 6.8(a) shows an inclined static surface halfway down the slope when the flow is on the opposite side of the heap at time $t = 0$. In this image, the layer near the free surface is loosely packed, as evident by the dark voids in the close up image, and the free surface is rough, similar to the free surfaces observed in previous experiments of damp granular flows [**208, 170**]. A dashed reference line indicating the free surface location is reproduced at the same position in the three subsequent images.

Shortly after $t = 0$, the flow switches to the right side, and at $t = 0.35\,\mathrm{s}$ the downslope avalanche front, which is the blurred region on the upper-left portion of the surface in Fig. 6.8(b), enters the image. After the front passes, particles continue to flow through this image window, shown in Fig. 6.8(c) ($t = 0.96\,\mathrm{s}$). In this image, a thin flowing layer with a thickness of about $10d$ is observed on the free surface, while the particles below the flowing layer remain static with a clear interface between these two regions. The interface coincides with the reference line. There is minimal deposition or erosion that occurs between the flowing layer and the static region, though the bump of particles above the reference line in the close-up image in Fig. 6.8(a) and 6.8(b) has been eroded
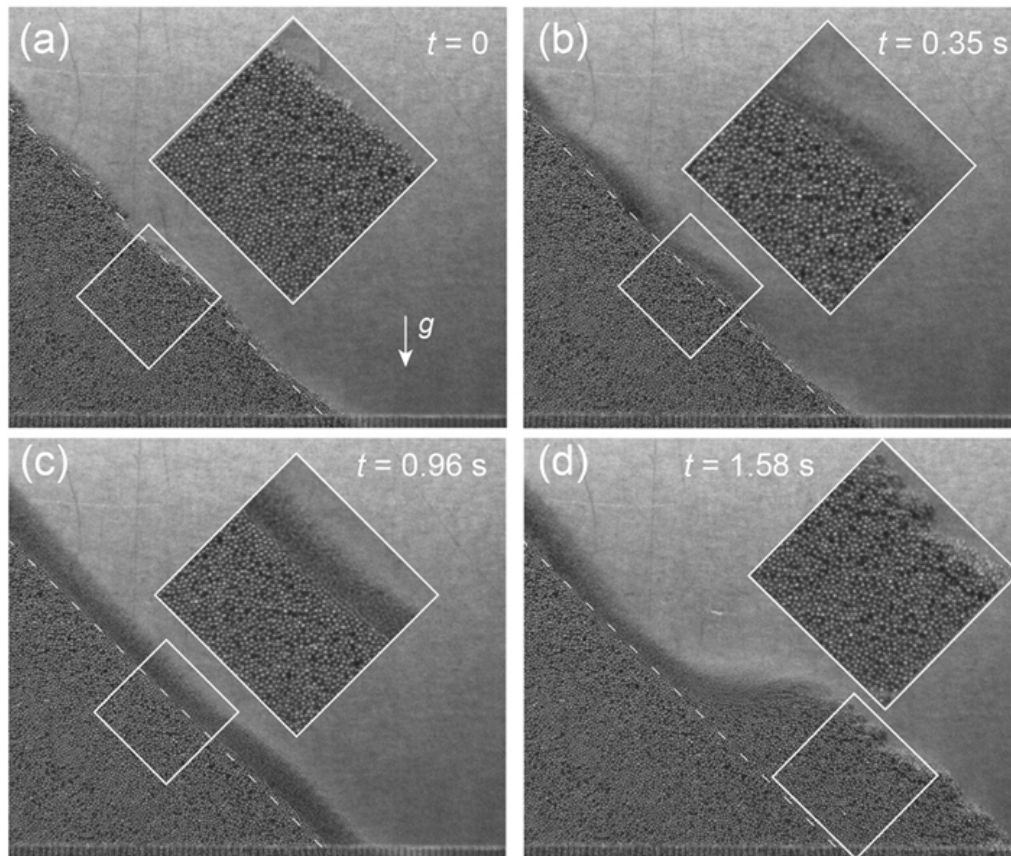
Figure 6.8. Images of an $80 \times 67\,\mathrm{mm}$ region halfway down the right slope with $d = 0.53\,\mathrm{mm}$, $W_c = 0.6 \times 10^{-3}$, and $\dot{m} = 37\,\mathrm{g/s}$. Insets show magnified surface regions as indicated. (a) Static slope when flow is on the left side. (b) Downslope avalanche front enters the window. (c) Flow after the downslope avalanche front passes. (d) Flow when the upslope jump propagates into the region. Dashed white reference lines are located at the same position in all panels.

in Fig. 6.8(c). In this case, $\theta \approx 40°$ because of the cohesion, so no deposition occurs during the downslope flow. Except for smoothing the surface, no erosion occurs, possibly because the cohesion also increases the yield stress in the static region [204, 12]. However, particles immediately below the flowing layer become densely packed evident in the close-up image in Fig. 6.8(c), leaving less densely packed particles below them, evident in the close up image. Apparently, collisions of particles in the flowing layer with particles in the

bed smooth and compact the very top of the "static" region, and the interface becomes smooth.

Finally, at $t = 1.58\,$s, the upslope traveling jump propagates into the image window from the lower right, shown in Fig. 6.8(d). The jump in this case has a height of approximately $30d$. The particles in the thin flowing layer approach the jump, climb up its face and then come to rest, thus propagating the jump upstream. Particles closer to the free surface are more loosely packed and form a rough surface, while particles deeper below the free surface are pressed together and are more densely packed. This results in a depthwise packing density gradient in the newly deposited region behind the jump. After the traveling jump passes, the slope is similar to the static slope at $t = 0$ in Fig. 6.8(a).

Figure 6.8 indicates that the dynamics of the unsteady flow at higher water content accounts for layering in the packing density. The loosely packed layers observed in Figs. 6.3, 6.5, 6.7(a), and 6.8(a) are formed when the traveling jumps propagate upslope. Consequently, the thickness of these layers is set by the height of the jumps. This can be demonstrated by comparing the layering patterns in Fig. 6.5 where the thickness of the layer in each case is indicated by the arrows. For $\dot{m} = 21\,$g/s, the jump height is small and the layers are thinner than the layers for $\dot{m} = 75\,$g/s, which has a higher jump. As discussed in previous studies of dry granular jumps demonstrated in chutes [**211, 210**], the shape of the jump is influenced by the base incline angle, the incoming velocity of the particles, and the thickness of the flowing layer. It is also possible that the packing density gradient in the depthwise direction varies depending on the height and the shape of the jump. However, exploring the relationship between the traveling jump and the layer packing density requires careful measurement of the flowing layer thickness, particle velocity, jump height, and the packing density distribution in the jump, which is beyond the scope of this study, but should be considered for future work.

6.5. Conclusions

In summary, we experimentally studied granular flows of damp sub-millimeter glass spheres in a quasi-2D bounded heap with a water content W_c, volume of water to volume of particles, ranging from 0 to 1×10^{-3}. At zero or low W_c, steady flow occurs simultaneously

and uniformly down both sides of the heap. At higher W_c, the flow becomes periodic. Each period is composed of a downslope avalanche and an upslope jump on alternating sides of the heap, similar to the flow pattern in spontaneous stratification of smooth and rough particles [88]. The flow is asymmetric on the two sides of the heap resembling the flow asymmetry found in 3D heap flows [214, 215]. The transition from steady to unsteady flows occurs when the surface angle is increased due to cohesion beyond a critical value which is approximately 30° for the case of sub-mm spherical glass particles studied here.

In addition to the flow mode transition, the packing density of the deposited heap for wet flow is lower than that for dry flow. It is known that cohesive particles tend to have a less dense poured packing density than non-cohesive particles [13, 220, 221, 218, 219, 222]. However, here we show that in addition to the reduced packing density, the packing in the deposited heap of damp granular materials is inhomogeneous with densely packed and loosely packed layers occurring as a result of the unsteady flow dynamic. These layers are formed during the upslope propagation of the traveling jump.

The mechanism for the wetted flow transition studied here could help in understanding unsteady flows in other flow geometries with particles slightly wetted either by adding liquid or by environmental humidity. The inhomogeneous packing could have important implications in various aspects such as slope stability, mechanical properties, thermal conductivity, and permeability of heaps in industrial and geophysical situations. Future work should focus on quantifying the formation of the traveling jump and its relation to the inhomogeneous packing distribution, as well as its implications for 3D heap formation.

6.6. Appendix: Bidisperse damp granular heap formation

In this appendix, we describe the influence of the unsteady damp flow on size-bidisperse segregation. Following the same experimental procedure as used earlier in this chapter, heap formation using a 50:50 mixture of large (0.53 mm) and small (0.20 mm) particles
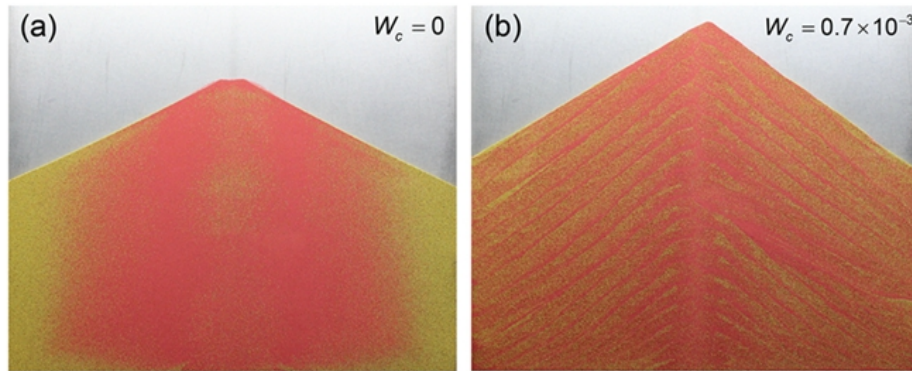
Figure 6.9.   Deposited heaps of bidisperse granular materials (0.53 mm gold and 0.20 mm red) with (a) $W_c = 0$ and (b) $W_c = 0.7 \times 10^{-3}$.

was tested with $W_c = 0$ and $W_c = 0.7 \times 10^{-3}$. Images of the deposited heaps are shown in Fig. 6.9. For heap formation with $W_c = 0$ (Fig. 6.9a), steady flow and uniform deposition occur which result in a streamwise segregated pattern where the larger gold particles are deposited closer to the sidewalls and the smaller red particles are deposited closer to the center of the heap, , which is the typical segregation pattern in a bounded heap [20]. For heap formation with $W_c = 0.7 \times 10^{-3}$ (Fig. 6.9b), unsteady flow occurs as described in Section 6.3, which, in combination with the size segregation mechanism, results in stratification where layers of small and large particles extend from the feed zone to the sidewalls. This pattern is similar to the spontaneous stratification pattern of large rough particles and small smooth particles [44], as the dynamic of the flow is similar [88]. That is, layers form due to segregation during the granular jump travels upslope. Note that with $W_c = 0.7 \times 10^{-3}$, even though the particle size ratio is large, no completely segregated region exists in the deposited heap. This is possibly because that percolation is reduced due to cohesion [166, 167], and also because that smaller particles may form clusters to reduce the effective size ratio [167]. The reduced segregation and the stratification pattern would likely reduce size segregation during hopper discharge, similar to the results in Section 4.3.4. This approach to minimize segregation is worthy of further investigation because of its potential for use in industrial hopper applications.

CHAPTER 7

Continuum modeling of granular segregation during hopper discharge

SUMMARY

Hopper discharge flow is a transient flow that can be considered as the process that follows hopper filling (heap formation). Modeling segregation of size disperse granular materials during hopper discharge is important as hoppers are widely used in various industries. However, due to the complexity of segregation and hopper discharge flows, accurately modeling this process has been challenging. In this chapter, the continuum transport model (Eq. 1.1) is applied to predict segregation of size bidisperse granular material during the discharge of quasi-2D hoppers. Discrete Element Method simulations reveal that segregation occurs mainly in a surface layer where particles are transported from the sidewalls to the hopper center. Velocity profiles are also developed based on a kinematic model and DEM data. The continuum model, which captures the interplay of advection, diffusion, and segregation, is then applied to predict the particle concentration distribution in the surface layer and the bulk. The model accurately predicts the segregation pattern inside the hopper during discharge and the concentration profile of the discharged materials, in agreement with experiments.

This chapter is based on the manuscript "Continuum modeling of granular segregation during hopper discharge" by H. Xiao, Yi Fan, K. V. Jacob, P. B. Umbanhowar, M. Kodam, J. F. Koch, and R. M. Lueptow that is in review for *Chemical Engineering Science* (Elsevier B.V.). This work is the result of my internship project at the Dow Chemical Company (summer, 2017) where I worked with Yi Fan, Karl Jacob, Madhusudhan Kodam, and James Koch. In this project, I performed DEM simulations, developed a continuum

segregation model for hopper discharge process, and performed lab experiments for validation later at Northwestern University. The plant data in Subsection 7.4.5 was collected by James Koch and Karl Jacob and I approximated the discharge segregation in this case with the continuum segregation model.

7.1. Introduction

Flowing granular materials with different properties (size, density, shape, etc.) tend to segregate spontaneously [**49, 53, 22, 97**]. Segregation has important implications in various industrial processes that handle bulk solids such as polymers, ores, agricultural products, and pharmaceutical materials [**52, 175**]. In these processes, a well-mixed bulk solid with homogenous bulk properties is essential for subsequent processes and final product quality. For segregation of dense granular mixtures of different size particles (size segregation), percolation (also called sifting or kinetic sieving) is often the dominant mechanism [**49, 53, 22**]. For example, during free surface flow of a granular mixture, shear generates voids between particles, and smaller particles are more likely to percolate through these voids and thus segregate downward under gravity. As a result, large particles move toward the free surface. This mechanism has been successfully used to explain various segregation patterns observed in several canonical granular systems associated with industrial applications such as inclined chute flow [**55, 68, 60, 164, 223, 45**], rotating tumbler flow [**91, 124, 83**], and heap flow (hopper and bin filling) [**54, 44, 224, 20, 145**]. However, when the flow geometry and kinematics become more complicated, the segregation behavior is more difficult to predict. One such example is segregation during hopper discharge. Ketterhagen et al. [**64**] showed that the segregation profile of the discharged particles can vary significantly for different flow modes (mass flow versus funnel flow), filling conditions, and hopper cross-section shapes. In hopper discharge flow, although percolation is still the dominant mechanism for segregation, other factors such as advection due to the mean flow and collisional diffusive motion of particles can also influence the final segregation pattern and discharge profile.

In general, there are two steps during hopper operations – hopper filling and hopper discharge. These two steps can occur either simultaneously or sequentially. In the continuously filling and discharging operation, the compositions for each size species during the filling and discharging processes are identical at the steady state based on mass balance for each component of the mixture. Therefore, the discharge profiles can be determined directly based on the filling composition. In contrast, in sequential hopper filling and discharge processes, where hopper discharge starts after the completion of hopper filling, significant segregation can occur during both hopper filling and discharge steps, resulting in complicated discharge profiles. Here, we focus on segregation during hopper discharge in the sequential operation of hopper filling and discharge with the aim of developing a quantitative model for predicting the discharge particle size profiles.

Hopper discharge segregation strongly depends on operating conditions and hopper geometry as reported in previous studies. In one of the most common industrial settings, bulk solids are first center filled into the hopper with the hopper outlet closed [175, 225]. A heap forms during the filling process and segregation often occurs. During heap formation, smaller particles (fines) deposit near the center region of the heap while larger particles (coarse) deposit near the sidewalls [224, 20]. Segregation during hopper filling and heap formation have been studied extensively and detailed information can be found in the review paper by Fan et al. [145]. The final state of the hopper filling process provides the initial condition for the hopper discharge process. For this initially segregated state and during hopper discharge, small particles in the center region flow out of the hopper first, followed by the large particles near the hopper sidewalls, which results in a segregated discharge profile [23, 175, 225]. This type of hopper discharge segregation is more significant for funnel flow hoppers than for mass flow hoppers, because of the significant velocity differences from the center to the sidewall of the hopper in funnel flows [23]. However, when the bulk solids are in a well-mixed condition before hopper discharge [226, 64, 227, 228, 229], the discharge profile can be quite different. In this situation, no segregation occurs initially, but it is often followed by a large particle enriched phase and concluded by a small particle enriched phase [226, 64, 227]. Other

initial conditions in the hopper, such as inversely graded (fines above coarse) [**64, 227**] or stratified [**146**] particle distributions, can also result in different segregated discharge profiles. Moreover, changing the hopper geometry can also influence the discharge profile, possibly due to changes in the velocity field [**23, 230**].

Because hopper discharge segregation depends strongly on various operating conditions and the hopper geometry, predicting full industrial-scale hopper discharge segregation using lab-scale experiments and particle-based computational simulations (e.g., discrete element simulations) is challenging. Therefore, we use a continuum approach to predict the hopper discharge profile for segregation that can account for arbitrary initial conditions and hopper geometries. Experimental and computational approaches are utilized to develop the necessary scaling for the continuum model. This continuum approach is based on the modified advection-diffusion transport framework shown in Eq. (7.1). This framework has been successfully used to predict segregation quantitatively in various flows including heaps, rotating tumblers, and inclined chutes (e.g., [**73, 74, 55, 40, 231, 75, 46, 86, 85**]):

$$(7.1) \qquad \frac{\partial c_i}{\partial t} + \nabla \cdot (\boldsymbol{u} c_i) + \frac{\partial}{\partial z} (w_{s,i} c_i) - \nabla \cdot (D \nabla c_i) = 0.$$

Equation (7.1) captures the impact of advection due to the mean flow, segregation due to percolation, and diffusive mixing due to particle random collisions on the final segregation pattern in a given system. In Eq. (7.1), c_i is the volume concentration of species i in a bidisperse mixture ($i = s$ for the smaller, and $i = l$ for larger particles), defined as $c_i = f_i/f$, where f_i is the local solids volume fraction for species i, and f is the total local solids volume fraction. For a quasi-two-dimensional (quasi-2D) flow geometry, the x coordinate is in the streamwise direction while z coordinate is perpendicular to the streamwise direction, and is the direction in which segregation occurs. The mean velocity field for the quasi-2D system is $\boldsymbol{u} = u\hat{x} + w\hat{z}$ and D is the diffusion coefficient assuming diffusion is isotropic. In contrast to the conventional advection-diffusion equation, a segregation term is included in the $z-$direction in this model. The segregation velocity, defined as $w_{s,i} = w_i - w$, depends on the local shear rate and local species volume

concentration [**55, 84, 76, 231, 40**]. The specific mathematical form for the segregation velocity is the key for successful prediction of segregation. Recently, we proposed a model for the segregation velocity based on extensive DEM simulations and previous models [**55, 84**], which accurately predicted segregation in a variety of flow geometries [**40, 83, 65**], for both particle size and density polydispersity [**86, 57**], and even for particles of different shapes [**132**]. In this model, the segregation velocity is

$$(7.2) \qquad\qquad w_{s,i} = \pm S\dot{\gamma}(1 - c_i),$$

where $\dot{\gamma} = |\partial u/\partial z|$ is the shear rate and S is a segregation length scale that depends on the particle diameter ratio and small particle diameter and is well approximated by $S = d_s C_s \ln(d_l/d_s)$, where d_s and d_l are the diameter of small and large particles, respectively, when $d_l/d_s < 3$. For mixtures with larger size ratios, spontaneous percolation might occur [**55**], where small particles can percolate through large particles without shear. This effect is not considered in this study as we are focusing on mixtures with $d_l/d_s < 3$. C_s is a dimensionless constant that depends on particle material properties such as particle surface friction, stiffness and shape. For millimeter sized glass spheres, $C_s = 0.26$ [**40, 65**]. The segregation velocity is positive for large particles and negative for small particles, which is consistent with the segregation phenomena observed in free surface flows where large particles segregate to the free surface and small particles segregate to the bottom of the flow.

In this work, we use the continuum framework and segregation model described by Eqs. (7.1) and (7.2) to predict the hopper discharge segregation profile. However, compared with other flows such as bounded heap flow and rotating tumbler flow, the hopper discharge flow is a transient problem with a moving free surface, so predicting the velocity field presents significant additional challenges. Moreover, identifying the segregating region where Eq. (7.1) applies is critical, because all the particles inside the hopper are flowing and shearing except for the static region in funnel flow, which further complicates

the problem. Therefore, we use DEM simulations to examine flow and segregation dynamics in the hopper for necessary kinematic information along with a kinematic model for the bulk velocity field [232] to solve the continuum model.

Note that recent work by Bertuola et al. [233] used a continuum approach to predict segregation. However, there are key differences from our work, particularly for the segregation model. Bertuola et al. [233] used the segregation model proposed by Hajra et al. [113]

$$(7.3) \qquad w_{s,i} = \pm[K_T + (1 - c_i)K_S]\dot{\gamma}(1 - c_i)(d_l - d_s),$$

where K_T and K_S are coefficients that have to be determined by fitting to experimental data for each simulation with different conditions. Therefore, from a practical standpoint the model needs to be calibrated for each application by experiments or DEM simulations, because K_T and K_S depend on both flow and material properties. In contrast, the segregation model in Eq. (7.2), separates the flow properties from the material properties, so that C_S is a material-dependent constant that can be measured independent of the flow and then used for different flow geometries and conditions [83, 65, 86]. Equation 7.3 depends linearly on the particle size difference, whereas our model depends logarithmically on the particle size ratio and has been validated by DEM simulations [65]. Moreover, in Bertuola et al. [233], the segregation is assumed to occur in the gravity direction and Eq. (7.3) is applied to the entire hopper, without considering the dependence of segregation on the confining pressure in deep bed [130, 234]. In this work, we use DEM simulations to identify a surface flowing layer where segregation occurs, and apply Eq. (7.2) in this region only, and segregation is assumed to be in the direction normal to the inclined free surface as in previous work [74, 55, 40, 231, 75, 46, 86, 85, 83]. Lastly, the segregation model used here is supported by extensive computational results [65] and has been verified for a wide range of flow geometries [83, 40], size and density dispersivity [83, 40, 57, 235], size polydisperse particles [86], and particles of different shapes [132].

The remainder of the chapter is organized as follows: Section 7.2 describes the DEM simulation method; Section 7.3 examines the simulation results and develops necessary kinematic scalings for the continuum model; Section 7.4 details the continuum model
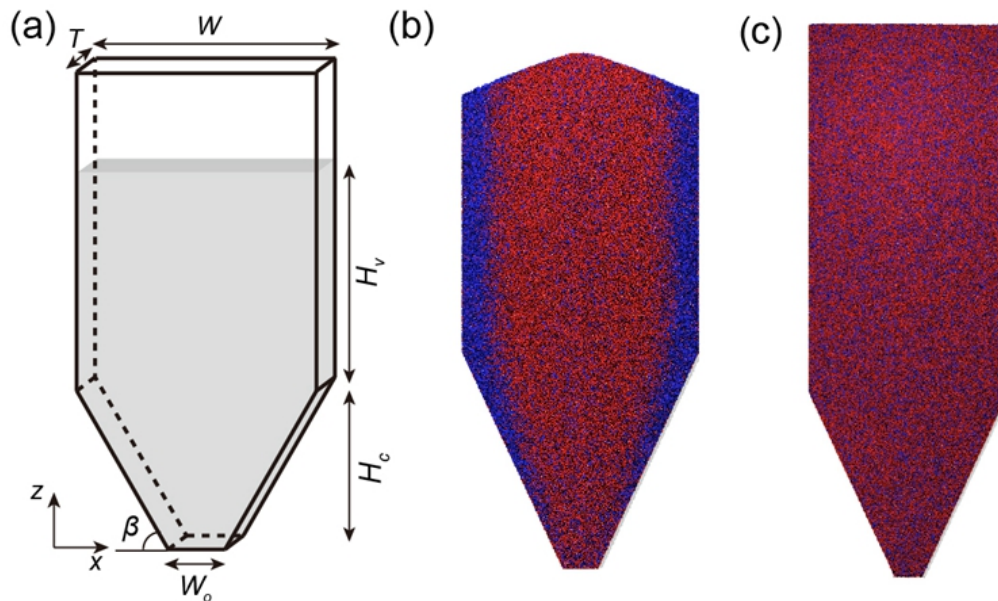
Figure 7.1. Quasi-2D hopper setup. (a) Schematic of a quasi-2D hopper. (b) Snapshot of the segregated initial condition after center filling from a DEM simulation with $W = 0.4\,\text{m}$, $W_o = 0.06\,\text{m}$, $\beta = 65°$, and $H_c + H_v = 0.84\,\text{m}$. (c) Snapshot of a mixed initial condition from a DEM simulation with $W = 0.4\,\text{m}$, $W_o = 0.06\,\text{m}$, $\beta = 65°$, and $H_c + H_v = 1.1\,\text{m}$.

for hopper discharge flow and compares the model prediction with DEM simulation and experimental results; and Section 7.5 presents the conclusions.

7.2. DEM Simulations

7.2.1. DEM simulation model and post processing method

DEM simulations were performed to study segregation and kinematics of the flow during discharge of a quasi-2D hopper. Figure 7.1a illustrates the geometry of a quasi-2D hopper with width W, outlet width W_o, gap thickness T, and hopper half width $L = W/2$. Like typical industrial hoppers, the quasi-2D hopper consists of an upper part (vertical section) with vertical sidewalls and a lower part (converging section) with sidewalls inclined at an angle β from horizontal. The height of the lower section is $H_c = 1/2(W - W_o)\tan\beta$, and the initial filling height of the vertical section is H_v. When the free surface of the

initial condition is not flat, as results from center filling, H_v is set to the value of a flat surface case that has the equivalent volume. Similar to previous studies of quasi-2D hopper filling [40, 20, 65, 57, 146], all sidewalls are frictional, which allows comparison between the simulation results and experiments [228, 236]. The origin of the global 2D coordinate system is selected such that the origin is fixed at the lower-left corner of the system with x horizontal and z vertical.

A previously experimentally-validated in-house DEM code is used for the simulations [21, 86, 57]. To model the flow, the translational and rotational momenta of the constituent particles are tracked by integrating Newton's second law. For particle interactions, the normal contact force is specified by a linear spring dashpot model [21, 72, 119], namely $\boldsymbol{F}_{ij}^n = [k_n \epsilon_n - 2\gamma_n m_{eff}(\boldsymbol{V}_{ij} \cdot \hat{\boldsymbol{r}}_{ij})] \hat{\boldsymbol{r}}_{ij}$, where the overlap and the relative velocity between two contacting particles i and j are ϵ_n and $\boldsymbol{V}_{ij}$, respectively, the unit normal vector between the two particles is $\hat{\boldsymbol{r}}_{ij}$, and $m_{eff} = m_i m_j / (m_i + m_j)$ is the effective mass. The restitution coefficient, e, and the binary collision time, t_c, are related to the spring stiffness and damping by $k_n = [(\pi/t_c)^2 + \gamma_n^2] m_{eff}$ and $\gamma_n = -\ln e / t_c$. In the tangential direction, the contact force is modeled as $\boldsymbol{F}_{ij}^t = -\min\left(|k_s \epsilon_t|, |\mu \boldsymbol{F}_{ij}^n|\right) sgn(\epsilon_t)\hat{\boldsymbol{s}}$, which is a combination of a linear spring model and Coulomb friction [21, 119]. In this relation, $k_s = \frac{2}{7}k_n$ is the tangential stiffness and μ is the friction coefficient. The tangential displacement is $\epsilon_t = \int\limits_{t_s}^{t} \boldsymbol{V}_{ij}^s dt$, where t_s is the initial contact time. $\boldsymbol{V}_{ij}^s$ is the relative tangential velocity and the unit vector in the tangential direction is $\hat{\boldsymbol{s}}$. For particle-wall contact, the same force models are applied where the wall is modeled as a sphere of infinite mass and radius. For all simulations, the binary collision time is $t_c = 1 \times 10^{-4}$ s, the restitution coefficient is $e = 0.8$, and the friction coefficient is $\mu = 0.4$. These values accurately simulate surface flows of glass particles [21, 40, 65, 86]. The simulation time step is set to $t_c/40$, which ensures numerical stability for gravity driven shear flows [21, 40, 57, 120].

To study segregation during hopper discharge, a size bidisperse mixture of equal volumes of large and small particles is simulated. Particle sizes are $d_l = 3$ mm and $d_s = 1.5$ mm for large and small particles, respectively, and a uniform distribution within $\pm 10\%$ of the particle diameter is added to both species to prevent particle ordering in

segregated phases. The density of the particles is $\rho = 2500 \,\text{kg/m}^3$. To generate the initial condition prior to discharge, two methods are used. The first method is center filling, in which particles are dropped at the center of the hopper at a 2D volumetric feed rate q_f [20, 175, 224]. This is a typical industrial case, and an example is shown in Fig. 7.1b, which exhibits heap segregation with more small particles (red) deposited near the center and more large particles (blue) near the sidewalls [20]. The second method extends the width of the feed stream to the hopper width (W). As a result, no heap forms during filling, thus generating an approximately well-mixed packing of the mixture (Fig. 7.1c), as in previous studies using well-mixed initial conditions [226, 64, 225, 228]. While the second filling mechanism is not practical in industry, it helps isolate the segregation that occurs only as a result of the discharge flow [228]. Various simulations with different hopper widths, opening sizes, and bottom angles are performed for both initial conditions. A constant gap thickness $T = 0.012 \,\text{m}$ is used for all cases. In our DEM simulations, the discharge flow can be configured to either mass flow or funnel flow with large velocity gradients in the $x-$direction. In both scenarios, segregation during discharge is a concern. The dimensions of the simulated systems, with a width of about $0.5 \,\text{m}$ and a height of about $1 \,\text{m}$, are comparable to small industrial hoppers. Approximately one million particles are simulated in the hopper.

In DEM simulations, particle positions and velocities are recorded every $0.01 \,\text{s}$ and used to calculate c_i and $\boldsymbol{u}$ using a local averaging method [237, 238, 236]. At a location $\boldsymbol{r}$ inside the hopper, the total local solids volume fraction is calculated as

$$(7.4) \qquad f(\boldsymbol{r}, t) = \frac{1}{\pi r_c^2 T} \sum_{i=1}^{N} V_i,$$

where $V_i = \pi d_i^3 / 6$ is the volume of each of the N particles whose center is within a cutoff radius $r_c = 1.5 d_l$ at time t and the average is calculated across the gap thickness T. The species volume fraction, f_i, is also found using equation Eq. 7.4 by considering the specified species only. To determine the local velocity $\boldsymbol{u}$, we use a Gaussian weighting

function, $\Phi\left[\boldsymbol{r}-\boldsymbol{r}_i(t)\right]=\exp\left(-|\boldsymbol{r}-\boldsymbol{r}_i(t)|^2/2\omega^2\right)$, with an rms width of $\omega=0.5d_l$ [236], which gives

$$(7.5) \qquad \boldsymbol{u}(\boldsymbol{r},t)=\frac{\sum_{i=1}^{N}\boldsymbol{u}(t)_i V_i\Phi\left[\boldsymbol{r}-\boldsymbol{r}_i(t)\right]}{\sum_{i=1}^{N}V_i\Phi\left[\boldsymbol{r}-\boldsymbol{r}_i(t)\right]},$$

where $\boldsymbol{r}_i(t)$ is the position of each particle inside the cutoff radius at t. Particle radii of the discharged materials are recorded during discharge, so that the volumetric discharge rate q_d and the volume concentration of the discharged materials can be calculated. Both the DEM simulations and the post processing are performed on an Nvidia GTX 1080 GPU (Graphics Processing Unit) [65].

7.2.2. Validation of DEM simulations

While the DEM code used here has been validated in several previous studies [21, 40, 57], we provide further validation to demonstrate that the simulation results for hopper discharge agree with existing scalings and experimental results, as shown in Fig. 7.2. First, we compare the 2D discharge rate q_d (3D volumetric discharge rate divided by the gap thickness) with the Beverloo equation [239, 236, 240]:

$$(7.6) \qquad q_d=C\sqrt{g}(W_o-k\bar{d})^{N_d-1/2}/[\tan\left(\pi/2-\beta\right)]^n,$$

where $\bar{d}=(d_l+d_s)/2$ is the arithmetic mean particle diameter. Constants $C=0.58$ and $k=1.5$ are selected according to previous studies [239, 240], and $N_d=2$ for two-dimensional systems [239, 236]. The term $(\tan\left(\pi/2-\beta\right))^n$ is a correction for angled bottom walls with $n=0.35$ [240]. For each simulation, the discharge rate, which is measured as the slope of the linear region in the relation between the discharged volume V_{dis} versus t (Fig. 7.2a inset), stays nearly constant for most of the discharge duration, consistent with previous results [241]. The discharge rate q_d measured for all simulations is plotted in Fig. 7.2a along with the Beverloo scaling [Eq. (7.6)]. The DEM results agree well with the Beverloo scaling, demonstrating that the DEM simulations accurately
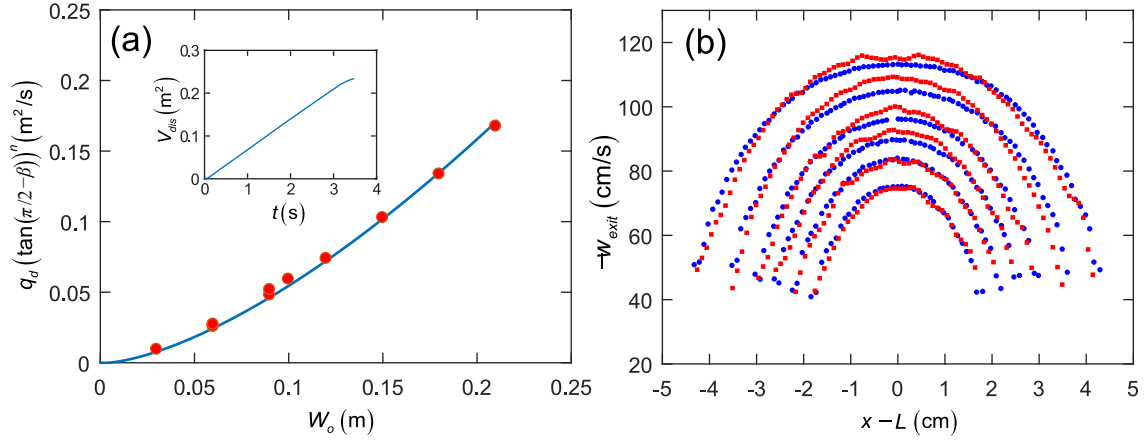
Figure 7.2. Validating the DEM simulation. (a) Comparison of the opening angle corrected discharge rate vs. the size of the hopper opening between DEM simulation results (red circles) and Beverloo's equation (solid curve) [**239**]. Inset: discharged volume normalized by gap thickness T vs. time for a single DEM simulation with $W_o = 0.1\,\mathrm{m}$ and $\beta = 60°$. (b) Comparison of vertical velocity profiles at the exit from experimental measurements (blue circles) by Gella *et al.* [**236**] with DEM simulation results (red squares) for W_o =8.92 cm, 7.62 cm, 6.32 cm, 5.58 cm, 4.74 cm, and 3.92 cm.

capture the discharge dynamics. Note that recent studies show that the discharge rate of a size bidisperse mixture depends weakly on the volume fraction ratio of the two species [**242, 243**]. Here, we do not observe this effect as we only examine an equal volume mixture.

We also compare our DEM results with experiments conducted in flat bottom hoppers using monodisperse 4 mm stainless steel spheres [**236**]. To match the experimental conditions, the simulation geometry is modified to $W = 0.61\,\mathrm{m}$, $\beta = 0$, and $T = 0.004\,\mathrm{m}$, and particle properties are adjusted to $d = 4\,\mathrm{mm}$, $\rho = 7800\,\mathrm{kg/m^3}$, $e = 0.8$, $\mu = 0.45$, and $t_c = 1 \times 10^{-4}\,\mathrm{s}$. Six simulations with different opening widths W_o are performed to compare the time-averaged vertical velocity profiles at the exit, $w_{exit} = w(z = 0)$. The simulation data matches the experimental results well for all six cases, as shown in Fig. 7.2b, which further demonstrates that our DEM simulations accurately reproduce the kinematic details of the hopper discharge process.

7.3. Segregation during hopper discharge

We first focus on hopper discharge with a well-mixed initial condition [**228, 226, 64, 225**], so that it is easier to identify the segregating region when the local species volume concentrations deviate from the well-mixed initial condition. Figure 7.3 shows an example of a hopper discharge process using the DEM simulation with a well-mixed initial condition and flat free surface. At $t = 0$, the volume concentration of large particles is around 0.5 in the entire hopper with some small random fluctuations. After the outlet opens, the top free surface quickly develops a V-shape (already evident at $t = 1\,\text{s}$), which agrees with observations from previous experiments and simulations [**228, 244, 245**]. At this point, no significant segregation has occurred. However, after the V-shape forms on the surface, segregation starts to appear near the free surface, with large particles concentrated on the surface near the bottom of the V-shape ($t = 3\,\text{s}$). This segregated large particle enriched region grows to a narrow vertical band along the centerline of the hopper as particles move toward the outlet. This band is "sandwiched" by small particle enhanced regions (light blue) on both sides, which also extend toward the outlet (t=5.0 s and t=8.0 s). Other regions of the hopper except for the thin surface flowing layer and the center downflow region remain mixed during discharge. This segregation pattern persists even when the free surface reaches the converging flow region (t=10.0 s). The segregation pattern occurs for other flow conditions including different outlet sizes, hopper widths, and bottom angles.

These observations from the DEM simulations suggest that segregation is initiated in the flowing layer near the free surface, so we first focus on the flow kinematics in this region, as shown Fig. 7.4. Due to the symmetric nature of the hopper flow with respect to its centerline, only the left half of the hopper is investigated. The instantaneous velocity field in Fig. 7.4a shows a strong streamwise velocity gradient in the depth direction along the entire length of the flowing layer, similar to other free surface flows such as inclined chute flows [**55, 68, 60, 164**], tumbler flows [**91, 124, 83**], and heap flows [**54, 44, 224, 20**], indicating strong shear in the surface flowing layer. Near the hopper centerline (right side of the image), the streamwise velocity becomes vertical. Deeper in the bulk
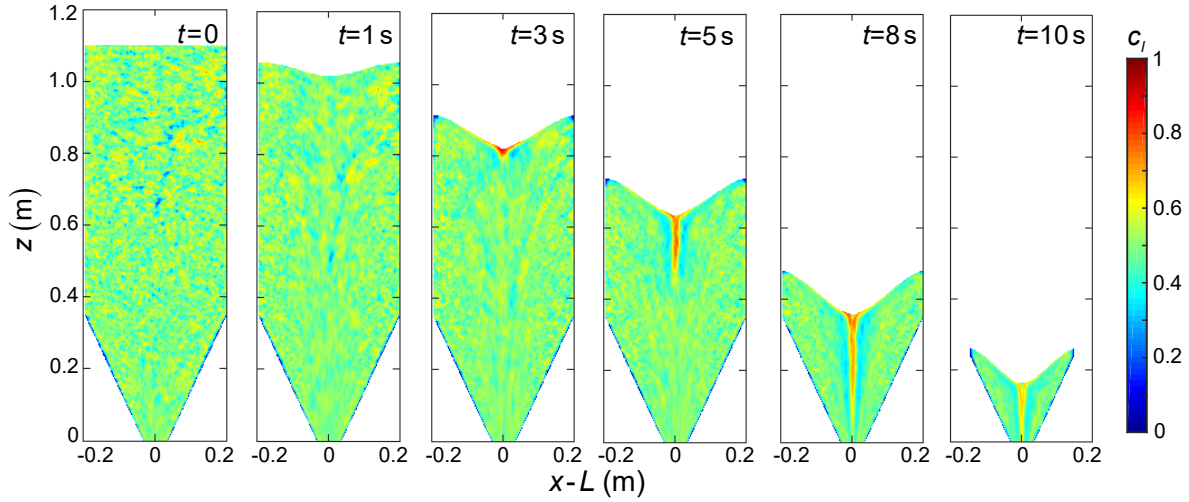
Figure 7.3. Concentration of large particles using a mixed initial condition from DEM simulations at different states of hopper discharge with $W = 0.4\,\mathrm{m}$, $W_o = 0.06\,\mathrm{m}$, $\beta = 65°$, $H_c + H_v = 1.1\,\mathrm{m}$, $d_l = 3\,\mathrm{mm}$, $d_s = 1.5\,\mathrm{mm}$, and $q_d = 0.034\,\mathrm{m^2/s}$.

region beneath the surface layer, the velocity vectors are mostly vertical and are directed approximately toward the outlet. The velocity magnitude is largest in the center of the hopper and smallest adjacent to the wall [23, 230]. Note that the velocity magnitude near the sidewall is close to zero, which is a typical funnel flow scenario. Unlike heap and chute flows where particles are continuously added in the upstream region to sustain the flow [20, 55] or rotating tumbler flow where particles recirculate back to the flowing layer through the solid body rotation [83], the hopper discharge process has no external source of new particle addition or particle recirculation. Instead, as particles in the surface flowing layer flow out of the hopper through the fast flow center region, the free surface level continuously decreases. As a result, particles under the surface flowing layer are exposed to the surface flowing layer and start to flow toward the center region of the hopper. This process continues until all particles are discharged from the hopper. Because of the strong shear in the surface flowing layer during hopper discharge, percolation is the dominant segregation mechanism [55]. When particles flow from the sidewall of the hopper toward the center in the surface flowing layer, small particles segregate to the
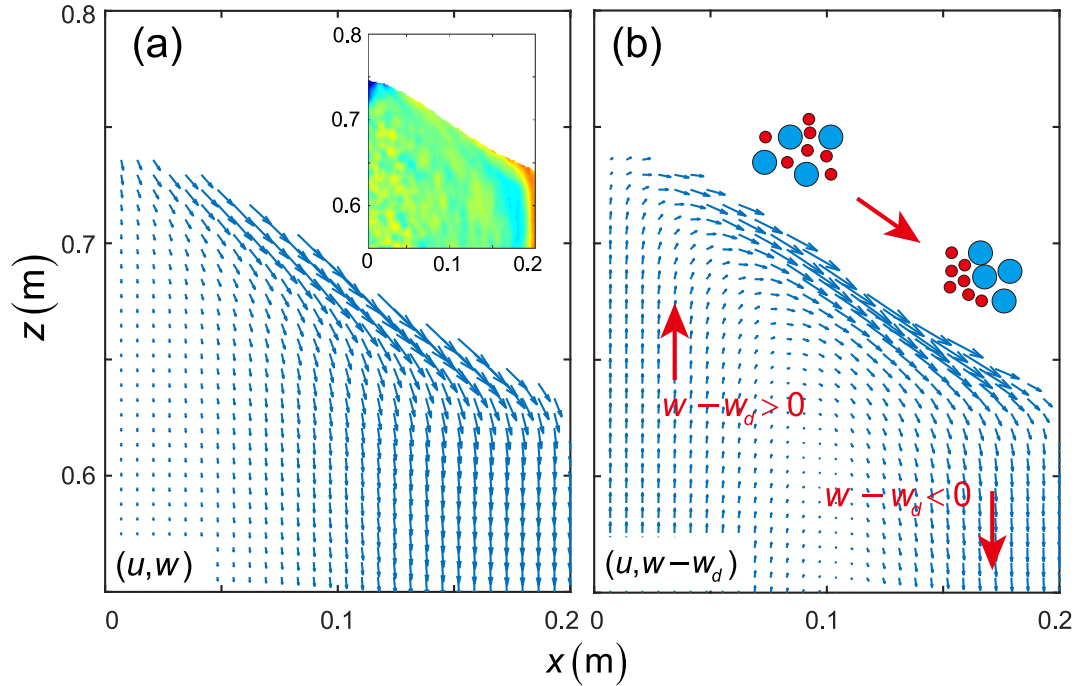
Figure 7.4.   The mean velocity field near the free surface (left side) at $t = 5\,\text{s}$ during the same discharge process shown in Fig. 7.3. (a) Mean velocity field (u, w). Inset shows the corresponding large particle concentration using the same color scheme as in Fig. 7.3. (b) Mean velocity field relative to the free surface $(u, w - w_d)$, where $w_d = -0.086\,\text{m/s}$.

bottom region of the surface layer, and large particles segregate to the free surface, as shown in the inset of Fig. 7.4a. These segregated layers from the left and the right of the hopper combine and reorient to the vertical direction after entering the fast flow center region of the hopper to form the sandwich-like segregated pattern shown in Fig. 7.3 (t=5.0 s and t=8.0 s).

To better demonstrate how particles enter the surface layer, we plot the velocity field $\boldsymbol{u}_r = u\hat{\boldsymbol{x}} + w_r\hat{\boldsymbol{z}}$ relative to the descending free surface in Fig. 7.4b, where $w_r = w - w_d$ and w_d is the surface descent velocity. When the free surface is in the vertical sidewall section of the hopper with an approximately constant incline angle α, the surface descent velocity is uniform along the surface flowing layer and can be approximated as $w_d = -q_d/W$. Near the sidewall, particles in the bulk region move downward slower than the surface does

($w_r > 0$), so their velocities relative to the surface are upward. Thus, they eventually enter the surface flowing layer, and segregate when they flow along the surface layer toward the hopper center. In the center region, particles move downward faster than the free surface ($w_r < 0$), so their relative velocities are downward toward the hopper outlet, meaning that they flow away from the surface layer. The way that particles enter, segregate, and exit the surface flowing layer during hopper discharge in this moving coordinate system (Fig. 7.4b) is similar to that in rotating tumbler flow [83], except that it is the solid body rotation in tumblers that recirculates particles in and out of the flowing layer. Of course, this flow pattern evident in the moving coordinate system results from the vertical velocity difference across the hopper width. No particles actually move upward during hopper discharge in the lab coordinate system (Fig. 7.4a). Note that based on the velocity field in Fig. 7.4a, this flow can be classified as a funnel flow [227]. However, we do not explicitly differentiate funnel and mass flow, as this velocity difference from the sidewall to the center of the hopper exists in most practical situations for both flow modes [227]. In the rare case of a plug flow, there is no velocity difference so there is no shear to drive segregation, which can be considered as a limiting case for this phenomenon.

The above discussion of the velocity field and segregation pattern in the surface layer and bulk region is not limited to the well-mixed initial condition. It also applies to the initially segregated condition resulting from heap segregation during hopper filling, shown in Fig. 7.5. The segregated pattern due to hopper filling is evident at $t = 0$. More large particles are deposited near the sidewalls, and more small particles are deposited closer to the center with mixed particles in the feed zone at the centerline of the hopper, similar to previous studies of heap segregation [20, 40, 54, 224]. When the hopper discharge process begins, the free surface becomes V-shaped (t=1.5 s), and large particles start to segregate to the hopper center region (t=3 s, t=4 s, t=5.5 s, and t=6.5 s). This is similar to the well-mixed initial condition in Fig. 7.4, where particles from the more slowly descending region ($w - w_d > 0$) near the sidewall move toward the faster descending region ($w - w_d < 0$) near the hopper center through the surface flowing layer where segregation occurs. However, for the segregated initial condition, large particles dominate the sidewall
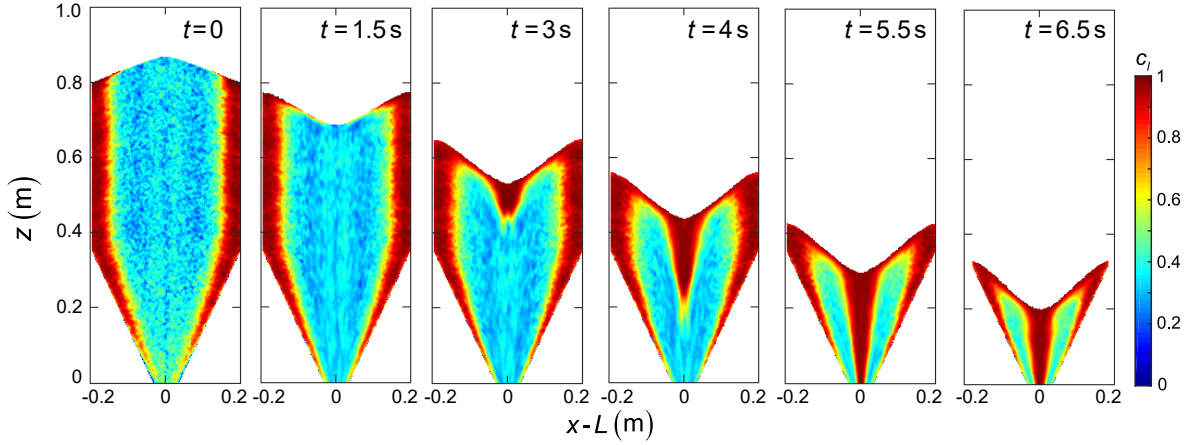
Figure 7.5. Concentration of large particles during hopper discharge from DEM simulations with a segregated initial condition (center filled with $q_f = 0.0024 \, \text{m}^2/\text{s}$) with $W = 0.4 \, \text{m}$, $W_o = 0.06 \, \text{m}$, $\beta = 65°$, $H_c + H_v = 0.84 \, \text{m}$, $d_l = 3 \, \text{mm}$, $d_s = 1.5 \, \text{mm}$, and $q_d = 0.033 \, \text{m}^2/\text{s}$.

region before entering the surface layer; consequently, the segregation pattern observed in Fig. 7.5 results from the combined effects of the segregation during both filling and discharge. As a result, the degree of segregation in the hopper center during discharge is much stronger than that for the mixed initial condition (Fig. 7.3).

7.4. Continuum modeling of hopper discharge segregation

7.4.1. Flow kinematics

7.4.1.1. Velocity profiles in the bulk. To use the continuum segregation model in Eqs. (7.1) and (7.2), the velocity fields in the surface flowing layer and the bulk are needed. The kinematics of hopper discharge flow are relatively complicated [23] compared to other free surface flows such as heap flow or rotating tumbler flow, so there are no standard velocity fields in the existing literature. Consequently, we use DEM simulations along with an existing kinematic model to develop an expression for these velocity fields. This approach ensures that we capture the key characteristics related to segregation but with less computational complexity when compared with recent work using continuum approaches to solve the velocity fields in hopper discharge flow [233, 245, 246, 247].

A kinematic model [**230, 232, 248, 249, 228, 4**] can capture the velocity field in both vertical and converging sections of the hopper, using the constitutive relation

$$(7.7) \qquad u = -b\frac{\partial w}{\partial x},$$

where b is a kinematic parameter with dimensions of length. This relation is based on the assumption that the horizontal velocity component is proportional to the horizontal gradient of the vertical velocity component (horizontal shear) [**230, 232**]. During discharge, the flow also satisfies the continuity equation,

$$(7.8) \qquad \frac{\partial u}{\partial x} + \frac{\partial w}{\partial z} = 0$$

when the bulk solid is considered incompressible as a first order approximation. Note that the variation of packing density due to the local concentration change and to the dilatation near the hopper outlet is neglected. Combining Eqs. (7.7) and (7.8), results in an equation for the vertical velocity:

$$(7.9) \qquad \frac{\partial w}{\partial z} = b\frac{\partial^2 w}{\partial x^2}.$$

Equation (7.9) is similar to a diffusion equation (consider the vertical direction as time), so that when the vertical velocity profile at the hopper outlet is specified, the vertical velocity "diffuses" upward. For the vertical velocity profile at the outlet, i.e., the bottom boundary condition, we assume a uniform outlet velocity profile, $w(x,0) = q_d/W_o$, so that no additional parameters are needed [**230, 250**]. Note that this assumption is neglecting the variation of the velocity at the exit (Fig. 7.2b). However, this assumption is acceptable, because the model prediction is not sensitive to the bottom boundary condition except for regions very close to the outlet [**230**]. For the boundary conditions at the sidewalls, the velocity must be parallel to the sidewall, $u\hat{n}_x + w\hat{n}_z = 0$, where $(\hat{n}_x, \hat{n}_z)$ is the unit normal vector at the boundary [**250**]. In this way, the model is applicable to both the converging and the vertical sections of the hopper, and predictions can be made for
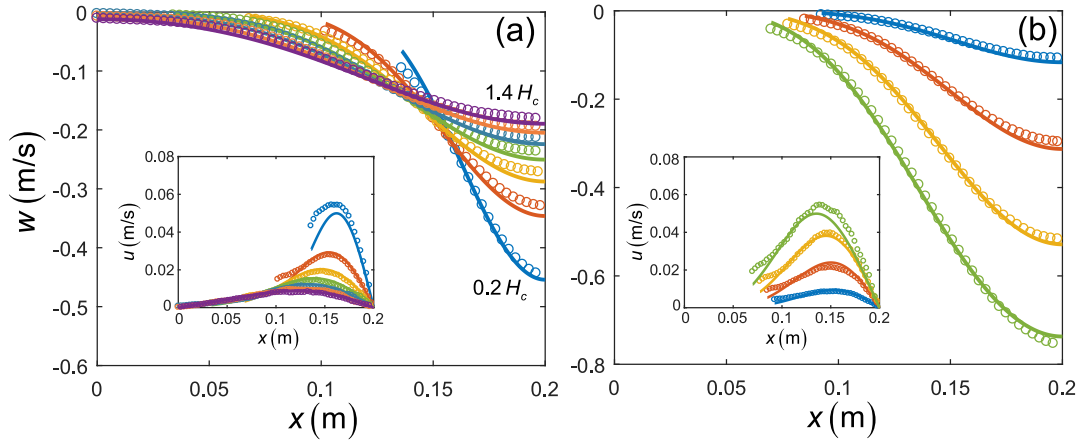
Figure 7.6. Vertical and horizontal (insets) velocity profiles of the left half of the hopper from DEM simulations (circles) and corresponding kinematic model predictions (curves). (a) Velocity profiles from DEM and model predictions for a single case with $W = 0.4\,\text{m}$, $W_o = 0.06\,\text{m}$, and $\beta = 65°$. Profiles at different heights $0.2H_c$, $0.4H_c$, $0.6H_c$, $0.8H_c$, $1.0H_c$, $1.2H_c$, and $1.4\ H_c$ are plotted in different colors. (b) Velocity profiles at $z = 0.5H_c$ for four cases with different outlet sizes: $0.03\,\text{m}$ (blue), $0.06\,\text{m}$ (red), $0.09\,\text{m}$ (orange), and $0.12\,\text{m}$ (green). For all cases, $W = 0.4\,\text{m}$ and $\beta = 65°$.

various hopper widths, bottom angles, and outlet sizes. We solve the velocity field in the bulk region numerically following the approach used in [**250**]. To determine the value of b, we note that previous studies found that b ranges from $1.5d$ to $4d$, where d is the particle diameter [**230, 249, 248, 250, 228**], and that the model predictions are relatively insensitive to the specific choice of b. In this study, we use a constant $b = 3\bar{d}$, which gives relatively good agreement with all DEM simulation results as demonstrated below.

Figure 7.6a compares the velocity profiles at different heights between one DEM simulation and the model prediction from Eq. (7.9). Note that we again only consider the left half of a hopper due to its symmetry. At all heights, the model prediction matches well with DEM simulation results. The agreement is imperfect for the horizontal velocity profile at $z = 0.2H_c$ (Fig. 7.6a), probably as a result of assuming a uniform bottom outlet velocity profile as discussed above. Figure 7.6b further validates the kinematic model at four different hopper outlet sizes. Here, only velocity profiles at $z = 0.5H_c$ are shown, while velocity profiles at other $z-$locations also match well.

7.4.1.2. Velocity profiles for the surface flowing layer. As discussed in previous studies [**228, 250**], this kinematic model does not capture the velocity field near the free surface because no top boundary is specified in this model. To resolve this issue, we construct the velocity field in the surface flowing layer separately using information from the kinematic model for the bulk and observations from DEM simulations for the surface flowing layer. Here, we only consider the situation where the surface layer is within the vertical section of the hopper. At any horizontal location x, the largest horizontal velocity occurs at the free surface, and the velocity decreases in the depth direction z. We define thickness of the surface flowing layer, δ, as the distance from the free surface, $z_s(x)$, to the bottom of the surface layer, $z_b(x)$. The location of the bottom of the flowing layer is defined to be where $u = 0.1u_s$ [**21**], where u_s is the horizontal velocity at the free surface. Following the approach used previously for bounded heap flow, we plot u/u_s versus z/δ at different x in Fig. 7.7a, which collapses all data into a single curve that can be well approximated by $u/u_s = \exp\left[k(z - z_s)/\delta\right]$ [**40, 57, 132**]. The measured δ from DEM simulations is shown in the inset of Fig. 7.7a, and is between 10 and 20 average particle diameters for most of the surface layer, consistent with previous studies [**228**].

To construct the surface layer kinematics, we assume a constant flowing layer thickness, $\delta = 15\bar{d}$, as a first order approximation and also assume that the free surface is flat with a constant slope α throughout the discharge process (see Figs. 7.3 and 7.5). Setting the position of the upper-left corner of the surface layer to (x_0, z_0), the surface and the bottom of the surface layer can be expressed as $z_s = z_0 - x\tan\alpha$ and $z_b = z_0 - x\tan\alpha - \delta$, respectively. To derive the local horizontal flux profile, $q_x(x)$, in the surface layer, a mass balance equation is applied,

$$(7.10) \qquad \frac{\partial q_x}{\partial x} = w_{rb} + u_b \tan\alpha,$$

where u_b and $w_{rb} = w_b - w_d$ are the horizontal and relative vertical velocity at z_b, respectively. This relation results from the particle exchange between the surface layer and the bulk region, as demonstrated in Fig. 7.4b. For the boundary condition at the sidewall $(x = 0)$, we use $q_x(0) = 0$, because no flux enters from the sidewall. To match the flux
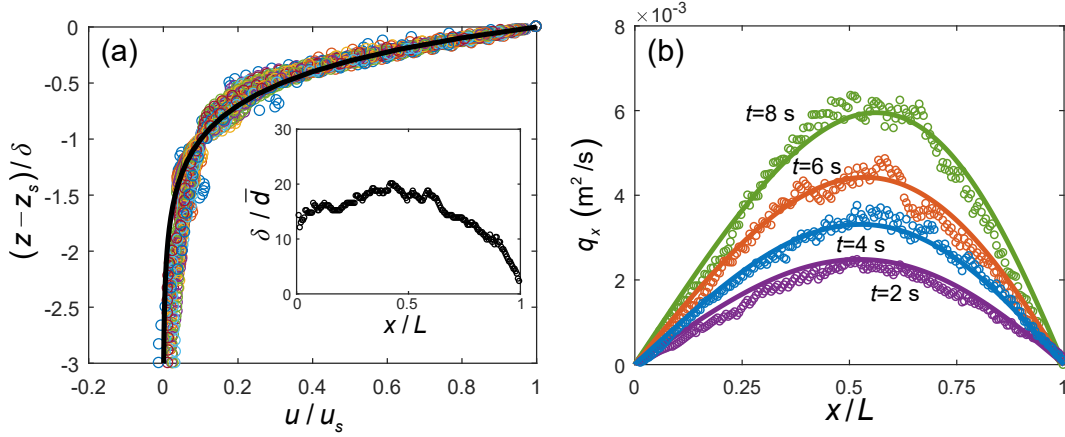
Figure 7.7. Instantaneous kinematics in the surface layer at $t = 6\,\mathrm{s}$ in a discharge process with $W = 0.4\,\mathrm{m}$, $W_o = 0.06\,\mathrm{m}$, and $\beta = 65°$. (a) Scaling of the horizontal velocity profiles vs. depth in the surface layer at horizontal locations at increments of $1\,\mathrm{mm}$ in the horizontal direction (different colored circles) measured in the DEM simulation. The solid curve is $\exp(k(z - z_s)/\delta)$. Inset: local surface layer thickness across hopper width. (b) Horizontal flux profile across hopper width from DEM simulation (circles) and the constructed surface kinematics (solid curves) at $t = 2\,\mathrm{s}$, $4\,\mathrm{s}$, $6\,\mathrm{s}$, and $8\,\mathrm{s}$.

at the bottom of the surface layer, u_b and w_b are specified using predictions at $z_b(x)$ from the kinematic model for the bulk region. In this way, Eq. (7.10) can be integrated for the horizontal flux profile $q_x(x)$ from the wall to the centerline of the hopper. An example of the calculation results at different time instants is shown in Fig. 7.7b, which agrees well with measurements from the corresponding DEM simulation and gives $q_x(x = L) = 0$ at the hopper center as required by symmetry. The match between DEM simulation and the flux calculated from Eq. (7.10) for other conditions is similar. Note that although time does not explicitly appear in the above calculations, as the surface layer moves downward, its bottom continually encounters different u_b and w_b from the bulk region at different heights. Thus, the kinematics in the surface layer are constantly evolving during discharge.

To this point, to derive the horizontal velocity profile $u(x, z)$ in the surface layer, we have specified q_x, u_b, and the scaling, $u/u_s = \exp(k(z - z_s)/\delta)$. However, mathematically,
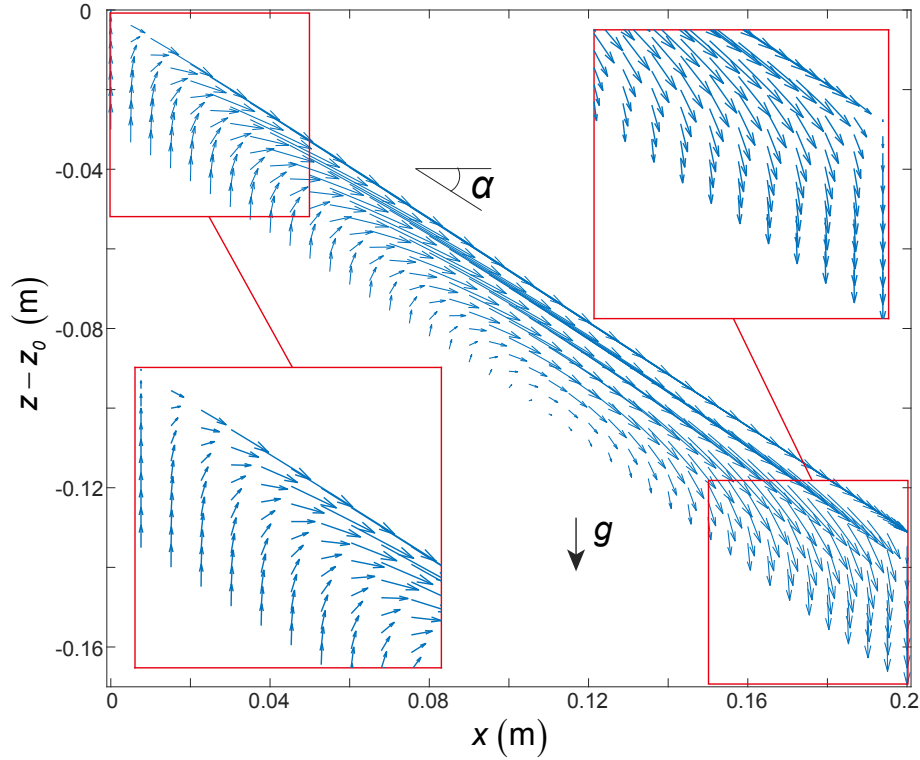
Figure 7.8. The model surface layer relative velocity field $\boldsymbol{u}_r = u\hat{\boldsymbol{x}} + w_r\hat{\boldsymbol{z}}$ constructed from Eqs. (7.11) and (7.12) for the same case as Fig. 7.7.

we can only use either q_x or u_b to derive the horizontal velocity assuming an exponential profile with a constant δ, so specifying all three parameters is redundant. To address this, we propose the following functional form for u,

$$(7.11) \qquad u(x,z) = M(q_x - u_b\delta)(e^{k(z-z_s)/\delta} - e^{-k}) + u_b,$$

where $M = \frac{k}{\delta(1-(1+k)e^{-k})}$. This profile satisfies $q_x = \int_{z_b}^{z_s} u\,dx$ and $u = u_b$ at $z = z_b$. The relative vertical velocity in the surface layer can be derived from continuity [Eq. (7.8)] by replacing w with w_r and using the horizontal velocity profile in Eq. (7.11), which yields

$$(7.12) \quad w_r(x, z) = -M \left(\frac{\partial q_x}{\partial x} - \delta \frac{\partial u_b}{\partial x} \right) \left[\frac{\delta}{k} \left(e^{k(z-z_s)/\delta} - e^{-k} \right) - (z - z_b)e^{-k} \right]$$

$$+ M(q_x - u_b \delta) \frac{\partial z_s}{\partial x} \left(e^{k(z-z_s)/\delta} - e^{-k} \right) - \frac{\partial u_b}{\partial x}(z - z_b) + w_{rb}.$$

This profile ensures that $w_r = w_{rb}$ at $z = z_b$ and $w_r/u = \partial z_s/\partial x$ at $z = z_s$, meaning that the relative velocity direction is parallel to the free surface, so there is no flux perpendicular to the free surface.

The velocity field expressions in the moving coordinate system [Eqs. (7.11) and (7.12] capture all the important kinematic features of the surface flowing layer, as shown in Fig. 7.8, which matches well with the DEM simulations in Fig. 7.4b. Thus, the velocity field of the surface flowing layer defined by Eqs. (7.11) and (7.12) serves as a "closure" for the kinematic model developed for the bulk region [**230**], which provides necessary information to solve the continuum segregation model, as discussed below.

7.4.2. Continuum model for hopper discharge flow

In this section, we formulate the continuum model for the hopper discharge process. Because most of the segregation occurs in the surface layer, the modified transport equation [Eq. (7.1)] is only applied to the surface layer. For the bulk region, the standard advection-diffusion equation with no segregation describes the transport of material into and out of the bulk region as discussed previously. Material at the interface between the surface layer and the bulk region is exchanged continuously during the discharge process, as depicted in Fig. 7.9a. Thus, the entire discharge process is modeled as a transient moving boundary problem.

To capture advection, segregation, and diffusion inside the surface layer, the continuum model [Eq. (7.1)] is applied. Here, just like heap flow and tumbler flow [**40, 83, 76**], the segregation term in Eq. (7.1) is one dimensional and acts normal to the free surface. Equation (7.1) can be solved more readily by establishing a moving coordinate system with its origin at the upper-left corner of the surface flowing layer, (x_0, z_0), the streamwise
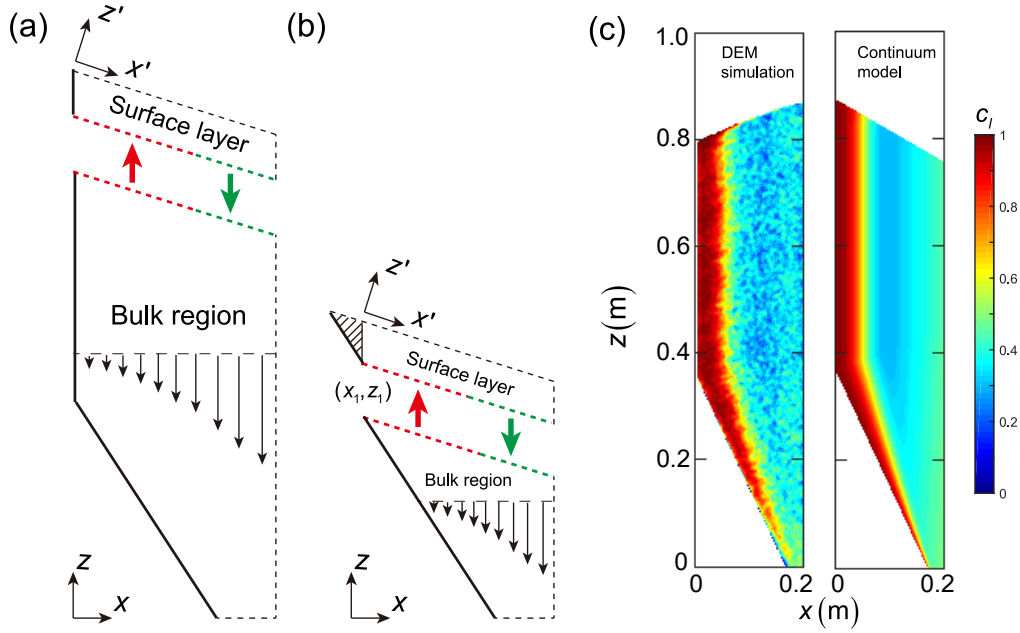
Figure 7.9. Continuum modeling of segregation during hopper discharge. (a, b) Schematic of the coupling between the surface layer and the bulk region for (a) vertical and (b) converging sections of the hopper. (c) Comparison of the initial condition generated by the continuum model and the corresponding DEM simulation for fill rate of $q_f = 0.0024\,\mathrm{m^2/s}$ with $W = 0.4\,\mathrm{m}$, $W_o = 0.06\,\mathrm{m}$, $\beta = 65°$, $H_c + H_v = 0.84\,\mathrm{m}$, $d_l = 0.003\,\mathrm{m}$, and $d_s = 0.0015\,\mathrm{m}$.

direction x' parallel to the free surface, and the normal direction z' perpendicular to the free surface, as shown in Fig. 7.9a. In this coordinate system that moves with the free surface, the new velocity field $\boldsymbol{u}'_r = u'\hat{\boldsymbol{x}}' + w'_r\hat{\boldsymbol{z}}'$ can also be defined, as $u' = u\cos\alpha - w_r\sin\alpha$ and $w'_r = u\sin\alpha + w_r\cos\alpha$. Accordingly, Eq. (7.1) becomes,

$$(7.13) \qquad \frac{\partial c_i}{\partial t} + \nabla \cdot (\boldsymbol{u}'_r c_i) + \frac{\partial}{\partial z'}(w_{s,i} c_i) - \frac{\partial}{\partial z'}\left(D\frac{\partial c_i}{\partial z'}\right) = 0.$$

Here, we only consider diffusion in the normal direction, as diffusion in the streamwise velocity is negligible compared to advection [40, 83, 57]. The segregation velocity $w_{s,i}$ is well-approximated by the semi-empirical relation Eq. (7.2).

163

The diffusion coefficient is determined from a scaling law related to the local shear rate and local particle size used in several previous studies [**40, 56, 161, 126**]:

$$D = C_D \dot{\gamma} \bar{d}^2,$$ (7.14)

where $C_D = 0.1$ for spherical particles and $\bar{d}$ is the average particle diameter [**161**]. In the rotated and moving reference frame, no particles pass through the left, top, and right boundaries of the surface layer, as the relative velocity field $\boldsymbol{u}'_r$ is parallel to these boundaries. To ensure no flux passes through these three boundaries, the segregation and diffusion fluxes are set equal [**40, 75**] at these boundaries:

$$w_{s,i} c_i = D \frac{\partial c_i}{\partial z'}.$$ (7.15)

At the bottom boundary, particles enter the surface layer where $w_{rb} + u_b \tan \alpha > 0$ (marked red in Fig. 7.9a) with their concentration equal to the concentration in the adjacent location at the top of the bulk region, which is a Dirichlet boundary condition. Thus, the species concentration from the bulk region is needed for the surface flowing layer to realize the particle exchange coupling discussed in Sec. 7.3. Particles leave the surface layer where $w_{rb} + u_b \tan \alpha < 0$ (marked green in Fig. 7.9a), and Eq. (7.15) is used as the outflow boundary condition [**40, 75**]. Finally, at the location (x_{bf}, z_{bf}) where $w_{rb} + u_b \tan \alpha = 0$, there is no vertical flux. Defining this location is helpful when the surface flowing layer is in the converging section, as discussed later.

For the bulk region, as no significant segregation is observed, the transport can be accurately described by an advection-diffusion equation:

$$\frac{\partial c_i}{\partial t} + \nabla \cdot (\boldsymbol{u} c_i) - \frac{\partial}{\partial x} \left(D \frac{\partial c_i}{\partial x} \right) = 0,$$ (7.16)

where we consider diffusion in the horizontal direction only, because vertical transport is dominated by advection towards the outlet. Here, the same scaling for D is applied

[Eq. (7.14)], except that the shear rate is now calculated using the shear in the horizontal direction $\dot{\gamma} = |\partial w/\partial x|$, which is much smaller than that in the surface flowing layer. Note that the lab coordinate system (x, y) is used in the bulk region. For the right and left boundaries (including both the converging and the vertical sections), the boundary condition $D\partial c_i/\partial x = 0$ is applied to ensure no flux through the boundaries. For the bottom boundary (the hopper outlet), no boundary condition is needed for the outflow. The top boundary, which is the interface between the surface flowing layer and the bulk region, is a moving boundary due to the material discharge.

By assuming constant free surface inclination and constant surface flowing layer depth, the instantaneous position of the interface can be calculated from mass conservation, based on the relation that the volume enclosed by the initial free surface position and the free surface position at time t is equal to the discharged volume $q_d tT/2$, considering the left half of the hopper only. In this way, the instantaneous interface position between the surface flowing layer and the bulk can be calculated through geometry, and the interface descent velocity can be calculated from the time derivative of the interface position. We define the particle velocity relative to the moving interface as $\boldsymbol{u}_{rt} = u_{rt}\hat{\boldsymbol{x}} + w_{rt}\hat{\boldsymbol{z}}$. Thus for the region where $w_{rt} + u_{rt}\tan\alpha > 0$, $D\partial c_i/\partial x = 0$, which is essentially the boundary condition for particles to leave the bulk region and enter the surface layer, as marked by the red region in Fig. 7.9a. For the region where $w_{rt} + u_{rt}\tan\alpha < 0$ (marked by green in Fig. 7.9a), a Dirichlet boundary condition is imposed to map the concentration at the bottom of the surface layer to the bulk. At location x_{tb}, z_{tb} where $w_{rt} + u_{rt}\tan\alpha = 0$ within the vertical section of the hopper, the surface descent velocity is vertical and equals $(0, w_d)$. Thus, $\boldsymbol{u}_{rt} = \boldsymbol{u}_r$, which makes (x_{tb}, z_{tb}) overlap (x_{bf}, z_{bf}), meaning that the boundary between the surface layer and the bulk region matches.

When the surface layer enters the converging section of the hopper, the kinematics in the surface layer are more complicated. Instead of being a parallelogram (Fig. 7.9a), the surface flowing layer contains an additional triangular region on the left due to the inclined sidewall, shown as the shaded area in Fig. 7.9b. The velocity profile in this small triangular region is hard to specify. Moreover, the shape of the surface layer deforms in the converging

section, so a moving boundary is needed. To address these challenges, we make a few simplifications to the model. First, we neglect the small triangular region and continue to model the surface layer as a parallelogram, because this region does not exchange particles with the bulk region due to the sidewall below it. Second, to avoid solving a moving boundary transient problem for the surface flowing layer, we solve Eq. (7.13) assuming steady conditions at the width, $L_c(t) = L - x_1(t)$ with constant surface layer depth δ for each time instant, where (x_1, z_1) is the instantaneous position of the lower-left corner of the surface layer. Furthermore, we set the bottom relative velocity of the surface layer to $u_r(x, z) = 0$ and $w_r(x, z) = w(x, z = z_1) + q_d/2L_c(t)$, which ensures that the flux in and out of the surface layer is equal, so that a steady solution can be obtained. This assumption introduces a small discontinuity in the velocity field at the interface. As shown later in this section, these assumptions result in reasonable predictions for the discharge profile with only a small influence at the very end of the discharge process, corresponding to a very small portion of the total particle volume. However, these assumptions are much easier to implement than the other possible approaches such as using momentum balance and a granular rheological relation [**36**].

The initially segregated condition is calculated by using the heap segregation continuum model [**40, 65**]. This approach only requires the hopper fill rate q_f, particle sizes, the filling surface angle, and silo width as inputs [**65**]. For each case, we solve the hopper filling model for both the vertical section and the converging section. An example continuum model result for hopper filling segregation is shown in Fig. 7.9c along with the corresponding DEM simulation result, showing good agreement. For the well-mixed initial conditions, the concentration of each species is set to be uniform throughout the entire hopper. For simplicity, we neglect the initial transients before the V-shape develops. The V-shape typically develops quickly as shown in Figs. 7.3 and 7.5, so it has minimal influence. The free surface angle (angle of repose) during discharge, α, used in the continuum model is assumed to be a constant angle $\alpha = 30°$, which matches the quasi-2D DEM simulations in this study. Note that α could be influenced by factors such

as particle shape, friction coefficient, and hopper geometry in other systems and should be set accordingly. The discharge rate q_d is calculated using Eq. (7.6).

To solve the model, we use an in-house solver based on the Finite Element Method (FEM) approach, because it efficiently handles the non-rectangular geometry of the surface flowing layer and the bulk region [**251, 252**]. At each time step, we first solve Eq. (7.13) for the surface layer with the concentration at its bottom specified from that in the bulk region. Implicit time integration with Newton-Raphson iteration is used to handle the nonlinearity introduced by the segregation term. Then we solve Eq. (7.16) for the bulk region with the concentration at its top boundary obtained from the surface flowing layer to realize the particle exchange between the two regions. The Arbitrary Eulerian Lagrangian (ALE) method is implemented to handle the moving boundary for the bulk region and the Streamline Upwind Petrov Galerkin (SUPG) method is implemented for stabilizing advection dominated regions [**253, 254, 255, 256**].

7.4.3. Continuum model predictions

The continuum model is used to predict segregation during hopper discharge for conditions identical to both the initially well-mixed condition in Fig. 7.3 and the segregated condition in Fig. 7.5. Figure 7.10 shows the model predictions for large particle concentration in the surface flowing layer of the left half of the hopper during discharge. For the well-mixed initial condition (Fig. 7.10a), the continuum model predicts nearly mixed particles in the upstream portion of the flowing layer. In the downstream portion, segregation occurs with more large particles near the free surface and more small particles at the bottom of the flowing layer. Near the hopper center ($x/L = 1$), as the flow re-orients to the vertical direction, this segregation pattern causes increased large particles concentration in the hopper center and increased small particles concentration on the left side of the large particle enriched band. This is consistent with the DEM simulations in Fig. 7.3 and Fig. 7.4a inset, and also previous experimental observations [**228**]. Note that the small particle enriched region near the upper-left corner of the surface layer observed in DEM simulations (Fig. 7.4a inset) is also captured by the continuum model. For the
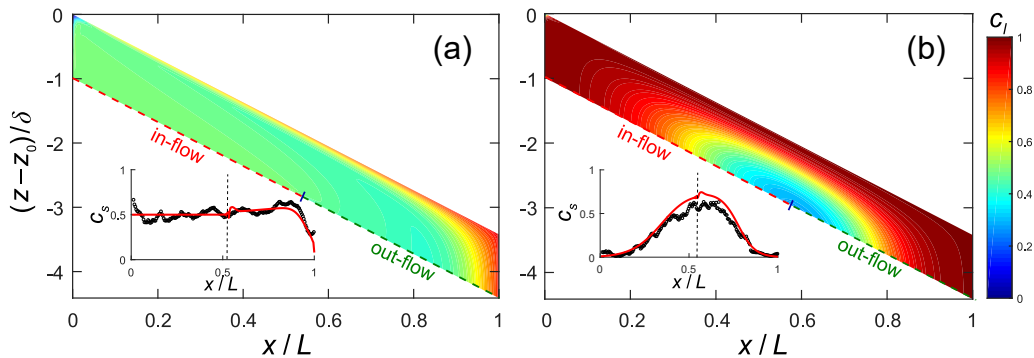
Figure 7.10. Examples of continuum model predictions for the large particle concentration in the surface layer. (a) Instantaneous distribution at $t = 6\,\mathrm{s}$ starting from mixed initial condition with $W = 0.4\,\mathrm{m}$, $\beta = 65°$, $W_o = 0.06\,\mathrm{m}$, $d_l = 3\,\mathrm{mm}$, $d_s = 1.5\,\mathrm{mm}$, $H_v + H_c = 1.1\,\mathrm{m}$, and $q_d = 0.034\,\mathrm{m^2/s}$. (b) Instantaneous distribution at $t = 4\,\mathrm{s}$ starting from segregated initial condition formed by center filling with $W = 0.4\,\mathrm{m}$, $\beta = 65°$, $W_o = 0.06\,\mathrm{m}$, $d_l = 3\,\mathrm{mm}$, $d_s = 1.5\,\mathrm{mm}$, $H_v + H_c = 0.84\,\mathrm{m}$, $q_f = 0.0024\,\mathrm{m^2/s}$, and $q_d = 0.033\,\mathrm{m^2/s}$. Insets compare concentration profiles at the bottom of the surface flowing layer for the two cases from the continuum model (red) and corresponding DEM simulations (black).

initially segregated case in Fig. 7.10b, large particles that are deposited during filling near the sidewalls are transported toward the hopper center through the surface flowing layer, while small particles remain in the middle region between the hopper center and sidewall. Segregation that occurs in the surface flowing layer further enhances the separation of large and small particles. This strongly segregated pattern is similar to that seen in the DEM simulations as shown in Fig. 7.7. The insets in Fig. 7.10 compare the small particle concentration profiles at the bottom of the flowing layer and top of the bulk region. For both initial conditions, the concentration profiles agree well.

The continuum model predictions for the entire hopper during discharge are shown in Figs. 7.11 and 7.12 to demonstrate how well the approach matches DEM simulation results. Figure 7.11 shows a time series of the large particle concentration distribution for the initially mixed condition corresponding to that used in Fig. 7.3. When the discharge begins, the continuum model captures the segregation occurring in the surface layer, where large particle enriched regions start to appear near the free surface ($t = 1\,\mathrm{s}$ and
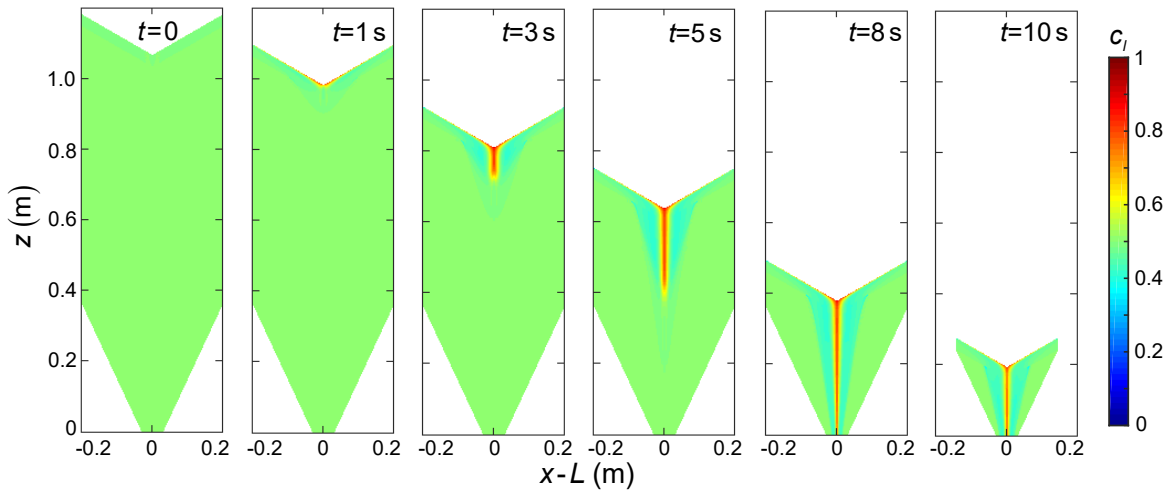
Figure 7.11. Continuum modeling predictions for the large particle concentration field with a mixed initial condition and $W = 0.4\,\text{m}$, $W_o = 0.06\,\text{m}$, $\beta = 65°$, $H_c + H_v = 1.1\,\text{m}$, $d_l = 3\,\text{mm}$, $d_s = 1.5\,\text{mm}$, and $q_d = 0.034\,\text{m}^2/\text{s}$.

$t = 3\,\text{s}$). The segregated particles are then transported by the mean flow in the bulk region in the vertical direction toward the outlet with a large particle enriched band sandwiched by small particle enriched regions ($t = 5\,\text{s}$ and $t = 8\,\text{s}$). This segregation pattern persists after the free surface enters the converging section ($t = 10\,\text{s}$). Segregation in the predictions occurs slightly earlier than in the DEM simulation, because the initial transition between a flat free surface to the V-shape free surface is not included in the continuum model. However, the segregation during hopper discharge predicted by the continuum model generally agrees well with DEM simulations (Fig. 7.3) and is consistent with previous experimental observations [228].

Figure 7.12 shows a time series of large particle concentration distribution for the initially segregated condition corresponding to that in Fig. 7.5. When the discharge begins, large particles near the sidewall are incorporated in the surface flowing layer and transported toward the center ($t = 1.5\,\text{s}$). Further segregation occurs in the surface flowing layer resulting in higher large particle concentrations at the hopper center, which becomes part of the bulk region and moves toward the outlet ($t = 3\,\text{s}$). Again, segregation develops earlier in the bulk than in the DEM simulation (Fig. 7.5). In this case, this occurs because
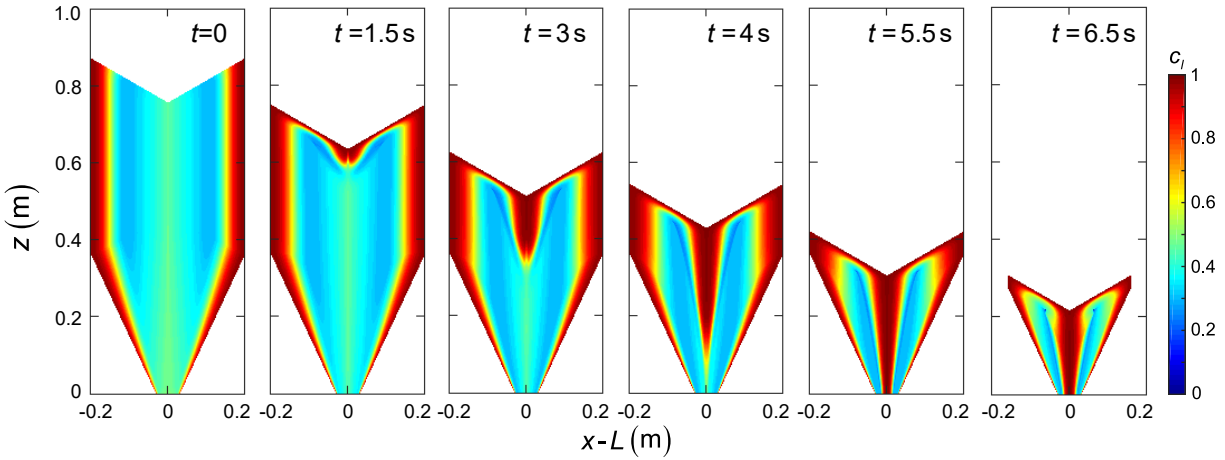
Figure 7.12. Continuum modeling predictions for the large particle concentration field with a segregated (center filled with $q_f = 0.0024\,\mathrm{m^2/s}$) initial condition and $W = 0.4\,\mathrm{m}$, $W_o = 0.06\,\mathrm{m}$, $\beta = 65°$, $H_c + H_v = 0.84\,\mathrm{m}$, $d_l = 3\,\mathrm{mm}$, $d_s = 1.5\,\mathrm{mm}$, and $q_d = 0.033\,\mathrm{m^2/s}$.

the continuum model starts with the V-shape free surface already developed. As discharge continues, the large particle region reaches the hopper outlet ($t = 4\,\mathrm{s}$ and $t = 5.5\,\mathrm{s}$). Note that in the bulk region, the weak horizontal motion (Fig. 7.6a inset) slowly transports large particles near the sidewalls toward the center, so the band of large particles near the sidewalls expands slightly with time. This results in a changing inlet concentration profile at the bottom of the surface flowing layer. After the surface flowing layer enters the converging section of the hopper ($t = 6.5\,\mathrm{s}$), the continuum model prediction also agrees well with the DEM simulation results in Fig. 7.5.

Figure 7.13 compares the discharge profiles between the continuum model prediction and DEM simulation results. Similar to previous studies [**175, 64, 225**], the small particle concentration, c_s, is normalized by the small particle concentration in the entire mixture $c_{s,tot}$. Thus, $c_s/c_{s,tot} > 1$ indicates more small particles than the average initial small particle concentration, and $c_s/c_{s,tot} < 1$ indicates more large particles. The volume of the discharged material V_{dis} is normalized by V_{tot}, the total volume of material initially filling in the hopper. For the initially mixed condition (Fig. 7.11), the continuum model concentration remains well-mixed until the large particle front in the center region reaches
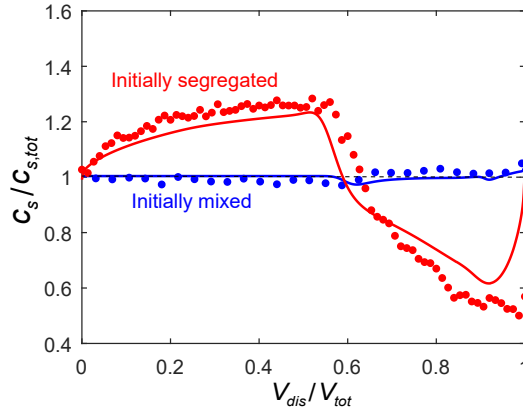
Figure 7.13.   Comparison of discharged material concentration between continuum model predictions (curves) and corresponding DEM simulation results (circles) for mixed initial conditions (Figs. 7.3 and 7.11, blue) and segregated initial conditions (Figs. 7.5 and 7.12, red).

the outlet, after which the small particle concentration decreases slightly ($c_s/c_{s,tot} < 1$). After most large particles are discharged, $c_s/c_{s,tot} > 1$. This trend agrees with the DEM simulation results and previous experiments with similar hopper geometries [**64, 225, 226, 228**].

For the initially segregated case, segregation during discharge is more significant. After the discharge begins, the small particles concentrated in the hopper center region (due to filling segregation) are discharged first, resulting in higher small particle concentration in the discharge profile. After the front of the large particle region reaches the hopper outlet at $V_{dis}/V_{tot} \approx 0.5$, the small particle concentration drops and large particles from the center segregated region dominate the discharge ($c_s/c_{s,tot} < 1$). In the continuum model prediction, the small particle concentration increases sharply at the end of the discharge process. However, this sharp increase is not observed in the corresponding DEM simulation. This may be because the advection field near the exit at the end of the discharge process is not well described by the continuum model, as discussed in Section 7.4.1. Near $V_{dis}/V_{tot} = 0.9$, for both initial conditions, a small dip in small particle concentration occurs. This is associated with the entrance of the surface layer into the converging section of the hopper and the corresponding steady state concentration

Figure 7.14. Comparison of continuum model predictions with corresponding experiment of hopper discharge for an initially segregated case (center filled). Here, $W = 0.45\,\text{m}$, $\beta = 60°$, $W_o = 0.06\,\text{m}$, $d_l = 3\,\text{mm}$ (gold), $d_s = 1\,\text{mm}$ (red), $H_c + H_v = 0.74\,\text{m}$, fill rate $q_f = 0.0016\,\text{m}^2/\text{s}$, and discharge rate $q_d = 0.03\,\text{m}^2/\text{s}$. (a) Instantaneous large particle concentration field predicted by the continuum model (left) and image from the corresponding experiment (right). (b) Comparison of small particle concentration in the discharge from the continuum model (solid curve) and experiment (circles). Error bars indicate the standard deviation of $c_s/c_{s,tot}$ and V_{dis}/V_{tot} measured in three separate experiments.

approximation in the surface layer. The drop in concentration occurs when this difference is advected to the hopper outlet. However, it only influences the prediction at the end of the discharge and the influence is small. Overall, the continuum model prediction agrees well with the DEM simulation results.

7.4.4. Experimental validation

Experiments to further validate the continuum model utilize a quasi-2D hopper that consists of a glass front wall, an aluminum back wall, and acrylic sidewalls. During experiments, a mixture of $3.12\pm0.14\,\text{mm}$ (gold) and $1.16\pm0.07\,\text{mm}$ (red) glass spherical particles, both having a density of 2500 kg/m^3, is first center-fed into the hopper by an auger feeder (101-1-DD/2, Acrison, Inc., NJ, USA) at a constant feed rate q_f while the
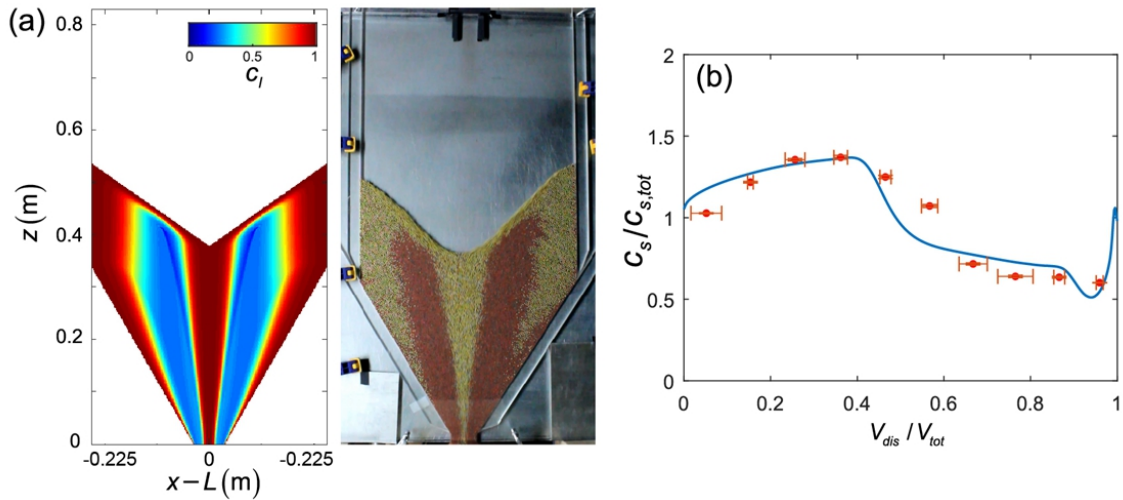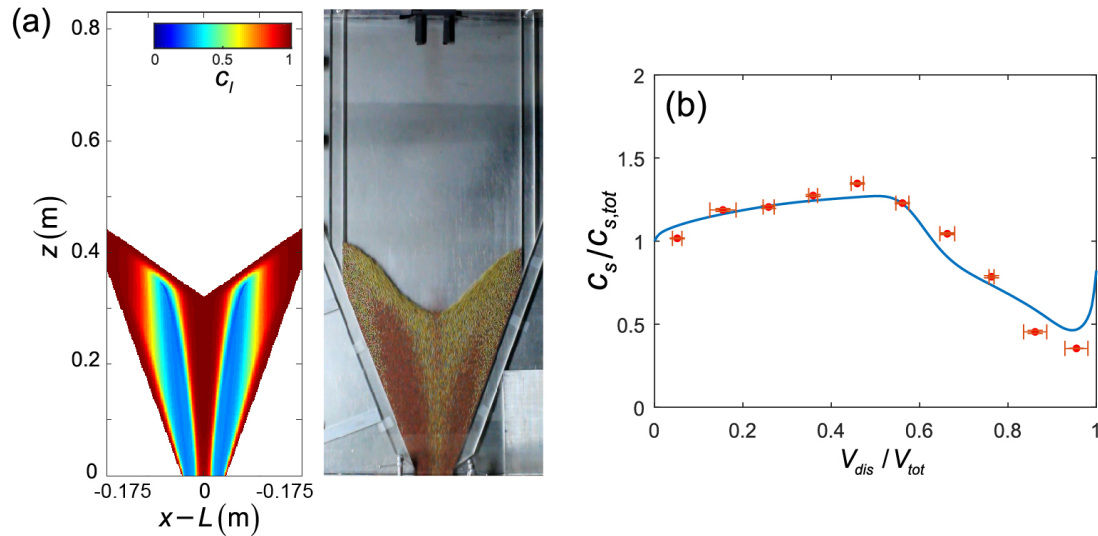
Figure 7.15. Comparison of continuum model predictions with corresponding experiment of hopper discharge for a segregated initial condition (center filled) using a different hopper geometry from that used in Fig. 7.14. Here, $W = 0.35$ m, $\beta = 70°$, $W_o = 0.08$ m, $d_l = 3$ mm (gold), $d_s = 1$ mm (red), $H_c + H_v = 0.81$ m, fill rate $q_f = 0.0016$ m^2/s, and discharge rate $q_d = 0.053$ m^2/s. (a) Instantaneous large particle concentration field predicted by the continuum model (left) and a snapshot from the corresponding experiment (right). (b) Comparison of the small particle concentration in the discharge from the continuum model (solid line) and experiment (circles). The error bars indicate the standard deviation of $c_s/c_{s,tot}$ and V_{dis}/V_{tot} measured in three separate experiments.

hopper outlet is closed. Two strips of paper are positioned near the feed zone on the heap surface to reduce particle bouncing. After filling, the hopper outlet is opened to discharge particles. A digital camera records segregation in the hopper through the glass front wall at 60 frames/s. A belt conveyor placed under the hopper outlet is used to measure the discharged particle concentration profile. During discharge, the belt moves forward preserving the sequence of the discharge. The belt conveyor has no influence on the flow inside the hopper. The material collected on the belt is divided into ten equal volume samples, and the concentration of small particles for each sample is measured by sifting out the small particles to calculate their volume fraction. Note that for the experiments,

the free surface angle (angle of repose) during discharge is approximately $\alpha = 35°$, which is slightly larger than the angle measured in DEM simulations ($\alpha = 30°$).

The large particle concentration field based on the continuum model and the corresponding snapshot from the experiment are shown in Fig. 7.14a. The segregation pattern with large particles concentrated near the hopper center and sidewalls is well captured by the continuum model. The large particles in the surface layer in the experiment are clearly evident on the free surface in the model prediction. Furthermore, the model captures the triangular shape of the large particle enriched region in the hopper center, as also observed in previous studies [228]. Figure 7.14b shows that the discharge profile for the small particle concentration matches well between the model prediction and experimental measurements. Figure 7.15 shows another comparison between the continuum model prediction and experiments for a segregated (center filled) initial condition, but with different hopper width, bottom incline angle, and outlet size. Again, the continuum model captures the segregation pattern inside the hopper during discharge, as shown in Fig. 7.15a. The discharge profiles for the small particle concentration in Figure 7.15b also shows a good match between the model prediction and experiment.

7.4.5. Plant data comparison

It is quite difficult to obtain plant data for industrial hoppers, but we are fortunate to have available plant data from several years ago for filling large bags from a hopper. Although the data was obtained for another purpose, it can be used for a rough comparison of the continuum model to an industrial 3D hopper. The hopper had a cylindrical section with a diameter of $1.2\,\mathrm{m}$ and a converging section with an inclination of $60°$ and an outlet diameter of $0.22\,\mathrm{m}$. Particles were center-fed to a height of $4.9\,\mathrm{m}$ at a volumetric feed rate of $0.0019\,\mathrm{m^3/s}$. The bulk solid was polydisperse and its size distribution is shown in the inset of Fig. 7.16a. To characterize segregation in the discharge, the solids were collected sequentially in six bags having equal volumes of $0.78\,\mathrm{m^3}$. The volume concentration of particles with diameter smaller than $0.106\,\mathrm{mm}$ (US 140 mesh), $c_{d<0.106}$, is shown in Fig. 7.16a. Although this data is for a 3D cylindrical hopper with polydisperse
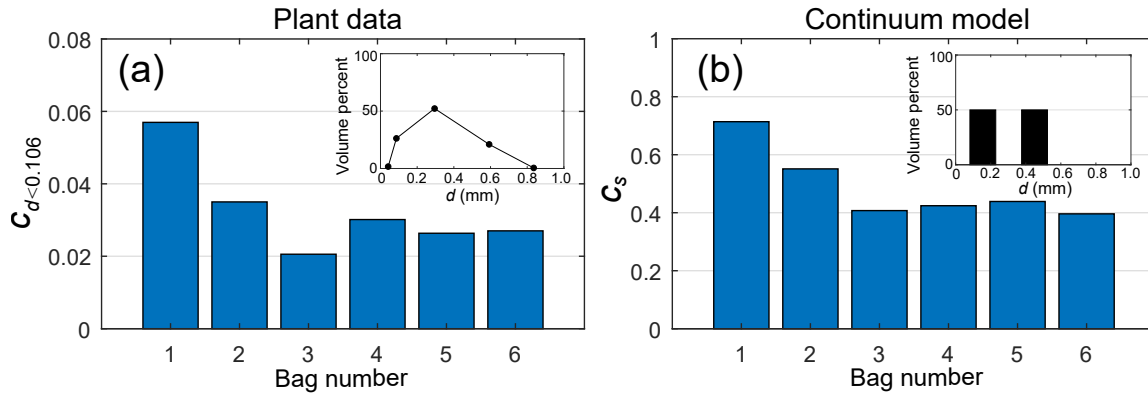
Figure 7.16. Qualitative comparison of the discharged small particle concentration from the historical plant data and the equivalent continuum modeling. (a) Plant data of discharge concentration for particles smaller than $0.106\,\mathrm{mm}$, $c_{d<0.106}$. Inset shows the polydisperse particle size distribution. (b) Equivalent 2D prediction of the small particle concentration by the continuum model with $W = 0.6\,\mathrm{m}$, $\beta = 60°$, $W_o = 0.11\,\mathrm{m}$, $d_l = 0.45\,\mathrm{mm}$, $d_s = 0.155\,\mathrm{mm}$, $H_c + H_v = 4.9\,\mathrm{m}$, and fill rate $q_f = 0.002\,\mathrm{m^2/s}$. Inset shows the bidisperse size distribution.

material, we approximate this discharge flow using our quasi-2D model of bidisperse hopper discharge segregation as a first approximation. To do this, the problem is converted to an equivalent 2D situation by setting the 2D hopper width equal to the diameter of the cylindrical hopper section, and the volumetric feed rate to a 2D feed rate with the same rise velocity in the vertical section. The polydisperse material is approximated with a bidisperse material composed of two equal-volume components (see inset of Fig. 7.16b).

Figure 7.16b shows the discharge concentration profile predicted using the continuum model, which is divided into six "bags" as in the plant measurement. Because of the bidisperse approximation, it is not possible to directly compare prediction results to the plant data ($c_{d<0.106}$), but a qualitative comparison can be achieved by using the small particle concentration c_s. The historical plant data and model prediction show a similar trend with more small particles for the first two bags and fewer small particles for the remaining four bags. The qualitative agreement clearly demonstrates the potential of the continuum model described here to predict segregation in industrial scale hoppers.

7.5. Conclusions

In this chapter, a continuum segregation model is developed to quantitatively predict size segregation during quasi-2D hopper discharge. The model predicts both the instantaneous segregation pattern inside the hopper and the discharge segregation profile. The essential part of this model is the material transport and segregation in the surface flow layer, where particles near the sidewall enter the surface layer and are transported toward the hopper center, during which segregation occurs. Our model predictions for the particle distribution in the hopper match quantitatively with DEM simulations and experiments for both well-mixed and segregated initial conditions resulting from center filling. Most significantly, we combined the hopper filling segregation (i.e., segregated initial condition) and discharge segregation by using a continuum segregation model to successfully predict the discharge segregation profile.

To quantitatively model segregation during hopper discharge in industrial applications, additional aspects need to be explored. First, differences between hopper discharge in a quasi-2D geometry (with frictional front and back walls) and in 3D geometries (cylindrical and wedge shaped) need to be explored and taken into account in the continuum model. Previous studies showed that during heap formation, the surface angle is increased due to the sidewall friction [34]. Similarly, for 3D hopper geometries, the surface incline angle is likely to be considerably reduced. For some mass flow hoppers, the free surface can even remain nearly horizontal in the vertical section and the V-shape surface only forms after it enters the converging section. This kinematic difference can be readily incorporated into the theoretical framework we have described here as an extreme condition where no velocity difference in the vertical section results in no horizontal transport, and thus no segregation. This would require turning off the surface layer flow in the vertical section or using an evolving free surface angle. Furthermore, the surface layer depth for 3D discharge flows could be considerably deeper than that in quasi-2D flows [34]. Another factor that we do not consider is the particle size polydispersity, density differences or shape effects. Real bulk solids often have a continuous particle size distribution rather than the idealized bidisperse particle size distribution considered here. Our continuum

model can be extended to such systems using approaches similar to those that have been used for size polydisersity [86] and density dispersity [57] in heap and chute flows.

CHAPTER 8

Summary and Future Work

This chapter summarizes the major findings and conclusions of this thesis. In addition, possible future research directions are also discussed.

8.1. Summary

This thesis first explored different segregation mechanisms in steady granular flows. In Chapter 2, segregation in flow of density bidisperse materials was studied using DEM simulations. Flow kinematics were extracted from DEM simulations, and a relation between the density segregation velocity and the particle density ratio, the local shear rate, and the local concentration was found. A continuum segregation model was adopted to include the density segregation velocity and the model accurately predicts density segregation in bounded heap flows. A similar study was presented in Chapter 3 where segregation of rod-like particles with different lengths was investigated. DEM simulations of cylindrical rod particles also revealed a relation between the segregation velocity and the local shear rate, the local species concentration, and the rod length ratio, similar to the relation for spherical particles. The segregation length scale and the diffusion coefficient of rod particles scale with the rod diameter, possibly because of the alignment of the rods to the flow. This information was again incorporated into the continuum segregation model which accurately predicts segregation of rod-like particles in bounded heap flows.

The remainder of this thesis focused on the flow kinematics and segregation in transient and unsteady flows. Chapter 4 demonstrated how modulating the feed rate in size bidisperse heap flows causes particles to stratify by forming alternating large and small particle layers, which is different from the streamwise segregation formed in steady flows. The stratification pattern formed in the modulated flow can be controlled by modulation parameters and demonstrates better overall mixing than the streamwise segregation. The

stratification mechanism is related to the non-uniform deposition during transient heap flows, which is discussed in detail in Chapter 5. When the feed rate suddenly changes, a growing (or vanishing) wedge of materials originates on the free surface near the feed zone and propagates downstream, resulting in non-uniform deposition or erosion occurring during the transient process. The transient flux and surface height profile can be modeled by a local relationship between the local flux and the local slope angle in combination with the continuity equation.

Modulating the feed rate is not the only method to generate unsteady heap flows. Chapter 6 showed that a transition from steady to unsteady flow occurs when the water content of damp granular materials increases. The unsteady flow was a time-periodic flow with each period consisting of a non-depositing downslope avalanche and an upslope propagating granular jump. The transition from steady to unsteady flow appears to occur when the surface angle of the heap is increased (as a result of increased cohesion) beyond the neutral angle of deposition. Inhomogeneous packing of particles results in the deposited heap consisting of layers of densely packed particles and loosely packed particles. The formation of these layers is closely related to the unsteady flow. As demonstrated in the appendix in Chapter 6, adding a small amount of water into a size-bidisperse mixture can also result in size stratification during heap formation.

In Chapter 7, hopper discharge segregation was considered. This is a transient process that almost always follows heap formation (hopper filling). DEM simulations revealed that segregation during hopper discharge mainly occurs in a surface layer where particles are transported from the sidewall to the hopper center. The velocity field was developed based on a kinematic model and DEM observations. Then, the continuum segregation model was applied to model the particle concentration distribution in the surface layer and the bulk region. The model successfully predicted the segregation pattern inside the hopper during discharge and the concentration profile of the discharged materials, which quantitatively match both DEM simulations and experiments.

8.2. Future work

For modeling density segregation, several improvements could be made. Since there are often more than two components in industrial mixtures and geophysical flows, it would be worthwhile to extend the bidisperse segregation model to capture multidisperse and polydisperse segregation, similar to what has been done for size segregation [**86, 235**]. Even more important is to consider combined size and density segregation. This will depend on both experiments and DEM simulations to extract a relation for segregation velocity that accounts for both size and density differences, similar to previous work where the combined size and density segregation velocity were developed based on mixture theories [**114, 76**]. The challenge here is that the impacts of size and density on segregation are not linearly additive, though insight can be possibly obtained from a recent study that suggests the net force on an intruder particle is related to both the particle size and density [**257**]. Moreover, the origin of the asymmetry in the segregation velocity and the segregation flux between the heavy particle enriched situation and the light particle enriched situation (Section 2.4) requires further study, and possible modifications of the segregation velocity relation (Eq. 2.4) may be necessary to better capture segregation at extreme concentrations. Lastly, the feedback of density segregation on the flow kinematics should be studied. An extreme example is shown in Fig. 2.8 where for a large density ratio, the segregated heavy particles undercut the light particles. Apparently, density segregation induces variation of the local density, which for large density ratios influences the inertia (the inertial number I) of the flow and relevant local rheology parameters.

For segregation of non-spherical particles, it is important to understand the dependence of characteristic segregation length scale on particle parameters. For rod-like particles with equal diameters, it is clear that the characteristic length is the length of the rods. But it is not clear how the rods segregate when the diameter also differs, and if the characteristics "length" should actually be area- or volume-based. In addition, for segregation of non-spherical particles, especially for particles with large aspect ratios like rods, segregation should not only depend on particle shapes but also on particle orientations in the flow. In heap flows with long rods, particles align with the flow direction, which makes

the length of the rods the characteristic length for segregation, while the rod diameter appears to be the scaling factor for the diffusion coefficient in the direction normal to the flow. However, the orientation of particles and the segregation direction could be more complicated in tumbler flows and hopper discharge flows [258], which should be further studied. In addition, from the continuum modeling point of view, it is important to study the influence of local particle size, shape, and orientation on the flow kinematics, so that accurate velocity profiles can be obtained for the continuum segregation model.

For controlling granular segregation using unsteady flow, it is important to develop an approach that is effective and practical for 3D heap formation, which is quite relevant in industrial processes. It is demonstrated in Chapter 4 that the stratified layers of small and large particles formed in unsteady flows can result in better overall mixing and better hopper discharge uniformity. Chapters 4 and 6 have shown that stratification can be achieved in quasi-2D flows either by modulating the feed rate or by adding a small amount of water to trigger unsteady flow. It is also possible to modify particle shape to induce unsteady flow and stratification [44]. While it could be interesting to look for more approaches to reduce segregation in the quasi-2D geometry considered in this thesis, it is more important to realize these methods for 3D heap formation which generally has thicker flowing layers and slower velocities down the heap surface [259]. In addition, as more types of flow modes and instabilities, such as spiraling flow and alternating avalanches, can occur in 3D heap flows [215, 214], there are additional possibilities for implementing controlled unsteady flow to reduce segregation. Developing effective experimental methods to characterize segregation in 3D heaps is also an important problem because of the difficulty of measurements in a fully 3D geometry [259].

Understanding the underlying transient processes in unsteady flows is important for developing effective approaches to reducing segregation. Results in Chapter 5 have shown that non-uniform deposition occurs when the feed rate is suddenly changed, which is an important factor for the stratification. The results also indicate that the transient process is closely related to the dependence of the local surface angle on the local flux, which could be strongly influenced by the sidewall friction [34]. Thus, the transient

process could be different when sidewall friction is not present, such as for simulations with periodic lateral boundaries and for 3D heap flows. Understanding this difference could be important for developing flow modulation schemes to enhance stratification or otherwise reduce segregation. Also, this process could serve as a test model for rheology models [**79, 36, 18**] as it is transient and involves erosion and deposition, which are still challenging problems for the granular flow community. Similarly, unsteady flows and instabilities exist widely in wet granular flows, which requires further understanding and modeling particularly with regard to cohesive particles. Capturing the unsteady flow dynamics and the inhomogeneous packing using DEM simulations and continuum models can also be very challenging.

For modeling hopper discharge segregation, more work is needed to generalize the model from 2D to 3D cylindrical hoppers. In order to do this, it would be ideal to have a model that can capture the transient velocity field and the free surface profile based on particle properties and the system geometry. This kind of model could possibly be developed from classic hopper flow theories [**23, 230, 232**], but it is also worthwhile to predict the velocity field and the free surface shape using constitutive theories for granular materials, such as the $\mu(I)$ rheology [**36, 260**] or the elasto-plastic model [**246**]. Another direction is to minimize the segregation in combined filling-discharge operations, similar to the idea proposed in Chapter 4. Optimized hopper geometry and operation parameters need to be identified, as well as optimized filling and discharge schemes such as the flow modulation method. It could be much more efficient to do so using a continuum model than using lab experiments, particularly if the continuum model can be coupled with optimization models such as evolutionary algorithms to accelerate the design process to minimize segregation.

It is clear that this thesis has only scratched the surface with regard to segregation in transient granular flows. Much work remains to be done.

References

[1] de Gennes PG. Granular matter: a tentative view. Rev Mod Phys. 1999;71(2):S374.

[2] Jaeger HM, Nagel SR, Behringer RP. Granular solids, liquids, and gases. Rev Mod Phys. 1996;68(4):1259.

[3] Duran J. Sands, powders, and grains: an introduction to the physics of granular materials. Springer Science & Business Media; 2012.

[4] Tang Ys, Zhang Lg, Guo Qj, Cao Jz, Tong Jj. Numerical solutions for the kinematic model of pebble flow velocity profiles and its applications in pebble-bed nuclear reactor. J Nucl Sci Technol. 2017;p. 1–11.

[5] Iverson RM. The physics of debris flows. Rev Geophys. 1997;35(3):245–296.

[6] Mitani NK, Matuttis HG, Kadono T. Density and size segregation in deposits of pyroclastic flow. Geophys Res Lett. 2004;31(15).

[7] Hansen C, Bourke M, Bridges N, Byrne S, Colon C, Diniega S, et al. Seasonal erosion and restoration of Mars northern polar dunes. Science. 2011;331(6017):575–578.

[8] Schmidt F, Andrieu F, Costard F, Kocifaj M, Meresescu AG. Formation of recurring slope lineae on Mars by rarefied gas-triggered granular flows. Nat Geosci. 2017;10(4):270.

[9] Nagel SR. Experimental soft-matter science. Rev Mod Phys. 2017;89(2):025002.

[10] Schella A, Weis S, Schröter M. Charging changes contact composition in binary sphere packings. Phys Rev E. 2017;95(6):062903.

[11] Waitukaitis SR, Lee V, Pierson JM, Forman SL, Jaeger HM. Size-dependent same-material tribocharging in insulating grains. Phys Rev Lett. 2014;112(21):218001.

[12] Scheel M, Seemann R, Brinkmann M, Di Michiel M, Sheppard A, Breidenbach B, et al. Morphological clues to wet granular pile stability. Nat Mater. 2008;7(3):189.

[13] Parteli EJ, Schmidt J, Blümel C, Wirth KE, Peukert W, Pöschel T. Attractive particle interaction forces and packing density of fine glass powders. Sci Rep. 2014;4:6227.

[14] Forterre Y, Pouliquen O. Flows of dense granular media. Annu Rev Fluid Mech. 2008;40:1–24.

[15] Goldhirsch I. Rapid granular flows. Annu Rev Fluid Mech. 2003;35(1):267–293.

[16] Majmudar TS, Behringer RP. Contact force measurements and stress-induced anisotropy in granular materials. Nature. 2005;435(7045):1079.

[17] Pouliquen O, Forterre Y. A non-local rheology for dense granular flows. Phil Trans R Soc A. 2009;367(1909):5091–5107.

[18] Henann DL, Kamrin K. A predictive, size-dependent continuum model for dense granular flows. Proc Natl Acad Sci. 2013;110(17):6730–6735.

[19] MiDi G. On dense granular flows. Eur Phys J E. 2004;14(4):341–365.

[20] Fan Y, Boukerkour Y, Blanc T, Umbanhowar PB, Ottino JM, Lueptow RM. Stratification, segregation, and mixing of granular materials in quasi-two-dimensional bounded heaps. Phys Rev E. 2012;86(5):051305.

[21] Fan Y, Umbanhowar PB, Ottino JM, Lueptow RM. Kinematics of monodisperse and bidisperse granular flows in quasi-two-dimensional bounded heaps. Proc R Soc A. 2013;469:20130235.

[22] Gray JMNT. Particle segregation in dense granular flows. Annu Rev Fluid Mech. 2018;(0).

[23] Jenike AW. Storage and flow of solids. Bulletin 123, Utah Eng Exp Sta, Univ of Utah. 1964;.

[24] May LB, Golick LA, Phillips KC, Shearer M, Daniels KE. Shear-driven size segregation of granular materials: modeling and experiment. Phys Rev E. 2010;81(5):051301.

[25] Fan Y, Hill KM. Shear-driven segregation of dense granular mixtures in a split-bottom cell. Phys Rev E. 2010;81(4):041303.

[26] Dijksman JA, van Hecke M. Granular flows in split-bottom geometries. Soft Matter. 2010;6(13):2901–2907.

[27] Ferdowsi B, Ortiz CP, Houssais M, Jerolmack DJ. River-bed armouring as a granular segregation phenomenon. Nat Commun. 2017;8(1):1363.

[28] Grasselli Y, Herrmann HJ. On the angles of dry granular heaps. Physica A. 1997;246(3):301–312.

[29] Bouchaud JP, Cates ME, Prakash JR, Edwards SF. A model for the dynamics of sandpile surfaces. J Phys I. 1994;4(10):1383–1410.

[30] Boutreux T, Raphaël E, de Gennes PG. Surface flows of granular materials: a modified picture for thick avalanches. Phys Rev E. 1998;58(4):4692.

[31] Douady S, Andreotti B, Daerr A, Cladé P. From a grain to avalanches: on the physics of granular surface flows. C R Phys. 2002;3(2):177–186.

[32] Jenkins JT, Berzi D. Erosion and deposition in depth-averaged models of dense, dry, inclined, granular flows. Phys Rev E. 2016;94(5):052904.

[33] Trinh T, Boltenhagen P, Delannay R, Valance A. Erosion and deposition processes in surface granular flows. Phys Rev E. 2017;96(4):042904.

[34] Jop P, Forterre Y, Pouliquen O. Crucial role of sidewalls in granular surface flows: consequences for the rheology. J Fluid Mech. 2005;541:167–192.

[35] Silbert LE, Ertaş D, Grest GS, Halsey TC, Levine D, Plimpton SJ. Granular flow down an inclined plane: Bagnold scaling and rheology. Phys Rev E. 2001;64(5):051302.

[36] Jop P, Forterre Y, Pouliquen O. A constitutive law for dense granular flows. Nature. 2006;441(7094):727–730.

[37] Jop P, Forterre Y, Pouliquen O. Initiation of granular surface flows in a narrow channel. Phys Fluids. 2007;19(8):088102.

[38] Parez S, Aharonov E, Toussaint R. Unsteady granular flows down an inclined plane. Phys Rev E. 2016;93(4):042902.

[39] Zhang Q, Kamrin K. Microscopic description of the granular fluidity field in nonlocal flow modeling. Phys Rev Lett. 2017;118(5):058001.

[40] Fan Y, Schlick CP, Umbanhowar PB, Ottino JM, Lueptow RM. Modelling size segregation of granular materials: the roles of segregation, advection and diffusion. J Fluid Mech. 2014;741:252–279.

[41] Pohlman NA, Ottino JM, Lueptow RM. Unsteady granular flows in a rotating tumbler. Phys Rev E. 2009;80(3):031302.

[42] Pohlman NA, Paprocki Jr DF. Transient behavior of granular materials as result of tumbler shape and orientation effects. Granul Matter. 2013;15(1):39–47.

[43] du Pont SC, Fischer R, Gondret P, Perrin B, Rabaud M. Instantaneous velocity profiles during granular avalanches. Phys Rev Lett. 2005;94(4):048003.

[44] Makse HA, Havlin S, King PR, Eugene S. Spontaneous stratification in granular mixtures. Nature. 1997;386:379–382.

[45] Edwards AN, Vriend NM. Size segregation in a granular bore. Phys Rev Fluids. 2016;1(6):064201.

[46] Gray JMNT, Ancey C. Segregation, recirculation and deposition of coarse particles near two-dimensional avalanche fronts. J Fluid Mech. 2009;629:387–423.

[47] Edwards AN, Gray JMNT. Erosion–deposition waves in shallow granular free-surface flows. J Fluid Mech. 2015;762:35–67.

[48] Altshuler E, Ramos O, Martínez E, Batista-Leyva A, Rivera A, Bassler K. Sandpile formation by revolving rivers. Phys Rev Lett. 2003;91(1):014501.

[49] Ottino JM, Khakhar DV. Mixing and segregation of granular materials. Annu Rev Fluid Mech. 2000;32(1):55–91.

[50] Johnson CG, Kokelaar BP, Iverson R, Logan M, LaHusen R, Gray JMNT. Grain-size segregation and levee formation in geophysical mass flows. J Geophys Res Earth Surf. 2012;117(F1).

[51] Kokelaar BP, Graham RL, Gray JMNT, Vallance JW. Fine-grained linings of leveed channels facilitate runout of granular flows. Earth Planet Sci Lett. 2014;385:172–180.

[52] Muzzio FJ, Shinbrot T, Glasser BJ. Powder technology in the pharmaceutical industry: the need to catch up fast. Powder Technol. 2002;124(1):1–7.

[53] Bridgwater J. Mixing of powders and granular materials by mechanical means–A perspective. Particuology. 2012;10(4):397–427.

[54] Williams JC. The mixing of dry powders. Powder Technol. 1968;2(1):13–20.

[55] Savage SB, Lun C. Particle size segregation in inclined chute flow of dry cohesionless granular solids. J Fluid Mech. 1988;189:311–335.

[56] Tripathi A, Khakhar DV. Density difference-driven segregation in a dense granular flow. J Fluid Mech. 2013;717:643–669.

[57] Xiao H, Umbanhowar PB, Ottino JM, Lueptow RM. Modelling density segregation in flowing bidisperse granular materials. In: Proc. R. Soc. A. vol. 472. The Royal Society; 2016. p. 20150856.

[58] Gillemot KA, Somfai E, Börzsönyi T. Shear-driven segregation of dry granular materials with different friction coefficients. Soft Matter. 2017;13(2):415–420.

[59] Brito R, Enríquez H, Godoy S, Soto R. Segregation induced by inelasticity in a vibrofluidized granular mixture. Phys Rev E. 2008;77(6):061301.

[60] Thornton A, Weinhart T, Luding S, Bokhove O. Modeling of particle size segregation: calibration using the discrete particle method. Int J Mod Phys C. 2012;23(08):1240014.

[61] Jain N, Ottino JM, Lueptow RM. Combined size and density segregation and mixing in noncircular tumblers. Phys Rev E. 2005;71(5):051301.

[62] Fiedor SJ, Ottino JM. Mixing and segregation of granular matter: multi-lobe formation in time-periodic flows. J Fluid Mech. 2005;533:223–236.

[63] Pouliquen O, Delour J, Savage SB. Fingering in granular flows. Nature. 1997;386(6627):816.

[64] Ketterhagen WR, Curtis JS, Wassgren CR, Kong A, Narayan PJ, Hancock BC. Granular segregation in discharging cylindrical hoppers: a discrete element and experimental study. Chem Eng Sci. 2007;62(22):6423–6439.

[65] Schlick CP, Fan Y, Isner AB, Umbanhowar PB, Ottino JM, Lueptow RM. Modeling segregation of bidisperse granular materials using physical control parameters in the quasi-2D bounded heap. AIChE J. 2015;61(5):1524–1534.

[66] Lueptow RM, Akonur A, Shinbrot T. PIV for granular flows. Exp Fluids. 2000;28(2):183–186.

[67] Crocker JC, Grier DG. Methods of digital video microscopy for colloidal studies. J Colloid Interface Sci. 1996;179(1):298–310.

[68] Wiederseiner S, Andreini N, Épely-Chauvin G, Moser G, Monnereau M, Gray JMNT, et al. Experimental investigation into segregating granular flows down chutes. Phys Fluids. 2011;23(1):013301.

[69] Hill K, Caprihan A, Kakalios J. Bulk segregation in rotated granular material measured by magnetic resonance imaging. Phys Rev Lett. 1997;78(1):50.

[70] Pöschel T, Schwager T. Computational granular dynamics: models and algorithms. Springer Science & Business Media; 2005.

[71] Guo Y, Curtis JS. Discrete element method simulations for complex granular flows. Annu Rev Fluid Mech. 2015;47:21–46.

[72] Cundall PA, Strack OD. A discrete numerical model for granular assemblies. Geotechnique. 1979;29(1):47–65.

[73] Bridgwater J, Foo WS, Stephens DJ. Particle mixing and segregation in failure zonestheory and experiment. Powder Technol. 1985;41(2):147–158.

[74] Dolgunin VN, Ukolov AA. Segregation modeling of particle rapid gravity flow. Powder Technol. 1995;83(2):95–103.

[75] Gray JMNT, Chugunov VA. Particle-size segregation and diffusive remixing in shallow granular avalanches. J Fluid Mech. 2006;569:365–398.

[76] Tunuguntla DR, Bokhove O, Thornton AR. A mixture theory for size and density segregation in shallow granular free-surface flows. J Fluid Mech. 2014;749:99–112.

[77] Marks B, Rognon P, Einav I. Grainsize dynamics of polydisperse granular segregation down inclined planes. J Fluid Mech. 2012;690:499–511.

[78] Gajjar P, Gray JMNT. Asymmetric flux models for particle-size segregation in granular avalanches. J Fluid Mech. 2014;757:297–329.

[79] Capart H, Hung CY, Stark CP. Depth-integrated equations for entraining granular flows in narrow channels. J Fluid Mech. 2015;765:R4.

[80] Hung CY, Stark C, Capart H. Granular flow regimes in rotating drums from depth-integrated theory. Phys Rev E. 2016;93(3):030902.

[81] Khakhar DV, Orpe AV, Andresén P, Ottino JM. Surface flow of granular materials: model and experiments in heap formation. J Fluid Mech. 2001;441:255–264.

[82] Rognon PG, Roux JN, Naaïm M, Chevoir F. Dense flows of bidisperse assemblies of disks down an inclined plane. Phys Fluids. 2007;19(5):058101.

[83] Schlick CP, Fan Y, Umbanhowar PB, Ottino JM, Lueptow RM. Granular segregation in circular tumblers: theoretical model and scaling laws. J Fluid Mech. 2015;765:632–652.

[84] Gray JMNT, Thornton AR; The Royal Society. A theory for particle size segregation in shallow granular free-surface flows. Proc R Soc A. 2005;461(2057):1447–1473.

[85] Tunuguntla DR, Weinhart T, Thornton AR. Comparing and contrasting size-based particle segregation models. Comput Part Mech. 2016;p. 1–19.

[86] Schlick CP, Isner AB, Freireich BJ, Fan Y, Umbanhowar PB, Ottino JM, et al. A continuum approach for predicting segregation in flowing polydisperse granular materials. J Fluid Mech. 2016;797:95–109.

[87] Jones RP, Isner AB, Xiao H, Ottino JM, Umbanhowar PB, Lueptow RM. Asymmetric concentration dependence of segregation fluxes in granular flows. arXiv preprint arXiv:180607993. 2018;.

[88] Makse HA, Ball RC, Stanley HE, Warr S. Dynamics of granular stratification. Phys Rev E. 1998;58(3):3357.

[89] Gray JMNT, Kokelaar BP. Large particle segregation, transport and accumulation in granular free-surface flows. J Fluid Mech. 2010;652:105–137.

[90] Baker JL, Johnson CG, Gray JMNT. Segregation-induced finger formation in granular free-surface flows. J Fluid Mech. 2016;809:168–212.

[91] Gray JMNT, Hutter K. Pattern formation in granular avalanches. Contin Mech Thermodyn. 1997;9(6):341–345.

[92] East RD, McGuinness P, Box F, Mullin T, Zuriguel I. Granular segregation in a thin drum rotating with periodic modulation. Phys Rev E. 2014;90(5):052205.

[93] Shi D, Abatan AA, Vargas WL, McCarthy JJ. Eliminating segregation in free-surface flows of particles. Phys Rev Lett. 2007;99(14):148001.

[94] Fineberg J. From Cinderella's dilemma to rock slides. Nature. 1997;386:323–324.

[95] Lueptow RM, Deng Z, Xiao H, Umbanhowar PB. Modeling segregation in modulated granular flow. In: EPJ Web of Conferences. vol. 140. EDP Sciences; 2017. p. 03018.

[96] Drahun JA, Bridgwater J. The mechanisms of free surface segregation. Powder Technol. 1983;36(1):39–53.

[97] Meier SW, Lueptow RM, Ottino JM. A dynamical systems approach to mixing and segregation of granular materials in tumblers. Adv Phys. 2007;56(5):757–827.

[98] Ahmad K, Smalley I. Observation of particle segregation in vibrated granular systems. Powder Technol. 1973;8(1-2):69–75.

[99] Knight JB, Jaeger HM, Nagel SR. Vibration-induced size separation in granular media: The convection connection. Phys Rev Lett. 1993;70(24):3728.

[100] Huerta D, Ruiz-Suárez J. Vibration-induced granular segregation: a phenomenon driven by three mechanisms. Phys Rev Lett. 2004;92(11):114301.

[101] Santomaso A, Olivi M, Canu P. Mechanisms of mixing of granular materials in drum mixers under rolling regime. Chem Eng Sci. 2004;59(16):3269–3280.

[102] Saxton J, Fralick P, Panu U, Wallace K. Density segregation of minerals during high-velocity transport over a rough bed: implications for the formation of placers. Econ Geol. 2008;103(8):1657–1664.

[103] Khakhar DV, McCarthy JJ, Ottino JM. Radial segregation of granular mixtures in rotating cylinders. Physics of Fluids. 1997;9(12):3600–3614.

[104] Hsiau SS, Chen WC. Density effect of binary mixtures on the segregation process in a vertical shaker. Adv Powder Technol. 2002;13(3):301–315.

[105] Burtally N, King PJ, Swift MR. Spontaneous air-driven separation in vertically vibrated fine granular mixtures. Science. 2002;295(5561):1877–1879.

[106] Yang S. Density effect on mixing and segregation processes in a vibrated binary granular mixture. Powder Technol. 2006;164(2):65–74.

[107] Shi Q, Sun G, Hou M, Lu K. Density-driven segregation in vertically vibrated binary granular mixtures. Phys Rev E. 2007;75(6):061302.

[108] Tai CH, Hsiau SS, Kruelle CA. Density segregation in a vertically vibrated granular bed. Powder Technol. 2010;204(2-3):255–262.

[109] Liao C, Hsiau S, Nien H. Density-driven spontaneous streak segregation patterns in a thin rotating drum. Phys Rev E. 2014;89(6):062204.

[110] Liao CC, Hsiau SS, Nien HC. Effects of density ratio, rotation speed, and fill level on density-induced granular streak segregation in a rotating drum. Powder Technol. 2015;284:514–520.

[111] Fan Y, Hill KM. Shear-induced segregation of particles by material density. Phys Rev E. 2015;92(2):022211.

[112] Fan Y, Hill K. Theory for shear-induced segregation of dense granular mixtures. New J Phys. 2011;13(9):095009.

[113] Hajra SK, Shi D, McCarthy J. Granular mixing and segregation in zigzag chute flow. Phys Rev E. 2012;86(6):061318.

[114] Gray JMNT, Ancey C. Particle-size and-density segregation in granular free-surface flows. J Fluid Mech. 2015;779:622–668.

[115] Boutreux T, Makse HA, De Gennes PG. Surface flows of granular mixtures. Eur Phys J B. 1999;9(1):105–115.

[116] Baxter J, Tüzün U, Heyes D, Hayati I, Fredlund P. Stratification in poured granular heaps. Nature. 1998;391(6663):136–136.

[117] Goyal RK, Tomassone MS. Power-law and exponential segregation in two-dimensional silos of granular mixtures. Phys Rev E. 2006;74(5):051301.

[118] Rahman M, Shinohara K, Zhu H, Yu A, Zulli P. Size segregation mechanism of binary particle mixture in forming a conical pile. Chem Eng Sci. 2011;66(23):6089–6098.

[119] Shäfer J, Dippel S, Wolf DE. Force schemes in simulations of granular materials. J Phys I. 1996;6(1):5–20.

[120] Ristow GH. Pattern formation in granular materials. 164. Springer Science & Business Media; 2000.

[121] Rapaport DC. Simulational studies of axial granular segregation in a rotating cylinder. Phys Rev E. 2002;65(6):061306.

[122] Freireich B, Kodam M, Wassgren C. An exact method for determining local solid fractions in discrete element method simulations. AIChE J. 2010;56(12):3036–3048.

[123] Nichol K, Zanin A, Bastien R, Wandersman E, van Hecke M. Flow-induced agitations create a granular fluid. Phys Rev Lett. 2010;104(7):078302.

[124] Jain N, Ottino JM, Lueptow RM. Regimes of segregation and mixing in combined size and density granular systems: an experimental study. Granul Matter. 2005;7(2-3):69–81.

[125] Pacheco-Vázquez F, Ruiz-Suárez J. Cooperative dynamics in the penetration of a group of intruders in a granular medium. Nature Comm. 2010;1:123.

[126] Utter B, Behringer RP. Self-diffusion in dense granular shear flows. Phys Rev E. 2004;69(3):031308.

[127] Christov IC, Ottino JM, Lueptow RM. From streamline jumping to strange eigenmodes: Bridging the Lagrangian and Eulerian pictures of the kinematics of mixing in granular flows. Phys Fluids. 2011;23(10):103302.

[128] Schlick CP, Christov IC, Umbanhowar PB, Ottino JM, Lueptow RM. A mapping method for distributive mixing with diffusion: Interplay between chaos and diffusion in time-periodic sine flow. Phys Fluids. 2013;25(5):052102.

[129] van der Vaart K, Gajjar P, Epely-Chauvin G, Andreini N, Gray J, Ancey C. Underlying asymmetry within particle size segregation. Phys Rev Lett. 2015;114(23):238001.

[130] Golick LA, Daniels KE. Mixing and segregation rates in sheared granular materials. Phys Rev E. 2009;80(4):042301.

[131] Makse HA. Continuous avalanche segregation of granular mixtures in thin rotating drums. Phys Rev Lett. 1999;83(16):3186.

[132] Zhao Y, Xiao H, Umbanhowar PB, Lueptow RM. Simulation and modeling of segregating rods in quasi-2D bounded heap flow. AIChE J. 2018;64(5):1550–1563.

[133] Moakher M, Shinbrot T, Muzzio FJ. Experimentally validated computations of flow, mixing and segregation of non-cohesive grains in 3D tumbling blenders. Powder Technol. 2000;109(1-3):58–71.

[134] Wegner S, Börzsönyi T, Bien T, Rose G, Stannarius R. Alignment and dynamics of elongated cylinders under shear. Soft Matter. 2012;8(42):10950–10958.

[135] Börzsönyi T, Szabó B, Wegner S, Harth K, Török J, Somfai E, et al. Shear-induced alignment and dynamics of elongated granular particles. Phys Rev E. 2012;86(5):051304.

[136] Guo Y, Wassgren C, Ketterhagen W, Hancock B, James B, Curtis J. A numerical study of granular shear flows of rod-like particles using the discrete element method. J Fluid Mech. 2012;713:1–26.

[137] Guo Y, Wassgren C, Hancock B, Ketterhagen W, Curtis J. Granular shear flows of flat disks and elongated rods without and with friction. Phys Fluids. 2013;25(6):063304.

[138] Kodam M, Bharadwaj R, Curtis J, Hancock B, Wassgren C. Force model considerations for glued-sphere discrete element method simulations. Chemical Engineering Science. 2009;64(15):3466–3475.

[139] Kodam M, Bharadwaj R, Curtis J, Hancock B, Wassgren C. Cylindrical object contact detection for use in discrete element method simulations. Part I–Contact detection algorithms. Chem Eng Sci. 2010;65(22):5852–5862.

[140] Kodam M, Bharadwaj R, Curtis J, Hancock B, Wassgren C. Cylindrical object contact detection for use in discrete element method simulations, Part IIExperimental validation. Chem Eng Sci. 2010;65(22):5863–5871.

[141] Guo Y, Wassgren C, Ketterhagen W, Hancock B, Curtis J. Some computational considerations associated with discrete element modeling of cylindrical particles. Powder Technol. 2012;228:193–198.

[142] Zhao Y, Umbanhowar PB, Lueptow RM. Discrete element simulation of rod-like cylindrical particles using super-ellipsoids. Particuology. 2018;submitted.

[143] Ma H, Xu L, Zhao Y. CFD-DEM simulation of fluidization of rod-like particles in a fluidized bed. Powder Technol. 2017;314:355–366.

[144] Cleary PW. DEM prediction of industrial and geophysical particle flows. Particuology. 2010;8(2):106–118.

[145] Fan Y, Jacob KV, Freireich B, Lueptow RM. Segregation of granular materials in bounded heap flow: A review. Powder Technol. 2017;312:67–88.

[146] Xiao H, McDonald D, Fan Y, Umbanhowar PB, Ottino JM, Lueptow RM. Controlling granular segregation using modulated flow. Powder Technol. 2017;312:360–368.

[147] Makse HA, Cizeau P, Stanley HE. Possible stratification mechanism in granular mixtures. Physical review letters. 1997;78(17):3298.

[148] Schlick CP, Isner AB, Umbanhowar PB, Lueptow RM, Ottino JM. On mixing and segregation: from fluids and maps to granular solids and advection–diffusion systems. Ind Eng Chem Res. 2015;54(42):10465–10471.

[149] Barr AH. Superquadrics and angle-preserving transformations. IEEE Comput Graph Appl. 1981;1(1):11–23.

[150] Lu G, Third J, Müller C. Discrete element models for non-spherical particle systems: from theoretical developments to applications. Chem Eng Sci. 2015;127:425–465.

[151] Chen P, Ottino JM, Lueptow RM. Subsurface granular flow in rotating tumblers: A detailed computational study. Phys Rev E. 2008;78(2):021303.

[152] Zhao Y, Jiang M, Liu Y, Zheng J. Particle-scale simulation of the flow and heat transfer behaviors in fluidized bed with immersed tube. AIChE J. 2009;55(12):3109–3124.

[153] Zhao Y, Cheng Y, Wu C, Ding Y, Jin Y. Eulerian–Lagrangian simulation of distinct clustering phenomena and RTDs in riser and downer. Particuology. 2010;8(1):44–50.

[154] Zhao Y, Xu L, Zheng J. CFD–DEM simulation of tube erosion in a fluidized bed. AIChE J. 2017;63(2):418–437.

[155] Jing L, Kwok C, Leung Y. Micromechanical origin of particle size segregation. Phys Rev Lett. 2017;118(11):118001.

[156] Ting JM, Corkum BT. Computational laboratory for discrete element geomechanics. J Comput Civil Eng. 1992;6(2):129–146.

[157] Börzsönyi T, Halsey TC, Ecke RE. Two scenarios for avalanche dynamics in inclined granular layers. Phys Rev Lett. 2005;94(20):208001.

[158] Campbell CS. Elastic granular flows of ellipsoidal particles. Phys Fluids. 2011;23(1):013306.

[159] Natarajan V, Hunt M, Taylor E. Local measurements of velocity fluctuations and diffusion coefficients for a granular material flow. J Fluid Mech. 1995;304:1–25.

[160] Katsuragi H, Abate A, Durian D. Jamming and growth of dynamical heterogeneities versus depth for granular heap flow. Soft Matter. 2010;6(13):3023–3029.

[161] Fan Y, Umbanhowar PB, Ottino JM, Lueptow RM. Shear-rate-independent diffusion in granular flows. Phys Rev Lett. 2015;115(8):088001.

[162] Lees A, Edwards S. The computer study of transport processes under extreme conditions. J Phys C. 1972;5(15):1921.

[163] Félix G, Thomas N. Evidence of two effects in the size segregation process in dry granular media. Phys Rev E. 2004;70(5):051307.

[164] Larcher M, Jenkins JT. The evolution of segregation in dense inclined flows of binary mixtures of spheres. J Fluid Mech. 2015;782:405–429.

[165] Gharat SH, Khakhar DV. Granular segregation in quasi-2d rectangular bin. In: POWDERS AND GRAINS 2013: Proceedings of the 7th International Conference on Micromechanics of Granular Media. vol. 1542. AIP Publishing; 2013. p. 755–758.

[166] Li H, McCarthy JJ. Controlling cohesive particle mixing and segregation. Phys Rev Lett. 2003;90(18):184301.

[167] Samadani A, Kudrolli A. Segregation transitions in wet granular matter. Phys Rev Lett. 2000;85(24):5102.

[168] Liao CC, Hsiau SS, Tsai TH, Tai CH. Segregation to mixing in wet granular matter under vibration. Chem Eng Sci. 2010;65(3):1109–1116.

[169] Liu PY, Yang RY, Yu AB. The effect of liquids on radial segregation of granular mixtures in rotating drums. Granul Matter. 2013;15(4):427–436.

[170] Samadani A, Kudrolli A. Angle of repose and segregation in cohesive granular matter. Phys Rev E. 2001;64(5):051301.

[171] Vallance JW, Savage SB. Particle segregation in granular flows down chutes. In: IUTAM Symposium on Segregation in Granular flows. Springer; 2000. p. 31–51.

[172] Thornton AR, Gray JMNT, Hogg AJ. A three-phase mixture theory for particle size segregation in shallow granular free-surface flows. J Fluid Mech. 2006;550:1–25.

[173] Spurling RJ, Davidson JF, Scott DM. The transient response of granular flows in an inclined rotating cylinder. Chem Eng Res Des. 2001;79(1):51–61.

[174] Shinohara K, Shoji K, Tanaka T. Mechanism of size segregation of particles in filling a hopper. Ind Eng Chem Proc Des Dev. 1972;11(3):369–376.

[175] Standish N. Studies of size segregation in filling and emptying a hopper. Powder Technol. 1985;45(1):43–56.

[176] Grasselli Y, Herrmann HJ. Experimental study of granular stratification. Granul Matter. 1998;1(1):43–47.

[177] Abate AR, Katsuragi H, Durian DJ. Avalanche statistics and time-resolved grain dynamics for a driven heap. Phys Rev E. 2007;76(6):061301.

[178] Makse HA. Stratification instability in granular flows. Phys Rev E. 1997;56(6):7008.

[179] Danckwerts PV. The definition and measurement of some characteristics of mixtures. Appl Sci Res A. 1952;3(4):279–296.

[180] Xiao H, Ottino JM, Lueptow RM, Umbanhowar PB. Transient response in granular quasi-two-dimensional bounded heap flow. Phys Rev E. 2017;96(4):040902.

[181] Grasselli Y, Herrmann H. Shapes of heaps and in silos. Eur Phys J B. 1999;10(4):673–679.

[182] Daerr A, Douady S. Two types of avalanche behaviour in granular media. Nature. 1999;399(6733):241.

[183] Saingier G, Deboeuf S, Lagrée PY. On the front shape of an inertial granular flow down a rough incline. Phys Fluids. 2016;28(5):053302.

[184] Taberlet N, Richard P, Henry E, Delannay R. The growth of a super stable heap: An experimental and numerical study. EPL. 2004;68(4):515.

[185] Hu H, Argyropoulos SA. Mathematical modelling of solidification and melting: a review. Model Simul Mater Sci E. 1996;4(4):371.

[186] Redner S, Krapivsky P. Diffusive escape in a nonlinear shear flow: Life and death at the edge of a windy cliff. J Stat Phys. 1996;82(3-4):999–1014.

[187] Ã-zisik MN, Özışık MN. Heat conduction. John Wiley & Sons; 1993.

[188] Taberlet N, Richard P, Valance A, Losert W, Pasini JM, Jenkins JT, et al. Superstable granular heap in a thin channel. Phys Rev Lett. 2003;91(26):264301.

[189] Xiao H, Hruska J, Ottino JM, Lueptow RM, Umbanhowar PB. Unsteady flows and inhomogeneous packing in damp granular heap flows. arXiv preprint arXiv:180604315. 2018;.

[190] Strauch S, Herminghaus S. Wet granular matter: a truly complex fluid. Soft Matter. 2012;8(32):8271–8280.

[191] Kudrolli A. Granular matter: sticky sand. Nat Mat. 2008;7(3):174.

[192] Mitarai N, Nori F. Wet granular materials. Adv Phys. 2006;55(1-2):1–45.

[193] Herminghaus S. Dynamics of wet granular matter. Adv Phys. 2005;54(3):221–261.

[194] Bocquet L, Charlaix E, Ciliberto S, Crassous J. Moisture-induced ageing in granular media and the kinetics of capillary condensation. Nature. 1998;396(6713):735.

[195] Bertho Y, Brunet T, Giorgiutti-Dauphiné F, Hulin JP. Influence of humidity on granular packings with moving walls. EPL. 2004;67(6):955.

[196] Gómez-Arriaran I, Ippolito I, Chertcoff R, Odriozola-Maritorena M, De Schant R. Characterization of wet granular avalanches in controlled relative humidity conditions. Powder Technol. 2015;279:24–32.

[197] Fraysse N, Thomé H, Petit L. Humidity effects on the stability of a sandpile. Eur Phys J B. 1999;11(4):615–619.

[198] Faschingleitner J, Höflinger W. Evaluation of primary and secondary fugitive dust suppression methods using enclosed water spraying systems at bulk solids handling. Adv Powder Technol. 2011;22(2):236–244.

[199] Hornbaker DJ, Albert R, Albert I, Barabási AL, Schiffer P. What keeps sandcastles standing? Nature. 1997;387(6635):765.

[200] Tegzes P, Vicsek T, Schiffer P. Avalanche dynamics in wet granular materials. Phys Rev Lett. 2002;89(9):094301.

[201] Albert R, Albert I, Hornbaker D, Schiffer P, Barabási AL. Maximum angle of stability in wet and dry spherical granular media. Phys Rev E. 1997;56(6):R6271.

[202] Nowak S, Samadani A, Kudrolli A. Maximum angle of stability of a wet granular pile. Nat Phys. 2005;1(1):50.

[203] Kohonen MM, Geromichalos D, Scheel M, Schier C, Herminghaus S. On capillary bridges in wet granular materials. Physica A. 2004;339(1-2):7–15.

[204] Fournier Z, Geromichalos D, Herminghaus S, Kohonen MM, Mugele F, Scheel M, et al. Mechanical properties of wet granular materials. J Phys Condens Matter. 2005;17(9):S477.

[205] Mason TG, Levine AJ, Ertaş D, Halsey TC. Critical angle of wet sandpiles. Phys Rev E. 1999;60(5):R5044.

[206] Halsey TC, Levine AJ. How sandcastles fall. Phys Rev Lett. 1998;80(14):3141.

[207] Willett CD, Adams MJ, Johnson SA, Seville JP. Capillary bridges between two spherical bodies. Langmuir. 2000;16(24):9396–9405.

[208] Tegzes P, Vicsek T, Schiffer P. Development of correlations in the dynamics of wet granular avalanches. Phys Rev E. 2003;67(5):051303.

[209] Cizeau P, Makse HA, Stanley HE. Mechanisms of granular spontaneous stratification and segregation in two-dimensional silos. Phys Rev E. 1999;59(4):4408.

[210] Faug T, Childs P, Wyburn E, Einav I. Standing jumps in shallow granular flows down smooth inclines. Phys Fluids. 2015;27(7):073304.

[211] Mejean S, Faug T, Einav I. A general relation for standing normal jumps in both hydraulic and dry granular flows. J Fluid Mech. 2017;816:331–351.

[212] Gray JMNT, Tai YC. Particle size segregation, granular shocks and stratification patterns. In: Physics of Dry Granular Media. Springer; 1998. p. 697–702.

[213] Savage SB. Gravity flow of cohesionless granular materials in chutes and channels. J of Fluid Mech. 1979;92(1):53–96.

[214] Altshuler E, Ramos O, Martínez E, Batista-Leyva AJ, Rivera A, Bassler KE. Sandpile formation by revolving rivers. Phys Rev Lett. 2003;91(1):014501.

[215] Altshuler E, Toussaint R, Martínez E, Sotolongo-Costa O, Schmittbuhl J, Måløy K. Revolving rivers in sandpiles: from continuous to intermittent flows. Phys Rev E. 2008;77(3):031305.

[216] Zhu R, Li S, Yao Q. Effects of cohesion on the flow patterns of granular materials in spouted beds. Phys Rev E. 2013;87(2):022206.

[217] Liao C, Hsiau S, Wen S. Effect of adding a small amount of liquid on density-induced wet granular segregation in a rotating drum. Adv Powder Technol. 2016;27(4):1265–1271.

[218] Liu W, Chen S, Li S. Influence of adhesion on random loose packings of binary microparticle mixtures. AIChE J. 2017;63(10):4296–4306.

[219] Yang RY, Zou RP, Dong KJ, An XZ, Yu AB. Simulation of the packing of cohesive particles. Comput Phys Commun. 2007;177(1-2):206–209.

[220] Feng CL, Yu AB. Effect of liquid addition on the packing of mono-sized coarse spheres. Powder technol. 1998;99(1):22–28.

[221] Li J, Cao Y, Xia C, Kou B, Xiao X, Fezzaa K, et al. Similarity of wet granular packing to gels. Nat Commun. 2014;5:5014.

[222] Yang RY, Zou RP, Yu AB. Numerical study of the packing of wet coarse uniform spheres. AIChE J. 2003;49(7):1656–1666.

[223] Woodhouse MJ, Thornton AR, Johnson CG, Kokelaar BP, Gray JMNT. Segregation-induced fingering instabilities in granular free-surface flows. J Fluid Mech. 2012;709:543–580.

[224] Hastie DB, Wypych PW. Segregation During Gravity Filling of Storage Bins. In: IUTAM Symposium on Segregation in Granular Flows. Springer; 2000. p. 61–72.

[225] Ketterhagen WR, Curtis JS, Wassgren CR, Hancock BC. Modeling granular segregation in flow from quasi-three-dimensional, wedge-shaped hoppers. Powder Technol. 2008;179(3):126–143.

[226] Artega P, Tüzün U. Flow of binary mixtures of equal-density granules in hopperssize segregation, flowing density and discharge rates. Chem Eng Sci. 1990;45(1):205–223.

[227] Ketterhagen WR, Curtis JS, Wassgren CR, Hancock BC. Predicting the flow mode from hoppers using the discrete element method. Powder Technol. 2009;195(1):1–10.

[228] Samadani A, Pradhan A, Kudrolli A. Size segregation of granular matter in silo discharges. Phys Rev E. 1999;60(6):7203.

[229] Zhao Y, Yang S, Zhang L, Chew JW. DEM study on the discharge characteristics of lognormal particle size distributions from a conical hopper. AIChE J;.

[230] Nedderman RM, Tüzün U. A kinematic model for the flow of granular materials. Powder Technol. 1979;22(2):243–253.

[231] Gajjar P, Van Der Vaart K, Thornton AR, Johnson CG, Ancey C, Gray JMNT. Asymmetric breaking size-segregation waves in dense granular free-surface flows. J Fluid Mech. 2016;794:460–505.

[232] Nedderman R, Tüzün U, Savage S, Houlsby G. The flow of granular materialsI: Discharge rates from hoppers. Chem Eng Sci. 1982;37(11):1597–1609.

[233] Bertuola D, Volpato S, Canu P, Santomaso AC. Prediction of segregation in funnel and mass flow discharge. Chem Eng Sci. 2016;150:16–25.

[234] Fry AM, Umbanhowar PB, Ottino JM, Lueptow RM. Effect of pressure on segregation in granular shear flows. Phys Rev E. 2018;97(6):062906.

[235] Deng Z, Umbanhowar PB, Ottino JM, Lueptow RM. Continuum modelling of segregating tridisperse granular chute flow. Proc R Soc A. 2018;474(2211):20170384.

[236] Gella D, Maza D, Zuriguel I. Role of particle size in the kinematic properties of silo flow. Phys Rev E. 2017;95(5):052904.

[237] Sela N, Goldhirsch I. Hydrodynamic equations for rapid flows of smooth inelastic spheres, to Burnett order. J Fluid Mech. 1998;361:41–74.

[238] Weinhart T, Hartkamp R, Thornton AR, Luding S. Coarse-grained local and objective continuum description of three-dimensional granular flows down an inclined surface. Phys Fluids. 2013;25(7):070605.

[239] Beverloo WA, Leniger HA, Van de Velde J. The flow of granular solids through orifices. Chem Eng Sci. 1961;15(3-4):260–269.

[240] Dhodapkar S, Jacob K, Kodam M. Determining discharge rates of particulate solids. Chem Eng Prog. 2016;112:50–61.

[241] Anand A, Curtis JS, Wassgren CR, Hancock BC, Ketterhagen WR. Predicting discharge dynamics from a rectangular hopper using the discrete element method (DEM). Chem Eng Sci;.

[242] Zhou Y, Ruyer P, Aussillous P. Discharge flow of a bidisperse granular media from a silo: Discrete particle simulations. Phys Rev E. 2015;92(6):062204.

[243] Madrid M, Asencio K, Maza D. Silo discharge of binary granular mixtures. Phys Rev E. 2017;96(2):022904.

[244] Xu J, Hu Z, Xu Y, Wang D, Wen L, Bai C. Transient local segregation grids of binary size particles discharged from a wedge-shaped hopper. Powder Technol. 2017;308:273–289.

[245] Tian T, Su J, Zhan J, Geng S, Xu G, Liu X. Discrete and continuum modeling of granular flow in silo discharge. Particuology. 2017;.

[246] Zheng Q, Xia B, Pan R, Yu A. Prediction of mass discharge rate in conical hoppers using elastoplastic model. Powder Technol. 2017;307:63–72.

[247] Zhou Y, Lagrée PY, Popinet S, Ruyer P, Aussillous P. Experiments on, and discrete and continuum simulations of, the discharge of granular media from silos with a lateral orifice. J Fluid Mech. 2017;829:459–485.

[248] Mullins W. Experimental evidence for the stochastic theory of particle flow under gravity. Powder Technol. 1974;9(1):29–37.

[249] Medina A, Cordova J, Luna E, Trevino C. Velocity field measurements in granular gravity flow in a near 2D silo. Phys Lett A. 1998;250(1-3):111–116.

[250] Choi J, Kudrolli A, Bazant MZ. Velocity profile of granular flows inside silos and hoppers. J Phys Condens Matter. 2005;17(24):S2533.

[251] Hughes TJ. The finite element method: linear static and dynamic finite element analysis. Courier Corporation; 2012.

[252] Belytschko T, Liu WK, Moran B, Elkhodary K. Nonlinear finite elements for continua and structures. John Wiley & Sons; 2013.

[253] Brooks AN, Hughes TJ. Streamline upwind/Petrov-Galerkin formulations for convection dominated flows with particular emphasis on the incompressible Navier-Stokes equations. Comput Methods Appl Mech Eng. 1982;32(1-3):199–259.

[254] Donea J, Giuliani S, Halleux JP. An arbitrary Lagrangian-Eulerian finite element method for transient dynamic fluid-structure interactions. Comput Methods Appl Mech Eng. 1982;33(1-3):689–723.

[255] Yan J, Korobenko A, Deng X, Bazilevs Y. Computational free-surface fluid–structure interaction with application to floating offshore wind turbines. Comput Fluids. 2016;141:155–174.

[256] Yan J, Deng X, Korobenko A, Bazilevs Y. Free-surface flow modeling and simulation of horizontal-axis tidal-stream turbines. Comput Fluids. 2016;.

[257] Shankar A, Umbanhowar PB, Ottino JM, M LR. Local Segregation Forces and Velocities in Granular Flows. in preparation;.

[258] Guillard F, Marks B, Einav I. Dynamic X-ray radiography reveals particle size and shape orientation fields during granular flow. Sci Rep. 2017;7(1):8155.

[259] Isner AB. A Quantitative Study of Size Segregation in Free Surface Granular Flows. Northwestern University; 2017.

[260] Lagrée PY, Staron L, Popinet S. The granular column collapse as a continuum: validity of a two-dimensional Navier–Stokes model with a μ (I)-rheology. J Fluid Mech. 2011;686:378–408.